Geodesic Geometry Of Some Static Axisymmetric Vacuum Spacetimes

A thesis presented to
The University of Waikato
in partial fulfilment of the thesis requirement
for the degree of

Doctor of Philosophy

by

David M. Harder

The University of Waikato
Te Whare Wānanga o Waikato

The University of Waikato
July 4, 2003

Well, I do not mind telling you I have been at work upon this geometry of Four Dimensions for some time. Some of my results are curious.

— H.G.Wells: The Time Machine (1895) —

Abstract

Solutions of Laplace's equation in terms of bispherical and toroidal coordinates are used to derive new exact exterior (vacuum), general relativistic fields, of static axially symmetric spacetimes.

For each new metric we calculate the first Geroch relativistic multipole moments. By selecting solutions that have even multipole moments, and thus a plane of equatorial symmetry, we numerically generate the timelike geodesics of test particles confined to these planes.

Approximate solutions of these orbits are calculated, from which the precession of the perihelion is compared to that of the numerical results and those predicted by a method of Fernández-Jambrina and Hoenselaers (2001). Similar calculations are done in the bispherical case for the precession rate of the line of nodes of a perturbed circular orbit.

Geodesics of zero angular momentum are also presented for various spacetimes. In general, it is observed that the trajectories of test particles can experience periods of gravitational repulsion. Furthermore, the toroidal solutions show that the period of oscillation of a test particle along the axis of a ring like mass distribution can increase as the mass of the source is increased.

We also consider the application of bicyclide coordinates. In doing so the computation of Lamé-Wangerin functions are required. New results for the eigenfunctions for the Lamé equation of order $-\frac{1}{2}$ are produced. Analytic and numerical results are compared. The multipole moments and timelike geodesics of this solution are also presented.

Acknowledgements

As this thesis comes to completion, I would like to take this opportunity to express my most sincere thanks to several people.

Firstly to those people involved with the Mathematics Department here at the University of Waikato. Special thanks must go to my supervisors Professors Ernie Kalnins and Ian Craig. The ability to ask questions, however trivial, to seek help and guidance at any time was greatly appreciated. Although I must admit, I do feel a little disappointed that I never had the joy of experiencing a ride in Ernie's infamous yellow Hillman nor a demonstration of Ian's belief in the Flying Monk of Cupertino. Of course I must thank Dr.Stephen Joe for his friendliness and help with all things related to computers (and guides to bargains). Thanks to Dr. Paul Watson as well for numerous insightful discussion on numerical matters.

To my fellow PhD students, (in my opinion!) Farhad Ali, Jacob Heerikhuisen and Sivajah Somasundaram, thanks for making G3.02 (and the tea room) a more enjoyable place to work and helping me out in various matters.

On a more personal level I would like to thank all my friends and flatmates from over the years, who no doubt, thought I was crazy to stay at university and not get a job (and therefore money!). So to Sveno, Michael, Dan, Beano, Doey, Skip, Duncan, Wally, Vaughn, Ben, Jas, Kyle, Nic, Inger, Ainz, Gin, Jodes, Megan and especially Kerron who made many unselfish sacrifices through the years here in Hamilton, thanks for being yourselves and having no idea what a Riemannian manifold is - and I suppose putting, up with me. I must mention the hospitality of Jenny, David and Robbie which was like having a home away from home. I would also like to thank two teachers from Katikati College: Mr Wilson for his wit and humor and Mr McKenzie my physics teacher who made science interesting – I still remember to this day the discussion on gravity we had.

Finally, to Mum and Dad. I am so fortunate to have such wonderful parents and I hope this work, in some way, repays you for your love and support given to me through the good and bad times. Without you I would not be who I am, so this work is dedicated to you both.

Contents

List of Figures

List of Tables

Like all other arts, the science of deduction and analysis
is one which can only be acquired by long and patient study,
nor is life long enough to allow any mortal to attain
the highest possible perfection in it.
Before turning to those moral and mental aspects
of the matter which present the greatest difficulties,
let the inquirer begin by mastering more elementary problems.

— Sherlock Holmes: A Study In Scarlet —

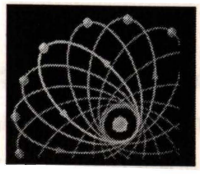

Chapter 1
Introduction

1.1 Thesis Motivation

The simplest geodesic problem in general relativity is concerned with the motions of test particles and photons in the vacuum gravitational field of a spherical body. The solution of Einstein's equations for the metric of such a vacuum field, the Schwarzschild solution, determines the geometrical properties of space and the rate of flow of time near the body which creates the field.

The Schwarzschild spacetime does not exactly represent the gravitational field of astrophysical objects which are, in general, not spherical. It is therefore worth while to investigate, with the help of test particles, the fields of non spherical mass distributions.

For astrophysical problems the deviations from spherical symmetry of greatest interest are those which accompany stellar rotation. Such deviations preserve axial symmetry which enables considerable simplification in the mathematical models of such astrophysical bodies. In some instances, exact solutions are possible.

Further simplifications can be made by assuming that the body is at rest and the deviations from spherical symmetry are related to variations in the mass distribution which creates the field rather than to rotation. Such relativistic fields are known as Weyl fields.

This work is restricted to the study of relativistic static axisymmetric fields. Furthermore we will limit ourselves to the exterior region of the gravitational source. The purpose of this work is to derive new Weyl fields and investigate their geometry via timelike geodesics. Particular emphasis will be made on calculating *exact* solutions.

1.2 Outline

This introductionary chapter provides a summary of results needed to achieve our goals. We begin, from first principles, in deriving the general metric describing a static axially symmetric spacetime satisfying Einstein's vacuum field equations (a Weyl metric). The specific field equations and boundary conditions required so the solutions can be considered as *realistic* are then introduced.

This is followed by a few examples of well known and important Weyl solutions and discussion of their significance.

As we are concerned with non-spherical mass distributions it is natural to introduce the concept of multipole moments. We do so in flat and curved space and show how they differ. Methods for their calculation in Weyl spacetimes are subsequently provided.

The vast majority of geodesic studies concerning Weyl spacetimes has concentrated on those of the Erez-Rosen metric which represents a field of a mass with quadrupole moment (and higher moments). We summarise the derivation of this metric in detail as the method serves as blueprint for subsequent chapters.

We conclude this chapter by discussing how the precession of the perihelia of bounded timelike geodesics can be calculated in terms of (covariant) multipole moments of a given spacetime.

Having established the necessary foundations and concepts we then proceed in the following chapters to calculate new spacetimes and explore their geodesics. In particular, chapter two is concerned with the application of bispherical coordinates. To simplify our task we seek solutions for which a plane of symmetry exists to which timelike geodesics are confined. The orbits of such motions are determined numerically and an approximate analytical solution is derived. Radial type geodesics (i.e. those of zero angular momentum), are also calculated.

Similar results are presented in chapter three where toroidal coordinates are used.

In chapter four bicyclide coordinates are employed. As solutions to Laplace's equation are difficult to find analytically in these coordinates (as we will see is a pivotal requirement for Weyl solutions) the majority of this chapter is spent in obtaining approximate and numerical solutions for the metric functions. Some geodesics are also presented.

1.3 Notations

We shall use a metric with the signature $(+,-,-,-)$. Generally geometrized units in which $c = G = 1$, c being the velocity of light in vacuum and G the gravitational constant are used. In the vacuum metrics of general relativity sources appear as singularities. By a physical singularity we will mean a location in spacetime where a curvature scalar is infinite, in particular we shall compute* the Kretschmann scalar

$$K := R_{abcd}R^{abcd}$$

to check for the existence of a physical singularity (Bonnor, 1992; Hawking and Ellis, 1973).

1.4 Axisymmetric Static Solutions of Einstein's Vacuum Field Equations

The initial work on static axially symmetric solutions of the Einstein field equations was done by Weyl (1917) and Levi-Civita (1918) shortly after the development of general relativity.

In addition to being of relevance to astrophysical problems (Morgan and Morgan, 1970; Semerák *et al.*, 1999a) and as possible final states of gravitational collapse (Doroshkevich *et al.*, 1966; Zel'dovich and Novikov, 1967), Weyl (i.e. static, axially symmetric) metrics are also of interest simply because they present us with the rare opportunity of explicitly determining and investigating a large class of relativistic metrics.

In principle all of the Weyl metrics are known since there exists a precise algorithm for generating them from an infinite set of Newtonian potential functions. In practice however the global structure of only a few such solutions is well understood.

In Newtonian physics the axial symmetry of a gravitational field is easily defined: by using cylindrical coordinates (ρ, z, φ) with $\rho = 0$ being the axis of symmetry, then the gravitational potential is independent of the azimuthal angle φ. We shall now formulate the analogous problem for general relativity. The following is given by Synge (1960).

Let $\mathcal{M}$ be a four dimensional Riemann manifold (without torsion) with the metric $g_{\mu\nu}$ $(\mu, \nu = 0, 1, 2, 3)$. If the spacetime is to be axisymmetric we require that the metric coefficients be independent of the azimuthal angle φ.

By introducing a stationary condition we also make them independent of t. Ten functions of two coordinates still remain - we now suppose φ and t to be reversible in the sense that the metric is unchanged if φ is replaced $-\varphi$ or t by $-t$. The physical meaning of this additional requirement is that the spacetime we are considering is not rotating†.

We note however, if the condition of simultaneous inversion is applied, that is $\varphi \to -\varphi$

*The symbolic software MAPLE is used to perform the necessary calculations.

†An intrinsic (coordinate independent) characterization of static axisymmetric spacetimes based on the existence of two Killing vectors can be found in Kramer *et al.* (1980), for example.

and $t \to -t$, then the metric is that of a rotating body. Details of this generalization can be found in Islam (1985).

The assumed invariances requires the metric to contain $d\varphi$ and dt only as squares, or

$$ds^2 = g_{tt}dt^2 - g_{\varphi\varphi}d\varphi^2 - \Psi \tag{1.1}$$

$$\Psi = g_{11}(dx^1)^2 + 2g_{12}dx^1dx^2 + g_{22}(dx^2)^2 \tag{1.2}$$

where $g_{\mu\nu} = g_{\mu\nu}(x^1, x^2)$ and we have five unknown functions. A further simplification can be made and reduce the number of unknown functions to three, the essential step is to use coordinates (x^1, x^2) for which Ψ has the diagonal form

$$\Psi = \alpha^2\left[(dx^1)^2 + (dx^2)^2\right] \tag{1.3}$$

where α is a function of (x^1, x^2) and so we can now write the general line element as

$$ds^2 = \zeta^2\, dt^2 - \beta^2\, d\varphi^2 - \alpha^2\,\left[(dx^1)^2 + (dx^2)^2\right] \tag{1.4}$$

where α, β, ζ are functions of (x^1, x^2).

From (1.4) the Ricci tensor has the components

$$R_{11} = \left(\frac{\alpha_1}{\alpha}\right)_1 + \left(\frac{\alpha_2}{\alpha}\right)_2 + \frac{\beta_{11}}{\beta} + \frac{\zeta_{11}}{\zeta} + \frac{\alpha_2}{\alpha}\left(\frac{\beta_2}{\beta} + \frac{\zeta_2}{\zeta}\right) - \frac{\alpha_1}{\alpha}\left(\frac{\beta_1}{\beta} + \frac{\zeta_1}{\zeta}\right) \tag{1.5}$$

$$R_{22} = \left(\frac{\alpha_1}{\alpha}\right)_1 + \left(\frac{\alpha_2}{\alpha}\right)_2 + \frac{\beta_{22}}{\beta} + \frac{\zeta_{22}}{\zeta} + \frac{\alpha_1}{\alpha}\left(\frac{\beta_1}{\beta} + \frac{\zeta_1}{\zeta}\right) - \frac{\alpha_2}{\alpha}\left(\frac{\beta_2}{\beta} + \frac{\zeta_2}{\zeta}\right) \tag{1.6}$$

$$R_{12} = \frac{\beta_{12}}{\beta} + \frac{\zeta_{12}}{\zeta} - \frac{\alpha_2}{\alpha}\left(\frac{\beta_1}{\beta} + \frac{\zeta_1}{\zeta}\right) - \frac{\alpha_1}{\alpha}\left(\frac{\beta_2}{\beta} + \frac{\zeta_2}{\zeta}\right) \tag{1.7}$$

$$R_{33} = \frac{\beta}{\alpha^2}\left(\Delta\beta + \frac{1}{\zeta}\left(\beta_1\zeta_1 + \beta_2\zeta_2\right)\right) \tag{1.8}$$

$$R_{44} = -\frac{\zeta}{\alpha^2}\left(\Delta\zeta + \frac{1}{\beta}\left(\beta_1\zeta_1 + \beta_2\zeta_2\right)\right) \tag{1.9}$$

where the subscripts on the right refer to partial derivatives with respect to x^1 and x^2 and

$$\Delta\beta = \beta_{11} + \beta_{22}$$

and so forth. In particular we have

$$\begin{aligned} R_3^3 + R_4^4 &= \beta^{-2}R_{33} - \zeta^{-2}R_{44} \\ &= \frac{1}{\alpha^2\beta\zeta}\Delta(\beta\zeta). \end{aligned} \tag{1.10}$$

As we are concerned with vacuum solutions the field equations are

$$R_{\mu\nu} = 0$$

and so from (1.10) we have $\Delta(\beta\zeta) = 0$, and thus it follows that $\beta\zeta$ is a harmonic function. We can therefore write $\beta\zeta = \rho(x^1, x^2)$ and introduce the harmonic function $z(x^1, x^2)$ such that

$$\rho + iz = f(x^1 + i\,x^2)$$

where f is an analytic function. By the (conformal) transformation $(x^1, x^2) \to (\rho, z)$ we can now write

$$\begin{aligned} \Psi &= \alpha^2 \left[(dx^1)^2 + (dx^2)^2\right] \\ &= A(\rho, z)\left(d\rho^2 + dz^2\right). \end{aligned} \tag{1.11}$$

Thus in any domain in which the conditions of axial symmetry are satisfied and in which $R_3^3 + R_4^4 = 0$ the metric is reducible to

$$ds^2 = e^{2\psi}dt^2 - e^{2\gamma-2\psi}(d\rho^2 + dz^2) - \rho^2 e^{-2\psi}d\varphi^2 \tag{1.12}$$

where ψ and γ are functions of (ρ, z).

From the Ricci components we have

$$\tfrac{1}{2}(R_{11} + R_{22}) = \Delta\gamma - \left(\Delta\psi + \frac{\psi_1}{\rho}\right) + \psi_1^2 + \psi_2^2 \tag{1.13}$$

$$\tfrac{1}{2}(R_{11} - R_{22}) = \psi_1^2 - \psi_2^2 - \frac{\gamma_1}{\rho} \tag{1.14}$$

$$R_{12} = 2\psi_1\psi_2 - \frac{\gamma_2}{\rho} \tag{1.15}$$

$$R_3^3 - R_4^4 = -\frac{2}{\alpha^2}\left(\Delta\psi + \frac{\psi_1}{\rho}\right) \tag{1.16}$$

or from the vacuum equations we obtain

$$\frac{\partial^2\psi}{\partial\rho^2} + \frac{1}{\rho}\frac{\partial\psi}{\partial\rho} + \frac{\partial^2\psi}{\partial z^2} = 0 \tag{1.17}$$

$$\frac{\partial\gamma}{\partial\rho} = \rho\left\{\left(\frac{\partial\psi}{\partial\rho}\right)^2 - \left(\frac{\partial\psi}{\partial z}\right)^2\right\} \tag{1.18}$$

$$\frac{\partial\gamma}{\partial z} = 2\rho\frac{\partial\psi}{\partial\rho}\frac{\partial\psi}{\partial z} \tag{1.19}$$

Equation (1.17) is recognized as Laplace's equation in cylindrical* coordinates (ρ, z, φ) in Euclidean 3-space for a function which is independent of φ.

If (1.17) is satisfied then (1.18) and (1.19) are integrable. Thus γ can be calculated to within an additive constant by

$$\gamma = \int \rho\left[(\psi_\rho^2 - \psi_z^2)\,d\rho + 2\,\psi_\rho\psi_z\,dz\right] \tag{1.20}$$

where the path of integration is any domain in which the vacuum equations are satisfied. We note although $\nabla^2\psi = 0$ is a linear partial differential equation, the equations for γ manifest the non-linearity of the Einstein field equations.

Therefore there is a straightforward method of obtaining static, axisymmetric, vacuum, general relativistic fields. Namely choose an appropriate Newtonian gravitational field and complete the process by integrating (1.20). As we will see in following sections, the true physical significance of a new solution can be difficult to isolate and quite often shows *no* resemblance to the Newtonian potential (ψ) from which it is generated.

*Often referred to as (canonical) Weyl coordinates.

1.5 Metric Boundary Conditions

Clearly for a solution to be physically relevant the metric functions ψ and γ must satisfy not only the Einstein vacuum field equations but also other conditions which follow from simple physical considerations.

The line element must reduce to the Minkowski metric at spatial infinity. This means that the gravitational field vanishes at large distances from the gravitational source i.e. it is asymptotically flat. From (1.12) we have the requirements

$$\lim_{\rho\to\infty} \psi(\rho, z) = 0 \tag{1.21}$$

$$\lim_{\rho\to\infty} \gamma(\rho, z) = 0. \tag{1.22}$$

Furthermore the metric must be invariant under the transformation $\varphi \to \varphi + 2\pi$.

The *singularities* of ψ will refer to sources of the gravitational field, but the metric

$$ds^2 = e^{2\psi}dt^2 - e^{2\gamma-2\psi}(d\rho^2 + dz^2) - \rho^2 e^{-2\psi}d\varphi^2 \tag{1.23}$$

may also have singularities representing stresses on the z-axis. Singularities of this type are called *conical* singularities (Bonnor, 1992).

To avoid such singularities we must have for any infinitesimal spacelike circle, the ratio of circumference to radius shall be 2π, of course the dangerous place is the z axis; if we take a small circle on which (ρ, z, t) are constant, with ρ infinitesimal, it is easy to see from the metric (1.23) that the requirement is satisfied if (Bergmann, 1942; Synge, 1960; Szekeres, 1968)

$$\lim_{\rho\to 0} \gamma(\rho, z) = 0. \tag{1.24}$$

1.6 Examples

Here we present a short summary of a few well known axisymmetric spacetimes. This is only a small selection of the many exact solutions known. Further examples and discussion can be found (for example) in Bonnor (1992); Kramer *et al.* (1980) or Scott (1988).

We refer to mass 'multipoles' in the following examples, a discussion on which is found in a following section, and how they must be redefined in curved space. Nevertheless for this section the classical (flat) definition will suffice: the coefficients of the potential ψ when written in terms of spherical coordinates.

1.6.1 Curzon Solution

The mathematically simplest example belonging to the Weyl class of metrics is the gravitational field produced by a spherically symmetric mass distribution with total mass m which is located at the origin of the cylindrical coordinate system. This is the Curzon (1924) solution in which

$$\psi = -\frac{m}{\sqrt{\rho^2 + z^2}} \equiv -\frac{m}{r} \tag{1.25}$$

$$\gamma = -\frac{m^2\rho^2}{2(\rho^2 + z^2)^2}. \tag{1.26}$$

Although generated by the Newtonian mass monopole, it is *not* equivalent to the Schwarzschild metric, which is known to be the unique spherically symmetric vacuum solution (Birkhoff's theorem). It's far field is that of a mass at $r = 0$ with multipole structure. Despite the ease with which it is generated, its source structure and global structure remained a mystery until the papers of Scott and Szekeres (1986a,b). It has no horizon (g_{tt} does not vanish for $r > 0$) but has a curvature (naked) singularity at $r = 0$.

One of the lessons which was learned from this solution is the *directional character* of the singularity at $r = 0$. The limit of the Kretschmann curvature scalar depends on the direction of approach to the singularity (Gautreau and Anderson, 1967). $K \to 0$ as $r \to 0$ along the z-axis, but $K \to \infty$ as $r = 0$ is approached from any other direction.

This suggested that the Weyl coordinates might be extensible through the singularity. Scott and Szekeres (1986a,b) showed this to be true and showed that the Curzon singularity is a ring (that is, rings comprised of curvature singularities occurring in the hyper-surfaces $t =$ constant of the Weyl space-times) on which some time-like geodesics terminate.

These rings are known to be a common feature throughout the *entire* Weyl class. That the Weyl metrics should exhibit singularities in the form of rings is not surprising, since all metrics in the class are axisymmetric.

Recently Bičák *et al.* (1993) have shown that the Curzon solution can arise as the metrics of counter-rotating relativistic disks. Interior solutions for $0 < r_0 < r$ matched to the Curzon metric are also known (Hernandez, 1967; Marek, 1967).

1.6.2 The Two-Particle Curzon Solution

The Curzon solution can be generalized in an obvious manner. The two-particle Curzon solution, which will come as no surprise, was discovered by Curzon (1924)*. It holds a special place in the hierarchy of exact solutions in general relativity and as Scott (1988) comments no survey of the Weyl metrics would be complete without mentioning it.

This solution which is probably the most enlightening of all exact solutions is generated by the Newtonian potential of two point masses of mass m_1 and m_2. For the mass configuration

*There seems a little confusion here. Scott (1988) claims that this solution was indeed discovered first by Curzon, however Bonnor (1992) claims it was Bach and Weyl in 1922. This is also supported by Misra (1960).

to be axisymmetric the two particles must both lie along the z axis at z_1 and z_2 respectively ($z_1 > z_2$). The metric terms are

$$\psi = -\frac{m_1}{R_1} - \frac{m_2}{R_2} \tag{1.27}$$

where

$$R_{1,2} = \sqrt{\rho^2 + (z - z_{1,2})^2} \tag{1.28}$$

and

$$\gamma = -\frac{1}{2}\rho^2 \left[\frac{m_1^2}{R_1^4} + \frac{m_2^2}{R_2^4}\right] + \frac{2m_1 m_2}{(z_2 - z_1)^2}\left[\frac{\rho^2 + (z - z_1)(z - z_2)}{R_1 R_2} - 1\right]. \tag{1.29}$$

Clearly ψ refers to two Curzon particles on the axis of symmetry. This is a static solution, therefore, how can a static (vacuum) solution consisting only of two point masses be at rest? Two masses at rest in vacuum should gravitate. This observation lead Silberstein (1936) to claim that the general theory of relativity was incorrect. Einstein and Rosen (1936) subsequently showed that in fact the two particle solution is *not* a purely vacuum solution and provided the following argument (Scott, 1988).

Consider a small circle given by t = constant, z = constant $(z_1 < z < z_2)$, ρ = constant and small. The circumference C and radius R of this circle as $R \to 0^+$ behaves as

$$C/R \to 2\pi\, e^{-\gamma} \quad \text{where} \quad \gamma = \gamma(0, z). \tag{1.30}$$

Now for $z_1 < z < z_2$, $\gamma(0, z) \neq 0$ and so C/R does not approach 2π as $R \to 0^+$. Hence the spacetime violates the condition of elementary flatness on the section of the axis between the two particles suggesting the existence of a strut holding them apart and explaining the static nature of the solution.* Furthermore Bonnor (1992) comments that the *matter* of this strut is precisely the sort that has zero active gravitational mass. Therefore it will exert no gravitational field (Israel, 1977) and hence does not appear in (1.27).

Interestingly Szekeres (1968) showed that static, two body solutions can exist in general relativity provided at least one of the two point masses is endowed with a multipole mass structure. This allows equilibrium to be achieved without the need for an intervening strut.

Furthermore Dietz and Hoenselaers (1982) using techniques to generate stationary solutions from static ones obtained from the two particle Curzon solution a stationary axisymmetric solution representing two particles precisely balanced by their spin-spin interaction. This solution is also a purely vacuum solution and no strut is required.

1.6.3 The Zipoy-Voorhees Metric

Various studies of the Weyl solutions indicated explicitly how important it is to always check whether a result is not just a consequence of the choice of coordinates. Consider the Zipoy-Voorhees metrics, which are a subclass of Weyl metrics. These solutions are generated by

*This lack of elementary flatness, i.e. lack of differentiability as the metric is only C_0 at the center of the circle considered gives via the Einstein equations rise to a non-vanishing energy momentum tensor. This energy momentum tensor has the form of a δ function and describes consequently a line source (Fodor *et al.*, 1989).

the Newtonian potential of a constant density *line* mass with total mass m and (coordinate) length l, which is located along the z-axis with the mid point at the origin:

$$\psi = \frac{m}{2l} \ln \frac{R_1 + R_2 - 2l}{R_1 + R_2 + 2l} \tag{1.31}$$

$$\gamma = -\frac{m^2}{2l^2} \ln \left[\frac{4R_1 R_2}{(R_1 + R_2)^2 - 4l^2} \right] \tag{1.32}$$

where

$$R_{1,2} = \sqrt{(z \pm l)^2 + \rho^2}. \tag{1.33}$$

This metric was first derived by Bach and Weyl (1922). It has since been discussed and investigated to a varying extent by numerous authors (Zipoy, 1966; Gautreau, 1969; Voorhees, 1970; Cooperstock and Junevicus, 1974) and is more commonly referred to as the Voorhees or Zipoy-Voorhees metric or the γ-metric.

Again this metric has a directional singularity if $m > 2l$, but not for $m < 2l$ (Gautreau and Anderson, 1967). At infinity the metric represents an isolated body with monopole and higher mass moments. An interior solution for it has been given by Stewart *et al.* (1982)

The Curzon metric is obtained by letting $l \to 0$ and keeping m finite. The Schwarzschild metric is obtained when $l = m$. Thus in Weyl coordinates the Newtonian potential ψ corresponding to the Schwarzschild solution is that of a finite rod with mass density $1/2$ and length $2m$.

1.7 Aspects Relating To This Thesis

Let us make precise the meaning of the terms *solution* and *source*. In referring to a solution of the field equations, we mean a metric $g_{\mu\nu}$ which satisfies the static axially symmetric vacuum field equations. This metric is then to be thought of as the exterior solution for some configuration of matter referred to as the source. For example, the Schwarzschild metric can be considered as the exterior gravitational field of a spherically symmetric shell of matter, which would then be referred to as the source.

The idea of fitting a coordinate system to the problem at hand is not new and is frequently used in physics. It has been established earlier in this chapter that the Weyl coordinates (ρ, z) can be tentatively regarded as cylindrical (they are actually the analog to the cylindrical coordinates in flat space), it is then natural, in the quest for solutions of Laplace's equation (fundamental in the construction of any Weyl field) to go one step further, guided by the symmetries of the source configuration, and consider other coordinates which are related in the usual way to the cylindrical coordinates of flat space.

Throughout this thesis, it will be assumed that coordinates (x^α) are chosen; these are adapted to the symmetries of the source in the sense that the exterior solutions obtained will be valid outside of some hypersurface $x^1 = \text{const.}$ and this hypersurface will be said to correspond to the (surface of the) source.

The method employed throughout this thesis then is to explore Weyl-type coordinate systems whose eigensolutions, that is the solutions ψ and γ which result when separable solutions of Laplace's equation are used, can represent exteriors of bounded, physical sources. This thesis will consider several exact solutions of Einstein's equations. Regarding the astrophysical motivation, those solutions that are relevant and therefore studied here are generally (exceptions arise in the bicyclide chapter) those that do not contain struts (the two particle Curzon solution for example) and membranes - the supporting singularities, the presence of which indicates that a given system of sources cannot remain static according to the field equations.

We reiterate however, that no matching of interior to exterior solutions is considered in this work, although an extension of the thesis does naturally lead to potential applications of matter-vacuum matching problems.

1.8 Multipole Moments

It is apparent from the examples given in section 1.6 that in general there is no correspondence between the geometry of the source for a Weyl metric, and the geometry of the Newtonian source from which it is generated*. How then can we obtain some meaningful physical interpretation of a newly generated Weyl solution?

One means of constructing an intuitive picture in *Newtonian* theory is provided by multipole moments. Given that Newtonian theory is contained in Einstein's theory perhaps one can gain some information about the gravitational field by calculating the corresponding Newtonian limit of the metric. Unfortunately, it will be shown that this limit is not unique and depends on the choice of coordinates (Thorne, 1980) and thus a covariant means of calculating the multipole moments of the source is required.

1.8.1 Overview

Multipole moments give useful information about the gravitational field of an isolated source. In Newtonian theory they can be calculated by appropriately weighted integrals over the source. Such a prescription is also available in general relativity and defines the so-called Dixon moments (Hoenselaers, 1992). Furthermore in Newtonian theory there is also the possibility of reading off the moments from the gravitational far field and they agree as the theory is linear with the source moments. For relativistic stationary fields, far field moments can be defined, however there is no link known between them and the source moments.

The multipole moments of solutions of Einstein's equation might similarly suggest interpretations of these fields. For example, if a Newtonian potential exists having the same multipole structure as a given solution of Einstein's equation, that potential could be regarded as the Newtonian analog of the given solution. One would not expect however, that all fea-

*Furthermore, there is not a strict $1-1$ correspondence between the Weyl metrics and their generating Newtonian potentials, for example there exists four distinct Newtonian potentials which generate flat space! (Scott, 1988).

tures of Newtonian multipole moments will survive the transition to general relativity, for curvature is likely to destroy the moments in regions near the sources. However, the moments may reappear as the curvature dies away, that is for large distances from the sources. Thus it would be reasonable to expect that multipole moments exist for asymptotically flat space times and these moments should be quantities at infinity.

Geroch (1970a,b) considered multipole moments in curved, static, asymptotically flat and empty spacetimes and proposed a covariant and thus coordinate-invariant definition for them. We shall be interested in these moments throughout this thesis.

Geroch's definition was generalized by Hansen (1974) to include stationary fields. Clarke and Sciama (1971) defined multipole moments for static fields by using Sommerfelds's method for solving Poisson's equation although this work is coordinate dependent. Another coordinate dependent definition of multipole moments was proposed by Thorne (1980) although the coordinates were investigated from a physical point of view and a method for choosing suitable coordinates was given. Beig and Simon (1981a,b) formulated a coordinate independent definition by using the previous works of Geroch and Hansen.

1.8.2 Classical Definitions

Since Newton's gravitation theory is contained in Einstein's theory as a special case one can investigate certain cases of a given metric in order to understand its physical meaning and structure*. One of these limiting cases is the linear approximation which involves the gravitational field at large distances from the source. The explicit calculation of the linear approximation is related to the coordinates in which the metric is given.

The linearized line element can be written (Misner *et al.*, 1973)

$$ds^2 = c^2\left(1+\frac{2\Phi}{c^2}\right)dt^2 - \left(4\epsilon_{ijk}J^j\frac{x^k}{r^3}+A_i\right)dt\,dx^i - \left[\left(1-\frac{2\Phi}{c^2}\right)\delta_{ij}+A_{ij}\right]dx^i dx^j \qquad (1.34)$$

where $i,j,k = 1,2,3$. A_{ij} are time-dependent quantities of order $O(r^{-1})$ which lead to the appearance of gravitational waves. We shall be concerned with static fields thus we will neglect these quantities and likewise the angular momentum J^i can be eliminated (the source static, i.e. is not rotating). The quantities A_i are of $O(r^{-3})$. They determine higher order moments of the angular momentum distribution. The function Φ satisfies Poisson's equation

$$\nabla^2\Phi = 4\pi\mu \qquad (1.35)$$

where μ = mass density. Thus we conclude that Φ represents the Newtonian gravitational potential. As we are interested in axisymmetric fields, solutions of (1.35) can be written in terms of spheroidal harmonics

$$\begin{aligned}\Phi(\mathbf{x}) &= -G\int\frac{\mu(\mathbf{x}')}{|\mathbf{x}-\mathbf{x}'|}\,d^3x' \\ &= -G\sum_{l=0}^{\infty}\frac{P_l(\cos\theta)}{r^{l+1}}\int\mu(\mathbf{x}')r'^l P_l(\cos\theta')\,d^3x' \qquad (1.36)\end{aligned}$$

*We shall explicitly include the velocity of light in vacuum c and G the gravitational constant in this section.

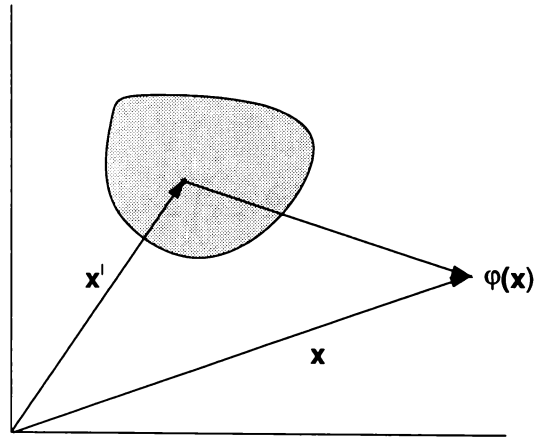

FIGURE 1.1: *Coordinates employed for spheroidal harmonic expansion for the potential at* $\mathbf{x}$ *of a body who's elements have position* $\mathbf{x}'_{\mathbf{i}}$.

where $P_l(\cos\theta)$ are Legendre polynomials. We define the multipole moments of a mass distribution of density $\mu(\mathbf{x}')$ as

$$\mathcal{M}_l = \int \mu(\mathbf{x}') r'^l P_l(\cos\theta')\, d^3x'.$$

Then the Newtonian gravitational potential of an axisymmetric distribution is

$$\Phi(\mathbf{x}) = -G\sum_{l=0}^{\infty} \frac{\mathcal{M}_l}{r^{l+1}} P_l(\cos\theta). \tag{1.37}$$

The monopole moment, $\mathcal{M}_0 = M$, is the total mass of the system. The dipole moment $\mathcal{M}_1$ can be made to vanish by a change of coordinates so that the new systems origin is located at the center of mass of the distribution. The mass quadrupole moment is defined as

$$\mathcal{M}_2 = Q = \frac{1}{2}\int \mu(\mathbf{x}') \left[3(x'^3)^2 - r'^2\right] d^3x'. \tag{1.38}$$

For a prolate source $Q > 0$. If $Q = 0$ then the mass distribution is spherically symmetric, and if $Q < 0$ then the source is oblate.

One can calculate all multipole moments of a given metric by investigating the respective expansion in inverse powers of a *suitable radial coordinate*. The multipole moments can then be obtained in the static case, from the metric coefficients g_{tt}. Although it must be remembered that this computation is coordinate dependent. For example, consider the Schwarzschild metric:*

1. In spherical coordinates

$$ds^2 = c^2\left(1 - \frac{2GM}{c^2 r}\right)dt^2 - \left(1 - \frac{2GM}{c^2 r}\right)^{-1} dr^2 - r^2\left(d\theta^2 + \sin^2\theta\, d\varphi^2\right).$$

Clearly from (1.34) and (1.37) we have $\mathcal{M}_0 = M$ with all other moments null. Thus the Schwarzschild metric describes the gravitational field of a spherically symmetric mass distribution of total mass M.

*This example is from Quevedo (1990).

2. In isotropic coordinates the coordinate R is related to the radial coordinate by

$$r = R\left(1 + \frac{GM}{2c^2R}\right)^2$$

the metric reads

$$ds^2 = \left(\frac{1 - \frac{GM}{2c^2R}}{1 + \frac{GM}{2c^2R}}\right)^2 dt^2 - \left(1 + \frac{GM}{2c^2R}\right)^4 \left[dR^2 + R^2\left(d\theta^2 + \sin^2\theta\, d\varphi^2\right)\right].$$

Expanding g_{tt} in inverse powers of R we have

$$g_{tt} \sim 1 - 2\frac{GM/c^2}{R} + 2\frac{(GM/c^2)^2}{R^2} + \cdots$$

implying the multipole values

$$\mathcal{M}_0 = M, \qquad \mathcal{M}_1 \propto -(GM/c^2)^2,$$

and hence, in isotropic coordinates the Schwarzschild metric appears to represent the gravitational field of a non spherically symmetric source.

It is clear from this simple example that the determination of the multipole moments is reliant upon the coordinates used to determine them. The comments of Bondi and Rindler (1991) seem particularly applicable here,

> *"Non-linearity is such an integral feature of general relativity that we did not feel it profitable to look at the purely linear approximations, even far from the source, where deviations from flat space are bound to be small, but the featureless character of Minkowski space makes it difficult to separate relevant deviations from coordinate peculiarities."*

1.8.3 Geroch Multipole Moments

We now briefly describe the Geroch multipole moments corresponding to a static axisymmetric field. There importance is based on the fact that they are defined in a covariant fashion and thus are coordinate independent.

This section is a summary of the works of Hansen (1974); Geroch (1970b); Quevedo (1990) and Hernãndez-Pastora and Martin (1994). Further details can be found in these references.

Recall that in Newtonian gravity the mass multipole moments can be defined in two equivalent forms. Firstly, as moments of a mass distribution (see (1.36)) if the mass density is known, or secondly as the coefficients of the multipole expansion given by (1.37). The following definition was proposed by Geroch (1970b).

The multipole moments are conformal Killing tensors in an Euclidean space $\mathcal{N}$ with the metric h_{ij}. Thus the tensors $\xi^{ij\cdots}$ satisfy the equation $\nabla^{(i}\xi^{jk\ldots l)} = h^{(ij}T^{k\ldots l)}$, where ∇ is the gradient operator in $\mathcal{N}$ and $T^{k\ldots l}$ is an arbitrary tensor in $\mathcal{N}$.

The multipole moments of a solution of $\nabla^2\phi = 0$ in flat space, whose solution is

$$\phi = r^{-1}Q + r^{-3}Q_i x^i + \tfrac{1}{2}r^{-5}Q_{ij}x^i x^j + \cdots \tag{1.39}$$

where $\mathbf{x}$ is the vector and r its norm, are the set of totally symmetric, trace-free, independent matrices $Q, Q_i, Q_{ij}, \ldots$. Suppose that these matrices are defined at the origin of the coordinates which is not related to a given point but it can be any arbitrary point of $\mathcal{N}$. Then the matrices $Q, Q_i, Q_{ij}, \ldots$ are Killing tensor fields.

Due to the coordinate invariance and covariant character of this interpretation, one can expect that the corresponding generalization to general relativity permits a similar relativistic definition for multipole moments with the same properties.

This idea was developed by Geroch (1970b) for static and by Hansen (1974) for stationary asymptotically flat solutions of Einstein's vacuum equations.

Let $\mathcal{M}$ be a torsion free four-dimensional Riemannian manifold with the metric g_{ab} which has signature $(+---)$ and satisfies Einstein's vacuum field equations. Let ξ^a be a timelike Killing vector field defined in $\mathcal{M}$. The norm f, and twist ω_a are defined by

$$f = \xi^a \xi_a, \qquad \omega_a = \epsilon_{abcd}\, \xi^b \nabla^c \xi^d. \tag{1.40}$$

The vacuum field equations require $\nabla_{[a}\omega_{b]} = 0$, thus there exists a scalar field Ω satisfying $\omega_a = \nabla_a \Omega$. The set $\mathcal{S}$ of trajectories of ξ^a in $\mathcal{M}$ is (at least locally) a differentiable manifold with the metric

$$s_{ij} = g_{00} g_{ij} + g_{0i} g_{0j}.$$

The following definition given by Geroch guarantees the curvature of $\mathcal{S}$ dies away at large distances from the sources. This amounts to adding the "point at infinity" (Λ) to the manifold $\mathcal{S}$ by means of a conformal transformation. The asymptotic behaviour of a field in $\mathcal{S}$ is then determined by the behaviour at Λ.

A three-dimensional manifold $\mathcal{S}$ with metric s_{ij} is called asymptotically flat if there exists a manifold $\tilde{\mathcal{S}}$ with the metric $\tilde{s}_{ij}$ which satisfies the following conditions:

1. $\tilde{\mathcal{S}} = \mathcal{S} \cup \Lambda$ where Λ is a single point.
2. $\tilde{s}_{ij} = \Theta^2 s_{ij}$ where Θ is a scalar field defined on $\tilde{\mathcal{S}}$.
3. $\Theta|_\Lambda = 0, \quad \tilde{D}_i \Theta|_\Lambda = 0, \quad \tilde{D}_i \tilde{D}_j \Theta|_\Lambda = 2\tilde{s}_{ij}|_\Lambda$.

Here $\tilde{D}_i$ represents the covariant derivative operator associated with $\tilde{s}_{ij}$. For example, Euclidean 3-space is asymptotically flat in this sense: choose the conformal factor $\Theta = r^{-2}$, where r is the distance from the origin.

Furthermore, one introduces the scalar fields*

$$\Phi^M = \frac{1}{4f}\left(f^2 + \Theta^2 - 1\right), \qquad \tilde{\Phi}^M = \frac{1}{\sqrt{\Theta}}\Phi^M \tag{1.41}$$

in $\tilde{\mathcal{S}}$ and defines the symmetric, trace-free tensor fields $P^M_{a_1 \ldots a_l}$ by

$$\begin{aligned} P^M &= \tilde{\Phi}^M \\ P^M_{a_l \ldots a_{l+1}} &= \mathcal{C}\left[\tilde{D}_{a_{l+1}} P^M_{a_1 \ldots a_l} - \frac{1}{2} l\,(2l-1)\tilde{R}_{a_l a_{l+1}} P^M_{a_2 \ldots a_{l-1}}\right] \end{aligned}$$

*There also exist scalar fields corresponding to the angular momentum distribution, but as we are considered with static fields we omit these terms.

where $\mathcal{C}[T_{a\ldots c}]$ denotes the totally symmetric trace-free part of $T_{a\ldots c}$ and $\tilde{R}_{a_1a_2}$ is the Ricci tensor in $\tilde{\mathcal{S}}$ and is present to ensure the correct behaviour of the moments under an additional conformal rescaling of $\tilde{s}_{ij}$. This conformal rescaling of the unphysical metric $\tilde{s}_{ij}$ reflects a change of origin respective to which to the moments are defined in the unphysical manifold $\tilde{\mathcal{S}}$. The 2^l-pole (mass) moments of Φ^M are determined by the value of the *tensors* $P^M_{a_l\ldots a_l}$ at Λ

$$M_{a_1\ldots a_l} = P^M_{a_1\ldots a_l}|_\Lambda. \tag{1.42}$$

It is natural to ask whether this definition when applied to a Newtonian potential in Euclidean space produces the usual multipole moments for that system. For illustrative purposes, let ϕ be a Newtonian potential, which clearly satisfies $\nabla^2\phi = 0$ in Euclidean space. Then ϕ possesses a multipole-moment expansion of the form given by (1.39).

Define the new position vector $\bar{x}^a = r^{-2}x^a$ with respect to the origin *at infinity*. The series (1.39) expressed in terms of $\bar{x}^a$ takes the form

$$\phi = r^{-1}Q + r^{-1}Q_a\bar{x}^a + \tfrac{1}{2}r^{-1}Q_{ab}\bar{x}^a\bar{x}^b + \cdots. \tag{1.43}$$

It was noted above that $\Omega = r^{-2}$ is an appropriate choice of conformal factor for completing Euclidean 3-space. Making this choice, and setting $\tilde{\phi} = \Omega^{-1/2}\phi$ we have

$$\tilde{\phi} = Q + Q_a\bar{x}^a + \tfrac{1}{2}Q_{ab}\bar{x}^a\bar{x}^b + \cdots \tag{1.44}$$

and it follows then

$$Q = \tilde{\phi}|_\Lambda, \qquad Q_a = \tilde{D}_a\tilde{\phi}|_\Lambda, \qquad Q_{ab} = \tilde{D}_a\tilde{D}_b\tilde{\phi}|_\Lambda, \ldots \tag{1.45}$$

where $\tilde{D}_a$ is the derivative operator associated with s_{ij}. We note that these expressions coincide, in the case of zero curvature, with those of (1.42). Thus this formulation applied to a Newtonian potential in flat space yields the correct values for the multipole moments of the system.

Recall that multipole moments of a system are implicitly defined with respect to some origin, and depend on this choice of origin. The behaviour of the Newtonian multipole moments under a change of origin is also reflected in this new formulation under a change of conformal factor.

The conditions (1)-(3) above for asymptotic flatness do not determine the conformal factor uniquely. In fact, one can choose any conformal factor Ω' of the form

$$\Omega' = \Omega w$$

where Ω is a conformal factor satisfying conditions (1)-(3) and w is any smooth function whose value at Λ is unity. Since arbitrary conformal transformations can be generated by repeated application of infinitesimal ones, it suffices to consider the case in which w differs infinitesimally from 1.

The multipole moments which result from the use of the conformal factor Ω' are related to those associated with Ω by

$$P'_{a_1\ldots a_l}|_\Lambda = P_{a_1\ldots a_l} - \tfrac{1}{2}l(2l-1)\mathcal{C}\left[P_{a_1\ldots a_{l-1}}\tilde{D}_{a_l}w\right]\Big|_\Lambda. \tag{1.46}$$

Notice that the change in the 2^l moment depends only on the 2^{l-1} moment. Geroch has shown that his behaviour reflects precisely the usual dependence of Newtonian multipole moments on the choice of origin.

The actual calculation of the moments for a given exact solution is laborious. The axis of an axisymmetric solution, i.e. the set of fixed points of the action of the angular Killing vector, passes through Λ and only the geometric objects invariant under the action at Λ are the axis vector and the metric itself. Hence the multipole moments are proportional to the symmetrized trace-free product of the axis vector with itself and it suffices to know the *numbers*

$$M_l = \frac{1}{n!} P^M_{a_1 \ldots a_l} n^{a_1} \ldots n^{a-n}|_\Lambda \tag{1.47}$$

where n^a is the unit axis vector to determine the multipole moments.

The covariant character of the Geroch-(Hansen) moments follows from the tensor character of the quantities $P^M_{a_1 \ldots a_l}$, whose explicit value is not related to any coordinate system, thus this definition is coordinate invariant.

For a given static axisymmetric solution one can calculate the Geroch moments via

1. Calculate f and Ω from (1.40).
2. Choose the conformal factor, Ω such that the conditions for asymptotic flatness are satisfied
3. Calculate the potential $\tilde{\Phi}^M$ from (1.41)
4. Calculate the multipole moments from (1.47).

Even with this simplification, (1.47), the explicit calculation of the multipole moments is still time consuming. Hoenselaers (1986) has found a relation between the Ernst potential of a metric and its Geroch-Hansen multipole moments.

The procedure is outlined in the next section and is used throughout this thesis. Note: throughout this work the phrase 'relativistic moments' refers to these Geroch moments and use of the symbols $M_0 = m$, $M_2 = Q$, M_4 etc for the mass, quadrupole and 2^4-pole respectively.

1.8.4 Algorithm to Compute the Relativistic Moments

To calculate the Geroch multipole moments of a static axisymmetric (Weyl) metric

$$ds^2 = e^{2\psi} dt^2 - e^{2\gamma - 2\psi}(d\rho^2 + dz^2) - \rho^2 e^{-2\psi} d\varphi^2 \tag{1.48}$$

where $\psi = \psi(\rho, z)$ we begin by computing*

$$\xi = \frac{1 - e^{2\psi}}{1 + e^{2\psi}}.$$

*This function is related to the Ernst potential E, which, for static fields is given by $E = e^{2\psi}$.

Introduce the new coordinate $\bar{z} = 1/z$, and calculate

$$\begin{aligned} h_1 &= \frac{d\psi}{d\bar{z}} \\ h_l &= \frac{dh_{l-1}}{d\bar{z}} + 2\xi\, h_{l-1}\, h_1 \quad \text{for} \quad l \geq 2. \end{aligned} \tag{1.49}$$

The mass multipole is given by

$$M_l = d_l - \left.\frac{h_{l+1}}{(l+1)!}\right|_{\rho=0,\bar{z}=0} \tag{1.50}$$

the term d_l in (1.50) vanishes for $l < 4$, afterwards the expressions gets complicated and indeed no closed formulae are known for them. Here we give the first few terms, a comprehensive set up to d_{10} can be found in Fodor *et al.* (1989).

$$\begin{aligned} d_0 &= d_1 = d_2 = d_3 = 0 \\ d_4 &= \tfrac{1}{7} m_0 (m_1^2 - m_2 m_0) \\ d_5 &= \tfrac{1}{3} m_0 (m_2 m_1 - m_3 m_0) + \tfrac{1}{21} m_1 (m_1^2 - m_2 m_0) \end{aligned} \tag{1.51}$$

where the m_l terms are given by

$$m_l = \frac{1}{(l+1)!} \left.\frac{d^{l+1}\xi(\bar{z},0)}{d\bar{z}^{l+1}}\right|_{\bar{z}=0}.$$

1.8.5 Weyl Moments

Recall that the metric function ψ in (1.48) is a solution to Laplace's equation in flat space, $\nabla^2\psi = 0$. They have the following asymptotically flat general solution

$$\psi = \sum_{n=0}^{\infty} \frac{a_n}{r^{n+1}} P_n(\cos\theta) \tag{1.52}$$

where $r^2 = \rho^2 + z^2$, $\cos\theta = z/r$ and $P_n(\cos\theta)$ are the Legendre polynomials. The coefficients a_n are real constants which will be called "Weyl moments" since evidently they cannot be identified with the relativistic moments despite the formal equality between expression (1.52) and the classical potential (1.37). For example the Schwarzschild solution, which defines a pure monopole (mass M), is defined in the Weyl structure as

$$a_{2n} = -\frac{M^{2n+1}}{2n+1}, \quad a_{2n+1} = 0 \tag{1.53}$$

which is very different from the "Weyl monopole" defined by the only non null coefficient a_0 corresponding to the Curzon solution (see section 1.6).

Making use of a procedure defined by Thorne (1980) for the calculating of the multipole moments of a stationary metric, Hernãndez-Pastora and Martin (1994) give expressions for the Geroch moments M_n in terms of the Weyl moments a_n. They concentrate on even multipoles, thus they assume that the source has equatorial symmetry and the origin of the coordinates

is in the symmetry plane. They find that the moments are related by*

$$\begin{aligned} M_0 &= -a_0 \\ M_2 &= \frac{1}{3}a_0^3 - a_2 \\ M_4 &= -\frac{19}{105}a_0^5 + \frac{8}{7}a_0^2 a_2 - a_4 \\ M_6 &= \frac{389}{3465}a_0^7 - \frac{23}{21}a_0^4 a_2 + \frac{60}{67}a_0 a_2^2 + \frac{17}{11}a_0^2 a_4 - a_6, \end{aligned} \tag{1.54}$$

or inverting

$$\begin{aligned} a_0 &= -M_0 \\ a_2 &= -\frac{1}{3}M_0^3 - M_2 \\ a_4 &= -\frac{1}{5}M_0^5 - \frac{8}{7}M_0^2 M_2 \\ a_6 &= -\frac{1}{7}M_0^7 - \frac{25}{21}M_0^4 M_2 - \frac{60}{77}M_0 M_2^2. \end{aligned} \tag{1.55}$$

These result will become useful in later chapters when the expansion (1.52) is required.

1.9 Erez-Rosen Spacetime

It is obvious that the Schwarzschild solution does not exactly represent the gravitational fields of astrophysical objects which are, in general, not spherical. Of physical importance is the Weyl metric of Erez and Rosen (1959) whose exterior (static) gravitational field is of a mass *with* quadrupole moment.

The method used to formulate this metric serves as a prototype used *throughout this thesis.* In essence the method is based on introducing new coordinates in which Laplace's equation separates into ordinary differential equations. Clearly numerical techniques could be used to solve the field equations. We have strived to obtain exact solutions.

1.9.1 The Metric

Prolate coordinates (λ, ν, φ) are related to cylindrical coordinates by (m is a constant)

$$\lambda = \frac{r_+ + r_-}{2m}, \quad \mu = \frac{r_+ - r_-}{2m} \tag{1.56}$$

where

$$r_\pm^2 = \rho^2 + (z \pm m)^2, \quad \lambda \geq 1, \quad -1 \leq \mu \leq 1. \tag{1.57}$$

The Weyl metric (1.12) in these coordinates is

$$ds^2 = e^{2\psi}dt^2 - m^2 e^{-2\psi}\left[e^{2\gamma}(\lambda^2 - \mu^2)\left(\frac{d\lambda^2}{\lambda^2 - 1} + \frac{d\mu^2}{1 - \mu^2}\right) + (1 - \mu^2)(\lambda^2 - 1)\, d\varphi^2\right] \tag{1.58}$$

*Expressions up to M_{12} are given in Hernãndez-Pastora and Martin (1994), it is interesting to note that they computed the first 20 Geroch moments but state to publish them would require the whole journal by itself.

with $\psi = \psi(\lambda, \mu)$ and $\gamma = \gamma(\lambda, \mu)$ which satisfy

$$\left[(\lambda^2 - 1)\psi_\lambda\right]_\lambda + \left[(1 - \mu^2)\psi_\mu\right]_\mu = 0 \tag{1.59}$$

$$\frac{\partial\gamma}{\partial\lambda} = \frac{1-\mu^2}{\lambda^2-\mu^2}\left[\lambda(\lambda^2-1)\psi_\lambda^2 - \lambda(1-\mu^2)\psi_\mu^2 - 2\mu(\lambda^2-1)\psi_\lambda\psi_\mu\right] \tag{1.60}$$

$$\frac{\partial\gamma}{\partial\mu} = \frac{\lambda^2-1}{\lambda^2-\mu^2}\left[\mu(\lambda^2-1)\psi_\lambda^2 - \mu(1-\mu^2)\psi_\mu^2 + 2\lambda(1-\mu^2)\psi_\lambda\psi_\mu\right]. \tag{1.61}$$

The differential equation (1.59) can be solved by the method of separation of variables, let

$$\psi(\lambda, \mu) = \Lambda(\lambda)M(\mu) \tag{1.62}$$

then (1.59) becomes

$$\left[(\lambda^2 - 1)\Lambda_\lambda\right]_\lambda - a\Lambda = 0 \tag{1.63}$$

$$\left[(1 - \mu^2)M_\mu\right]_\mu + aM = 0 \tag{1.64}$$

where a is a constant. In order to avoid singularities at $\mu = \pm 1$ we take

$$a = \nu(\nu + 1) \quad \nu = 0, 1, 2, \ldots$$

The general solution of (1.64) is given by Legendre polynomials $P_\nu(\mu)$. As ψ must be asymptotically flat we take for the solution of (1.63) to be the Legendre functions of the second kind $Q_\nu(\lambda)$. Thus we take $\psi = P_\nu(\mu)Q_\nu(\lambda)$.

The special case $\nu = 0$, after the coordinate change $\lambda = -\lambda$ is

$$\psi = P_0(\mu)Q_0(-\lambda) = \frac{1}{2}\ln\left(\frac{\lambda-1}{\lambda+1}\right) \tag{1.65}$$

which corresponds to the Schwarzschild metric in prolate spheroidal coordinates.

The Erez-Rosen [ER] solution is that generated by taking

$$\psi = P_0(\mu)Q_0(-\lambda) + qP_2(\mu)Q_2(-\lambda) \tag{1.66}$$

$$= \frac{1}{2}\ln\left(\frac{\lambda-1}{\lambda+1}\right) + \frac{1}{2}q\,(3\mu^2-1)\left[\frac{1}{4}(3\lambda^2-1)\ln\left(\frac{\lambda-1}{\lambda+1}\right) + \frac{3}{2}\lambda\right] \tag{1.67}$$

from which we calculate

$$\gamma = \frac{1}{2}(1+q)^2\ln\left(\frac{\lambda^2-1}{\lambda^2-\mu^2}\right) - \frac{3}{2}q\,(1-\mu^2)\left[\lambda\ln\left(\frac{\lambda-1}{\lambda+1}\right) + 2\right] \tag{1.68}$$

$$+\frac{9}{16}q^2\,(1-\mu^2)\left[\lambda^2 + 4\mu^2 - 9\lambda^2\mu^2 - \frac{4}{3}\right. \tag{1.69}$$

$$+ \lambda\left(\lambda^2 + 7\mu^2 - 9\lambda^2\mu^2 - \frac{5}{3}\right)\ln\left(\frac{\lambda-1}{\lambda+1}\right) + \tag{1.70}$$

$$\left.\frac{1}{4}(\lambda^2-1)(\lambda^2+\mu^2-9\lambda^2\mu^2-1)\ln^2\left(\frac{\lambda-1}{\lambda+1}\right)\right]. \tag{1.71}$$

The meaning of the parameter q can be elucidated by the asymptotic behaviour of the metric function $g_{tt} = e^{2\psi}$. We introduce spherical coordinates via $\lambda = r/m - 1$ and $\mu = \cos\theta$. As $r \to \infty$ we have

$$g_{tt} = 1 + 2\left\{-\frac{m}{r} - \frac{Q}{r^3}P_2(\cos\theta) + \frac{9}{14}\frac{Qm^2}{r^5}P_2(\cos\theta) + \frac{1}{r^6}\left[-\frac{5}{14}Qm^3P_2(\cos\theta) + \frac{1}{2}Q^2P_2^2(\cos\theta)\right] + \cdots\right\}. \quad (1.72)$$

Accordingly we see that the asymptotic expansion of g_{tt} leads to the Newtonian gravitational potential of a mass m with quadrupole moment*

$$Q = \frac{2}{15}m^3q.$$

This determination of the quadrupole moment is not coordinate invariant. However in this specific case, the quadrupole moment Q coincides with that obtained by using the relativistic, coordinate independent Geroch definition (Quevedo and Parkes, 1991). The physical meaning of the ER solution has been investigated by Zel'dovich and Novikov (1965).

Unlike most Weyl spacetimes, the geodesics of the ER solution have been extensively studied (Quevedo and Parkes, 1991; Quevedo, 1990; Krori and Sarmah, 1991; Armenti, 1972). The asymptotic spacelike geodesics in the Curzon solution have been presented (Scott and Szekeres, 1986a,b) and Semerák *et al.* (1999a) have studied the geodesics in superimposed Weyl spacetimes, in particular those of the form of a Schwarzschild + ring field. Generally speaking the literature is short of geodesics studies of Weyl metrics.

1.10 Perihelion Precession

An aim of this thesis to generate bound timelike geodesics governed by the new metrics derived in the upcoming chapters. Here we summarise the paper of Fernández-Jambrina and Hoenselaers (2001) who determine the influence of high order (relativistic) multipoles in the perihelion precession of an equatorial orbit.

Bertrand's theorem (Goldstein, 1980) states that stable bounded orbits of particles moving under the influence of a central force which is neither Newtonian nor harmonic are not closed. Thus whenever the source of the gravitational field is not monopolar, the bounded trajectories in the equatorial plane will no longer be the elliptic orbits described by Kepler's first law but will be of a precessing ellipse if the deviation from spherical symmetry is small.

It has been proven for general relativity that there are just two asymptotically flat static spherically symmetric spacetimes in which the stable orbits are closed but they are rather different from the classical physical situations (Perlick, 1992). When relativistic effects are taken into account, not even the motion around a spherical distribution of mass is closed and is referred to as perihelion precession. Of course higher multipole moments of the mass distribution will also contribute to this effect.

*Higher multipole moments do not vanish. A pure mass plus quadrupole solution is given by Hernãndez-Pastora and Martin (1994).

Using (1.52) (and the associated general expression for the remaining metric term γ), Fernández-Jambrina and Hoenselaers solve the general (geodesic) equations of motion for a test particle (in the $\theta = \pi/2$ plane) by a perturbative expansion.

In order to evaluate the contribution to the precession of higher order multipole moments the equations are not expressed in terms of the Weyl moments a_n but in the more physical Geroch relativistic moments M_n. They use the dimensionless parameter*

$$\epsilon = \frac{M_0}{L} \tag{1.73}$$

to expand the equations, where M_0 is the mass of the gravitational source and L the angular momentum (per unit mass) of the test particle (L is a constant of the motion). Furthermore the energy per unit mass of the particle can also be expanded in ϵ

$$E = 1 + \epsilon^2 \sum_{n=0} E_n \epsilon^n \tag{1.74}$$

the expansion starts at this order because the expression for the energy associated with the Kepler ellipse ($-1/2 < E_0 < 0$) which is expected to be the first term, is second order in ϵ.

As we are concerned with static† fields we have in the expansion of E

$$E_1 = E_3 = E_5 = 0 \tag{1.75}$$

$$E_2 = -6 - 10E_0 - \tfrac{1}{2}E_0^2 \tag{1.76}$$

$$E_4 = -\tfrac{47}{4} - 20E_0 - 13E_0^2 + \tfrac{1}{2}E_0^3 + (2 + 3E_0)\frac{M_2}{M_0^3} \tag{1.77}$$

and the perihelion shift is given by

$$\Delta\varphi = \pi(\Delta_0 + \Delta_1 + \Delta_4 + \Delta_{16}). \tag{1.78}$$

The first term Δ_0 comprises the Newtonian contribution to the precession, that is, the terms which remain after taking the classical limit $c \to \infty$. It is given by

$$\Delta_0 = -\frac{3M_2}{M_0^3}\epsilon^4 + \left\{\left(\frac{105}{8} + \frac{45E_0}{4}\right)\frac{M_4}{M_0^5} + \left(\frac{105}{8} + \frac{15E_0}{4}\right)\frac{M_2^2}{M_0^6}\right\}\epsilon^8 \tag{1.79}$$

it is seen that it only contains only mass multipole moments since rotation has no influence in Newtonian theory.

Although‡ these (and subsequent) terms are expressed in geometrical units, if the usual constants are included the actual magnitudes of each term is recovered.

For example, the first term in (1.79) has a factor G^2 and the second a G^4. For oblate gravitational sources the quadrupole moment M_2 is negative, thus it contributes to a positive shift of the perihelion in the first order. The next order shift, the contribution of the

*According to Kepler's law which is assumed to be a good approximation at a great distance from the source, $L \sim \sqrt{m\,r}$, where m is the mass of the particle.Thus the dimensionless number M/L should be small.

†Fernández-Jambrina and Hoenselaers compute the shift for stationary spacetimes thus the original $\Delta\varphi$ result contains terms dependent upon the angular momentum moments which are null for static fields.

‡c refers to the speed of light and G to the gravitational constant.

quadrupole is, always positive, but the M_4 (sedecimpole) term bears the opposite sign to the quadrupole moment.

The second term Δ_1 comprises the contribution to the perihelion precession due to a spherically symmetric mass distribution (Schwarzschild)

$$\begin{aligned}\Delta_1 &= 6\epsilon^2 + \left(\frac{105}{2} + 15E_0\right)\epsilon^4 + \left(\frac{975}{2} + 165E_0\right)\epsilon^6 \\ &+ \left(\frac{159105}{32} + \frac{16725E_0}{8} + \frac{705E_0^2}{8}\right)\epsilon^8 \\ &+ \left(\frac{1701507}{32} + \frac{216375E_0}{8} + \frac{20115E_0^2}{8}\right)\epsilon^{10} \end{aligned} \tag{1.80}$$

it is of the order G^2/c^2 and can be calculated exactly in terms of elliptic functions (e.g. see Chandrasekhar (1983)), and the contribution of every order is positive.

The term

$$\begin{aligned}\Delta_4 &= -(90 + 42E_0)\frac{M_2}{M_0^3}\epsilon^6 - \left(\frac{25383}{16} + \frac{28305E_0}{28} + \frac{375E_0^2}{4}\right)\frac{M_2}{M_0^3}\epsilon^8 \\ &+ \left\{ - \left(\frac{2686203}{112} + \frac{503379E_0}{28} + \frac{80187E_0^2}{28}\right)\frac{M_2}{M_0^3} \right. \\ &\left. + \left(\frac{12471}{16} + 519E_0 + \frac{165E_0^2}{4}\right)\frac{M_2^2}{M_0^6} \right\}\epsilon^{10} \end{aligned} \tag{1.81}$$

contains relativistic terms depending only on the quadrupole moment M_2 and the the mass M_0. The first correction has a factor G^4/c^2 in front of it.

The influence of the M_4 moment is included in Δ_{16} and does occur until the tenth order of ϵ. It is proportional to G^6/c^2,

$$\Delta_{16} = \left(\frac{7425}{16} + 570E_0 + \frac{495E_0^2}{4}\right)\frac{M_4}{M_0^5}\epsilon^{10}. \tag{1.82}$$

We shall compare these theoretical perihelion shifts to the numerical determined shifts of bounded geodesics in several differing spacetimes.

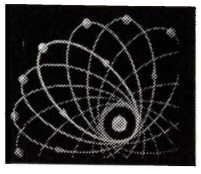

Chapter 2
Bispherical Coordinates

2.1 Introduction

Often mathematical models used to represent a particular realistic physical situation can be simplified by a wise selection of coordinates. In general relativity this is immaterial in theory, however from a practical point a judicious choice of coordinate system can be the difference between solving the problem or not.

Fundamental in any Weyl solution is the calculation of the harmonic function ψ. This chapter will be concerned with constructing axisymmetric static fields by using bispherical coordinates. The advantage of these coordinates are manifest in the ability to calculate ψ by separation of variables.

Carminati and Sarracino (1981) first considered these coordinates and the idealized mass distributions for which these harmonic solutions could model. The mass distributions were inferred from the singularities of ψ and the behaviour of the Kretschmann scalar. Generally speaking this thesis will concentrate on solutions that could model realistic astrophysical bodies, thus this chapter deals with ψ solutions that model point like masses.

By determining the relativistic multipole moments we construct two bispherical solutions that exhibit an equatorial plane of symmetry. We introduce mass centered spherical coordinates and calculate numerically timelike geodesics in these planes of symmetry and formulate an analytic approximation to these orbits.

The numerical precession of the perihelion and nodes are compared to the theoretical predictions based on the work of Fernández-Jambrina and Hoenselaers (2001).

The geodesics of test particle with zero angular momentum are also determined.

2.2 Coordinates

Bispherical coordinates* (α, β) are connected to the cylindrical coordinates ρ, z by the relations

$$\rho = \frac{c \sin \alpha}{\cosh \beta - \cos \alpha} \qquad z = \frac{c \sinh \beta}{\cosh \beta - \cos \alpha} \tag{2.1}$$

where

$$0 \leq \alpha \leq \pi, \qquad -\infty < \beta < \infty \tag{2.2}$$

and c is a fixed positive scale factor. The corresponding triply orthogonal family of surfaces, illustrated in figure 2.1, consists of the *spindle-shaped* surfaces of constant α described by the equation

$$\rho^2 + z^2 - 2c\rho \cot \alpha = c^2$$

and the spheres of constant β described by the equation

$$\rho^2 + (z - c \coth \beta)^2 = c^2 / \sinh^2 \beta.$$

The remaining coordinate surface are the planes φ = constant. The points $\rho = 0$, $z = \pm c$

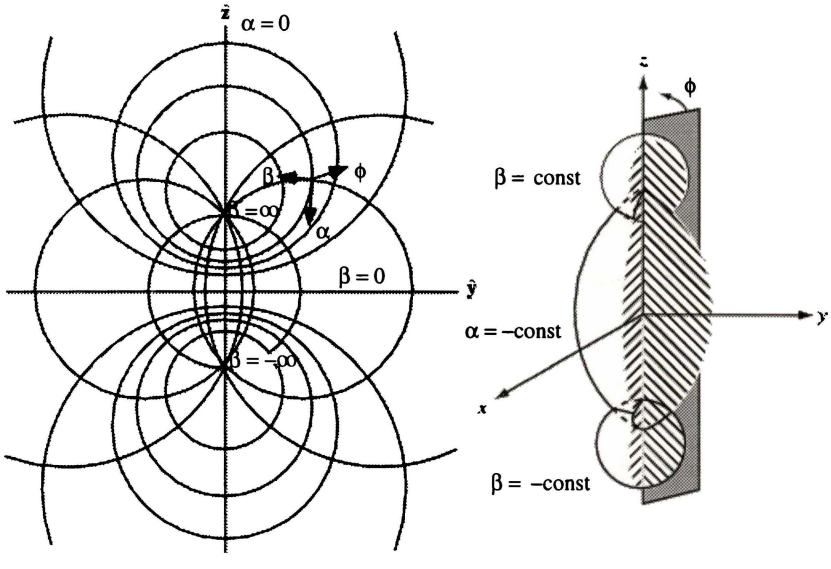

FIGURE 2.1: *Typical coordinate surfaces for the bispherical coordinate system.*

correspond to the values $\beta \to \pm\infty$, while $\rho = 0$, $z \to \pm\infty$ if $\alpha = 0$, $\beta \to 0\pm$. The region $|z| < c$, $\rho = 0$ corresponds† to $\alpha = \pi$.

The coordinates (2.1) in terms of cylindrical coordinates are

$$\alpha(\rho, z) = \arctan\left(\frac{2c\rho}{\rho^2 + z^2 - c^2}\right) \tag{2.3}$$

$$\beta(\rho, z) = \frac{1}{2} \ln\left(\frac{\rho^2 + z^2 + 2cz + c^2}{\rho^2 + z^2 - 2cz + c^2}\right). \tag{2.4}$$

*These coordinates are sometimes referred to as *bipolar* coordinates. For example see Lebedev (1972) or Moon and Spencer (1988) for conflicting terminology.

†Moon and Spencer (1988) label the regions of the z-axis incorrectly.

Additionally, by introducing spherical coordinates (r, θ, φ) via the transformations $\rho = r\sin\theta$ and $z = r\cos\theta$ into the expressions for α and β we obtain

$$\alpha(r,\theta) = \arctan\left(\frac{2cr\sin\theta}{r^2 - c^2}\right) \tag{2.5}$$

$$\beta(r,\theta) = \frac{1}{2}\ln\left(1 + \frac{4rc\cos\theta}{r^2 + c^2 - 2rc\cos\theta}\right). \tag{2.6}$$

Expanding for large r we obtain the useful asymptotic relations

$$\alpha \approx \frac{2c}{r}\sin\theta + \frac{2c^3}{3r^3}\sin(3\theta) + \cdots = \sum_{n=1,3,5\ldots}^{\infty} \frac{2c^n}{n}\frac{\sin(n\theta)}{r^n} \tag{2.7}$$

$$\beta \approx \frac{2c}{r}\cos\theta + \frac{2c^3}{3r^3}\cos(3\theta) + \cdots = \sum_{n=1,3,5\ldots}^{\infty} \frac{2c^n}{n}\frac{\cos(n\theta)}{r^n}. \tag{2.8}$$

2.3 Metric

The general axially symmetric metric (Weyl) in bispherical coordinates becomes

$$ds^2 = e^{2\psi(\alpha,\beta)}dt^2 - \frac{c^2 e^{-2\psi(\alpha,\beta)}}{(\cosh\beta - \cos\alpha)^2}\left[e^{2\gamma(\alpha,\beta)}\left(d\alpha^2 + d\beta^2\right) + \sin^2\alpha\, d\varphi^2\right]. \tag{2.9}$$

2.3.1 ψ Solutions

The function ψ satisfies Laplace's equation (with $\partial_\varphi\psi = 0$)

$$\frac{\partial}{\partial\alpha}\left(\frac{\sin\alpha}{\cosh\beta - \cos\alpha}\frac{\partial\psi}{\partial\alpha}\right) + \frac{\partial}{\partial\beta}\left(\frac{\sin\alpha}{\cosh\beta - \cos\alpha}\frac{\partial\psi}{\partial\beta}\right) = 0. \tag{2.10}$$

Solutions are most readily obtained by separation of variables. By setting

$$\psi(\alpha,\beta) = \sqrt{\cosh\beta - \cos\alpha}\, F(\alpha)G(\beta)$$

and introducing a separation constant ν, F and G satisfy the independent equations

$$\frac{d^2G}{d\beta^2} - (\nu + \tfrac{1}{2})^2 G = 0$$

$$\frac{1}{\sin\alpha}\frac{d}{d\alpha}\left(\sin\alpha\frac{dF}{d\alpha}\right) + \nu(\nu+1)F = 0.$$

Solutions are respectively hyperbolic and Legendre functions. The general axially symmetric solutions can be written ($A - D$ are arbitrary constants)

$$\psi = \sqrt{\cosh\beta - \cos\alpha}\,[AP_\nu(\cos\alpha) + BQ_\nu(\cos\alpha)] \times [C\cosh(\nu + \tfrac{1}{2})\beta + D\sinh(\nu + \tfrac{1}{2})\beta]. \tag{2.11}$$

Some knowledge of the possible (idealized) sources for the space-time generated by these solutions can be obtained by studying the singular behavior of ψ and the Kretschmann scalar.

Carminati and Sarracino (1981) showed that various values of the constants A, B, C and D in (2.11) enable the bispherical eigensolutions to model many possible sources. These include

infinite mass distribution along the z axis, semi-infinite line mass distributions (mass located $z \geq c$ and $z \leq -c$), single point sources (at $z = c$ or $z = -c$) or two point mass sources at $z = \pm c$.

Our aim here is to study solutions that may in some approximate limit model astrophysical bodies. Motivated by these assumptions we can simplify the general solution (2.11) by choosing solutions that are finite.

Given that, $Q_\nu(x) \to \infty$ as $x \to 1$ and $P_\nu(x) \to \infty$ as $x \to -1$ unless ν is a non-negative integer, we set

$$B = 0 \quad \text{and} \quad \nu = n = 0, 1, 2 \ldots$$

and ψ now contains Legendre polynomial functions. Furthermore we restrict our study to the case when

$$C = D = 1$$

as this assumption permits the eigensolutions to represent the spacetime of a single point mass located at the singular point $\rho = 0$, $z = c$ ($\alpha = 0, \pi$ $\beta \to \infty$).

Accordingly the asymptotically flat ψ solution has the typical form

$$\psi_n(\alpha, \beta) = \sqrt{\cosh\beta - \cos\alpha}\; A_n\, P_n(\cos\alpha)\, e^{(n+1/2)\beta}. \tag{2.12}$$

2.3.2 γ Solutions

To complete the determination of the metric (2.9) the remaining function $\gamma(\alpha, \beta)$ must be calculated. To provide a general method we write (2.12) as*

$$\psi(\alpha, \beta) = -\sqrt{\cosh\beta - \cos\alpha}\, F(\alpha, \beta)$$

from which γ satisfies the following equations (see equations (1.18) and (1.19))

$$\begin{aligned} \frac{\partial\gamma}{\partial\alpha} &= \sin\alpha \Big[(F_\alpha^2 - F_\beta^2 + \tfrac{1}{4}F^2)(\cosh\beta\cos\alpha - 1) - \\ &\quad 2\sinh\beta\sin\alpha\, F_\alpha F_\beta - F(F_\alpha\cosh\beta\sin\alpha + F_\beta\sinh\beta\cos\alpha)\Big] \qquad (2.13) \\ \frac{\partial\gamma}{\partial\beta} &= \sin\alpha \Big[(F_\alpha^2 - F_\beta^2)\sinh\beta\sin\alpha + 2F_\alpha F_\beta(\cosh\beta\cos\alpha - 1) \\ &\quad -\tfrac{1}{4}F^2\sin\alpha\cosh\beta + F(F_\alpha\sinh\beta\cos\alpha - F_\beta\cosh\beta\sin\alpha)\Big]. \qquad (2.14) \end{aligned}$$

We begin by calculating a partial solution by integrating (2.13)

$$\gamma_p(\alpha, \beta) = \int \frac{\partial\gamma}{\partial\alpha}\, d\alpha \tag{2.15}$$

evaluation of this integral is straightforward, albeit tedious as only trigonometric functions are being integrated. Thus $\gamma = \gamma_p + u(\beta)$ where $u(\beta)$ is an unknown function. However

$$\frac{\partial\gamma_p}{\partial\beta} + \frac{du}{d\beta} = \frac{\partial\gamma}{\partial\beta}$$

*This generalization obviously incorporates the possibility of the superposition of eigensolutions. Partial differentiation represented by subscripts.

which must be valid for all α values. Thus by setting $\alpha = 0$ we see from (2.14) that

$$\frac{\partial \gamma_p(0,\beta)}{\partial \beta} + \frac{du}{d\beta} = 0$$

and after integrating we obtain $\gamma_p(0,\beta)+u(\beta) = \text{const}$. Here we set the constant of integration to zero so the solution is asymptotically flat. Thus to complete the determination of the metric (2.9) we calculate γ via

$$\gamma(\alpha,\beta) = \gamma_p(\alpha,\beta) - \gamma_p(0,\beta). \tag{2.16}$$

By construction the required boundary conditions

$$\gamma|_{\text{axis}} = 0 \qquad \text{and} \qquad \gamma|_{r\to\infty} \to 0 \tag{2.17}$$

are satisfied. Carminati and Sarracino (1981) give general formulae for obtaining γ from general superposition of ψ solutions.

2.4 Bispherical Relativistic Multipoles

The procedure outlined in section 1.8.4 will now be used to calculate the relativistic moments of a bispherical spacetime.

Recall that the multipole moments are in essence, determined by the values of the derivatives of ψ with respect to $\bar{z} = 1/z$ at the point $\bar{z} = 0$ on the symmetry axis ($\alpha = 0$). The analysis of this section utilizes the explicit inversion formulae, nevertheless the multipole moments can also be evaluated using the implicit relationships given by (2.1) on the symmetry axis, namely

$$\bar{z}(\beta) = 1/z = \frac{\cosh\beta - 1}{c\sinh\beta}$$

and realizing that $\bar{z} \to 0 \equiv \beta \to 0$.

Consider the most general ψ solution formed by a linear superposition of eigensolutions

$$\psi_S(\alpha,\beta) = -\sqrt{\cosh\beta - \cos\alpha}\sum_{n\in S} A_n P_n(\cos\alpha)\, e^{(n+1/2)\beta}. \tag{2.18}$$

The summation is over S, a set which contains unique n values. On the symmetry axis we have $P_n(\cos\alpha)|_{\alpha=0} = 1$ and from (2.4)

$$\beta(\rho = 0, z) = \ln\left(\frac{z+c}{z-c}\right). \tag{2.19}$$

Anticipating non-vanishing dipole moments let us displace the origin of the coordinates by the translation*

$$z' = z - \epsilon \tag{2.20}$$

*This translation to the center of mass frame, is equally valid in determining relativistic multipole moments as in the classical scenario (Geroch, 1970b).

where ϵ is a scalar that in turn will be evaluated to eliminate the dipole contribution. Substituting (2.20) and (2.19) into (2.18) we obtain

$$\psi(z') = -\sqrt{2}\,c\,[(z'+\epsilon-c)(z'+\epsilon+c)]^{-1/2} \sum_{n\in S} A_n \left(\frac{z'+\epsilon+c}{z'+\epsilon-c}\right)^{n+1/2} \tag{2.21}$$

It then follows from section 1.8.4 that the mass and dipole moments are (we suppress the obvious limits on the summations henceforth)

$$M_0 = \sqrt{2}c\sum A_n \tag{2.22}$$

$$M_1 = \sqrt{2}c\Big[\sum (c\,(2n+1)-\epsilon)A_n\Big]. \tag{2.23}$$

To eliminate the dipole term we set

$$\epsilon = \frac{c\sum A_n(2n+1)}{\sum A_n}. \tag{2.24}$$

Letting

$$f = \sum A_n$$

and

$$g = \sum A_n(2n+1)$$

the quadrupole term becomes

$$M_2 = \frac{\sqrt{2}\,c^3}{6}\left[3\sum \frac{A_n(2n+1)}{f}\Big[f(1+2n)-2g\Big] + 3f - 4f^3\right]. \tag{2.25}$$

The next moment is

$$\begin{aligned} M_3 = -\frac{\sqrt{2}}{6}\frac{c^4}{f}\Bigg[3g\sum \frac{A_n(2n+1)}{f}\Big[f(1+2n)-2g\Big] + 6fg \\ -f\sum \frac{A_n(2n+1)}{f^2}\Big[(4n^2+4n+3)f^2 - 6fg(1+2n) + 6g^2\Big]\Bigg] \end{aligned} \tag{2.26}$$

the general M_4 term is lengthly and will be omitted here.

We note from (2.24) for a single term solution the dipole term is eliminated by the simple coordinate shift (2.20) with $\epsilon = (2n+1)c$.

2.5 $n = 0$ Solution

The first bispherical solution is obtained by setting $n = 0$ in (2.12). The resulting metric functions, containing the arbitrary constant A are

$$\psi = -\sqrt{\cosh\beta - \cos\alpha}\,A\,e^{\beta/2} \tag{2.27}$$

$$\gamma = -\tfrac{1}{4}A^2\,e^{2\beta}\,\sin^2\alpha. \tag{2.28}$$

2.5.1 Multipole Moments

From the general computations of section 2.4 the $n = 0$ solution has the following (dipole eliminated) multipole moments

$$M_0 = m = \sqrt{2}\,cA \tag{2.29}$$
$$M_1 = M_3 = 0 \tag{2.30}$$
$$M_2 = -\tfrac{1}{3}m^3 \tag{2.31}$$
$$M_4 = \tfrac{19}{105}m^5 \tag{2.32}$$
$$M_6 = -\tfrac{389}{3465}m^7 \tag{2.33}$$

additional computation reveals that the M_5 and M_7 moments also vanish. Assuming that *all* odd multipoles moments vanish indicates that the source generating this field exhibits equatorial symmetry (about the center of mass $z = \epsilon = c$). We note that the moments of this solution are solely dependent upon the value of the mass m of the source.

2.5.2 New Coordinates and Solution

We have seen for the $n = 0$ solution, the dipole and subsequent odd multipole moments are nullified by the elementary transformation $z = z' + c$. Let us introduce spherical coordinates (r, θ, φ) centered at $(\rho = 0, z = c)$.

From (2.5) and (2.6) we have

$$\alpha(r,\theta) = \arctan\left(\frac{2c\sin\theta}{r + 2c\cos\theta}\right) \tag{2.34}$$
$$\beta(r,\theta) = \tfrac{1}{2}\ln\left(r^2 + 4cr\cos\theta + 4c^2\right) - \ln(r) \tag{2.35}$$

from which the terms (2.27) and (2.28) become

$$\psi(r) = -\frac{m}{r} \tag{2.36}$$
$$\gamma(r,\theta) = -\frac{m^2\sin^2\theta}{2r^2} \tag{2.37}$$

and the metric (2.9) reduces to

$$ds^2 = e^{2\psi}dt^2 - e^{-2\psi+2\gamma}(dr^2 + r^2d\theta^2) - e^{-2\psi}r^2\sin^2\theta\,d\varphi^2. \tag{2.38}$$

From (2.36) we can readily verify the multipole moments given earlier by the method outlined in section 1.8.5. Indeed the method described there was used to evaluate the M_6 moment (see (2.33)) and to show that the next odd multipole moments vanish.

Results (2.36), (2.37) and (2.38) form the well known Curzon solution which is discussed in the introduction of this thesis. We can conclude that the $n = 0$ bispherical solution is equivalent to a displaced $(z = c)$ Curzon solution.

Scott and Szekeres (1986a) discuss geodesics approaching $r = 0$ on a hypersurface $t =$ const. Furthermore in Scott and Szekeres (1986b) the behavior of all geodesics approaching

$r = 0$ is analyzed. de Felice (1991) deduces the general pattern of the potential surfaces for timelike geodesics in the Curzon metric which reveal that for fairly small energies and angular momenta, the timelike geodesics group into two sets; the geodesics of one set tend to the z-axis as $r \to 0$ and the others tend to the ρ-axis. It is shown that stable circular motion is confined to the $z = 0$ plane.

We shall now examine the timelike geodesics pertaining to this metric. In particular we will restrict our study to two types of test particle trajectories. We begin with motions characterized by zero angular momentum. This is followed by bounded trajectories in the equatorial plane.

To simplify computations we use the spherical coordinates introduced above. This is simply a matter of convenience and identical simulations can be performed (which were done and used to confirm numerical results) in the original bispherical coordinate description. Thus the true application of bispherical coordinates is somewhat diminished with the benefit of hindsight (i.e. the realization that we are in fact considering the Curzon solution). Of course the natural progression of matching interior and exterior solutions could deem the use of the original coordinates more beneficial, but is not considered here.

We note that null geodesics, which are interesting in their own right, are not studied in this chapter or in general throughout this thesis.

2.5.3 Equations of Motion

The Lagrangian associated with the metric (2.38) is

$$2\mathcal{L} = e^{2\psi}\dot{t}^2 - e^{-2\psi+2\gamma}(\dot{r}^2 + r^2\dot{\theta}^2) - e^{-2\psi}r^2\sin^2\theta\dot{\varphi}^2 \tag{2.39}$$

where in general we have $\psi(r,\theta)$ and $\gamma(r,\theta)$. The dot refers to the derivative with respect to an affine parameter s. The geodesic equations can be computed from the Euler-Lagrange equations

$$\frac{\partial\mathcal{L}}{\partial x^\mu} = \frac{\partial}{\partial s}\left(\frac{\partial\mathcal{L}}{\partial\dot{x}^\mu}\right). \tag{2.40}$$

As the Lagrangian (2.39) is independent of the coordinates t and φ we have

$$\dot{t} = Ee^{-2\psi} \tag{2.41}$$

$$\dot{\varphi} = -\frac{L\,e^{2\psi}}{r^2\sin^2\theta} \tag{2.42}$$

the constants of the motion E and L can be interpreted as the test particles specific* energy and (azimuthal) angular momentum respectively.

The remaining equations are

$$\ddot{r} + \psi_r E^2 e^{-2\gamma} + (\gamma_r - \psi_r)(\dot{r}^2 - r^2\dot{\theta}^2) - r\,\dot{\theta}^2 + 2(\gamma_\theta - \psi_\theta)\,\dot{r}\,\dot{\theta} - \frac{L^2}{r^3\sin^2\theta}(1 - r\,\psi_r)\,e^{4\psi-2\gamma} = 0 \tag{2.43}$$

*Per unit mass. Justifications for these interpretations can be found in Misner *et al.* (1973).

$$\ddot{\theta} + \psi_\theta \frac{E^2}{r^2} e^{-2\gamma} + \frac{1}{r^2}(\gamma_\theta - \psi_\theta)(r^2\dot{\theta}^2 - \dot{r}^2) + \frac{2}{r}(r(\gamma_r - \psi_r) + 1)\dot{r}\,\dot{\theta} + \frac{L^2}{r^4 \sin^3\theta}(\psi_\theta \sin\theta - \cos\theta)\, e^{4\psi - 2\gamma} = 0. \quad (2.44)$$

An energy integral of motion follows from the Lagrangian

$$\epsilon = e^{2\psi}\dot{t}^2 - e^{-2\psi+2\gamma}(\dot{r}^2 + r^2\dot{\theta}^2) - e^{-2\psi} r^2 \sin^2\theta \dot{\varphi}^2 \quad (2.45)$$

where $\epsilon = 0, -1, +1$ for null, spacelike or timelike geodesics. As we are concentrating specifically on timelike geodesics we accordingly set $\epsilon = 1$. Introducing (2.41) and (2.42) we obtain

$$\dot{r}^2 + r^2\,\dot{\theta}^2 = e^{-2\gamma}\left[E^2 - \frac{L^2 e^{4\psi}}{r^2 \sin^2\theta} - e^{2\psi} \right]. \quad (2.46)$$

We solve these equations of motion numerically. Although explicit *symplectic* algorithms exist for numerically integrating Hamiltonian systems (e.g. Mikkola *et al.* (2002); Tang *et al.* (2002); Regan (2002)) and can be used to conserve E and L to high accuracy we have not endeavored to employ these techniques. Instead adaptive Runge-Kutta (RK) routines are used throughout.

This is because the RK method is more elementary to understand, readily available and simpler to code.* Numerous authors have also employed RK routines in other geodesic studies (e.g. see Scott and Szekeres (1986a), Semerák *et al.* (1999a), or Sengupta (1997)). We shall demonstrate in subsequent sections the accuracy of the numerical method used to conserve L and E.

2.5.4 $L = 0$ Timelike Geodesics

Geodesics On The Axis

We begin by looking at the geodesics of test particles with zero angular momentum which start from rest on the z axis. These initial conditions imply that $\theta_0 = 0$, $\dot{\theta}_0 = 0$ and from (2.44) we see that $\ddot{\theta} = 0$ and so the motion is confined to the z axis. Given γ and its derivatives are zero along the z axis we have the simplified equation of motion ($r \equiv z$)

$$\dot{z}^2 = E^2 - e^{-2m/z} \quad (2.47)$$

where the starting point is related to the constant E via

$$\ln E = -2m/z_0.$$

A typical trajectory as a function of proper time s and coordinate time t is illustrated in figure 2.2. In terms of s the particle reaches the origin in finite time, however the coordinate time

*The `Matlab` adaptive forth order RK method `ode45` was used extensively. To vindicate solutions additional numerical methods were used namely, the multi-step predictor-corrector method `ode113` from the `Matlab` suite and routines written in Fortran 90/95 implementing algorithms presented in numerical recipes (Press *et al.*, 1986).

tends to infinity. These results are consistent with the analysis of Scott and Szekeres (1986b), who showed that as $z \to 0^+$ then

$$t(z) \sim \int_z e^{2m/u} du - \frac{mA^2}{2z^2} - \frac{mAB}{z} + t_0 + Cz \tag{2.48}$$

$$s(z) \sim s_0 - (z/K) \tag{2.49}$$

where A, B, C, K, t_0 and s_0 are constants.

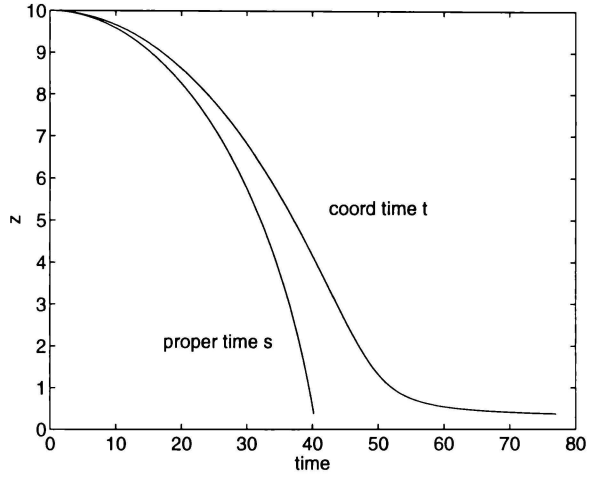

FIGURE 2.2: *The variation of the coordinate time* (t) *and the proper time* (s) *along a timelike geodesic of a test particle, starting at rest at* $z_0 = 10$ *and falling towards the origin* ($m = 1$).

General Geodesics

General geodesics of zero angular momentum are presented in figure 2.3. Due to symmetry we only consider motion in the quadrant $0 \leq \theta \leq \pi/2$. Here several trajectories of in falling test particles are illustrated. The initial release distance r_0 is increased in the plots. Given that the test particles start from rest, $\dot{r_0} = \dot{\theta_0} = 0$, from (2.44) for large r then initially ($L = 0$)

$$\ddot{\theta} \approx 0 \qquad \text{thus} \qquad \theta(s) \approx \theta_0 = \text{const.} \tag{2.50}$$

so the initial motion will be in the radial direction. This is clearly seen in the figures, more so in the lower plots where r_0 is increased. After this initial radial inflow all trajectories curve towards to z axis and approach the singular point (at the origin) 'from above'. This also occurs for particles that are released near the x axis.

Included in figure 2.3 is a plot of r as a function of s of the trajectories released from $r_0 = 1$. It demonstrates an interesting feature observed in all geodesics that are released close to the $z = 0$ plane: the 'bump' indicating the test particle is repelled from the source (at the origin) then subsequently attracted towards the source. Further plots demonstrating this behaviour are found in figure 2.4.

In figure 2.4 we also include the difference between the constant of the motion E and its numerical value $E_n(s) = \dot{t}\, e^{2\psi}$ for the the geodesic beginning at $r_0 = 1, \theta_0 = 88^o$. This

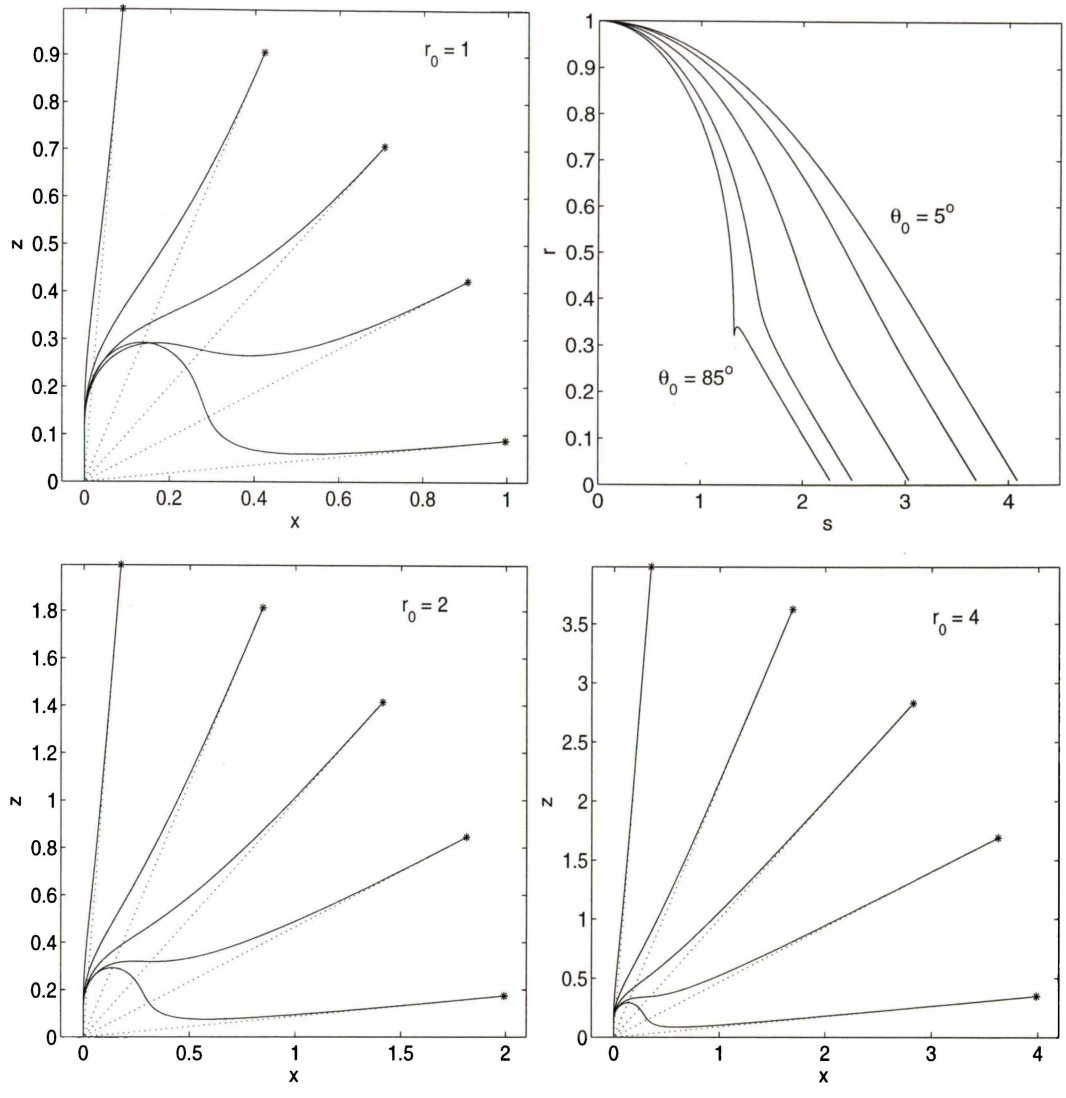

FIGURE 2.3: . *Trajectories of in falling test particles in the Curzon spacetime released from various initial positions* (r_0, θ_0). $\theta_0 = 5^o, 25^o, \ldots, 85^o$. *The source* $(m = 1)$ *is located at the origin. The dashed curves are radial lines. The upper right plot corresponds to the first plot and shows* r *as a function of* s.

particular geodesic has a pronounced 'repulsive' segment. The computation suggests that the numerical scheme is still producing accurate results for this particular initial condition (this is also verified by altering the integration tolerances and observing the predicted increase in accuracy as the tolerances become more demanding). This would suggest that the repulsive motion is not a numerical artifact.

We should interpret these results with caution. Clearly near the source, where curvature is large, the validity of the coordinate r is questionable. Lets us examine these geodesics using coordinates having more geometrical meaning. For fixed r and t the metric (2.38) becomes

$$ds^2 = -r^2 e^{-2\psi} \left(e^{2\gamma} d\theta^2 + \sin^2\theta \, d\varphi^2 \right) \tag{2.51}$$

from which the element of surface area is given by

$$dS_A = r^2 e^{-2\psi} e^{\gamma} \sin\theta \, d\theta \, d\varphi. \tag{2.52}$$

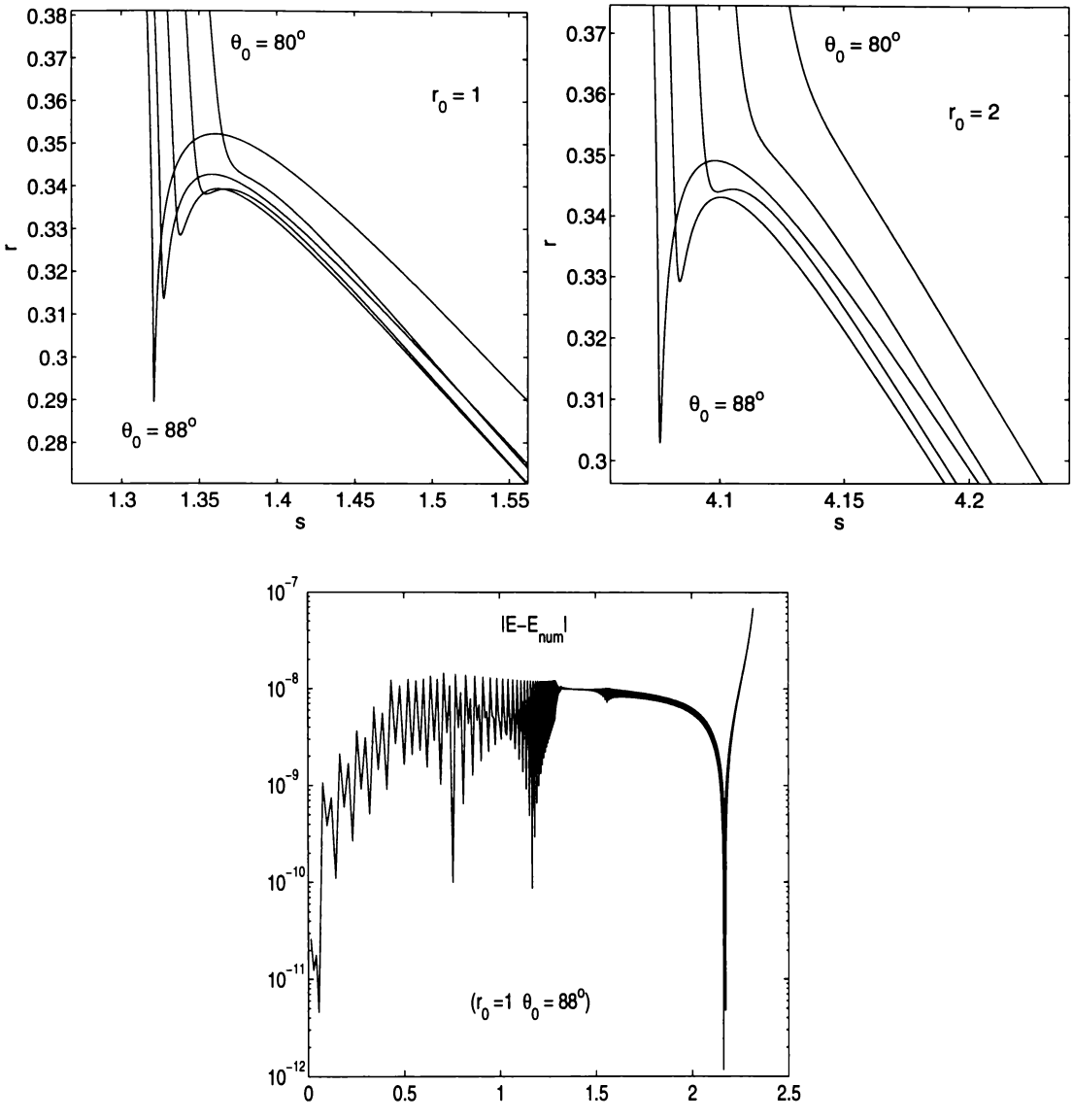

FIGURE 2.4: . *Close in plot of $r(s)$ of in-falling test particles that are released near the x axis ($\theta_0 = 80^o, 82^o, \ldots 88^o$). The repulsion, or increase, in r is clearly seen. The bottom plot illustrates the conservation of the constant E corresponding to a particle released from $r_0 = 1, \theta_0 = 88^o$. ($m = 1$).*

Given $\psi = \psi(r)$ and $\gamma = \gamma(r, \theta)$ then the surface area for fixed r is

$$S_A(r) = 2\pi r^2 e^{-2\psi} \int_0^\pi e^\gamma \sin\theta \, d\theta \tag{2.53}$$

for r large, $\psi, \gamma \to 0$ and $S_A = 4\pi r^2$, the surface area of a 2 sphere which is expected since the space is asymptotically flat.

From (2.53) lets us define a more physical radial coordinate, rather than r used previously*

$$R^2 = \tfrac{1}{2} r^2 e^{-2\psi} \int_0^\pi e^\gamma \sin\theta \, d\theta \tag{2.54}$$

*Similar introduction of a more physical radial coordinate is discussed in Semerák *et al.* (1999b,a) for example.

for large r then $r \approx R$ and has the usual interpretation as a radial coordinate.

Figures 2.5 and 2.6 compare $r(s)$ and $R(s)$ for various geodesics. We set $r_0 = 1$ and the mass of the source $m = 1$. Simulations with various r_0 and m values produce results with the identical qualitative behaviour, thus without loss of generality we concentrate on these specific parameter values.

All R curves obtain a local minimum of value $R_m = 2.0852$, thereafter R tends to infinity, indicating that the source is getting further away (in terms of the physical radius) from the test particle.

We note that a local minimum in the r curve (the onset of the apparent repulsive motion) corresponds to a local maximum in the R curve. This is evident in figure 2.6.

Unfortunately the calculation of R does not shed light on the observed 'repulsion'. It is likely that this is a manifestation of directional character of the singularity at the origin. Investigation of the Kretschmann scalar, for example, may provide explanations for this non physical behaviour.

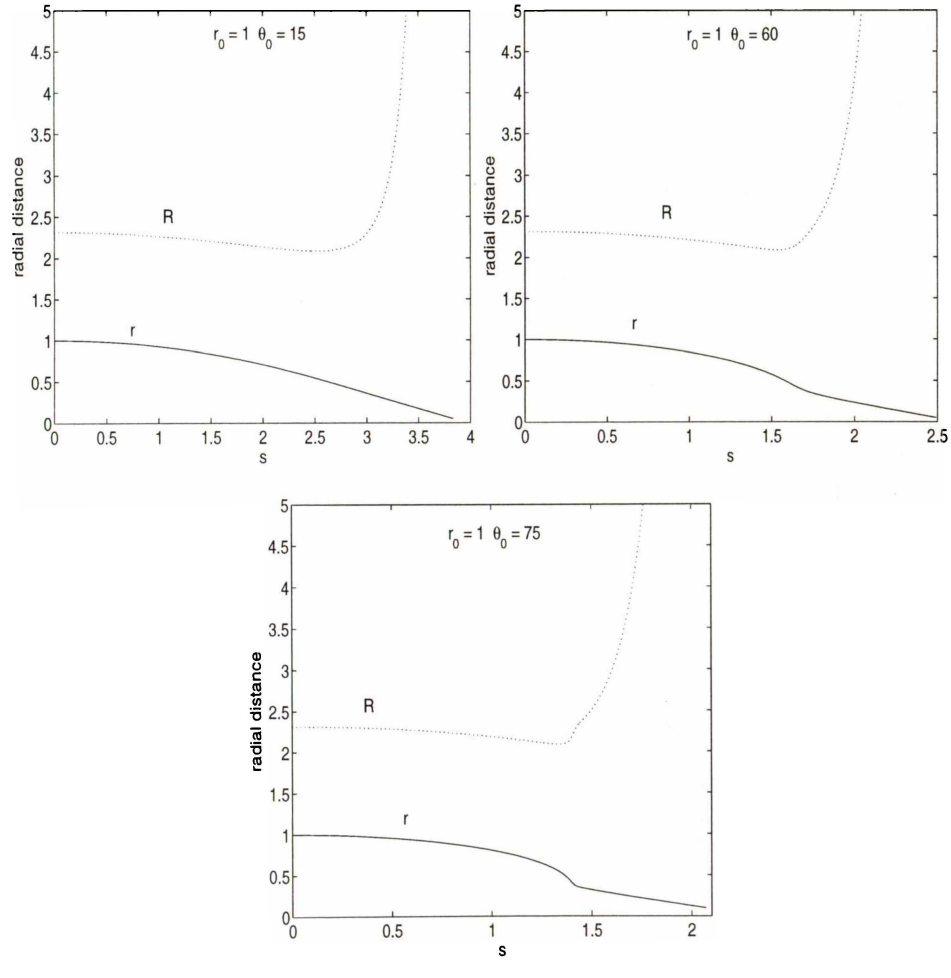

FIGURE 2.5: $r(s)$ *and* $R(s)$ *plots.*

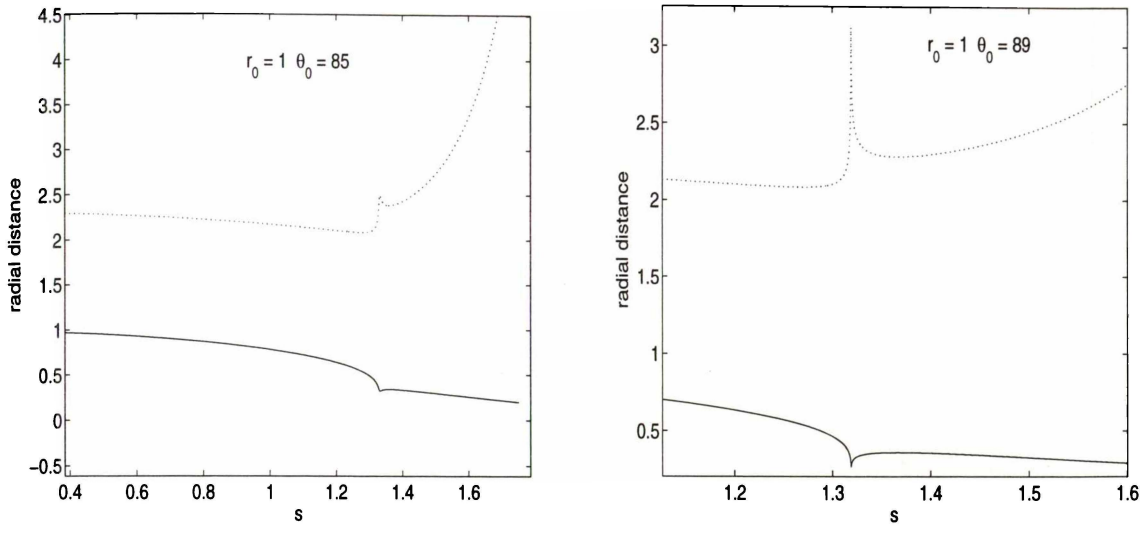

FIGURE 2.6: *$r(s)$ and $R(s)$ plots.*

2.5.5 Bound Equatorial Geodesics

We shall now consider geodesics with non zero angular momentum. We shall concentrate on those orbits that remain bounded in the $z = 0$ plane, and as all odd multipole moments vanish, will remain in this invariant plane. This is also evident from (2.44). Given $\theta_0 = \pi/2$, $\dot{\theta_0} = 0$ and $\gamma_\theta|_{\theta=\theta_0} = 0$ then $\ddot{\theta} = 0$ and therefore the motion is confined to the $\theta = \pi/2$ plane.

The metric functions simplify to

$$\psi = -m/r, \qquad \gamma = -m^2/2r^2$$

and the equations of motion become

$$r^4\ddot{r} + r^2E^2e^{-2\gamma} + \tfrac{mr^2}{2}(m-2r)\dot{r}^2 - L^2(r-m)e^{4\psi-2\gamma} = 0 \tag{2.55}$$

$$\dot{t} = Ee^{-2\psi}, \qquad \dot{\varphi} = -Lr^{-2}e^{2\psi}. \tag{2.56}$$

Furthermore (2.46) becomes

$$\dot{r}^2 = e^{-2\gamma}\left[E^2 - \frac{L^2e^{4\psi}}{r^2} - e^{2\psi}\right] \tag{2.57}$$

from which we can determine the r values for which $\dot{r} = 0$, i.e. the turning points of the motion. Accordingly setting $\dot{r} = 0$ in (2.57) and solving for the energy E we obtain

$$E^2 = e^{2\psi}\left[\frac{L^2e^{2\psi}}{r^2} + 1\right] \equiv V^2(r;L). \tag{2.58}$$

Here $V^2(r;L)$ is the potential function for the timelike geodesics parameterized by L. Typical curves are shown in figure 2.7.

de Felice (1991) has analyzed the general pattern of the potential *surfaces* (i.e not confined to the $z = 0$ plane) for timelike geodesics for the Curzon metric. In particular he finds that

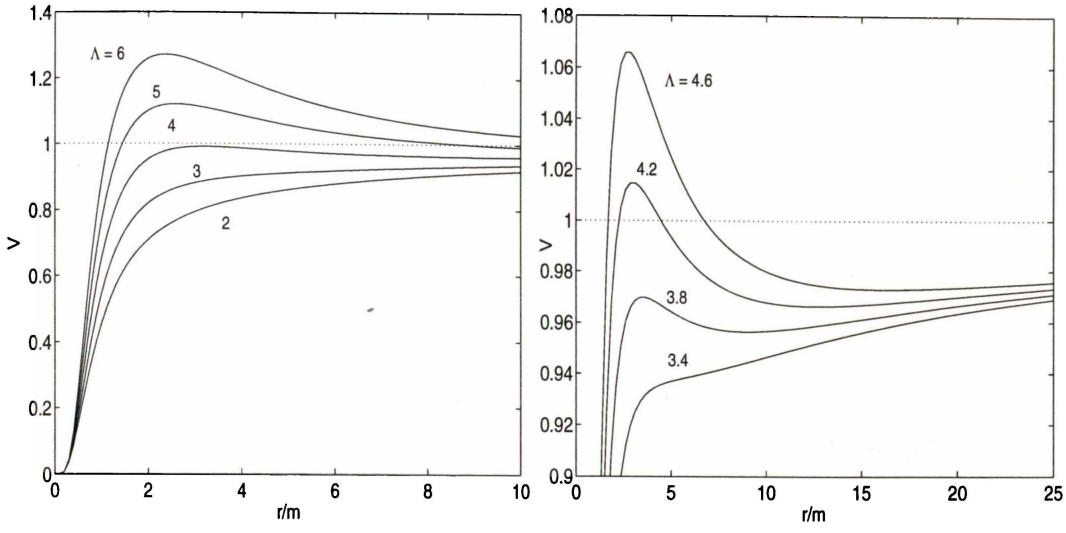

FIGURE 2.7: *Curzon potential curves.* ($\Lambda = L/m$).

the potential has turning points corresponding to real values of L only at $r > 2m$ and the last stable circular orbit occurs at $r = (3 + \sqrt{5})m$ with $L \approx 3.5m$.

We will solve (2.55) numerically with the initial conditions

$$\dot{r}_0 = \varphi_0 = t_0 = 0 \quad \text{at} \quad r = r_0. \tag{2.59}$$

Therefore we can use the potential $V^2(r; L)$ to determine the constant E. Given we are interested in bounded motion E (or r_0) will also be chosen so that there are two turning points of the motion which will in turn correspond to the aphelion and perihelion radii of the orbit.

2.5.6 Approximate Solution

Although (2.55) must be solved numerically we can, by assuming the test particle moves at large distances from the source, formulate an analytical (approximate) solution. Quevedo and Parkes (1991) using the same assumption analyzed the equatorial timelike geodesics in the Erez-Rosen spacetime.

We are interested in the shape of the orbit rather that its time evolution. Define the dimensionless variables*

$$u(\varphi) = \frac{m}{r}, \quad \Lambda = \frac{m}{L}. \tag{2.60}$$

From (2.56) and (2.57) we calculate

$$\left(\frac{du}{d\varphi}\right)^2 = u'^2 = \Lambda^2 e^{u^2}\left[E^2 e^{4u} - \frac{u^2}{\Lambda^2} - e^{2u}\right]. \tag{2.61}$$

Expanding up to the order u^3 (recall we are assuming the motion is far from the source) then

$$u'^2 = Au^3 + Bu^2 + Cu - D \tag{2.62}$$

*Recall that L, is the angular momentum per *unit mass* thus has units of length.

where the coefficients are

$$A = \tfrac{2}{3}\Lambda^2(22E^2 - 5) \tag{2.63}$$

$$B = 3\Lambda^2(3E^2 - 1) - 1 \tag{2.64}$$

$$C = 2\Lambda^2(2E^2 - 1) \tag{2.65}$$

$$D = \Lambda^2(1 - E^2). \tag{2.66}$$

It follows from equation (2.62) that motion is possible for

$$F(u) := Au^3 + Bu^2 + Cu - D \geq 0 \tag{2.67}$$

that is, the geometry of the geodesics is determined by the roots of the equations $F(u) = 0$. Since $F(u)$ is cubic in u there exists two possibilities: either all roots are real or one of them is real and the other two are complex conjugates of each other.

Let us assume that the parameters m, E and L have been chosen so that we have three unequal positive roots* of (2.62) (the potential $V^2(r; L)$ is useful to satisfy this requirement). The behaviour of the curve $F(u)$ is presented in figure 2.8.

Bounded motion is possible in the region $u_1 \leq u \leq u_2$. The particle's trajectory oscillates between the aphelion ($r_a = m/u_1$) and the perihelion ($r_p = m/u_2$). The trajectory is an (precessing) ellipse.

In the region $u > u_3$ the motion is unbounded and the test particle can move only in the direction of the gravitational source and reaches it in a finite interval of time. We cannot describe this type of motion because the approximation (2.62) is not valid near the source.

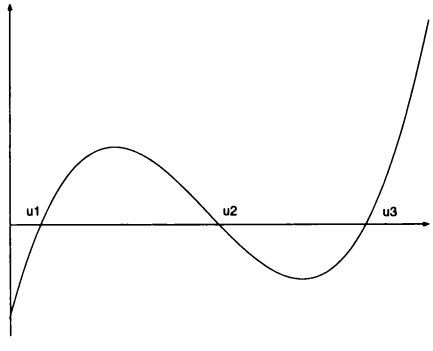

FIGURE 2.8: *The curve $F(u)$ with three distinct positive roots.*

The three roots $u_1 < u_2 < u_3$ satisfy (Abramowitz and Stegun, 1965)

$$u_1u_2 + u_2u_3 + u_3u_1 = \frac{3(2E^2 - 1)}{22E^2 - 5} \tag{2.68}$$

$$u_1u_2u_3 = \frac{3(1 - E^2)}{44E^2 - 10} \tag{2.69}$$

$$u_1 + u_2 + u_3 = \frac{3 - 9\Lambda^2(3E^2 - 1)}{2\Lambda^2(22E^2 - 5)} \equiv \xi. \tag{2.70}$$

*When two roots coincide there exists circular orbits. See Chandrasekhar (1983) for a comprehensive breakdown of differing orbits based on the analysis of the roots of $F(u)$.

For all roots to be positive these results require

$$\tfrac{1}{2} < E^2 < 1 \quad \text{and} \quad L^2 > 6m^2.$$

Following Chandrasekhar (1983) we write the three positive roots as

$$u_1 = \frac{m}{l}(1-e) \tag{2.71}$$

$$u_2 = \frac{m}{l}(1+e) \tag{2.72}$$

$$u_3 = \xi - u1 - u2 = \xi - \frac{2m}{l} \tag{2.73}$$

here l is the latus rectum, a positive constant and e is the eccentricity for which, by virtue of requiring $u_1 > 0$ satisfies,

$$0 \le e \le 1.$$

Furthermore as $u_2 < u_3$ we have $\xi - 3\mu - \mu e > 0$ where $\mu = m/l$. Substituting (2.71)-(2.73) into (2.68) and (2.69) we have

$$2\mu\xi - \mu^2(3+e^2) = \frac{3(2E^2-1)}{22E^2-5} \tag{2.74}$$

$$\mu^2(1-e^2)(\xi - 2\mu) = \frac{3(1-E^2)}{44E^2-10} \tag{2.75}$$

which relate explicitly the parameters μ and e, which describe the particles trajectory, with the parameters* E, Λ and m which determine the particles energy, angular momentum and the mass of the source. These non-linear equations are solved numerically when computing the analytic approximate solution.

Recall we wish to solve (2.62). It can be written as

$$\left(\frac{du}{d\varphi}\right)^2 = A(u-u_1)(u-u_2)(u-u_3), \tag{2.76}$$

or

$$\sqrt{A}\,\varphi = \int \left[\,(u-u_1)(u-u_2)(u-u_3)\,\right]^{-1/2} du. \tag{2.77}$$

By introducing the new variable

$$u = u_1 + 1/t^2$$

then (2.77) becomes

$$\sqrt{A}\,\varphi = \frac{-2}{\sqrt{(u_2-u_1)(u_3-u_1)}} \int \left[\,(t^2-a^2)(t^2-b^2)\,\right]^{-1/2} dt \tag{2.78}$$

where

$$a^2 = 1/(u_2-u_1) \quad \text{and} \quad b^2 = 1/(u_3-u_1).$$

Solutions are†

$$\sqrt{A}\,\varphi = \frac{-2}{\sqrt{u_3-u_1}}\,\mathrm{ns}^{-1}\left(t\sqrt{u_2-u_1}, k\right), \qquad k^2 = \frac{u_2-u_1}{u_3-u_1} \tag{2.79}$$

*Recall that ξ is a function of Λ and E.

†See entry 3.152.12 in Gradshteyn and Ryzhik (1980). Notation: Jacobi (odd) elliptic function $\mathrm{ns}(x,k) \equiv 1/\mathrm{sn}(x,k)$. And $0 \le k \le 1$ is the modulus. $K(k)$ determines the period.

thus the equation of the orbit is

$$u = u_1 + (u_2 - u_1)\,\mathrm{sn}^2\left(\tfrac{1}{2}\sqrt{A(u_3 - u_1)}\,\varphi, k\right). \tag{2.80}$$

From (2.71)–(2.73) the modulus is determined by

$$k^2 = \frac{2\mu e}{\xi - 3\mu + \mu e}$$

and satisfies $0 \leq k \leq 1$ as required.

The orbit equation can also be written as

$$\frac{l}{r} = 1 + e\left(2\,\mathrm{sn}^2(\eta\,\varphi, k) - 1\right) \tag{2.81}$$

with

$$\eta^2 = \tfrac{1}{4}A(\xi - 3\mu + \mu e). \tag{2.82}$$

Trajectories derived by means of (2.81) are illustrated in figure 2.10. In each plot the approximate solution (2.81) and the numerical solution of (2.55) are shown. Each trajectory begins at $r_0 = 180$ but have differing energy E and angular momentum values L. The corresponding potential curves for each orbit is shown in figure 2.9.

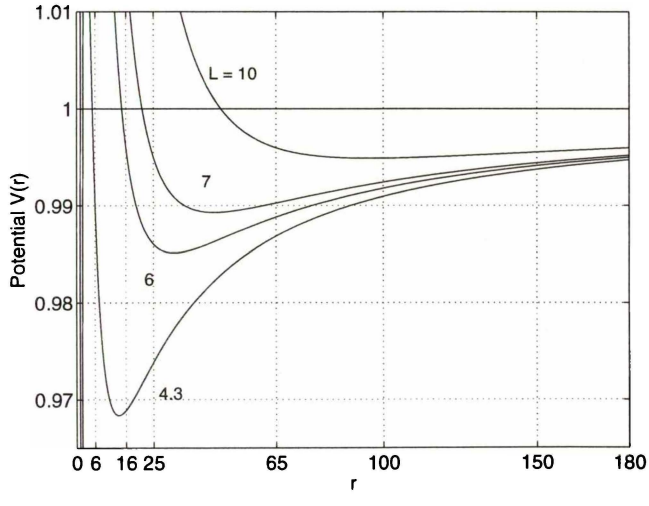

FIGURE 2.9: *Potential curves* ($m = 1$) *corresponding to the orbits shown in figure 2.10.*

From the potential curves it is evident as L increases the perihelion (closest approach) radii increases. As the approximate solution is based on the premise that the test particle moves at large distances from the gravitational source as L increases the agreement between the true (numerical) and approximate solutions should improve. This is indeed seen in the orbit comparisons illustrated in figure 2.10.

As mentioned earlier a Runge-Kutta (order 4/5) method (RK) was used to numerically solve the equations of motion. Figure 2.11 shows the typical *conservation* of the constants of the motion E and L as the integration tolerances are increased.

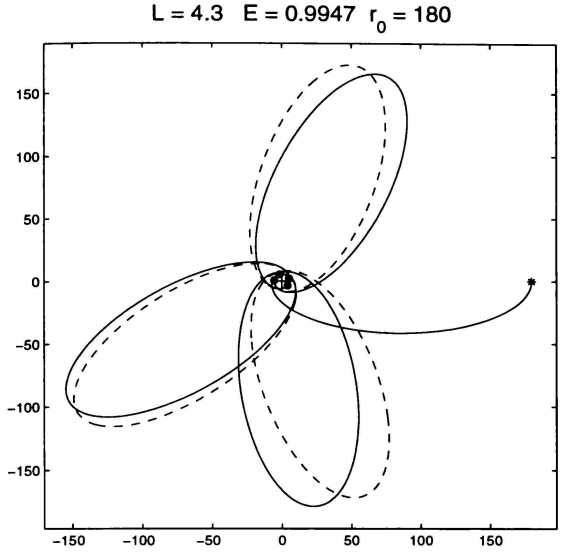

(a) $\xi = 1.1257$, $e = 0.9400$, $\mu = 0.0926$, $r_{min} = 5.5$

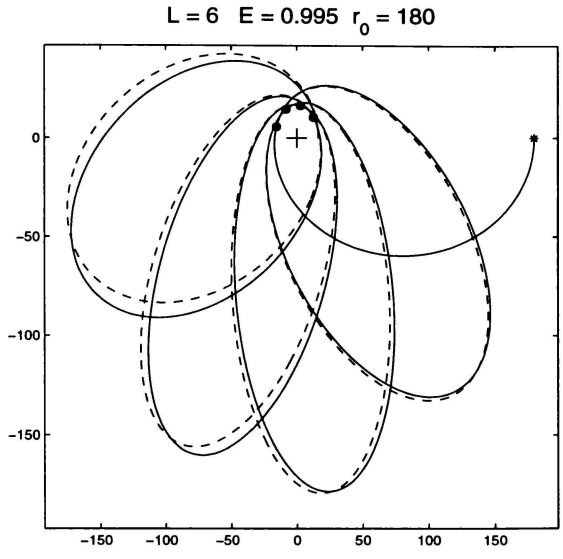

(b) $\xi = 2.6896$, $e = 0.8333$, $\mu = 0.0333$, $r_{min} = 16.4$

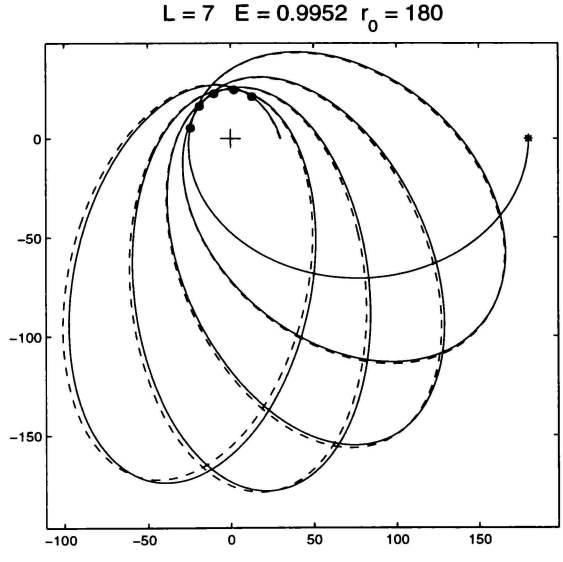

(c) $\xi = 3.8444$, $e = 0.7586$, $\mu = 0.0230$, $r_{min} = 24.7$

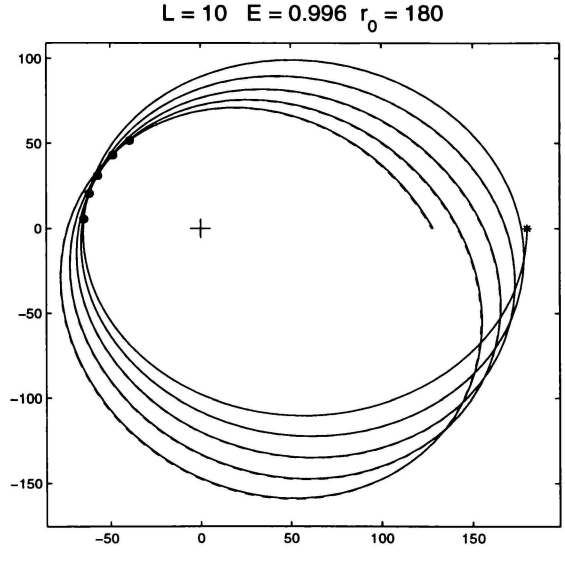

(d) $\xi = 8.3877$, $e = 0.4699$, $\mu = 0.0105$, $r_{min} = 65.0$

FIGURE 2.10: *Timelike geodesics in the equatorial plane of the Curzon solution. The solid line is the numerical solution of equation (2.55) the dashed line the is analytic approximation given by (2.81). In each the mass of the source (at the origin) is set to* 1. *The figure captions refer to the constants used in (2.81) and* r_{min} *refers to the perihelion value (marked by dots on in the plots).*

Here for a given s, the absolute difference between the numerical (n) value of the constant, e.g. $E_n(s) = \dot{t}\, e^{2\psi}$ or $L_n(s) = -\dot{\varphi} r^2 e^{-2\psi}$ and its given value E or L is plotted.

Although, not perfect, the conservation of these constants is good and the error systematically decreases as the integration tolerances are increased (although this is difficult to see in the E plot as this constant is conserved to high accuracy for any tolerance value).

The gradual rise in either quantity is due to this lack of conservation, but in our application as most computational runs are short this will not be of major consequence.

From these results we can justify the use and reliability of the RK method. In any numerical run (including the upcoming chapters) similar plots to figure 2.11 were drawn to check the output.

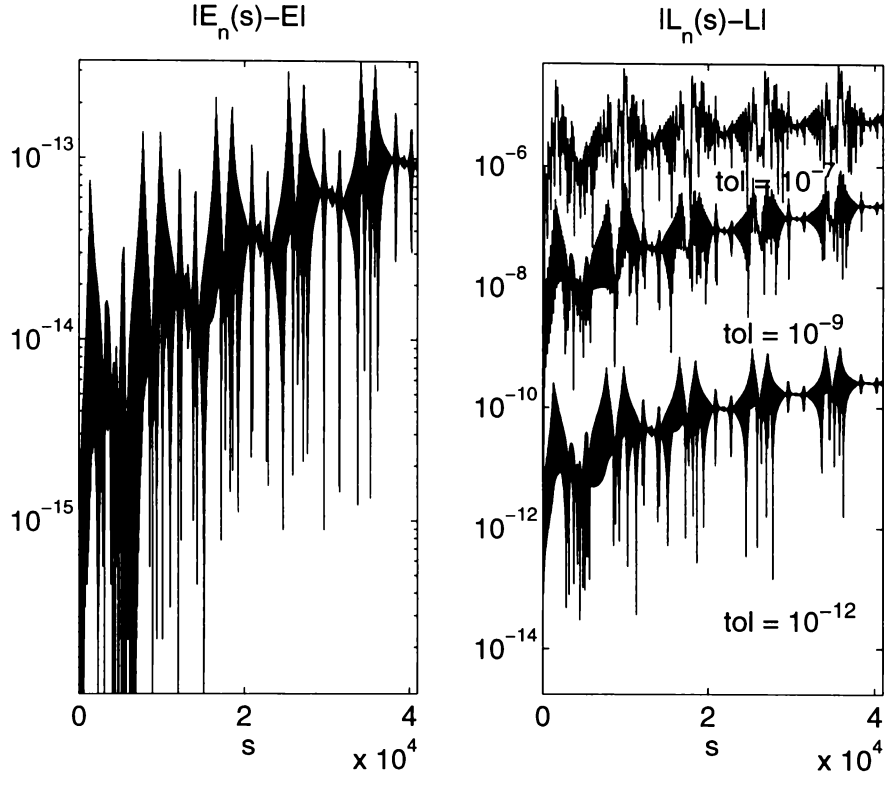

FIGURE 2.11: *Conservation of E and L.*

2.5.7 Precession of Perihelion

The trajectories shown in figure 2.10 reveal that the shift in the perihelion decreases (as indicated by the solid black dots) as the angular momentum of the test particle increases. This is anticipated, as eluded too previously in section 1.10, where it was pointed out that bounded timelike geodesics will not be closed curves but be precessing ellipses.

We now compare the numerical precession rates, Δ_N with those predicted by the elliptic approximation (2.81) and the multipole moment method described in section 1.10.

Given $\mathrm{sn}\, K = -\mathrm{sn}\, 3K = 1$ we see the approximate solution (2.81) reaches perihelion when $\varphi = K(k)/\eta$ and on the next occasion, when $\varphi = 3K/\eta$. Thus φ increases by $2K/\eta$ between two passages through perihelion. Thus the shift in perihelion given by this elliptic approximation is

$$\Delta\varphi_E = 2\pi - 2K/\eta.$$

Comparisons are given in the following tables and accompanying figures. In all, the mass

of the source is set to one: $m = 1$. Two sets of data are given. The first is that of orbits beginning at $r_0 = 90$ and the second $r_0 = 180$.

For a given L the perihelion value for the orbit beginning at $r_0 = 180$ will be less than the corresponding orbit beginning at $r_0 = 90$ (compare the second columns of tables 2.1 and 2.2). Thus the $\Delta\varphi_E$ results for the $r_0 = 180$ orbits should be the less accurate of the two. Indeed this is observed in comparing the last column of the two tables.

The accuracy of both $\Delta\varphi_M$ and $\Delta\varphi_E$ increase as L grows. This is not surprising for the $\Delta\varphi_M$ calculations, as they are based on the (small) parameter $\epsilon = M/L$. Similarly as discussed earlier, as L increases so does the perihelion value of a given orbit and the assumption that the test particle is moving at large distances from the source used to derive the elliptic approximation and thus $\Delta\varphi_E$, becomes more valid.

$m = 1 \quad r_0 = 90$						
L	$r_{\min}$	$\Delta\varphi_N$	$\Delta\varphi_M$	$\Delta\varphi_E$	$\lvert\Delta\varphi_N - \Delta\varphi_M\rvert$	$\lvert\Delta\varphi_N - \Delta\varphi_E\rvert$
5.0	10.558	1.21519	1.19620	1.24718	0.01899	0.03199
5.5	14.243	0.88964	0.88493	0.91310	0.00471	0.02346
6.0	18.496	0.69193	0.69053	0.70844	0.00140	0.01651
6.5	23.460	0.55886	0.55838	0.57060	0.00048	0.01174
7.0	29.302	0.46346	0.46328	0.47199	0.00018	0.00853
7.5	36.233	0.39204	0.39197	0.39836	0.00006	0.00632
8.0	44.537	0.33684	0.33680	0.34162	0.00004	0.00478
8.5	54.609	0.29309	0.29307	0.29678	0.00002	0.00369
9.0	67.010	0.25773	0.25772	0.26063	0.00001	0.00290
9.5	82.573	0.22866	0.22866	0.23099	0.00000	0.00233

TABLE 2.1: *Numerical and theoretical precession rates for Curzon solution (in the $z = 0$ plane) for geodesics starting at $r_0 = 90$ and various angular momentum L values . r_{min} refers to the perihelion radii. $\Delta\varphi_N$ is the numerical perihelion shift (in radians), $\Delta\varphi_M$ the predicted shift based on the relativistic multipole moments and $\Delta\varphi_E$ is the shift predicted by the elliptic solution. The final two columns illustrates the differences between the numerical and predicted shifts.*

Figure 2.12 clearly demonstrates that the accuracy of two methods increases with L. The multipole method out performs the elliptic approximation for any L and its accuracy dramatically improves for larger L.

$m = 1$ $r_0 = 180$						
L	$r_{\min}$	$\Delta\varphi_N$	$\Delta\varphi_M$	$\Delta\varphi_E$	$\lvert\Delta\varphi_N - \Delta\varphi_M\rvert$	$\lvert\Delta\varphi_N - \Delta\varphi_E\rvert$
5.0	9.690	1.24606	1.22434	1.28008	0.02172	0.03402
5.5	12.876	0.90687	0.90149	0.93234	0.00538	0.02547
6.0	16.407	0.70294	0.70134	0.72103	0.00160	0.01809
6.5	20.345	0.56641	0.56586	0.57935	0.00055	0.01294
7.0	24.747	0.46884	0.46863	0.47827	0.00021	0.00943
7.5	29.673	0.39595	0.39587	0.40296	0.00008	0.00701
8.0	35.187	0.33970	0.33966	0.34500	0.00004	0.00530
8.5	41.368	0.29518	0.29516	0.29925	0.00002	0.00407
9.0	48.308	0.25921	0.25920	0.26240	0.00001	0.00319
9.5	56.117	0.22968	0.22968	0.23220	0.00000	0.00252
10.0	64.933	0.20509	0.20509	0.20711	0.00000	0.00201
11.0	86.293	0.16671	0.16671	0.16805	0.00000	0.00134
12.0	114.312	0.13841	0.13841	0.13934	0.00000	0.00093
13.0	152.178	0.11689	0.11689	0.11756	0.00000	0.00067

TABLE 2.2: *Precession rates of geodesics starting at* $r_0 = 180$ *(see table 2.1).*

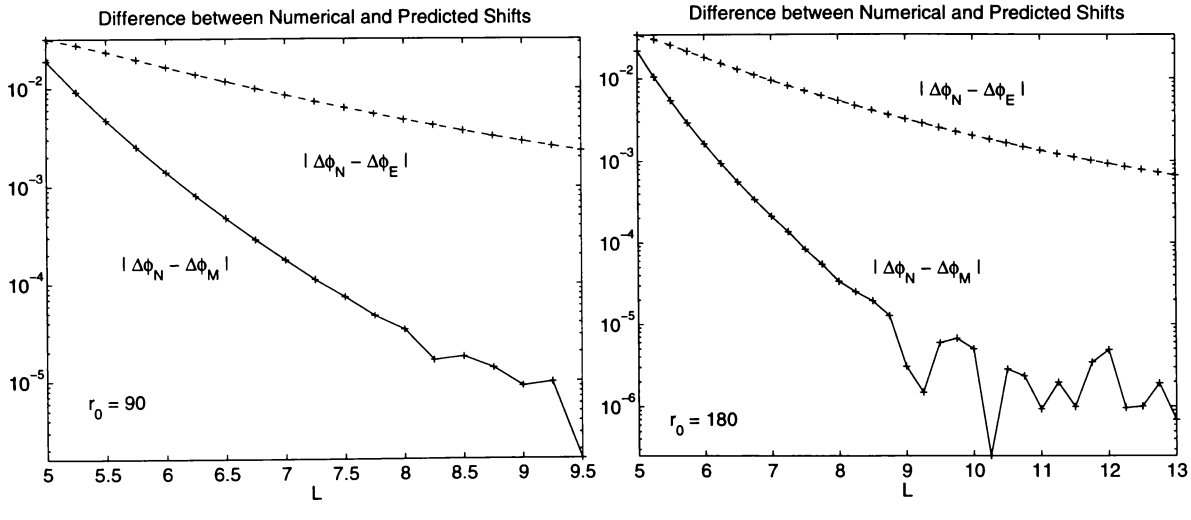

FIGURE 2.12: *Convergence of precession calculations.*

2.5.8 Precession of the Line of Nodes

We have considered the trajectories of test particles in the equatorial plane $\theta = \pi/2$. We shall now consider a bounded orbit that deviates slightly from the equatorial plane.

If the mass distribution of the source were spherically symmetric the equatorial plane would not be at all privileged and the orbit would always intersect it at the same points (nodes). This is no longer the situation when the source is not spherical, if the trajectory of the particle does not lie on the equatorial plane, then the orbit cannot be a plane curve and the orbit rotates around the symmetry axis of the mass distribution.

In Newtonian gravity this is referred to as the precession of the line of nodes and the first contribution to the precession arises from the quadrupole moment. In general relativity it is the rotational dipole moment that appears first.

Fernández-Jambrina and Hoenselaers (2001) [FH] have formulated, in terms of relativistic multipole moments of the source, the angle in which the line of nodes precesses in one revolution of a reference geodesic (in the equatorial plane).

Quevedo and Parkes (1991) [QP] calculated the contribution of the quadrupole moment in the precession of the line of nodes for the Erez-Rosen spacetime. Their method is based on Hoenselaers and Ernst (1983) work. The following analysis is a summary of [FH] and [QP].

Consider a reference geodesics $x^\mu(s)$ in the equatorial plane of the mass distribution. For simplicity we assume this geodesics is circular. Let ζ^μ be an infinitesimal vector representing the separation vector between the reference geodesic and the geodesic of the test particle (see figure 2.13), whose plane of motion is inclined by θ_0 (infinitesimally small) with respect to the equatorial plane. ζ^μ satisfies the equation of geodesic deviation

$$\frac{D^2\zeta^\mu}{Ds^2} = R^\mu_{\nu\lambda\kappa}\dot{x}^\nu\dot{x}^\lambda\dot{x}^\kappa \qquad \mu,\nu,\ldots = 0,1,2,3 \tag{2.83}$$

or equivalently

$$\ddot{\zeta}^\mu + \Gamma^\mu_{\nu\lambda,\kappa}\dot{x}^\nu\dot{x}^\lambda\zeta^\kappa + 2\Gamma^\mu_{\nu\lambda}\dot{x}^\nu\dot{\zeta}^\lambda = 0. \tag{2.84}$$

Evaluating (2.84) for the reference geodesic, $\dot{r} = \dot{\theta} = 0$, and noting that the first derivatives of the metric with respect to θ vanish on it, (2.84) becomes ($\zeta^\theta \equiv \zeta$)

$$\ddot{\zeta} - \frac{1}{2g_{\theta\theta}}(g_{tt,\theta\theta}\,\dot{t}^2 + g_{\varphi\varphi,\theta\theta}\,\dot{\varphi}^2)\Big|_{\theta=\pi/2}\zeta = 0. \tag{2.85}$$

Since

$$\dot{\zeta} = \zeta'\dot{\varphi}, \quad \ddot{\zeta} = \zeta''\dot{\varphi}^2, \quad \zeta' = \frac{d\zeta}{d\varphi} \tag{2.86}$$

(2.85) can be written

$$\zeta'' + \Omega^2\zeta = 0 \tag{2.87}$$

with

$$\Omega^2 = -\frac{1}{2\dot{\varphi}^2 g_{\theta\theta}}(g_{tt,\theta\theta}\,\dot{t}^2 + g_{\varphi\varphi,\theta\theta}\,\dot{\varphi}^2) \tag{2.88}$$

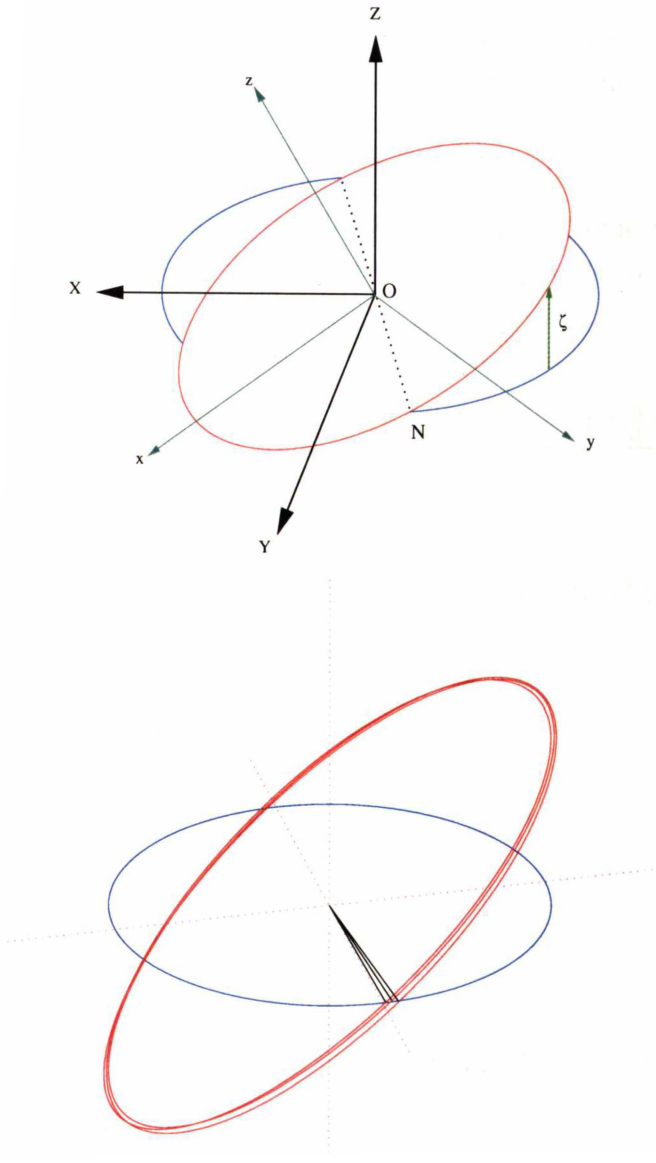

FIGURE 2.13: *The infinitesimal vector ζ is used for the calculation of the precession of the line of nodes: ON the intersection between the XY plane and the orbital plane. The components of ζ change their values after rotating once around the reference geodesic. This change corresponds to the precession of the line of nodes around the symmetry axis of the source. The bottom plot is of an actual orbit (axis are not of equal scale). The parameters are $L = 4$, inclination $\theta_0 = 5^o$, $R = 10.6$ (radius of reference circular geodesic), the rays from the origin (source $m = 1$) indicate the nodes positions of each orbit.*

where every function is to be calculated on $\theta = \pi/2$ and $r = R$, the radius of the geodesic circle. Equation (2.87) states that the nodes of nearby geodesics are separated by regular intervals of the coordinate φ. If Ω is different from one, these nodes will travel around the geodesic circle instead of remaining at constant values of the azimuthal angle, the ascending node advances by the angle $\Delta\Phi = 2\pi/\Omega - 2\pi$ per revolution.

Fernández-Jambrina and Hoenselaers (2001) show that the frequency of the precession of the nodes can be written independently of the choice of coordinates. The angle through which the line of nodes has precessed in one revolution of the reference circle is given by*

$$\Delta\Phi = \pi(\Delta_0 + \Delta_4 + \Delta_{16}) \tag{2.89}$$

where the Δ_i terms contain the relativistic (Geroch) multipole moments $M_0, M_2, \ldots$ of the source and the angular momentum of the test particle, L. Explicitly we have

$$\Delta_0 = \frac{3\,M_0M_2}{L^4} + \left(-\frac{15\,M_0^3M_4}{2} + \frac{9\,M_0^2M_2^2}{4}\right)L^{-8} + \left(\frac{105\,M_0^5M_6}{8} + \frac{45\,M_0^4M_2M_4}{8} + \frac{81\,M_0^3M_2^3}{8}\right)L^{-12}, \tag{2.90}$$

$$\Delta_4 = \frac{24\,M_0^3M_2}{L^6} + \frac{2799\,M_0^5M_2}{14L^8} + \left(-24\,M_0^4M_2^2 + \frac{12396\,M_0^7M_2}{7}\right)L^{-10} + \left(-\frac{327223\,M_0^6M_2^2}{308} + \frac{361993\,M_0^9M_2}{22}\right)L^{-12}, \tag{2.91}$$

and

$$\Delta_{16} = -\frac{120\,M_0^5M_4}{L^{10}} - \frac{2905M_0^7M_4}{2L^{12}}. \tag{2.92}$$

The following tables illustrate the precession of the nodes for the Curzon solution. Recall for this solution

$$M_0 = m, \quad M_2 = -\tfrac{1}{3}m^3, \quad M_4 = \tfrac{19}{105}m^5, \quad M_6 = -\tfrac{389}{3465}m^7$$

and the last stable circular orbit occurs at $r = (3+\sqrt{5})m$ with $L \approx 3.5m$ (de Felice, 1991). We compare the numerical (true) precession rate $\Delta\Phi_N$ and the predicted rates $\Delta\Phi_P$ calculated by (2.89) for various L values and inclination angles θ_0. The mass of the source is $m = 1$.

In general, for a fixed L, as θ_0 increases the difference between the numerical and predicted shifts (e) grows. For small θ_0 the agreement is excellent and is typically within a tenth of a percent. The above theoretical calculations are based on the assumption that the inclination angle is small. Thus this observed increase in e is expected. For values of $L < 8$ the error is a little less predictable but can be attributed to the numerical method used to calculate the (numerical) precession of the nodes. It is still encouraging to note the the relative error is still less than one percent.

*In their paper (2.89) contains terms related to the angular momentum distribution (i.e. that moments due to rotation of the source) we are considering static fields thus we have omitted these terms.

Precession of Nodes. $m = 1$					
L	θ_0	$\Delta\Phi_N$	$\Delta\Phi_P$	$e = \lvert\Delta\Phi_N - \Delta\Phi_P\rvert$	$100 * e/\Delta\Phi_N$
5	0.20	-7.5041e-03	-7.4532e-03	5.0896e-05	0.6782
	0.50	-7.5026e-03	-7.4532e-03	4.9446e-05	0.6590
	1.00	-7.4974e-03	-7.4532e-03	4.4270e-05	0.5905
6	0.20	-3.1330e-03	-3.1299e-03	3.1640e-06	0.1010
	0.50	-3.1325e-03	-3.1299e-03	2.6020e-06	0.0831
	1.00	-3.1305e-03	-3.1299e-03	5.9500e-07	0.0190
8	0.20	-8.7764e-04	-8.7762e-04	2.1300e-08	0.0024
	0.50	-8.7749e-04	-8.7762e-04	1.2720e-07	0.0145
	1.00	-8.7696e-04	-8.7762e-04	6.5760e-07	0.0750
10	0.10	-3.4163e-04	-3.4163e-04	7.0000e-10	0.0002
	0.20	-3.4162e-04	-3.4163e-04	8.9000e-09	0.0026
	0.50	-3.4157e-04	-3.4163e-04	6.5900e-08	0.0193
	1.00	-3.4136e-04	-3.4163e-04	2.6950e-07	0.0790
	5.00	-3.3490e-04	-3.4163e-04	6.7289e-06	2.0092
12	0.10	-1.6045e-04	-1.6045e-04	1.1000e-09	0.0007
	0.20	-1.6044e-04	-1.6045e-04	4.9000e-09	0.0031
	0.50	-1.6042e-04	-1.6045e-04	3.1400e-08	0.0196
	1.00	-1.6032e-04	-1.6045e-04	1.2600e-07	0.0786
	5.00	-1.5732e-04	-1.6045e-04	3.1268e-06	1.9875
14	0.10	-8.5267e-05	-8.5267e-05	6.5000e-10	0.0008
	0.20	-8.5265e-05	-8.5267e-05	2.6400e-09	0.0031
	0.50	-8.5251e-05	-8.5267e-05	1.6600e-08	0.0195
	1.00	-8.5201e-05	-8.5267e-05	6.6420e-08	0.0779
	5.00	-8.3620e-05	-8.5267e-05	1.6469e-06	1.9695

TABLE 2.3: *Comparison between numerically determined precession of nodes per revolution of the reference circular geodesic* ($\Delta\Phi_N$) *and the predicted value* ($\Delta\Phi_P$) *evaluated from (2.89). L is the angular momentum of the test particle, θ_0 refers to the inclination (from the $z = 0$ plane) of the orbit, e is the absolute error and the final column is the relative percentage error. The radius of the reference circular geodesics corresponding to the above L values are: $r_{L=6} = 31.7$, $r_8 = 59.8$, $r_{10} = 95.9$, $r_{14} = 191.9$. The mass of the source is $m = 1$.*

2.6 $n = 1 + 2$ Solution

The previous section discussed the $n = 0$ bispherical solution. By calculating its relativistic multipole moments it was seen that the odd multipole moments vanish. This indicated that the solution had equatorial symmetry which ultimately lead to the conclusion that the $n = 0$ solution was indeed the Curzon metric. We now endeavor to formulate a further bispherical solution that has equatorial symmetry.

In section 2.4 it was shown for single term solutions of the form

$$\psi_n(\alpha, \beta) = -\sqrt{\cosh\beta - \cos\alpha}\, A_n P_n(\cos\alpha)\, e^{(n+1/2)\beta} \quad n = 0, 1, 2, \ldots \tag{2.93}$$

the associated metric generated by these particular solutions is that of a point source (of mass* $\sqrt{2}A_n m$) located at the singular point of the harmonic function (2.93): at $z = m$ on the symmetry axis. The dipole moment is nullified by the coordinate shift $z \to z + (2n+1)m$. After this translation the next odd moment in general is given by

$$M_3 = \tfrac{8}{3}\sqrt{2}\, m^4\, A_n\, n(n+1)(n+2) \tag{2.94}$$

from which it is clear that the only single term solution for which this moment vanishes is the $n = 0$ solution. Thus ψ_0 is the only single term solution that can exhibit a plane of symmetry.

Physically, for a plane of symmetry to exist the center of mass (effectively the location of the dipole) must coincide with the location of the source $z_s = m$. Clearly we must resort to a linear combination of the particular solutions (2.93). For simplicity we will consider the superposition of two particular solutions.

Firstly consider the two term solution of the form

$$\psi_{0n} = -\sqrt{\cosh\beta - \cos\alpha}\left[\, AP_0(\cos\alpha)e^{\beta/2} + BP_n(\cos\alpha)e^{(n+1/2)\beta}\,\right] \tag{2.95}$$

here $n = 1, 2, \ldots$. The center of mass is located at

$$z_{com} = \frac{m(A + B + 2Bn)}{A + B}. \tag{2.96}$$

Given we require $z_{com} = z_s = m$ then we must set $B = 0$. Thus no ψ_{0n} superpositions permit solutions that can have equatorial symmetry. Now consider the two term solution

$$\psi_{1n} = -\sqrt{\cosh\beta - \cos\alpha}\left[\, AP_1 e^{3\beta/2} + BP_n e^{(n+1/2)\beta}\,\right] \tag{2.97}$$

where $n = 2, 3 \ldots\ldots$ Its center of mass is located at

$$z_{com} = \frac{m(3A + B + 2Bn)}{A + B}. \tag{2.98}$$

Equating $z_{com} = z_s = m$ requires $B = -A/n$. Setting B to this value then

$$M_3 = -\tfrac{4}{3}\sqrt{2}m^4 A(n-1)(n-2) \tag{2.99}$$

which vanishes for $n = 2$. Thus the ψ_{12} solution is a likely to have a plane of symmetry.

*We have relabeled the coordinate scale factor c by m and will use this notation throughout the remainder of this chapter.

2.6.1 ψ and γ

If $n = 2$, ψ_{12} has mass moment

$$M_0 = \tfrac{1}{2}\sqrt{2}Am \tag{2.100}$$

thus for simplicity we set $A = \sqrt{2}$ then we have

$$\psi \equiv \psi_{12} = -\sqrt{2(\cosh\beta - \cos\alpha)}\left[P_1(\cos\alpha)\, e^{3\beta/2} - \tfrac{1}{2}P_2(\cos\alpha)\, e^{5\beta/2}\right] \tag{2.101}$$

and

$$\begin{aligned}\gamma \equiv \gamma_{12} \;=\; \frac{1}{32}\Big[&75e^{6\beta}\cos^6\alpha - 216e^{5\beta}\cos^5\alpha - (117e^{6\beta} - 222e^{4\beta})\cos^4\alpha + \\ &(288e^{5\beta} - 96e^{3\beta})\cos^3\alpha + (45e^{6\beta} - 252e^{4\beta} + 16e^{2\beta})\cos^2\alpha - \\ &(72e^{5\beta} - 96e^{3\beta})\cos\alpha - 3e^{6\beta} + 30e^{4\beta} - 16e^{2\beta}\Big].\end{aligned} \tag{2.102}$$

The relativistic moments of this solution are

$$M_0 = m \tag{2.103}$$

$$M_1 = M_3 = M_5 = 0 \tag{2.104}$$

$$M_2 = -\frac{13}{3}m^3 \tag{2.105}$$

$$M_4 = \frac{499}{105}m^5 \tag{2.106}$$

$$M_6 = -\frac{15189707}{928620}m^7 \;(\sim 16.4m^7). \tag{2.107}$$

We note in nullifying both the dipole and M_3 moments we are left with no arbitrary constants in the remaining higher moments. They are determined by the one parameter m.

As in the $n = 0$ solution it is useful to introduce mass centered ($z = m, \rho = 0$) spherical coordinates (r, θ, φ) into the above metric terms. From (2.34) and (2.35) we find

$$\psi \;=\; -\frac{m}{r} + \frac{2m^3}{r^3}(3\cos^2\theta - 1) \;=\; -\frac{m}{r} + \frac{4m^3}{r^3}P_2(\cos\theta) \tag{2.108}$$

$$\gamma = -\frac{m^2}{2r^2}\sin^2\theta\left[\frac{12m^4}{r^4}(25\cos^4\theta - 14\cos^2\theta + 1) + \frac{6m^2}{r^2}(5\cos^2\theta - 1) + 1\right]. \tag{2.109}$$

In section 2.6.3 we will show that this solution has a plane of symmetry and thus verifying our earlier assumption that all odd multipole moments vanish.

2.6.2 Geodesics on the Axis

Recall that the bispherical metric in spherical coordinates becomes

$$ds^2 = e^{2\psi}dt^2 - e^{-2\psi+2\gamma}(dr^2 + r^2 d\theta^2) - e^{-2\psi}r^2 \sin^2\theta\, d\varphi^2. \tag{2.110}$$

The geodesic equations determined from this metric are given in section 2.5.3 with ψ and γ given by (2.108) and (2.109) respectively.

In this section we will consider the geodesics of test particles released on the z axis with zero angular momentum. The particle's motion is confined to the axis and its equation of motion is given by ($r \equiv z$)

$$\dot{z}^2 = e^{2\psi}(E^2 e^{-2\psi} - 1) \tag{2.111}$$

where along the axis we have

$$\psi = -\frac{m}{z} + \frac{4m^3}{z^3}. \tag{2.112}$$

We shall assume that the particle starts from rest at z_0. The constant E is then given by

$$\ln E = \psi_0 = -mz_0^{-1} + 4m^3 z_0^{-3}. \tag{2.113}$$

Solving (2.111) for $\dot{z}^2 = 0$ determines the turning points of the motion. Introducing

$$u = \frac{m}{z} > 0$$

we have

$$4u_0^3 - u_0 = 4u^3 - u \tag{2.114}$$

where $u_0 = m/z_0$. Let $c_0 = 4u_0^3 - u_0$. Thus the roots of the cubic $f(u) := c_0 + u - 4u^3$ are required. $f(u)$ can be thought of as the potential function for the orbits along the axis. There are three cases to consider:

1. $c_0 = 0$ $\quad (u_0 = 0, \frac{1}{2})$
2. $c_0 < 0$ $\quad (0 < u_0 < \frac{1}{2})$
3. $c_0 > 0$ $\quad (u_0 > \frac{1}{2})$

If $c_0 = 0$, $f(u)$ will have roots $u_1 = 0, u_2 = \pm\frac{1}{2}$. Clearly the negative root is of no physical importance. Given that $f \to 0^+$ as $u \to 0$ and $f \to -\infty$ as $u \to \infty$, a particle released from $u_0 = \frac{1}{2}$ ($z_0 = 2m$) we be accelerated towards infinity, $u = 0$.

For $f(u)$ to permit three real roots we must have (Spiegel, 1997)

$$\frac{c_0^2}{64} - \frac{1}{1728} := \Delta \leq 0. \tag{2.115}$$

If $\Delta = 0$ at least two roots are equal, corresponding to

$$c_0 = \pm\frac{1}{3\sqrt{3}}. \tag{2.116}$$

If we take the positive value of (2.116) then the roots of $f(u)$ are $-\sqrt{3}/6, -\sqrt{3}/6, \sqrt{3}/3 = u_0$, as $f(0) = c_0 > 0$ and $f(u) \to -\infty$ as $u \to \infty$ then a particle released from u_0 will also be accelerated towards infinity.

Alternatively if we take the negative value for c_0 then $f(u)$ has roots $-\sqrt{3}/3, \sqrt{3}/6, \sqrt{3}/6 = u_0$ and as $f(0) < 0$ then the particle starting at u_0 ($z_0 = 6m/\sqrt{3}$) remains there. This however is an unstable critical point.

This possibility seems peculiar as we are considering static fields. Szekeres (1968) showed that static, *two body* solutions are possible in general relativity, if at least one of the two point masses is endowed with a multiple mass structure. We however only have one source.

If $\Delta < 0$ all roots are real and unequal. Furthermore if

$$-\frac{1}{3\sqrt{3}} < c_0 < 0 \tag{2.117}$$

for which $z_0 > 2m$ then the product of the three roots will be negative and thus we must have two positive roots corresponding to the two points on the axis the particle oscillates between. If

$$0 < c_0 < \frac{1}{3\sqrt{3}} \tag{2.118}$$

then the product of the roots is positive and thus only one positive roots exists, the particle begins from here and again accelerates towards infinity along the axis. Figures 2.14 and 2.15 demonstrate these different possibilities.

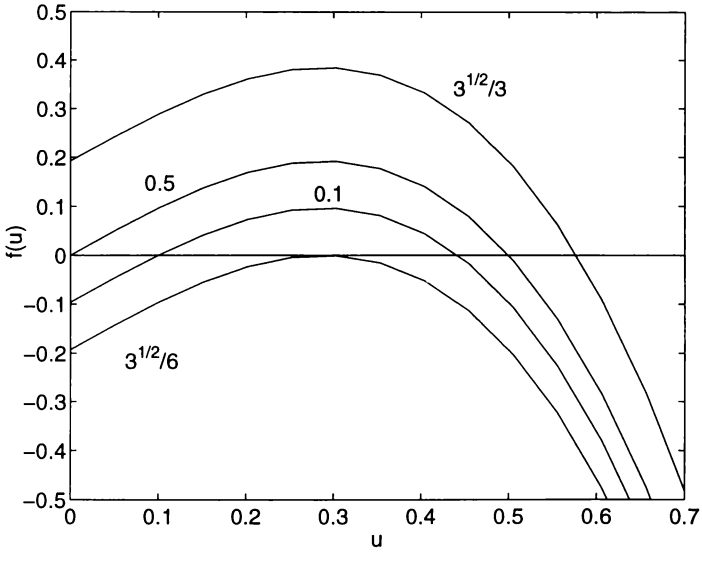

FIGURE 2.14: $f(u)$. *The labels refer to the* u_0 *value.*

Naturally, questions arises for this solution. For example, is this repulsive type motion true for directions (starting points) other than axial? How strong is the repulsion (i.e. can the repulsion be overcome by test particles moving down the axis with sufficient initial velocity? What is the velocity of the test particle in the repulsion type motion - what is its limiting value ($v \approx c$?).

We must emphasis the fact that these strange phenomena where confirmed in the original bispherical coordinates *and* spherical coordinates, along with numerous numerical ode solvers.

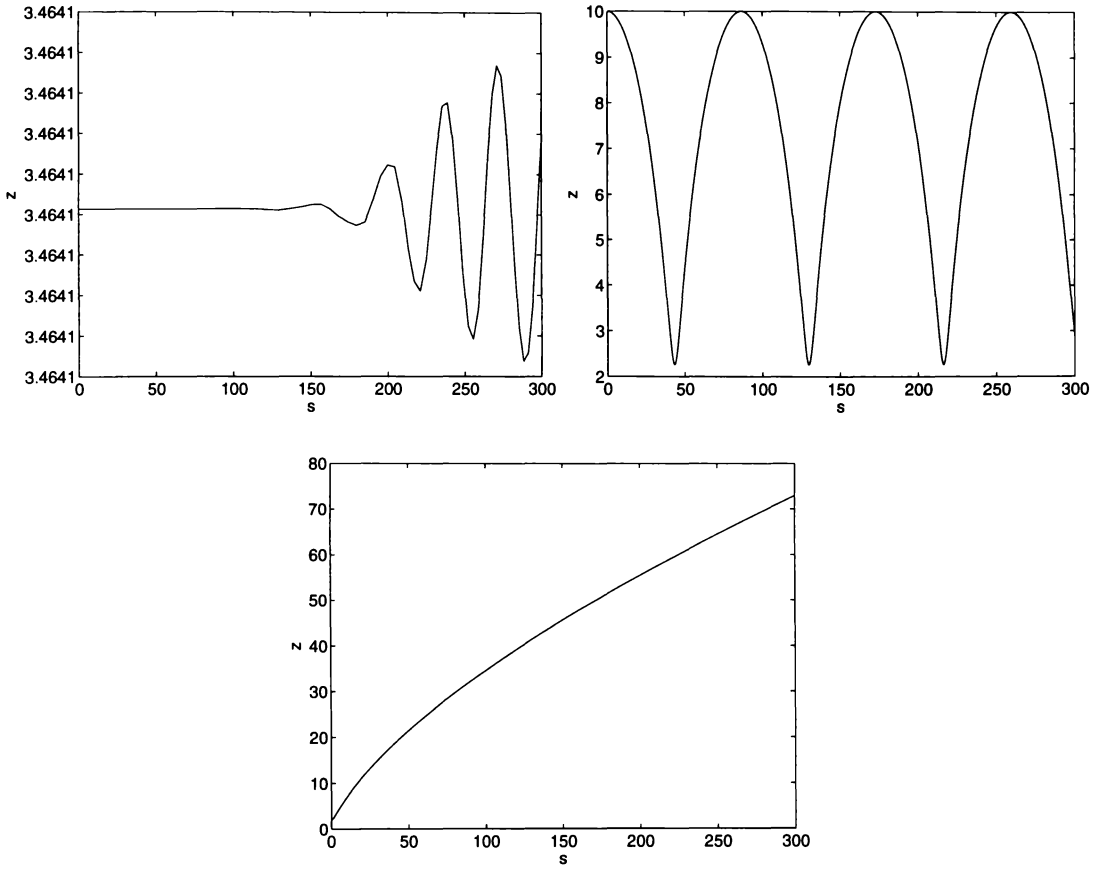

FIGURE 2.15: *Various types of orbits along the z axis. The first plot is that of the particle released at the critical point* $z_0 = 6m/\sqrt{3}$ *which corresponds to an unstable stationary point. This is indicated by the numerical 'junk' at later s values. The second is of the oscillatory type (see the above potential figure). The later plot is of a test particle repelled to infinity along the axis. For all we take* $m = 1$.

2.6.3 Geodesics in the Plane

We shall now consider the orbits of test particles in the equatorial plane of the metric (2.110). It is now possible to show that the $\theta = \pi/2$ equatorial plane is indeed a plane of symmetry for which geodesics will be confined.

Assume that a test particle has initial conditions $\theta_0 = \pi/2$, $\dot{\theta} = 0$, $r_0 \neq 0$ and $\dot{r}_0 \neq 0$. The θ geodesic equation (given by (2.44)) then reduces to the form

$$\ddot{\theta} = f(r, \dot{r})\psi_\theta + g(r, \dot{r})\gamma_\theta \tag{2.119}$$

given in the plane $\psi_\theta = \gamma_\theta = 0$ then $\ddot{\theta} = 0$ and the motion is thus confined to the plane. This implies all odd multipole moments must vanish.

Figure 2.17 gives examples of bounded equatorial orbits in this spacetime. The associated potential curves for these orbits are shown in figure 2.16. We supplement the numerical solutions with that of an approximate solution calculated in an analogous manner as described in section 2.5.5.

The only coefficient in the approximation (2.62) that needs altering is*

$$A = \frac{2}{3}\Lambda^2(34E^2 - 1). \tag{2.120}$$

The constants ξ, μ and e are now determined by

$$\xi = \frac{3 - 9\Lambda^2(3E^2 - 1)}{2\Lambda^2(34E^2 - 11)} \tag{2.121}$$

$$2\mu\xi - \mu^2(3 + e^2) = \frac{3(2E^2 - 1)}{34E^2 - 11} \tag{2.122}$$

$$\mu^2(1 - e^2)(\xi - 2\mu) = \frac{3(1 - E^2)}{68E^2 - 22}. \tag{2.123}$$

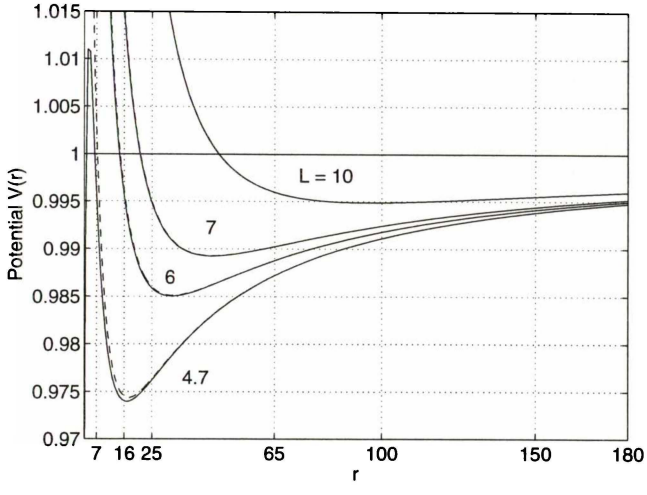

FIGURE 2.16: *Potential curves of the $n = 1 + 2$ solution ($m = 1$). They correspond to the orbits shown in figure 2.17. The dashed curves (hard to see in the higher L curves) are those of the Curzon solution used in the earlier section.*

2.6.4 Perihelion Precession

The perihelion precession rates for orbits beginning at $r_0 = 90$ with various L values are shown in table 2.4. The numerically determined values are compared with those given by the elliptic approximation and multipole moments method (section 1.10). As in the previous Curzon solution, we see as L increases the differences between the predicted and numerical values become less.

Each multipole moment for the $n = 1+2$ solution is of the same sign and of greater magnitude when compared with the corresponding $n = 0$ (Curzon) solution moments. Therefore given two equatorial orbits, one in the Curzon ($n = 0$) spacetime and the other in the $n = 1+2$ spacetime, with the same L and r_0 (and thus approximately the same E if r_0 is sufficiently large - see figure 2.16) the advance in the perihelion will be greater for the $n = 1+2$ solution. From comparing with table 2.1 we see that the precession rates are indeed greater than the corresponding Curzon orbits.

*The variables Λ, l, e etc are introduced in section 2.5.5.

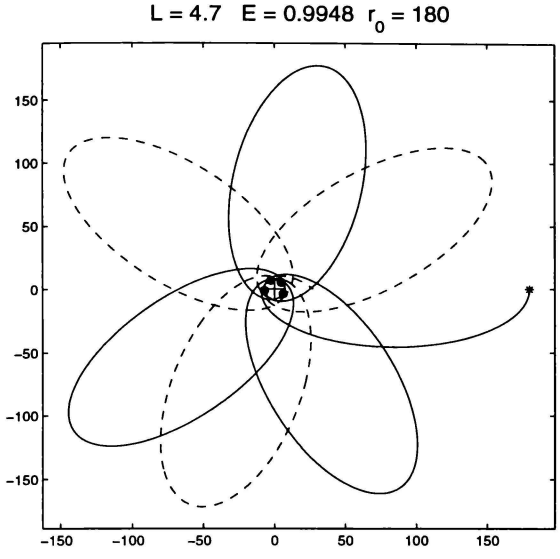

(a) $\xi = 1.0719$, $e = 0.9196$, $\mu = 0.0691$ $r_{min} = 7.1$, $\Delta\varphi_N = 2.45320$, $\Delta\varphi_E = 1.89818$

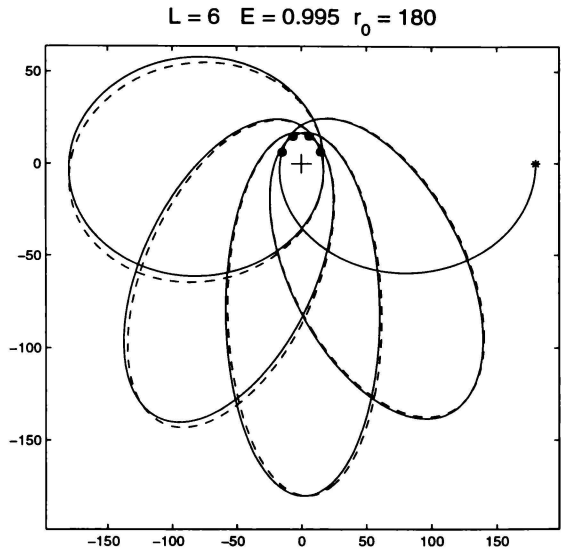

(b) $\xi = 1.9917$, $e = 0.8348$, $\mu = 0.0336$, $r_{min} = 16.2$, $\Delta\varphi_N = 0.78062$, $\Delta\varphi_E = 0.77065$

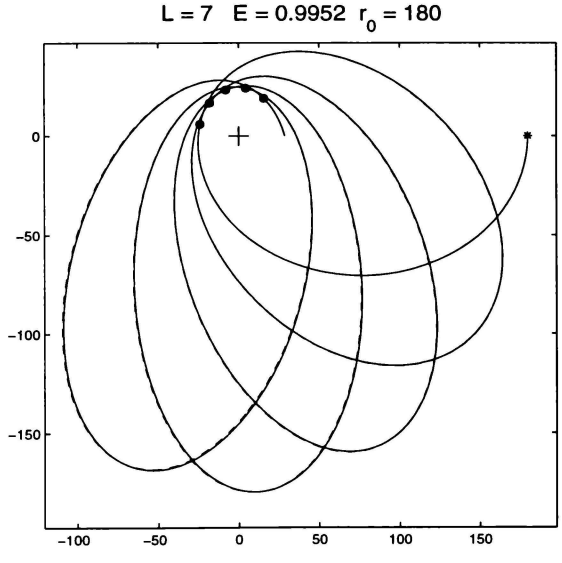

(c) $\xi = 2.8503$, $e = 0.7595$, $\mu = 0.0231$, $r_{min} = 24.6$, $\Delta\varphi_N = 0.49872$, $\Delta\varphi_E = 0.50037$

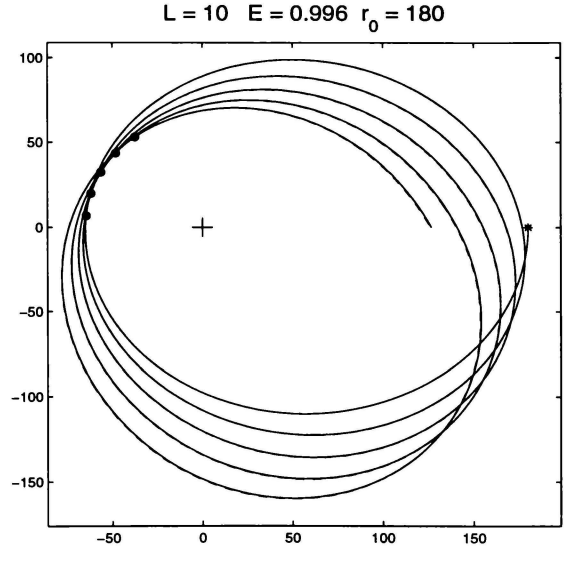

(d) $\xi = 6.2089$, $e = 0.4703$, $\mu = 0.0105$, $r_{min} = 64.8$, $\Delta\varphi_N = 0.20999$, $\Delta\varphi_E = 0.21141$

FIGURE 2.17: *Timelike geodesics in the equatorial plane of the $n = 1 + 2$ solution. The solid line is the numerical solution the dashed line the is analytic approximation. In each the mass of the source (at the origin) is set to 1. The figure captions refer to the constants used in the approximation and r_{min} refers to the perihelion value (marked by dots on in the plots). $\Delta\varphi_N$ and $\Delta\varphi_E$ are the numerical and elliptic approximation perihelion precession rates respectively. Compare with figure 2.10 and table 2.1.*

This can also be explained by the fact that the perihelion radii for the $n = 1 + 2$ solution are less than the Curzon orbits (compare column two of tables 2.4 and 2.1).

$m = 1 \quad r_0 = 90$						
L	$r_{\min}$	$\Delta\varphi_N$	$\Delta\varphi_M$	$\Delta\varphi_E$	$\lvert\Delta\varphi_N - \Delta\varphi_M\rvert$	$\lvert\Delta\varphi_N - \Delta\varphi_E\rvert$
5.00	10.084	1.53297	1.42798	1.39699	0.10498	0.13598
5.50	13.934	1.02406	1.00271	0.99173	0.02135	0.03233
6.00	18.265	0.76366	0.75791	0.75578	0.00575	0.00788
6.50	23.273	0.60208	0.60025	0.60151	0.00183	0.00057
7.00	29.141	0.49161	0.49095	0.49332	0.00065	0.00171
7.50	36.089	0.41141	0.41115	0.41369	0.00026	0.00229
8.00	44.403	0.35072	0.35061	0.35299	0.00011	0.00227
8.50	54.478	0.30337	0.30332	0.30543	0.00005	0.00206
9.00	66.878	0.26554	0.26552	0.26735	0.00002	0.00180
9.50	82.435	0.23475	0.23473	0.23630	0.00001	0.00156

TABLE 2.4: *Numerical and theoretical precession rates for $n = 1 + 2$ solution geodesics starting at $r_0 = 90$ and various angular momentum L values. r_{min} refers to the perihelion radii. $\Delta\varphi_N$ is the numerical perihelion shift (in radians), $\Delta\varphi_M$ the predicted shift based on the relativistic multipole moments and $\Delta\varphi_E$ is the shift predicted by the elliptic solution. The final two columns illustrates the differences between the numerical and predicted shifts. Compare with table 2.1.*

2.6.5 Precession of the Nodes

We now turn our attention to geodesics that deviate slightly from the equatorial plane and compare numerical and predicted values for the rate of the precession of the nodes of such geodesics.

The analysis given in section 2.5.8 assumes the reference geodesic is circular. These orbits correspond to the turning points of the potential

$$V^2(r, \theta; L) = e^{2\psi}\left[\frac{L^2 e^{2\psi}}{r^2 \sin^2\theta} + 1\right] \tag{2.124}$$

where in general $\psi = \psi(r, \theta)$. We are interested in circular orbits in the $\theta = \pi/2$ plane thus in (2.124) we have $\psi = -m/r - 2m^3/r^3$.

The turning points are found by solving

$$r^4 m + 6r^2 m^3 - e^{2\psi} L^2 (r^3 - 2mr^2 - 12m^3) = 0. \tag{2.125}$$

Solving with respect to L^2 we have

$$L^2 = \frac{r^4 m + 6r^2 m^3}{e^{2\psi}(r^3 - 2mr^2 - 12m^3)} \tag{2.126}$$

and as $L^2 > 0$ then $r > 3.2\,m$ approximately and the minimum of L^2 occurs at $r \approx 7.4\,m$. Thus $L^2_{min} \approx 15.5m^2$ or $L_{min} \approx 3.94m$ and this corresponds to the angular momentum of the last stable circular orbit.

Precession of Nodes. $m = 1$, $\theta_0 = 0.1^o$				
L	$\Delta\Phi_N$	$\Delta\Phi_P$	$e = \lvert\Delta\Phi_N - \Delta\Phi_P\rvert$	$100 * e/\Delta\Phi_N$
5.00	-9.851316e-02	-9.724505e-02	1.268105e-03	1.287245
6.00	-4.079276e-02	-4.071892e-02	7.384761e-05	0.181031
7.00	-2.038206e-02	-2.037476e-02	7.295433e-06	0.035793
8.00	-1.140917e-02	-1.140820e-02	9.674948e-07	0.008480
9.00	-6.911381e-03	-6.911244e-03	1.373156e-07	0.001987
10.00	-4.440856e-03	-4.440849e-03	6.981093e-09	0.000157

TABLE 2.5: *Comparison between numerically determined precession of nodes per revolution of the reference circular geodesic ($\Delta\Phi_N$) and the predicted value ($\Delta\Phi_P$) evaluated from (2.89). e is the absolute error and the final column is the relative percentage error.*

Table 2.5 compares the precession rates for an orbit that has inclination of $\theta_0 = 1^o$ from the equatorial plane. The agreement between the numerical and predicted values improves as L increases as indicated in the last two columns. The shifts are larger (more negative) than the Curzon solution and can be attributed to the larger multipole moments of this solution.

2.7 Summary

In this chapter we have constructed two bispherical solutions that have an equatorial plane of symmetry. It was shown that the $n = 0$ function is the only single term solution that has a plane of symmetry. Furthermore, no two term superposition containing the $n = 0$ solution can have a plane of symmetry. A linear combination of the $n = 1 + 2$ solutions does however, generate a field with no odd multipole moments.

It was evident for both bispherical solutions that the introduction of mass centered spherical coordinates (at $z = c = m$, $\rho = 0$) readily simplified the metric. In particular the $n = 0$ solution was the well known Curzon solution. The $n = 1 + 2$ solution is a generalization of the Curzon solution.

It was shown that for the Curzon solution the timelike geodesics with zero angular momentum experienced a repulsive force if released close from the ρ axis.

The introduction of a more physical radial coordinate in which to follow the trajectories did not, unfortunately, solve this enigma. It is anticipated that this phenomena is due to the directional dependence of the singularity. Further investigation of this is warranted and is an obvious extension of these investigations.

Test particle trajectories of zero angular momentum, released on the z axis in the $n = 1+2$ spacetime were also calculated. It was possible for the test particles to oscillate along the axis or be accelerated to infinity along the axis. There also exists an unstable release point for

which the particle remains stationary. This is especially interesting.

The beauty of solutions having equatorial symmetry is evident when considering orbits of test particles starting from rest in this plane: they are confined to it. The numerical and theoretical precession of the perihelion were computed and agreed well for those orbits of relativity high L values.

Similar results for the precession of the nodes for orbits slightly deviating from the plane (and of circular nature within the plane) was evident. Although it is clear that circular orbits are possible in the equatorial plane for the $n = 1+2$ solution we have not ascertained whether this is so for other planes.

Both solutions considered in this chapter represent the field of point like masses located on the z axis. In the next chapter we consider those fields generated from ring like mass distributions in the ρ plane.

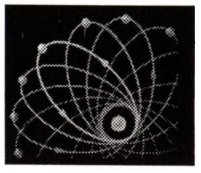

Chapter 3
Toroidal Coordinates

3.1 Introduction

This chapter is concerned with calculating Weyl fields using toroidal coordinates. In bispherical coordinates the singularities of ψ are located on the z axis. Now the sources (singularities of ψ) have a ring-like distribution in the $z = 0$ plane.

Bach and Weyl (1922) first constructed the relativistic field of a pure ring mass source in terms of elliptic functions. Misra (1961) calculated the external field due to any toroidal distribution in terms of toroidal functions. He gives gives one example, that of the Bach-Weyl ring solution. We derive three new solutions.

Timelike orbits of zero angular momentum are presented. It becomes evident for the ring solution, when the particle oscillates along the z axis, that the period of oscillation can increase as the mass of the ring is increases. This is in direct contrast to the Newtonian scenario.

The relativistic multipole structure of any arbitrary harmonic toroidal solution is calculated, enabling us to apply the results of Fernández-Jambrina and Hoenselaers (2001) to compare the advance of the perihelion of closed timelike orbits with that of numerical values and those computed from an approximate solution to these orbits.

3.2 Coordinates

Toroidal coordinates α, β, φ are related to cylindrical polar coordinates ρ and z by the formulas

$$\rho = \frac{c \sinh \alpha}{\cosh \alpha - \cos \beta} \qquad z = \frac{c \sin \beta}{\cosh \alpha - \cos \beta} \tag{3.1}$$

where

$$0 \leq \alpha < \infty \qquad 0 < \beta \leq 2\pi \qquad 0 < \varphi \leq 2\pi$$

and c is a positive scale factor. The triply orthogonal system of surfaces consists of the toroidal surfaces $\alpha = \alpha_0$ with axial circle of radius $(c \coth \alpha_0)$ in the xy plane with center at the origin and having a circular cross section of radius $(a \operatorname{cosech} \alpha_0)$.

The surface $\beta = \beta_0$ $(\beta_0 < \pi)$ is that part of the sphere of radius $(c \operatorname{cosec} \beta_0)$, with center $\rho = 0, z = c \cot \beta_0$ which is above the xy plane. The rest of the same sphere below the xy plane is given by $\beta = 2\pi - \beta_0$. The dividing line is the circle of radius c in the xy plane with center at the origin, which is also the degenerate surface $\alpha = \infty$.

The part of the xy plane inside the circle $\alpha = \infty$ corresponds to $\beta = \pi$ and the rest of the xy plane outside the circle corresponds to $\beta = 0$ or 2π.

The z axis corresponds to $\alpha = 0$ and as

$$\alpha, \beta \to 0 \qquad \text{then} \qquad r = \sqrt{\rho^2 + z^2} \to \infty. \tag{3.2}$$

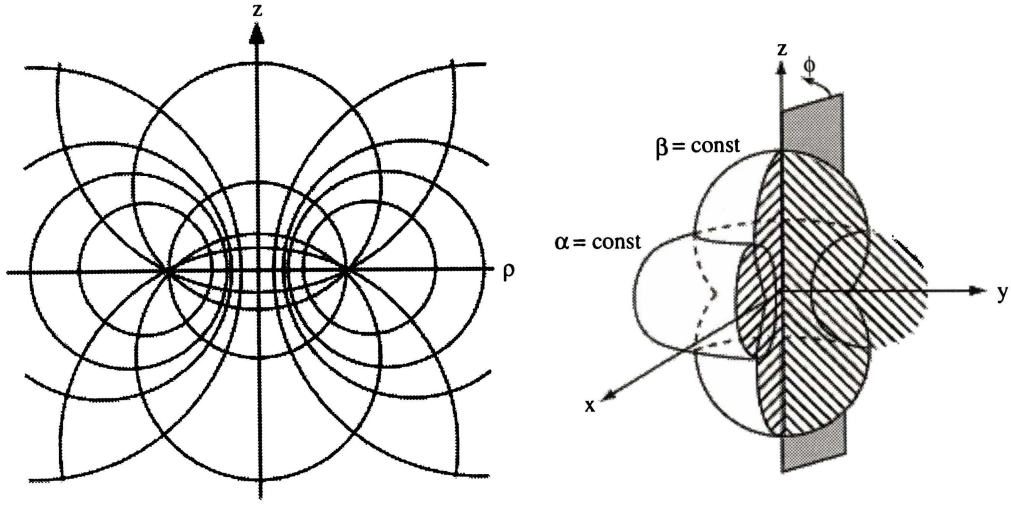

FIGURE 3.1: *Toroidal Coordinates.*

The inverse transformation of (3.1) is given by

$$\alpha = \frac{1}{2} \ln \left(\frac{\rho^2 + z^2 + 2c\rho + c^2}{\rho^2 + z^2 - 2c\rho + c^2} \right) \tag{3.3}$$

$$\beta = \arctan \left(\frac{2cz}{\rho^2 + z^2 - c^2} \right). \tag{3.4}$$

3.3 Metric

The general axially symmetric (Weyl) line element

$$ds^2 = e^{2\psi}dt^2 - e^{2\gamma-2\psi}(d\rho^2 + dz^2) - \rho^2 e^{-2\psi}d\varphi^2 \tag{3.5}$$

by virtue of (3.1) becomes

$$ds^2 = e^{2\psi}dt^2 - \frac{c^2 e^{-2\psi}}{(\cosh\alpha - \cos\beta)^2}\left[e^{2\gamma}(d\alpha^2 + d\beta^2) + \sinh^2\alpha\, d\varphi^2\right] \tag{3.6}$$

where ψ and γ are functions of α and β.

3.4 ψ Solutions

The metric function ψ satisfies Laplace's equation. In toroidal coordinates it has the form (with axial symmetry)

$$\frac{\partial}{\partial\alpha}\left(\frac{\sinh\alpha}{\cosh\alpha - \cos\beta}\frac{\partial\psi}{\partial\alpha}\right) + \frac{\partial}{\partial\beta}\left(\frac{\sinh\alpha}{\cosh\alpha - \cos\beta}\frac{\partial\psi}{\partial\beta}\right) = 0. \tag{3.7}$$

The substitution

$$\psi = \sqrt{\cosh\alpha - \cos\beta}\, A(\alpha)B(\beta) \tag{3.8}$$

enables (3.7) to separate:

$$\frac{1}{A}\frac{d^2A}{d\alpha^2} + \coth\alpha\frac{1}{A}\frac{dA}{d\alpha} + \frac{1}{4} = -\frac{1}{B}\frac{d^2B}{d\beta^2} = \nu^2. \tag{3.9}$$

Clearly,

$$B(\beta) = c_1\cos(\nu\beta) + c_2\sin(\nu\beta)$$

where ν is a separation constant (in what follows c_i are constants). The remaining equation for $A(\alpha)$ may be written

$$\frac{1}{\sinh(\alpha)}\frac{d}{d\alpha}\left(\sinh\alpha\frac{dA}{d\alpha}\right) - \left(\nu^2 - \frac{1}{4}\right)A = 0 \tag{3.10}$$

which is Legendre's equation,

$$[(1 - x^2)\,y']' + l(l+1)\,y = 0$$

with argument $x = \cosh\alpha$ and $l = \nu - \frac{1}{2}$. Thus the solutions of (3.10) are of the form

$$A(\alpha) = c_3 P_{\nu-1/2}(\cosh\alpha) + c_4 Q_{\nu-1/2}(\cosh\alpha) \tag{3.11}$$

where P and Q are Legendre functions of the first and second kind respectively.

By restricting the parameter ν to be an integer n, which, without loss of generality, we can assume to be nonnegative, then the continuity condition

$$\psi|_{\beta=0} = \psi|_{\beta=2\pi}$$

is satisfied. This is equivalent to the physical requirement that the solutions be periodic in the cyclic coordinate β (Lebedev, 1972).

The metric must become flat as $r \to \infty$, requiring $\psi \to 0$ as $\alpha, \beta \to 0$. For *general* ν

$$P_{\nu-1/2}(1) = 1 \qquad \text{and} \qquad \lim_{\alpha \to 0^+} Q_{\nu-1/2}(\cosh\alpha) = \infty.$$

Thus we set $c_4 = 0$ so that our solution remains finite at infinity. Therefore the general solution of (3.7) which is asymptotically flat can be formed by superposition of the solutions

$$\psi = \sqrt{\cosh\alpha - \cos\beta}\,[c_1 \cos(n\beta) + c_2 \sin(n\beta)] P_{n-1/2}(\cosh\alpha). \tag{3.12}$$

These general solutions correspond to solutions of Laplace's equation suitable for solving the exterior Dirichlet problem for a domain bounded by the toroidal surface $\alpha = \alpha_0$ (Lebedev, 1972; Misra, 1961).

3.5 Calculating γ

For generality write (3.12) as

$$\psi = -\sqrt{\cosh\alpha - \cos\beta}\,F(\alpha, \beta). \tag{3.13}$$

The function γ occurring in the metric (3.6) is obtained by solving

$$\begin{aligned} \frac{\partial\gamma}{\partial\alpha} &= \sinh\alpha\Big\{(F_\alpha^2 - F_\beta^2)(1 - \cosh\alpha\cos\beta) - \tfrac{1}{4}(1 + \cosh\alpha\cos\beta)F^2 - \\ &\quad F\,(\cosh\alpha\sin\beta\,F_\beta + \sinh\alpha\cos\beta\,F_\alpha) - 2\sinh\alpha\sin\beta\,F_\alpha F_\beta\Big\} \qquad (3.14) \\ \frac{\partial\gamma}{\partial\beta} &= \sinh\alpha\Big\{(F_\alpha^2 - F_\beta^2 + \tfrac{1}{4}F^2)\sinh\alpha\sin\beta + F(\cosh\alpha\sin\beta\,F_\alpha - \\ &\quad \sinh\alpha\cos\beta\,F_\beta) + 2F_\alpha F_\beta(1 - \cosh\alpha\cos\beta)\Big\} \qquad (3.15) \end{aligned}$$

subject to the boundary conditions that γ is zero along the z axis and is asymptotically flat:

$$\lim_{\rho\to 0}\gamma(\rho, z) \equiv \lim_{\alpha\to 0}\gamma(\alpha, \beta) = 0 \tag{3.16}$$

$$\lim_{r\to\infty}\gamma(\rho, z) \equiv \lim_{\alpha,\beta\to 0}\gamma(\alpha, \beta) = 0. \tag{3.17}$$

Integrating (3.15) we have

$$\gamma(\alpha, \beta) = \int \frac{\partial\gamma}{\partial\beta}\,d\beta = f(\alpha, \beta) + U(\alpha) \tag{3.18}$$

where the function $U(\alpha)$ remains to be determined. Calculating $f(\alpha, \beta)$ is always possible as only integration of trigonometric functions is required. From (3.14) when $\beta = \pi/2$ we have

$$\frac{d}{d\alpha}\,[f(\alpha, \pi/2) + U(\alpha)] = \left.\frac{\partial\gamma}{\partial\alpha}\right|_{\beta=\pi/2} \tag{3.19}$$

which leads to the differential equation for $U(\alpha)$

$$U'(\alpha) = -f'(\alpha, \pi/2) + \sinh\alpha\Big\{(F_\alpha^2 - F_\beta^2) - \tfrac{1}{4}F^2 - F\,F_\beta\cosh\alpha - 2\sinh\alpha\,F_\alpha F_\beta\Big\}\Big|_{\beta=\pi/2}. \quad (3.20)$$

Equation (3.20) is solved by quadrature. By construction the boundary conditions are satisfied. For our single *ring-like* solutions we must ensure that γ is continuous, especially at the coordinate boundaries $\beta = 0, 2\pi$. This is equivalent to having a γ function that is continuous around any circle $\alpha = const.$ (Gleiser and Pullin, 1989).

One must be cautious in checking the validity of γ: if the potential ψ is singular at some point in the plane $\rho > 0$ (which is clearly true for toroidal harmonic solutions) then γ may be multiply-defined.

This is especially evident when considering the situation (we *are not* however) of a field of a ring around the axis and a point particle on the axis. As in the two particle Curzon solution (see section 1.6), for such a situation to be static one expects some kind of supporting stresses to counteract the gravitational attraction between the objects. There are in principle two possibilities: one could have a Weyl strut along the axis connected to some kind of surface layer inside the ring, or one could have a surface layer extending in a conical fashion from the point particle to the ring which in turn is not a *ring* but a ring with a membrane inside. These possibilities are discussed in numerous places, for example Hoenselaers (1995); Thorne (1980); Gleiser and Pullin (1989).

3.5.1 Useful Integrals

Often in computing $U(\alpha)$ evaluation of integrals containing Legendre functions of the first kind squared, viz.

$$I = \int [P_\nu(z)]^2\,dz. \quad (3.21)$$

is required (ν is arbitrary). To calculate I we begin with the result (Abramowitz and Stegun, 1965; Magnus *et al.*, 1966)

$$(\nu - \sigma)(\nu + \sigma + 1)\int P_\nu P_\sigma\,dz = z(\nu - \sigma)P_\nu P_\sigma + \sigma P_\nu P_{\sigma-1} - \nu P_{\nu-1}P_\sigma. \quad (3.22)$$

Let $\sigma = \nu + h$, then

$$(2\nu + h + 1)\int P_\nu P_{\nu+h}\,dz = z\,P_\nu P_{\nu+h} - \frac{P_\nu P_{\nu+h}}{h}\left[(\nu + h)\frac{P_{\nu+h-1}}{P_{\nu+h}} - \nu\frac{P_{\nu-1}}{P_\nu}\right]. \quad (3.23)$$

Given that

$$\frac{\partial}{\partial\nu}\left(\frac{\nu P_{\nu-1}}{P_\nu}\right) = \lim_{h\to 0}\frac{1}{h}\left[(\nu + h)\frac{P_{\nu+h-1}}{P_{\nu+h}} - \nu\frac{P_{\nu-1}}{P_\nu}\right] \quad (3.24)$$

we have as $h \to 0$

$$I = \int [P_\nu]^2\,dz = \frac{1}{2\nu + 1}\left[z[P_\nu]^2 - [P_\nu]^2\frac{\partial}{\partial\nu}\left(\nu\frac{P_{\nu-1}}{P_\nu}\right)\right]. \quad (3.25)$$

Paramount in computing this derivative is the result

$$\frac{\partial}{\partial \nu} P_\nu^\sigma \bigg|_{\nu=-\frac{1}{2}} = 0 \tag{3.26}$$

and the identities

$$(2\nu+1) z P_\nu = (\nu+1) P_{\nu+1} + \nu P_{\nu-1} \tag{3.27}$$

$$z P_\nu = P_{\nu-1} + (\nu+1)(z^2-1)^{1/2} P_\nu^{-1} \tag{3.28}$$

which are used to lower the degree* of the Legendre functions in intermediary calculations so that (3.26) can be used.

In particular we have that†

$$2\int [P_{\frac{1}{2}}]^2 \, dz = z([P_{\frac{1}{2}}]^2 + [P_{-\frac{1}{2}}]^2) - 2 P_{\frac{1}{2}} P_{-\frac{1}{2}}. \tag{3.29}$$

$$4\int [P_{\frac{3}{2}}]^2 \, dz = 4z^2 P_{-\frac{1}{2}} P_{\frac{1}{2}} + z([P_{\frac{3}{2}}]^2 - 2[P_{\frac{1}{2}}]^2 - 3 P_{\frac{3}{2}} P_{-\frac{1}{2}}) + P_{\frac{1}{2}} P_{\frac{3}{2}} - P_{-\frac{1}{2}} P_{\frac{1}{2}}. \tag{3.30}$$

3.6 Relativistic Multipole Moments

The relativistic multipole moments of the metric generated by the general solution

$$\psi(\alpha,\beta) = -\sqrt{\cosh\alpha - \cos\beta} \sum_{n\in S} \left[A_n \sin(n\beta) + B_n \cos(n\beta) \right] P_{n-1/2}(\cosh\alpha) \tag{3.31}$$

where S is a set of unique n values, can be readily computed by the methods developed by Hoenselaers (1986) summarized in the earlier section 1.8.4.

The evaluation of the moments are in essence, determined by the values of the derivatives of ψ with respect to $\bar{z} = 1/z$ at the point $\bar{z} = 0$ on the symmetry axis ($\alpha = 0$).

On the axis, as $P_\nu(1) = 1$ we have

$$\psi(\beta) = -\sqrt{1-\cos\beta} \sum_{n\in S} \left[A_n \sin(n\beta) + B_n \cos(n\beta) \right]. \tag{3.32}$$

Furthermore from (3.4) on the axis we have

$$\beta = \arctan\left(\frac{2(z-\epsilon)c}{(z-\epsilon)^2 - c^2} \right) \tag{3.33}$$

where ϵ is subsequently used to nullify any dipole moment. Introducing $\bar{z} = 1/z$ into (3.33) and then into (3.32) expanding for small $\bar{z}$ and applying the algorithm described in section 1.8.4 the general mass and dipole moments are, respectively

$$M_0 = \sqrt{2}\, c \sum B_n \tag{3.34}$$

$$M_1 = \sqrt{2}\, c \left[2c \sum n A_n + \epsilon \sum B_n \right]. \tag{3.35}$$

*P_ν^{-1} is the Legendre function of order -1.

†Result (3.29) has also been shown in Piquette and Van Buren (1984).

From (3.35) we see that translating the origin ($z \to z - \epsilon$) by

$$\epsilon = \frac{-2c\sum nA_n}{\sum B_n} \tag{3.36}$$

nullifies the dipole moment. The quadrupole and M_3 moment, after this transformation become

$$M_2 = -\frac{\sqrt{2}}{6}c^3\left(12\sum\frac{n\,(2\,A_n\sum n\,A_n + B_n n\sum B_n)}{\sum B_n} + 3\sum B_n + 4\left(\sum B_n\right)^3\right) \tag{3.37}$$

$$\begin{aligned} M_3 = {} & \frac{2\sqrt{2}}{3}c^4\left(\sum B_n\right)^{-1}\left(6\sum nA_n\sum\frac{n\,(2\,A_n\sum nA_n + B_n n\sum B_n)}{\sum B_n} + \sum B_n \times\right. \\ & \sum\frac{n\left(12\,B_n n\sum nA_n\sum B_n - 2\,A_n n^2\left(\sum B_n\right)^2 + 12\,A_n\left(\sum nA_n\right)^2 - A_n\left(\sum B_n\right)^2\right)}{\left(\sum B_n\right)^2} \\ & \left.+3\sum nA_n\sum B_n\right). \end{aligned} \tag{3.38}$$

We observe for solutions with $A_n = 0$, then $M_1 = M_3 = 0$. It can be shown in general, that all odd moments vanish indicating a solution with equatorial symmetry (the $z = 0$ plane). This is also evident for the corresponding classical potential problem (Lebedev, 1972).

3.7 $n = 0$ Solution

The first solution considered will be that by setting $n = 0$ in (3.12). We therefore have

$$\psi_0 = -\sqrt{\cosh\alpha - \cos\beta}\,B\,P_{-\frac{1}{2}}(\cosh\alpha) \tag{3.39}$$

where B is a constant. From (3.13) we have

$$F(\alpha,\beta) = F(\alpha) = B\,P_{-\frac{1}{2}}(\cosh\alpha). \tag{3.40}$$

It follows from section 3.5 that*

$$\gamma(\alpha,\beta) = -\cos\beta\,[\sinh^2\alpha\,(F_\alpha^2 + \tfrac{1}{4}F^2) + \sinh\alpha\cosh\alpha\,FF_\alpha] + U(\alpha) \tag{3.41}$$

where

$$\begin{aligned} U(\alpha) &= \int \sinh\alpha\,F_\alpha^2\,d\alpha - \frac{1}{4}\int \sinh\alpha\,F^2\,d\alpha \\ &\equiv U_1 - U_2. \end{aligned} \tag{3.42}$$

Let $z = \cosh\alpha$ and write $P = P_{-\frac{1}{2}}(\cosh\alpha)$, then

$$U_2 = -\tfrac{1}{4}\int P^2(z)\,dz. \tag{3.43}$$

By integrating by parts we calculate

$$U_1 = (z^2-1)P_z P - \int 2zPP_z\,dz - \int (z^2-1)PP_{zz}\,dz. \tag{3.44}$$

*Subscripts refer to differentiation.

Recall that $P(z)$ satisfies Legendre's equation

$$(1 - z^2)P_{zz} - 2zP_z - \tfrac{1}{4}P = 0 \tag{3.45}$$

thus

$$U_1 = (z^2 - 1)P_z P + \tfrac{1}{4}\int P^2 dz. \tag{3.46}$$

From equations (3.42) and (3.43) we obtain

$$U(z) = (z^2 - 1)P_z P. \tag{3.47}$$

Given the identity

$$(z^2 - 1)P'_\nu(z) = \nu(zP_\nu - P_{\nu-1})$$

then

$$U(\alpha) = \tfrac{1}{2}B^2 P_{-\frac{1}{2}}\left[P_{\frac{1}{2}}(\cosh\alpha) - \cosh\alpha\, P_{-\frac{1}{2}}(\cosh\alpha)\right] \tag{3.48}$$

and it follows that

$$\gamma_0(\alpha,\beta) = -\tfrac{1}{4}B^2\left[\cos\beta\left\{[P_{\frac{1}{2}}]^2 - [P_{-\frac{1}{2}}]^2\right\} - 2\,P_{-\frac{1}{2}}P_{\frac{1}{2}} + 2\cosh\alpha[P_{-\frac{1}{2}}]^2\right]. \tag{3.49}$$

Solutions (3.39) and (3.49) form the Bach and Weyl (1922) solution, the relativistic field of a ring centered at $z = 0$ with radius $\rho = c$.

The ring itself has non-trivial structure, it has a directional singularity and is certainly not a simple line source (Israel, 1977; Thorne, 1980). The solution produces, sufficiently far away from the source, a toroidal gravitational field (Hoenselaers, 1995).

Semerák *et al.* (1999a) has investigated the timelike geodesics of a Schwarzschild plus Bach-Weyl field. Geodesics of the the Bach-Weyl solution are illustrated in later sections.

3.7.1 Multipole Moments

Section 3.6 gives the general multipole structure of any toroidal ψ solution. Here, for the $n = 0$ solution we evaluate them by introducing spherical coordinates.

The general static axisymmetric vacuum solution in spherical coordinates (t, r, θ, φ) can be written in the following form (Kramer *et al.*, 1980; Hernãndez-Pastora and Martin, 1994)

$$\psi = \sum_{l=0}^{\infty} \frac{a_l}{r^{l+1}} P_l(\cos\theta) \tag{3.50}$$

$$\gamma = \sum_{l,k=0}^{\infty} \frac{(l+1)(k+1)}{l+k+2} \frac{a_l a_k}{r^{l+k+2}} (P_{l+1}P_{k+1} - P_l P_k) \tag{3.51}$$

where $P_l(\cos\theta)$ are Legendre polynomials of order l and a_l are constants which determine the multipole moments.

Miller (1977) calculates the expansion of harmonic toroidal solutions in terms of solid spherical harmonics. After appropriate normalization and simplification of these general results, the $n = 0$ solution (3.39) can be written as

$$\psi_0 = -\sqrt{2}B\sum_{l=0}^{\infty} i^{3l}\, F(\tfrac{1}{2}, -l; 1; 2)\, \frac{P_l(\cos\theta)}{r^{l+1}} \tag{3.52}$$

where $i^2 = -1$ and $F(\cdot)$ is the Hypergeometric function. Let

$$\begin{aligned} b_l &= F(\tfrac{1}{2}, -l; 1; 2) \\ &= 1 - l + \frac{\frac{1}{2}\frac{3}{2}(-l)(-l+1)\,2^2}{(2!)^2} + \frac{\frac{1}{2}\frac{3}{2}\frac{5}{2}(-l)(-l+1)(-l+2)\,2^3}{(3!)^2} + \cdots \end{aligned} \tag{3.53}$$

Thus for $l = 1, 3, 5, \ldots$ from (3.53), (3.52) and (3.50) all (classical) odd multipole moments vanish. Therefore we can write (3.52) as

$$\psi_0 = \sum_{l=0}^{\infty} a_{2l} \frac{P_{2l}(\cos\theta)}{r^{2l+1}}, \qquad a_{2l} = (-1)^{l+1}\sqrt{2}B\, b_{2l}. \tag{3.54}$$

From section 1.8.5 we can now calculate the relativistic moments M_i. The first three are*

$$M_0 = -\sqrt{2}\,B\,a_0 = \sqrt{2}\,B = m \tag{3.55}$$

$$M_2 = -\frac{m}{6}\left(2m^2 + 3\right) \tag{3.56}$$

$$M_4 = \frac{m}{840}\left(152m^4 + 480m^2 + 315\right). \tag{3.57}$$

which can be readily confirmed (with $c = 1$) from the general results given in section 3.6.

Furthermore we can now write

$$\begin{aligned} \gamma_0 &= \frac{1}{2}\frac{a_0^2}{r^2}\left(P_1^2 - P_0^2\right) + \frac{6}{4}\frac{a_0 a_2}{r^4}\left(P_3 P_1 - P_2 P_0\right) + \cdots \\ &= -\frac{m^2}{2r^2}\sin^2\theta - \frac{3}{8}\frac{m^2\sin^2\theta}{r^4}\left(5\sin^2\theta - 4\right) + \cdots \end{aligned} \tag{3.58}$$

3.8 $n = 1$ Solution

We now proceed and formulate the solution for the case $n = 1$. From equations (3.12) and (3.13) we have

$$\psi_1 = -\sqrt{\cosh\alpha - \cos\beta}\, P_{\frac{1}{2}}(\cosh\alpha)\,[\,A\sin\beta + B\cos\beta\,]. \tag{3.59}$$

A and B are constants. From section 3.5 the unknown function U needed to complete the determination of the function γ satisfies ($z = \cosh\alpha$)

$$U'(z) = B^2(z^2 - 1)\left[P'_{\frac{1}{2}}(z)\right]^2 - \tfrac{1}{4}(B^2 + 4A^2)\left[P_{\frac{1}{2}}(z)\right]^2. \tag{3.60}$$

Integrating by parts and using the result (3.29) we obtain

$$U(z) = B^2 P_{\frac{1}{2}}\left[(z^2 - 1)P'_{\frac{1}{2}}(z)\right] - (B^2 + A^2)\int\left[P_{\frac{1}{2}}\right]^2 dz \tag{3.61}$$

$$= (\tfrac{1}{2}B^2 + A^2)P_{-\frac{1}{2}}P_{\frac{1}{2}} - \frac{z}{2}(B^2 + A^2)\left[P_{-\frac{1}{2}}\right]^2 - \frac{z}{2}A^2\left[P_{\frac{1}{2}}\right]^2. \tag{3.62}$$

*$M_0 = -a_0, \quad M_2 = \frac{1}{3}a_0^3 - a_2, \quad M_4 = -\frac{19}{105}a_0^5 + \frac{8}{7}a_0^2 a_2 - a_4.$

Thus we have

$$\begin{aligned}
\gamma_1 &= -\frac{B^2}{12}\Big\{\Big(16\left[P_{\frac{1}{2}}\right]^2\cosh^2\alpha - 8P_{-\frac{1}{2}}P_{\frac{1}{2}}\cosh\alpha + 9\left[P_{-\frac{1}{2}}\right]^2 - 9\left[P_{\frac{1}{2}}\right]^2\Big)\cos^3\beta + \\
&\quad 6\Big(P_{-\frac{1}{2}}P_{\frac{1}{2}} - \cosh\alpha\left[P_{\frac{1}{2}}\right]^2\Big)\cos^2\beta - 12\cos\beta\left[P_{\frac{1}{2}}\right]^2\sinh^2\alpha + \\
&\quad 6\cosh\alpha\Big(\left[P_{-\frac{1}{2}}\right]^2 + \left[P_{\frac{1}{2}}\right]^2\Big) - 12\,P_{-\frac{1}{2}}P_{\frac{1}{2}}\Big\} + \\
&\quad AB\Big\{\frac{1}{24}\left[P_{\frac{1}{2}}\right]^2\Big[-16\sin 3\beta\cosh^2\alpha + 12\sin 2\beta\cosh\alpha - 3\sin\beta + \\
&\quad 9\sin 3\beta\Big] + \frac{1}{6}P_{-\frac{1}{2}}P_{\frac{1}{2}}\Big[2\sin 3\beta - 3\sin 2\beta\Big] + \frac{1}{6}\left[P_{-\frac{1}{2}}\right]^2\sin^3\beta\Big\} \\
&\quad + A^2\Big\{\left[P_{\frac{1}{2}}\right]^2\Big[\frac{1}{6}(2\cos 3\beta\cosh^2\alpha - 3\cos^2\beta\cosh\alpha) - \\
&\quad \frac{1}{16}(5\cos\beta + 3\cos 3\beta)\Big] + \frac{1}{6}P_{\frac{1}{2}}P_{-\frac{1}{2}}\Big[(3\cos\beta - \cos 3\beta)\cosh\alpha + 6 \\
&\quad -3\sin^2\beta\Big] + \frac{1}{48}\left[P_{-\frac{1}{2}}\right]^2\Big[-24\cosh\alpha + \cos 3\beta - 9\cos\beta\Big]\Big\}. \qquad (3.63)
\end{aligned}$$

It is easily verified that γ_1 satisfies the required boundary conditions (3.16) and (3.17).

3.8.1 Multipole Moments

From the general results of section 3.6 we readily compute the first few multipole moments (dipole transformed away) of this particular solution to be (c is the coordinate scale factor)

$$\begin{aligned}
M_0 &= \sqrt{2}\,cB \\
M_2 &= -\frac{1}{6B}\sqrt{2}\,c^3\left(24A^2 + 15B^2 + 4B^4\right) \\
M_3 &= 4\sqrt{2}\,c^4A\left(3B^2 + 4A^2\right)B^{-2}. \qquad (3.64)
\end{aligned}$$

The next moment is

$$\begin{aligned}
M_4 &= -\frac{\sqrt{2}\,c^5}{840\,B^3}\Big(-7680\,A^2B^4 - 4800\,B^6 - 608\,B^8 + \\
&\qquad 30240\,A^2B^2 + 40320\,A^4 - 2835\,B^4\Big). \qquad (3.65)
\end{aligned}$$

3.8.2 Simplifications

Let $A = 0$ then the $n = 1$ solution becomes

$$\psi_1 = -\sqrt{\cosh\alpha - \cos\beta}\,B\,P_{\frac{1}{2}}(\cosh\alpha)\cos\beta \qquad (3.66)$$

$$\begin{aligned}
\gamma_1 &= -\frac{B^2}{12}\Big\{\Big(16\left[P_{\frac{1}{2}}\right]^2\cosh^2\alpha - 8P_{-\frac{1}{2}}P_{\frac{1}{2}}\cosh\alpha + 9\left[P_{-\frac{1}{2}}\right]^2 - 9\left[P_{\frac{1}{2}}\right]^2\Big)\cos^3\beta + \\
&\quad 6\Big(P_{-\frac{1}{2}}P_{\frac{1}{2}} - \cosh\alpha\left[P_{\frac{1}{2}}\right]^2\Big)\cos^2\beta - 12\cos\beta\left[P_{\frac{1}{2}}\right]^2\sinh^2\alpha + \\
&\quad 6\cosh\alpha\Big(\left[P_{-\frac{1}{2}}\right]^2 + \left[P_{\frac{1}{2}}\right]^2\Big) - 12\,P_{-\frac{1}{2}}P_{\frac{1}{2}}\Big\} \qquad (3.67)
\end{aligned}$$

with *even multipole* moments

$$M_0 = \sqrt{2}\,c\,B = m \tag{3.68}$$

$$M_2 = -\frac{m}{6}(15c^2 + 2m^2) \tag{3.69}$$

$$M_4 = \frac{m}{840}(2835c^4 + 2400c^2m^2 + 152m^4). \tag{3.70}$$

Given that the coefficients a_0 and a_2 in (3.50) are related to the relativistic multipole moments by (Hernãndez-Pastora and Martin, 1994)

$$a_0 = -M_0 = -m \tag{3.71}$$

$$a_2 = -\frac{1}{3}M_0^2 - M_2 = \frac{15}{6}\,c^2\,m \tag{3.72}$$

the expansion of (3.66) and (3.67) in terms of spherical coordinates (r, θ, φ) begins with

$$\psi_1 \approx -\frac{m}{r} + \frac{15c^2m}{6r^3}P_2(\cos\theta) \tag{3.73}$$

$$\gamma_1 \approx -\frac{m^2}{2r^2}\sin^2\theta - \frac{15c^2}{8}\frac{m^2\sin^2\theta}{r^4}\left(5\sin^2\theta - 4\right). \tag{3.74}$$

3.9 $n = 0 + 1$ Solution

Both $n = 0$ and $n = 1$ term solutions have a multipole structure that is determined by one parameter, the mass m of the source. Once the constant* $\sqrt{2}B \equiv m$ is chosen the higher multipole moments are fixed: $M_l = M_l(m)$.

To gain more flexibility we now determine the metric corresponding to a linear combination of solutions. We will consider solutions with equatorial symmetry, thus enabling the freedom to specify the mass and quadrupole ($M_2 = Q$) moments. It follows that all higher (even) moments are then determined by two parameters:

$$M_{2l} = M_{2l}(m, Q).$$

We will first consider the solution generated by the superposition of the $n = 0$ and $n = 1$ ψ solutions. Recall we are interested in solutions that have equatorial symmetry, thus we have

$$\psi_{01} = -\sqrt{\cosh\alpha - \cos\beta}\,\left[B_0\,P_{-\frac{1}{2}}(\cosh\alpha) + B_1\cos\beta\,P_{\frac{1}{2}}(\cosh\alpha)\right] \tag{3.75}$$

generating mass and quadrupole moments (again c is the coordinate scale factor)

$$m = \sqrt{2}c(B_0 + B_1) \tag{3.76}$$

$$Q = -\frac{\sqrt{2}}{6}\,c^3\,(12B_0B_1^2 + 12B_0^2B_1 + 3B_0 + 4B_0^3 + 15B_1 + 4B_1^3). \tag{3.77}$$

Inverting we have

$$B_0 = \frac{\sqrt{2}}{24c^3}(15mc^2 + 2m^3 + 6Q) \tag{3.78}$$

$$-B_1 = \frac{\sqrt{2}}{24c^3}(3mc^2 + 2m^3 + 6Q) \tag{3.79}$$

*We can set without loss of generality $c = 1$ (Hoenselaers, 1995).

from which we can write for the next moment

$$M_4 = -(\tfrac{1}{5}m^5 + \tfrac{1}{2}m^3c^2 + \tfrac{3}{8}mc^4) - Q(\tfrac{8}{7}m^2 + \tfrac{3}{2}c^2). \tag{3.80}$$

The calculation of γ requires the evaluation of

$$\begin{aligned} U(\alpha) &= \int B_0^2 \left[\sinh\alpha \left(\frac{dA_0}{d\alpha}\right)^2 - \frac{1}{4}\sinh\alpha A_0^2\right] d\alpha && (3.81)\\ &+ \int \left[2B_0B_1\frac{dA_0}{d\alpha}A_1\sinh^2\alpha + B_0B_1\cosh\alpha A_0A_1\sinh\alpha\right] d\alpha && (3.82)\\ &- \int B_1^2\sinh\alpha A_1^2\, d\alpha && (3.83) \end{aligned}$$

where $A_0 = P_{-\frac{1}{2}}(\cosh\alpha)$ and $A_1 = P_{\frac{1}{2}}(\cosh\alpha)$. From the results of section 3.7 it becomes clear that (3.81) is given by (3.48). After making the substitution $z = \cosh\alpha$ and using the identity $2(z^2-1)P'_{-\frac{1}{2}}(z) = P_{\frac{1}{2}}(z) - zP_{-\frac{1}{2}}(z)$ then (3.82) and (3.83) simplify to

$$(B_0B_1 - B_1^2)\int \left[P_{\frac{1}{2}}(z)\right]^2 dz \tag{3.84}$$

with solution given by (3.29). Thus combining and including the elementary integral (3.18) we have

$$\begin{aligned} \gamma_{01}(\alpha,\beta) = B_0B_1\Big\{ &\left(P_{-\frac{1}{2}}P_{\frac{1}{2}} - \cosh\alpha\left[P_{\frac{1}{2}}\right]^2\right)\cos^2\beta + \\ &\left(\left[P_{\frac{1}{2}}\right]^2 - P_{\frac{1}{2}}P_{-\frac{1}{2}}\cosh\alpha\right)\cos\beta + \\ &\tfrac{1}{2}\left(\left[P_{-\frac{1}{2}}\right]^2 + \left[P_{\frac{1}{2}}\right]^2\right)\cosh\alpha - P_{-\frac{1}{2}}P_{\frac{1}{2}}\Big\} + \gamma_0 + \gamma_1 \end{aligned} \tag{3.85}$$

where γ_0 and γ_1 are given by (3.49) and (3.67) respectively.

3.10 $n = 0 + 2$ Solution

We will also consider the metric generated by the superposition of the $n = 0$ and $n = 2$ solutions. Again demanding equatorial symmetry we have

$$\psi_{02} = -\sqrt{\cosh\alpha - \cos\beta}\,\left[B_0\,P_{-\frac{1}{2}}(\cosh\alpha) + B_2\cos 2\beta\,P_{\frac{3}{2}}(\cosh\alpha)\right]. \tag{3.86}$$

Given mass m and quadrupole values Q then

$$\begin{aligned} B_0 &= \frac{\sqrt{2}}{96c^3}(51mc^2 + 2m^3 + 6Q) && (3.87)\\ -B_2 &= \frac{\sqrt{2}}{96c^3}(3mc^2 + 2m^3 + 6Q) && (3.88) \end{aligned}$$

from which we can write for the next moment

$$M_4 = -(\tfrac{1}{5}m^5 + \tfrac{5}{6}m^3c^2 + \tfrac{7}{8}mc^4) - Q(\tfrac{8}{7}m^2 + \tfrac{5}{2}c^2). \tag{3.89}$$

For brevity we will write

$$A_0(\alpha) = P_{-\frac{1}{2}}(\cosh\alpha), \quad A_1(\alpha) = P_{\frac{1}{2}}, \quad A_2(\alpha) = P_{\frac{3}{2}}$$

and $'$ for differentiation with respect to α . The function $U(\alpha)$ which completes the determination of γ is determined by solving

$$\begin{aligned} U'(\alpha) &= \left[\sinh\alpha\,(A_0')^2 - \tfrac{1}{4}\sinh\alpha\,A_0^2\right] B_0^2 && (3.90)\\ &+ \left[2\cosh\alpha\,A_0' + \tfrac{1}{2}\sinh\alpha\,A_0 + 2\sinh\alpha\,A_0''\right] A_2\,B_0B_2 && (3.91)\\ &- \left[\cosh\alpha\,A_2' + \tfrac{1}{4}\sinh\alpha\,A_2 + \sinh\alpha\,A_2''\right] A_2\,B_2^2. && (3.92)\end{aligned}$$

The first term is given by the corresponding U solution for the γ_0 case, equation (3.48). As A_0 is a solution to Legendre equation (3.10) with $\nu = n = 0$ the term (3.91) vanishes. Similarly the third term, by virtue of (3.10) with $n = 2$ becomes

$$-4B_2^2\sinh\alpha\left[P_{\frac{3}{2}}(\cosh(\alpha)\right]^2. \tag{3.93}$$

The integral of (3.93) is given by (3.30). This completes the determination of U. The complete γ_{02} function is given by

$$\begin{aligned}\gamma_{02} &= B_2^2\Big\{\cos^5\beta\Big[A_2^2(5-\tfrac{64}{5}\cosh^2\alpha) + \tfrac{48}{5}A_2A_1\cosh\alpha - \tfrac{9}{5}A_1^2\Big] +\\ &\quad \cos^4\beta\Big[6A_2(A_2\cosh\alpha - A_1)\Big] +\\ &\quad \cos^3\beta\Big[A_2^2 - 12A_2A_1\cosh\alpha + 3A_1^2 + 8A_2^2\cosh(2\alpha)\Big] -\\ &\quad 6\cos^2\beta\Big[A_2\cosh\alpha - A_1\Big]A_2 -\\ &\quad \cos\beta\Big[-4A_2^2\cosh^2\alpha + \tfrac{1}{4}A_2^2 + 6A_2A_1\cosh\alpha - \tfrac{9}{4}A_1^2\Big] +\\ &\quad \tfrac{1}{2}\cosh\alpha A_2^2 + 3A_2A_0\cosh\alpha - \tfrac{5}{2}A_1A_2 + 2\cosh\alpha A_1^2 + A_0A_1 -\\ &\quad 4\cosh^2\alpha A_0A_1\Big\} \quad +\\ &B_0B_2\Big\{\cos^3\beta\Big[\tfrac{1}{3}A_2(5A_0 - 8\cosh\alpha A_1) + A_1^2\Big] +\\ &\quad A_2(A_0\cosh\alpha - A_1)(1 - 2\cos^2\beta) +\\ &\quad \tfrac{1}{2}\cos\beta\Big[A_2(4\cosh\alpha A_1 - A_0) - 3A_1^2\Big]\Big\} \quad + \quad \gamma_0. \end{aligned} \tag{3.94}$$

3.11 Numerical Calculation of γ

Analytic evaluation of the metric function γ to this point has been possible. In a certain sense this is a luxury. As the complexity of ψ increases, due to superposition of particular solutions,

or considering functions containing higher order $P_{n+1/2}(\cosh\alpha)$ terms, the evaluation of γ becomes a more arduous and tedious task, although in principle still possible.

In the next chapter γ must be computed numerically. This section serves to give evidence and a sense of assurance of the validity of the methods used in chapter 4 to calculate γ numerically. Our test problem, of non trivial nature, will be to generate the γ_{02} function given above. We set $B_0 = 1$ and $B_2 = 1/3$ and from (3.13) and (3.86) we have

$$F(\alpha,\beta) = P_{-\frac{1}{2}}(\cosh\alpha) + \tfrac{1}{3}\cos 2\beta\, P_{\frac{3}{2}}(\cosh\alpha). \tag{3.95}$$

We evaluate γ via the line integral (Semerák *et al.*, 1999b)

$$\gamma(\alpha,\beta) = \int_{\text{axis}}^{(\alpha,\beta)} \left[\frac{d\gamma}{d\alpha}\,d\alpha + \frac{d\gamma}{d\beta}\,d\beta\right] \tag{3.96}$$

where the integration is taken along a path going from the axis ($\alpha = 0$) to a given point. $d\gamma/d\alpha$ and $d\gamma/d\beta$ are given by (3.14) and (3.15). To satisfy the boundary conditions (3.16) and (3.17) we calculate (3.96) via two paths. Firstly

$$\gamma_{p1}(\alpha',\beta') = \int_0^{\alpha'} \left.\frac{d\gamma}{d\alpha}\right|_{\beta=0} d\alpha + \int_0^{\beta'} \left.\frac{d\gamma}{d\beta}\right|_{\alpha=\alpha'} d\beta. \tag{3.97}$$

As $\lim_{\alpha\to 0}\left[\sinh\alpha\, F_\alpha^2\right] = 0$, then the first integral in (3.97) does not become singular. As $d\gamma/d\beta|_{\alpha=0} = 0$ then we take for the second path

$$\gamma_{p2}(\alpha',\beta') = \int_0^{\alpha'} \left.\frac{d\gamma}{d\alpha}\right|_{\beta=\beta'} d\alpha. \tag{3.98}$$

Typical results are illustrated in figures 3.2 and 3.3. It is evident in the first figure that the evaluation of γ via (3.98) is superior to that of (3.97), although at higher integration tolerances (as in practice would be implemented) both paths perform similarly. To minimize computational time by reducing function evaluations path 2 would be used. Clear signs of convergence for either path is observed, and the numerical evaluation of γ_{02} is reliable.

Similar methods are used in the following chapter to evaluate γ. It will be seen that no analytic solution is possible, but these results here give some confidence in the numerical procedures used there to evaluate γ.

3.12 Equations of Motion

The Lagrangian associated with the metric (3.6) is

$$2\mathcal{L} = e^{2\psi}\dot{t}^2 - Xe^{2\gamma}(\dot{\alpha}^2 + \dot{\beta}^2) - X\sinh^2\alpha\,\dot{\varphi}^2. \tag{3.99}$$

The dot over the coordinate denotes the derivative with respect to the affine parameter s and

$$X(\alpha,\beta) = \frac{c^2 e^{-2\psi}}{(\cosh\alpha - \cos\beta)^2}. \tag{3.100}$$

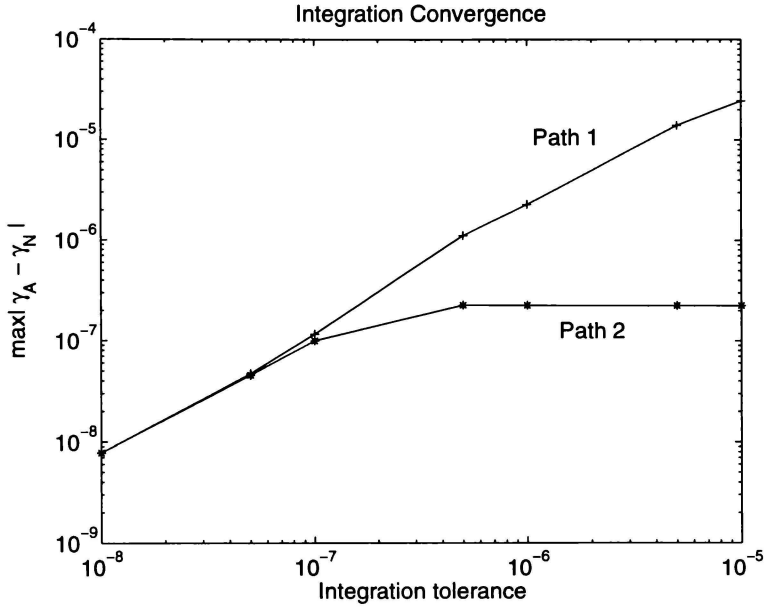

FIGURE 3.2: *The maximum error between the analytic* (γ_A) *and numerical* (γ_N) *functions. Here the numerical results are computed over a* 10×10 *uniform point grid where* $0 \leq \alpha \leq 1$ *and* $0 \leq \beta \leq 2\pi$. *The x-axis corresponds to the tolerance criteria used in the numerical integration algorithm.*

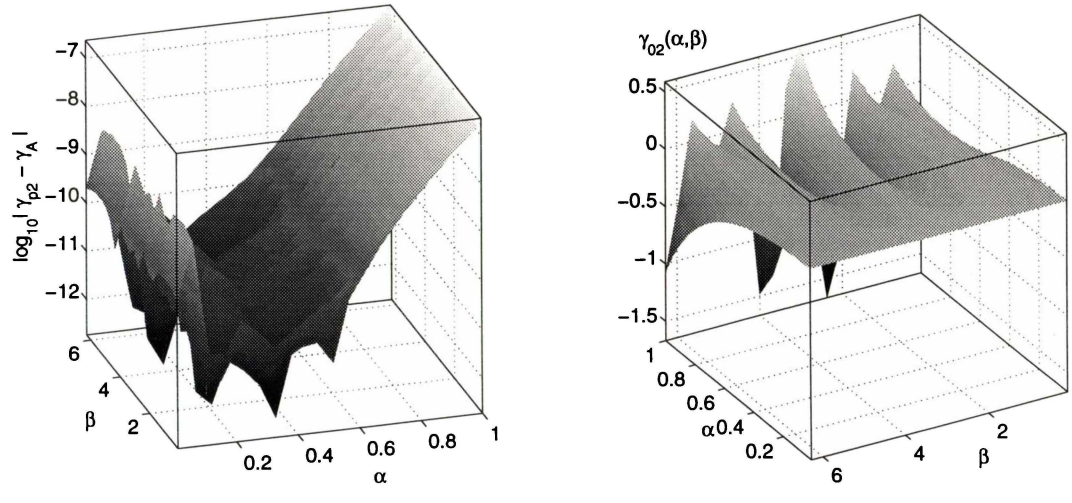

FIGURE 3.3: γ_{02} *given by (3.94) and the error between the analytical and numerical (path 2) calculations* ($tol = 1 \times 10^{-6}$).

The cyclic coordinates t and φ enable the constants of the motion E and L, which represent the total specific energy of the test particle and its angular momentum about the z axis respectively, to be defined from

$$\dot{t} = Ee^{-2\psi}, \qquad \dot{\varphi} = \frac{-L}{X \sinh^2 \alpha}. \tag{3.101}$$

The remaining equations of motion are

$$-\ddot{\alpha} = X^{-1}e^{-2\gamma}\Big\{\psi_\alpha e^{-2\psi}E^2 + \tfrac{1}{2}e^{2\gamma}(X_\alpha + 2X\gamma_\alpha)(\dot{\alpha}^2 - \dot{\beta}^2) + e^{2\gamma}(X_\beta + 2X\gamma_\beta)\dot{\alpha}\dot{\beta} - \frac{L^2}{2X^2}\left[\frac{X_\alpha \sinh\alpha + 2X\cosh\alpha}{\sinh^3\alpha}\right]\Big\} \tag{3.102}$$

$$-\ddot{\beta} = X^{-1}e^{-2\gamma}\Big\{\psi_\beta e^{-2\psi}E^2 - \tfrac{1}{2}e^{2\gamma}(X_\beta + 2X\gamma_\beta)(\dot{\alpha}^2 - \dot{\beta}^2) + e^{2\gamma}(X_\alpha + 2X\gamma_\alpha)\dot{\alpha}\dot{\beta} - \frac{L^2 X_\beta}{2X^2\sinh^2\alpha}\Big\} \tag{3.103}$$

here subscripts refer to partial differentiation.

By rescaling the affine parameter s we can arrange that $2\mathcal{L}$ has the value $\epsilon = +1, -1, 0$ for timelike, spacelike or null geodesics respectively. Thus a further integral of the motion follows from the Lagrange function (3.99) and (3.101) we have

$$\dot{\alpha}^2 + \dot{\beta}^2 = X^{-1}e^{-2\gamma}\left[E^2 e^{-2\psi} - \frac{L^2}{(X\sinh^2\alpha)} - \epsilon\right]. \tag{3.104}$$

We will investigate the motion of test particles. Thus in all subsequent calculations we will set $\epsilon = 1$. These equations of motion will be solved numerically via an adaptive Runge-Kutta fifth order scheme.

The toroidal functions $P_{n-\frac{1}{2}}(\cosh\alpha)$ were computed via quadrature using (Abramowitz and Stegun, 1965)

$$P_{n-\frac{1}{2}}(\cosh\alpha) = \frac{1}{\pi}\int_0^\pi \frac{d\varphi}{(\cosh\alpha + \cos\varphi\sinh\alpha)^{n+\frac{1}{2}}} \tag{3.105}$$

except for the functions

$$P_{-\frac{1}{2}}(\cosh\alpha) = \frac{2}{\pi}\,\mathrm{sech}(\tfrac{\alpha}{2})K(\tanh\tfrac{\alpha}{2}) \tag{3.106}$$

$$P_{\frac{1}{2}}(\cosh\alpha) = \frac{2}{\pi}\,e^{\alpha/2}E(\sqrt{1-e^{-2\alpha}}). \tag{3.107}$$

Here K and E are elliptic integrals of the first and second kind.

3.13 $L = 0$ Geodesics

We shall in this section consider the trajectories of particles which start from rest with zero angular momentum, $L = 0$. From (3.104) the initial release point (α_0, β_0) is related to the constant E by

$$E = e^{\psi(\alpha_0,\beta_0)}. \tag{3.108}$$

3.13.1 Motion along z axis

Consider a test particle released from rest at some finite point $z = z_0$ on the axis. This corresponds in toroidal coordinates to an initial position $(\alpha_0 = 0, \beta_0)$. Given $\dot{\alpha}_0 = \dot{\beta}_0 = 0$

then equation (3.102) becomes ($\gamma = 0$ along the axis)

$$\ddot{\alpha_0} \propto \psi_\alpha(0, \beta_0). \tag{3.109}$$

Consider the general solution ofψ, equation (3.31)

$$\psi(\alpha, \beta) = \sqrt{\cosh\alpha - \cos\beta} \sum_n f_n(\beta) P_{n-\frac{1}{2}}(\cosh\alpha). \tag{3.110}$$

It follows for $\alpha = 0$ that

$$\psi_\alpha = \sqrt{1 - \cos\beta} \sum f_n(\beta) \frac{d}{d\alpha} P_{n-\frac{1}{2}}(\cosh\alpha)\Big|_{\alpha=0}. \tag{3.111}$$

Expanding (3.105) for small α we have

$$P_{n-\frac{1}{2}}(\cosh\alpha) \approx 1 + \frac{1}{16}(4n^2 - 1)\alpha^2 + O(\alpha^4) \tag{3.112}$$

and thus for $\alpha = 0$ we have $\psi_\alpha = 0$. Therefore, given $\alpha_0 = \dot{\alpha_0} = 0$ then $\ddot{\alpha_0} = 0$ so $\alpha(s) = \alpha_0 = 0$ and motion is restricted to the z axis. The remaining equation of motion becomes ($\alpha = 0$)

$$-\ddot{\beta} = \psi_\beta E^2 c^{-2}(1 - \cos\beta)^2 - \left(\psi_\beta + \frac{\sin\beta}{1 - \cos\beta}\right)\dot{\beta}^2. \tag{3.113}$$

From (3.104) we have along the axis

$$\dot{\beta}^2 = c^{-2}(1 - \cos\beta)^2 \left(E^2 - e^{2\psi}\right) \tag{3.114}$$

therefore

$$-\ddot{\beta} = c^{-2}(1 - \cos\beta)\left[\psi_\beta e^{2\psi}(1 - \cos\beta) - \sin\beta(E^2 - e^{2\psi})\right]. \tag{3.115}$$

Motion along the z axis for the various solutions formulated in the previous section will now be examined.

$n = 0$ *Solution.*

For the $n = 0$ solution $\psi_0(0, \beta) = -B(1 - \cos\beta)^{1/2}$. Solving (3.115) requires some caution. Figure 3.4 illustrates the dependence upon integration tolerances used in the numerical method. These plots are generated with $m = 10$ and $c = 1$. The first two plots, using lower tolerances produce motion exhibiting characteristics of damped simple harmonic motion - an indication of incorrect numerics. The third plot, using the highest tolerance produces the expected (in the Newtonian sense) oscillatory motion.

Following Misra (1961) let us assume that the test particle is released from a small distance from the origin, $\beta = \pi - \xi$ where ξ is small. To the first order $E^2 = e^{-2m/c} + O(\xi^2)$. Recalling that $m = c\sqrt{2}B$ then (3.115) becomes

$$\ddot{\xi} = -k\xi, \qquad k = \frac{m}{c^3} e^{-2m/c}. \tag{3.116}$$

Thus the motion of the particle will be simple harmonic with period T given by

$$T^2 = 4\pi^2 c^3 \frac{e^{2m/c}}{m} \tag{3.117}$$

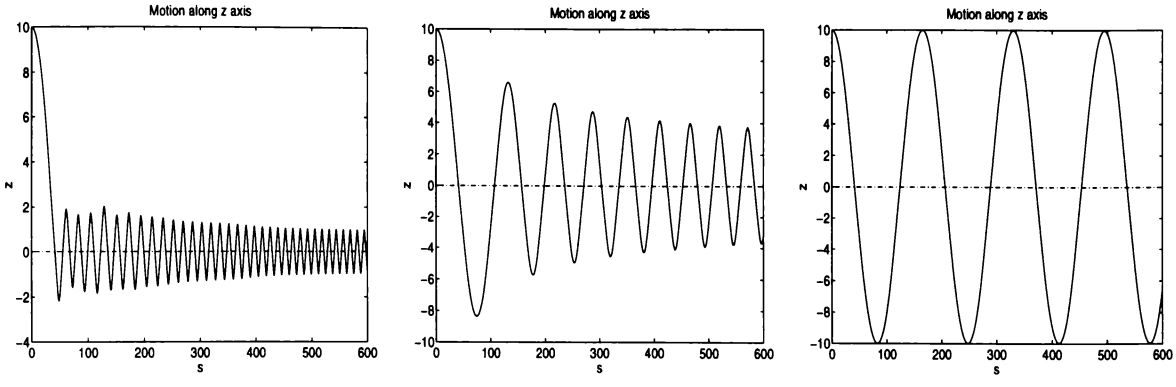

(a) tol $= 1 \times 10^{-5}$ (b) tol $= 1 \times 10^{-8}$ (c) tol $= 1 \times 10^{-11}$

FIGURE 3.4: *The motion of a particle released from* $z_0 = 10$ *as calculated using differing integration tolerances.*

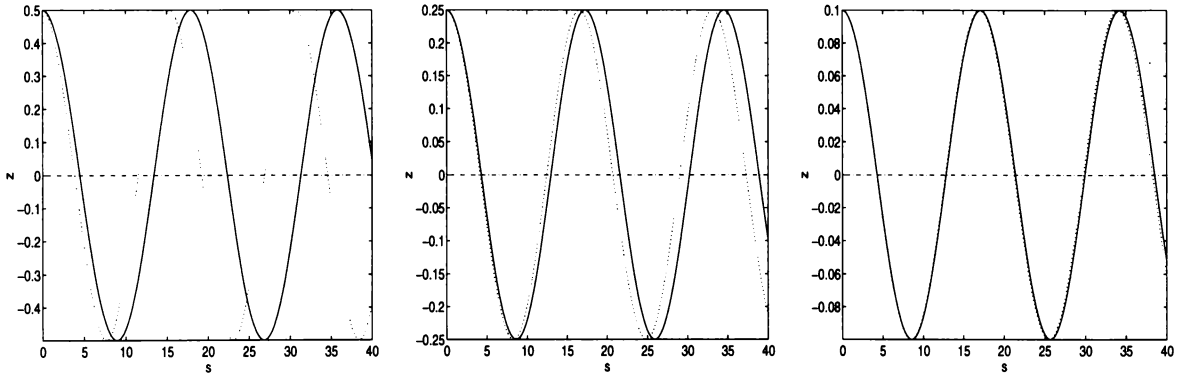

(a) $z_0 = 0.5$ (b) $z_0 = 0.25$ (c) $z_0 = 0.1$

FIGURE 3.5: *The shm approximation (3.116) and the numerical (solid line) solution (3.115) for various release points* z_0. *Here* $m = 1$ *(the ring mass) and* $c = 1$ *also. As expected the accuracy of this approximation increases as* z_0 *is lowered.*

This approximation is illustrated in figure 3.5. Trajectories (as functions of the proper time s) for a test particle released from $z_0 = 2$ are shown in figure 3.6.

As the mass of the ring increases, the period of oscillation *increases.* This is contrary to the Newtonian analogue and is clearly a perplexing result: *it would suggest that a test particle will oscillate quicker as the mass of the ring decreases.*

This in fact does not occur. There does exist critical m values for which the classical type behaviour is observed. Figure 3.7 illustrates this point. Here the period of oscillation (proper time) as a function of mass is plotted. Labelled with an asterix is the critical mass value. It is seen that the period decreases when the mass of the ring is increased to this value - the Newtonian type behaviour. Afterwards the period decreases as observed in figure 3.6 clearly a relativistic effect. It is also evident that the period is dependent upon the amplitude of oscillation, that is the initial release point.

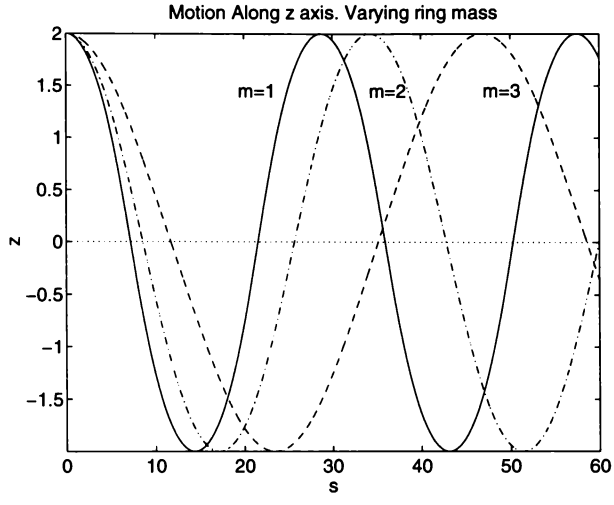

FIGURE 3.6: *The motion of a test particle as the mass of the ring (radius $c = 1$) is increased. Unlike the Newtonian situation the period of oscillation increases as the mass of the ring increases.*

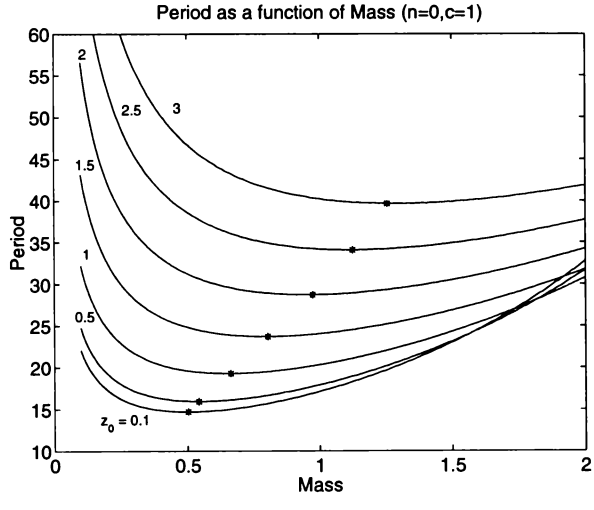

FIGURE 3.7: *Period of oscillation as a function of mass. The labels on the curves refer to the initial z_0 release point. The stars mark the minimum period, afterwards the motion behaves in a non-Newtonian manner.*

Some insight to this behaviour can be found from examining the Kretschmann scalar K, which gives the amount of curvature of spacetime as a function of position (Henry, 2000). Along the z axis ($\alpha = 0$) we have

$$\begin{aligned} K_z &= \frac{m^2}{32c^8} e^{-2m/c\sqrt{2-2\cos\beta}} (1-\cos\beta)^{5/2} \Big\{ \sqrt{1-\cos\beta} \times \\ &\quad \Big[16m^2 \sin^2\beta(1+\cos\beta) + c^2(123\cos^2\beta + 186\cos\beta + 139) \Big] \\ &\quad -2\sqrt{2}mc\sin^2\beta(29\cos\beta + 19) \Big\} \end{aligned} \tag{3.118}$$

which is plotted (relation (3.4) enables K_z to be plotted as a function of z) in figure 3.8. For $m < 0.5$ the curvature increases. Thereafter it decreases along the axis monotonically. By making the analogy between curvature and restoring force, this would then justify the longer periods observed in the oscillations shown in figure 3.6. These calculations do not indicate any

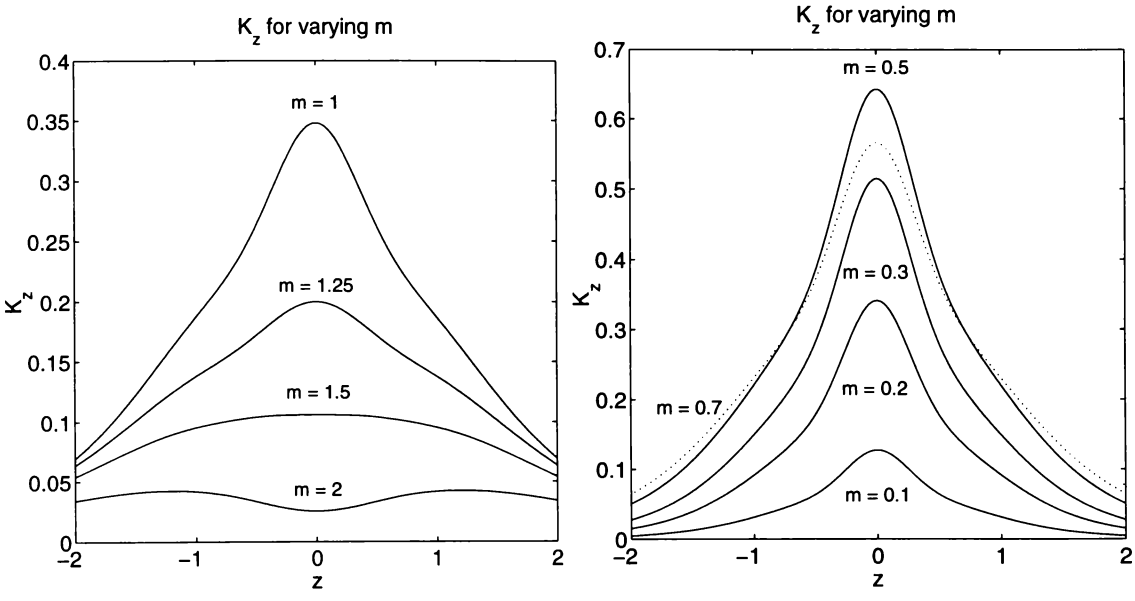

FIGURE 3.8: *The Kretschmann scalar* ($c = 1$) *along the* z *axis for the* $n = 0$ *solution. Note the symmetry about* $z = 0$.

dependence upon the amplitude of oscillation and fail to predict the transition from classical to relativistic oscillations. We note that the curvature at the origin is not zero, as one would expect on symmetry arguments.

Let us compare the relativistic and Newtonian orbits by calculating $\beta = \beta(t)$ that is a function of coordinate time. Subscripts t and dots will refer to differentiation with respect to t and proper time s respectively.

Along the axis

$$\psi = -\frac{m}{c\sqrt{2}}\sqrt{1-\cos\beta}.$$

Generally $\dot{t} = Ee^{-2\psi}$ thus

$$\dot{\beta} = \beta_t E e^{-2\psi} \tag{3.119}$$

$$\ddot{\beta} = E^2 e^{-4\psi}\left(\beta_{tt} - 2\psi_\beta \beta_t^2\right) \tag{3.120}$$

from which the geodesic equation (3.113) becomes

$$\beta_{tt} = \frac{m}{2\sqrt{2}\,c^3} e^{4\psi} \sin\beta(1-\cos\beta)^{3/2} + \frac{\sin\beta}{1-\cos\beta}\left[1 + \tfrac{3}{2}\psi\right]\beta_t^2. \tag{3.121}$$

The corresponding Newtonian equation of motion is

$$\beta_{tt} = \frac{m}{2\sqrt{2}\,c^3} \sin\beta(1-\cos\beta)^{3/2} + \frac{\sin\beta}{1-\cos\beta}\beta_t^2. \tag{3.122}$$

It will be illustrative to introduce the coordinate z using the inverse relationship (3.4). In doing so we have

$$\psi(z) = -\frac{m}{\sqrt{z^2 + c^2}} \tag{3.123}$$

and the relativistic and Newtonian equations of motion become respectively

$$z_{tt} = -\frac{mz}{(z^2 + c^2)^{3/2}} \left[e^{4\psi(z)} - 3\, z_t^2 \right] \tag{3.124}$$

$$z_{tt} = -\frac{mz}{(z^2 + c^2)^{3/2}}. \tag{3.125}$$

Thus, when ψ and z_t are small the relativistic and Newtonian trajectories should agree. Examples of this are given in the following figures. It is observed as m increases the two trajectories diverge.

The proper motion, $z(s)$ is also plotted. From figure 3.10 we see as m increases the expected increase in v is observed. We note that the amplitudes of the motion are identical. The relativistic orbits generally have longer periods (once $m > m_c$ as eluded too earlier).

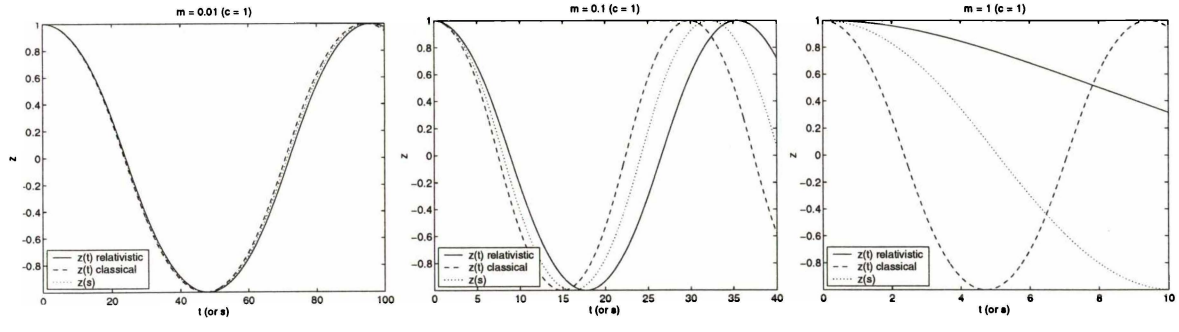

FIGURE 3.9: *Comparison of trajectories for increasing mass ($c = 1$).*

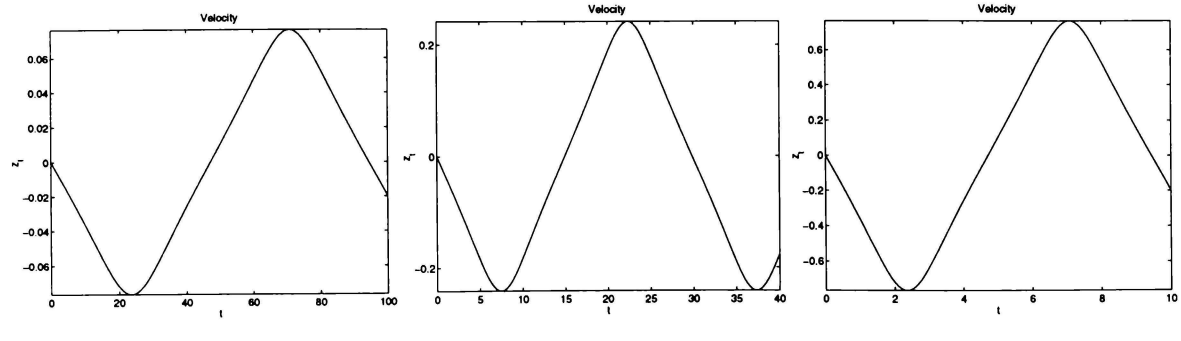

FIGURE 3.10: *Corresponding Newtonian velocity profiles. As m increases so does* $\max(v)$. *Thus the more prudent do relativistic considerations become. This is evident in these plots, where the deviations between the various trajectories become more apparent as the velocity increases.*

$n = 1$ Solution.

We now turn our attention to the $n = 1$ solution. This section concentrates on the trajectories of test particles released on the z axis with zero angular momentum. The simplified metric functions ψ_1 and γ_1 presented in section 3.8.2 are used in this section.

Along the axis the metric function ψ_1 becomes

$$\psi_1 = -B\sqrt{1-\cos\beta}\,\cos\beta \tag{3.126}$$

or, from the inverse coordinate transformation (3.4)

$$\psi_1 = -m\frac{z^2-c^2}{(z^2+c^2)^{3/2}}. \tag{3.127}$$

From the multipole determination, we have introduced the mass of the source via the relationship $m = \sqrt{2}\,c\,B$. We note that the potential (in a Newtonian sense) becomes zero when $z = c$ and is positive for $|z| < c$ although, ψ_1 and its derivatives remain bounded along the entire z axis.

This is also evident in the Kretschmann scalar along the axis

$$\begin{aligned} K_z \;=\; & \frac{m^2}{576\,c^8}(1-\cos\beta)^{5/2}\,e^{4\psi_1(\beta)}\Big\{\sqrt{1-\cos\beta}\Big[m^2(1-\cos\beta)\times \\ & (2268\cos^2\beta - 3024\cos\beta + 1009)(1+\cos\beta)^2(3\cos\beta-2)^2 + \\ & c^2(13824 + 4032\cos\beta - 46026\cos^2\beta - 9612\cos^3\beta + 45846\cos^4\beta)\Big] + \\ & 6\sqrt{2}\,m\,c\,(1-\cos\beta)(2-3\cos\beta)(1+\cos\beta)(2052\cos^3\beta - 1419\cos^2\beta - \\ & 1121\cos\beta + 776)\Big\} \end{aligned} \tag{3.128}$$

which at the origin $\beta = \pi$, obtains its maximum value

$$K_z(\pi) = 267\,\frac{m^2}{c^6}e^{4m/c}. \tag{3.129}$$

Thus K_z remains bounded (and positive) along the z axis indicating, along with (3.126) (or (3.127)) that there are no sources along the axis. This is expected as in toroidal coordinates the solutions to Laplace's equation becomes singular when $\alpha \to \infty$. We also note that the metric function γ_1 is zero along the axis.

Consider the Newtonian equations of motion for a test particle in the gravitational field described by the potential (3.127)

$$\ddot{z} = -\nabla\psi_1 = -\,m\,z\,\frac{z^2-5c^2}{(z^2+c^2)^{5/2}}. \tag{3.130}$$

Integrating, and noting that the initial velocity is zero at the release point z_0 we have

$$\dot{z}^2 = 2\,m\left[\frac{z^2-c^2}{(z^2+c^2)^{3/2}} - \frac{z_0^2-c^2}{(z_0^2+c^2)^{3/2}}\right]. \tag{3.131}$$

This equation serves to locate the turning points of the motion, that is, where the velocity becomes zero. The permitted range of z is then fixed by the inequality

$$\frac{z^2 - c^2}{(z^2 + c^2)^{3/2}} - \frac{z_0^2 - c^2}{(z_0^2 + c^2)^{3/2}} \equiv P(z\,; z_0\,; c) \geq 0. \tag{3.132}$$

Recall that this is the classical potential of the motion. Using (3.127), evaluation the relativistic analog of this equation given by (3.114) results in the same equation. Thus the two motions will exhibit the same qualitative features.

Examples of various potential curves are illustrated in figure 3.11.

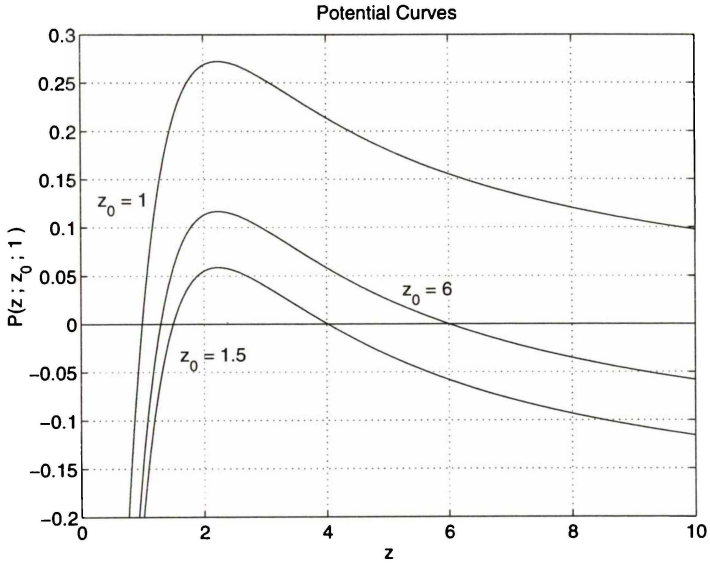

FIGURE 3.11: *Various potential curves, $P(z\,;\, z_0\,;\, 1)$, for the ψ_1 solution for motion along the z axis. Here $c = 1$ and the initial release point z_0 is varied.*

For $z_0 \leq 1$ then $P(z\,;\, z_0\,;\, c)$ has only one root, its starting position and the particles motion is unbounded and accelerates from the release point to infinity (the upper curve in figure 3.11).

When $z_0 > 1$ then $P(z\,;\, z_0\,;\, c)$ will have two roots and the test particle will oscillate along the z axis between these two points. We note, for example, in the $z_0 = 1.5$ curve figure 3.11, that the particle can experience initial repulsion from the origin.

When $z_0 = \sqrt{5}\,c$, we have a repeated root and there is no motion: the particle remains stationary. This is also evident by equation (3.130), as the particle starts from rest.

For $z_0 > \sqrt{5}\,c$ then the test particle exhibits oscillatory motion with initial displacement towards the origin. Examples of each type of motion is given in figure 3.12. Recall that this qualitative description is valid for either the Newtonian or relativistic motions.

The geodesic equation of motion ($\beta = \beta(s)$) in toroidal coordinates is

$$\ddot{\beta} = -\frac{m E^2}{\sqrt{2}c^3}\sin\beta(1-\tfrac{3}{2}\cos\beta)(1-\cos\beta)^{3/2} + \frac{\sin\beta}{1-\cos\beta}\left[1+\frac{m}{\sqrt{2}c}(1-\tfrac{3}{2}\cos\beta)(1-\cos\beta)^{1/2}\right]\dot{\beta}^2 \tag{3.133}$$

or in terms of coordinate time t we have

$$\beta_{tt} = -\frac{m}{\sqrt{2}c^3}e^{4\psi}\sin\beta(1-\tfrac{3}{2}\cos\beta)(1-\cos\beta)^{3/2} + \frac{\sin\beta}{1-\cos\beta}\left[1+\frac{3m}{\sqrt{2}c}(1-\tfrac{3}{2}\cos\beta)(1-\cos\beta)^{1/2}\right]\beta_t^2. \tag{3.134}$$

Again we will resort to numerical evaluation of these equations, in which we set $c = 1$ throughout. As for the previous $n = 0$ case, in the weak field limit, when velocities and m are small then the relativistic and Newtonian motions should be comparable. Indeed this is observed in the following figures. The initial positions correspond to those indicated in the potential plots of figure 3.11.

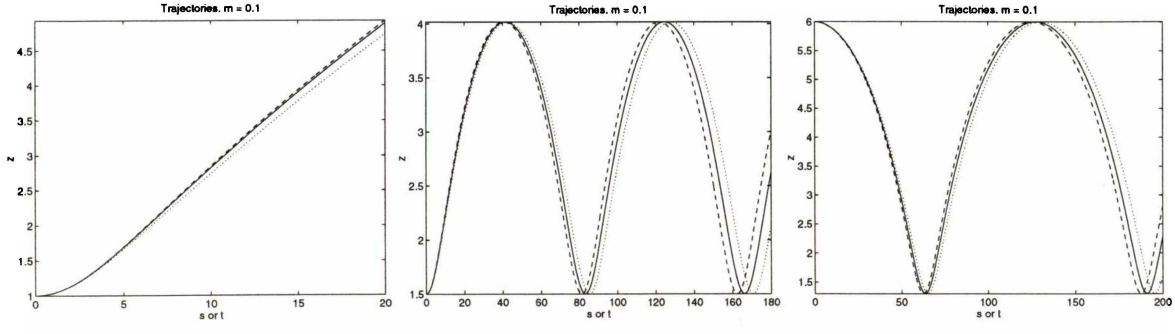

FIGURE 3.12: $n = 1$ *axis trajectories.* $m = 0.1$. *Dashed line (- -) is the Newtonian motion given by (3.131). The solid line (-) is that of the relativistic orbit as a function of proper time* s. *The remaining plot* $(\cdots)$ *is that of the relativistic orbit as a function of coordinate time* t, *given by equation (3.134).*

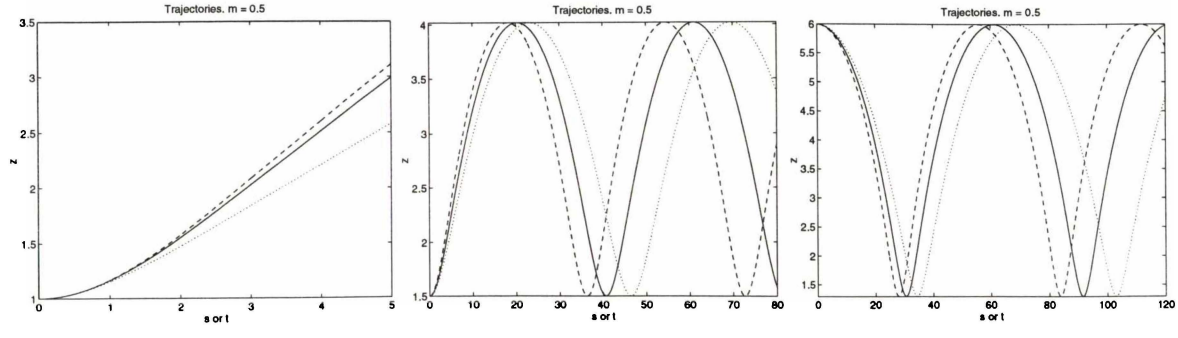

FIGURE 3.13: *As in the previous figure but* $m = 0.5$. *Note how the three trajectories, when compared to the previous figure, have little resemblance.*

The proper period of motion, T, like the earlier $n = 0$ solution, has a peculiar dependence upon of the source mass m. Again there is a critical value m_c, for which, when m approaches this value from the left, the period of oscillation decreases. Thereafter the period increases. In the Newtonian scenario $T \to 0$ as $m \to \infty$. This is illustrated in figure 3.14 for various z_0 values.

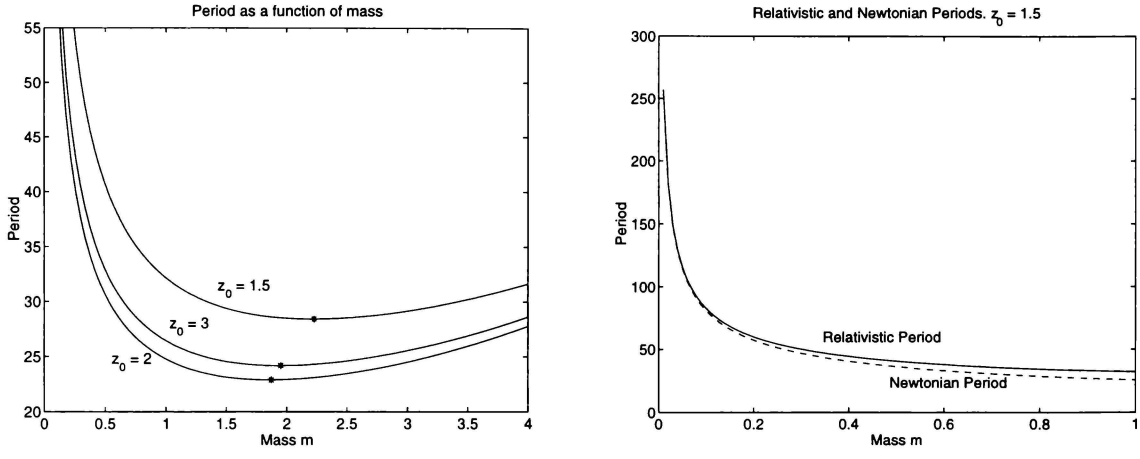

FIGURE 3.14: *Period of oscillation as a function of mass. In the left plot, the stars mark the minimum period, afterwards the motion behaves in a non-Newtonian manner. A comparison between the relativistic and Newtonian periods are given in the right hand plot. As m increases the difference grows.*

3.13.2 General Orbits

We will now illustrate various trajectories of test particles of zero angular momentum that do not start from the z axis.

Semerák *et al.* (1999a), in modeling accretion disks, produce various timelike geodesics of test particles in various superimposed Weyl metrics, including that of the toroidal $n = 0$ solution (the Weyl-Bach ring) and Schwarzschild metric.

Here we consider both the $n = 0$ and $n = 1$ solutions. The trajectories are determined by the general equations (3.102) and (3.103) with $L = 0$. We will set $c = 1$ and the mass of source $m = 1$ throughout.

Typical trajectories of the $n = 0$ solution are shown in figures 3.15 and 3.16. We begin with initial points close to the z axis. Initial values are indicated in the titles of the plots (r_0, θ_0) which are standard polar coordinates. An asterisk in the plots marks the initial position. The singular points ($\rho = c = 1, z = 0$) are indicated by solid black circles.

Typically for small θ_0 and $r_0 \leq 0.5$ approximately, the test particle oscillates in an orderly manner towards the (mass) singular point $\rho = c$. At approximately $r_0 = 0.685$ the motion becomes considerably different (figure 3.15(b)): the particle is initially accelerated towards the source but is then repelled and threads the ring several times until eventually terminating at the $\rho = c$ source point.

As r_0 is increased the motion becomes more erratic. At times, for example figure 3.15(c), the motion terminates at the 'left hand' singular point, in agreement with Semerák *et al.* (1999a), who also concluded that the test trajectories preferably hit the innermost regions around the rings along certain directions while being *repelled* elsewhere. This unphysical *repulsion* is an actual breakdown of the validity of the coordinates near the source of the gravitational field and the particles should appear *repelled* and *attracted* in the directions from which the ring is physically (proper length) nearby or far away*.

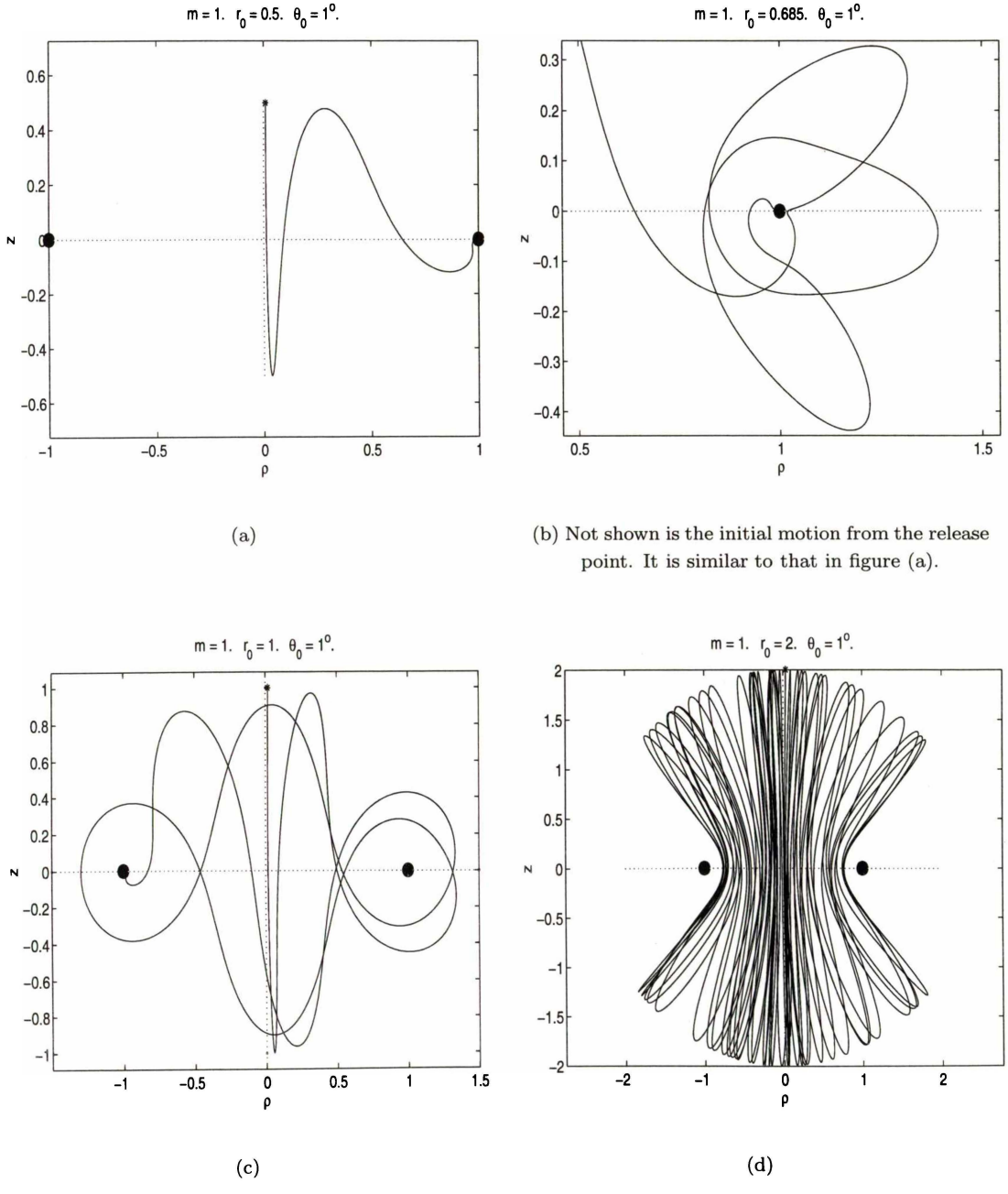

(a)

(b) Not shown is the initial motion from the release point. It is similar to that in figure (a).

(c)

(d)

FIGURE 3.15: *General $L = 0$ geodesics for the ring solution.*

*The singular points (the ring) having a directional dependency (Hoenselaers, 1992, 1995; Semerák *et al.*, 1999a).

An interesting case is presented in figure 3.15(d) where the motion (within numerically induced errors) is cyclic and the particle oscillates through the ring in a systematic and repetitive fashion. This general behaviour was observed in trajectories beginning with various

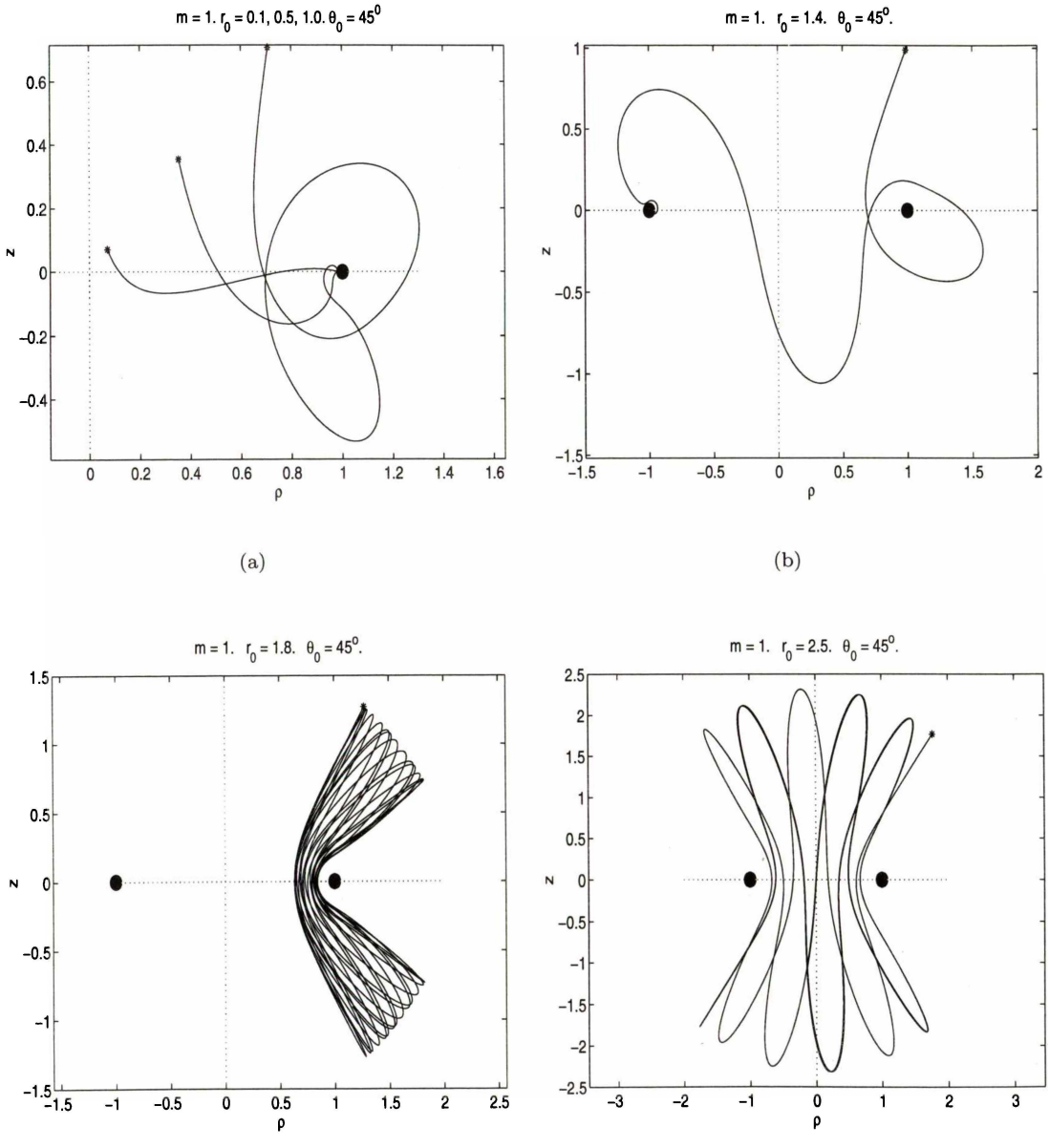

(d) The motion of the test particle oscillations between the release point (*) and the spike in the lower-left quadrant.

FIGURE 3.16: *Further general $L = 0$ geodesics for the ring solution.*

increasing θ_0 values. Examples are given in figure 3.16 where $\theta_0 = 45^o$. In particular plot (c) and (d) indicate the existence of closed orbits. Here the release points have been selected in order to produce orbits that do not "get too close" to the singular points and thus minimize the numerical errors generated*.

*The singular point corresponds to $\alpha \to \infty$, thus the accuracy in the integration near these points diminishes.

For completeness we have included in figure 3.17 trajectories beginning close to the $z = 0$ plane ($\theta_0 \to 90^o$). Due to the initial conditions, the particle inevitably passes close to the singular point shortly after release, and as eluded too above, the validity of the orbits, as the use of the coordinates become questionable near the singular points, should be viewed with caution. It is seen however, that again the motion is divided generally into two types: those that terminate at the left or right hand singular points.

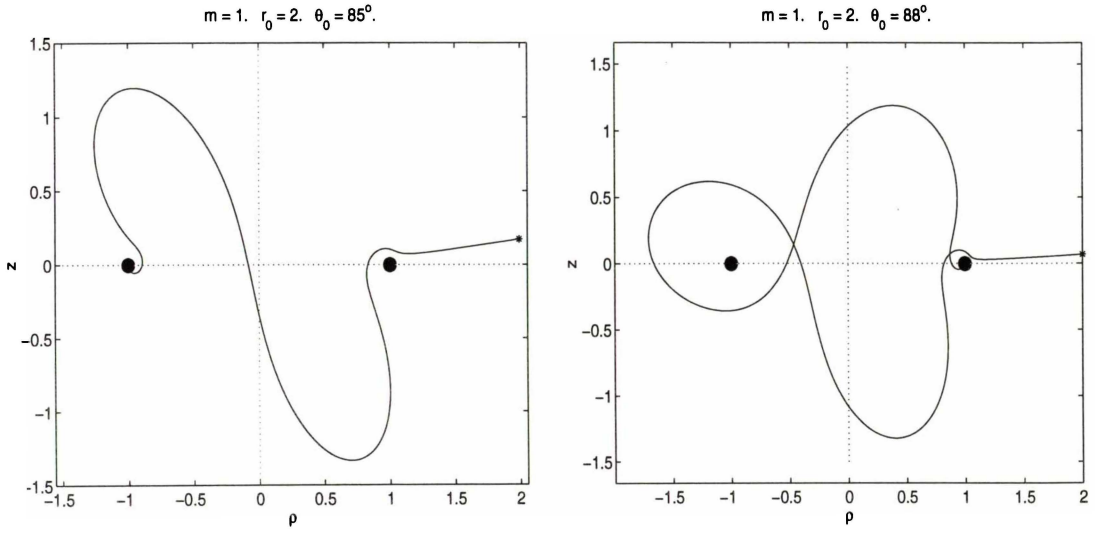

(a) (b)

FIGURE 3.17: $L = 0$ *geodesics for the ring solution near the* ρ *axis.*

Geodesics for test particles starting from rest with zero angular momentum for the $n = 1$ solution are presented in the following figures. The solution is singular at $\rho = c = 1, z = 0$ although the actual mass distribution is not known. From the multipole analysis calculated earlier, the field (with the appropriate selection of parameters) can exhibit equatorial symmetry about the $z = 0$ plane. We will concentrate on this particular form of the solution. Numerical results confirm this symmetry and thus we will illustrate typical geodesics beginning in the quadrant $z, \rho > 0$ only.

Clearly the equations of motion (3.102) and (3.103) are not separable in α and β. Solving for the zeros of equation (3.104),

$$\dot{\alpha}^2 + \dot{\beta}^2 = F(\alpha, \beta; E, L = 0) \tag{3.135}$$

at these points we have $\dot{\alpha} = 0$ and $\dot{\beta} = 0$ simultaneously. The permitted ranges of the α and β coordinates are then fixed by the inequality $F \geq 0$. The constant E is related to the initial release point (α_0, β_0) by $E = e^{\psi_0}$ where $\psi(\alpha, \beta)$ is given by (3.66). Thus the permitted ranges of the coordinates are governed by the relation $F \equiv \psi_0 - \psi \geq 0$.

This relation is useful in determining qualitative properties of the motion, in particular whether the geodesics will be unbounded or terminate. Two examples are given in figure 3.18.

Here F is plotted as a function of the cylindrical coordinates ρ, z rather than the toroidal coordinates α, β. Plots (a) and (b) refer to the motion beginning at $(r_0 = 1, \theta_0 = 5^o)$. The

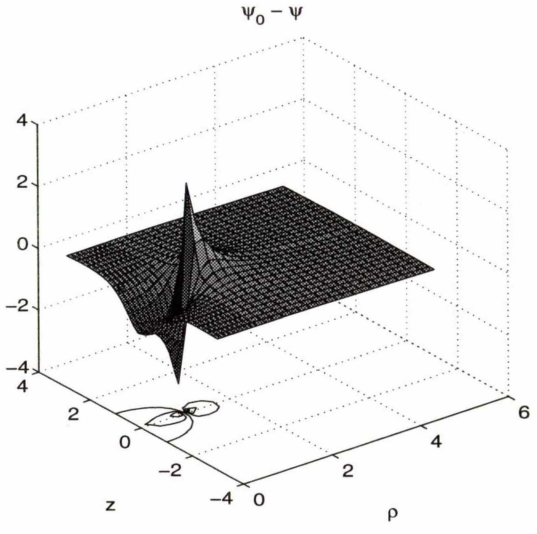

(a) F for $(r_0 = 1, \theta_0 = 5^o)$.

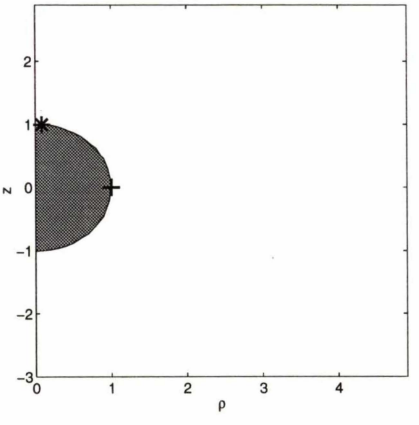

(b) Contour plot of figure (a).

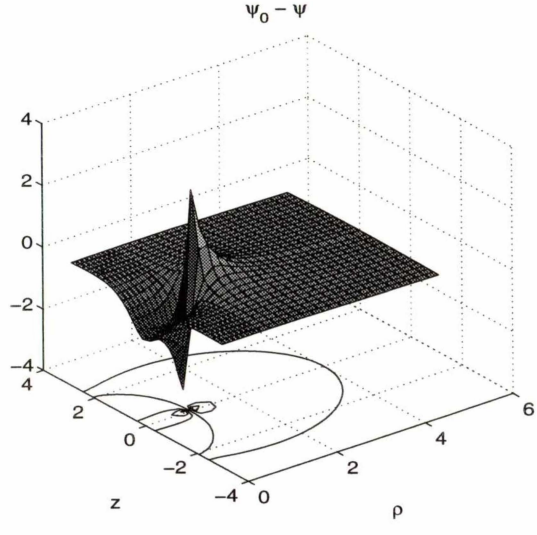

(c) F for $(r_0 = 2, \theta_0 = 5)$.

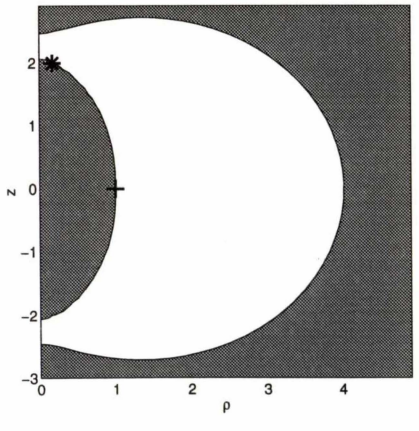

(d) Contour plot of figure (c).

FIGURE 3.18: *Potential plots for the $n = 1$ solution. In figures (b) and (d) the white area is the allowed range of the coordinates.*

contour plot (b) in which the unshaded (white) area corresponds to $F > 0$, is unbounded, thus the motion beginning from the indicated asterisks, will also be unbounded. The actual orbit exhibiting this behaviour is shown in figure 3.19(a).

Similar analysis holds for plots (c) and (d) which relate to the initial conditions $(r_0 = 2, \theta_0 = 5)$. Here, however there is a distinct region for which $F \geq 0$ and thus indicating bounded motion. Again this is reflected in figure 3.19(b).

Figure 3.19 illustrates the typical $L = 0$ geodesics for the $n = 1$ solution. In figure 3.19(a) examples of unbounded (repulsive) motion is shown, this occurs when the release position r_0 is small. As r_0 is increased the motion becomes bounded. For release points close to z axis (θ_0 small) there are initial repulsive parts of the motion. Typically the test particle terminates near the right hand singular point, although under certain initial conditions the particle can terminate at the left hand singular point.

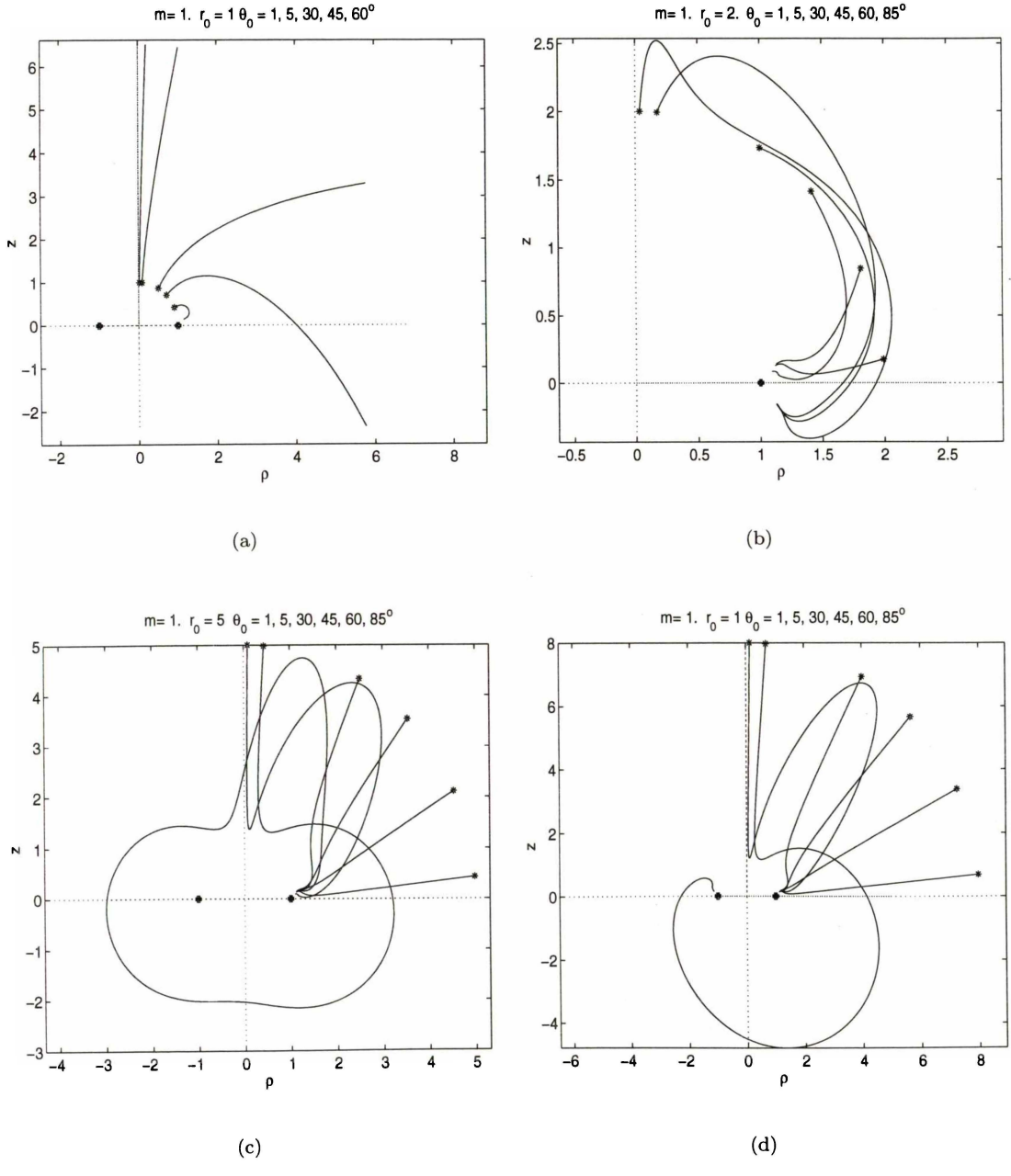

FIGURE 3.19: $L = 0$ *geodesics for the* $n = 1$ *solution.*

3.14 Bound Orbits

We will now consider the bounded geodesics of test particles starting from rest in the $z = 0$ plane with $L \neq 0$. We will restrict our study to the ψ_0 and ψ_{01} solutions that have even multipole moments (about the equatorial $z = 0$ plane).

From (3.12) and the analysis of section 3.6 we see in general, under these requirements, the ψ solutions are constructed from particular solutions of the form

$$\psi = \sqrt{\cosh\alpha - \cos\beta}\, P_{n-1/2}(\cosh\alpha)\, \cos(n\beta). \tag{3.136}$$

The $z = 0$ plane corresponds to an initial β value of $\beta_0 = \pi$ or 0 (inside or outside the singular ring at $\alpha \to \infty$ respectively), thus we readily compute from (3.136) that $\partial_\beta \psi|_{\beta=\beta_0} = 0$. We assume that $\dot{\beta}_0 = 0$, from (3.103) it follows that $\ddot{\beta}_0 = 0$ and thus $\beta(s) = \beta_0$ and so the motion is confined to the $z = 0$ plane as required due to the symmetry of the ψ solutions that are generating the field.

We can therefore write the geodesic equations as

$$-\ddot{\alpha} = X^{-1}e^{-2\gamma}\left\{\psi_\alpha e^{-2\psi}E^2 + \tfrac{1}{2}e^{2\gamma}(X_\alpha + 2X\gamma_\alpha)\dot{\alpha}^2 - \frac{L^2}{2X^2}\left[\frac{X_\alpha \sinh\alpha + 2X\cosh\alpha}{\sinh^3\alpha}\right]\right\}. \tag{3.137}$$

We will concentrate on motion beginning from $\rho > c$ requiring $\beta = 0$ thus

$$X(\alpha) = \frac{c^2\, e^{-2\psi}}{(\cosh\alpha - 1)^2} \tag{3.138}$$

where $\psi(\alpha, \beta) = \psi(\alpha, 0)$. The remaining equations for $\dot{t}$ and $\dot{\varphi}$ are given by (3.101).

Given $\dot{\alpha}_0 = 0$, solving the integral of the motion (3.104) with respect to E we obtain the general potential equation, parameterized by the angular momentum L,

$$V^2(\alpha\,; L) = e^{2\psi}\left(1 + \frac{L^2}{X\,\sinh^2\alpha}\right) \geq 0 \tag{3.139}$$

which can be employed to determine the turning points of the motion (if any) of the bounded trajectory. For easier interpretation we will plot V as a function of ρ enabled by the inverse transformation (3.3).

The toroidal functions $P_{n+1/2}(\cosh\alpha)$ cannot be written explicitly in terms of ρ thus we will numerically invert these functions used in evaluating ψ. As we are considering motion outside the singular point $\rho = c$ we have $\alpha = \ln[(\rho + c)/(\rho - c)]$ from which

$$\sinh\alpha = 2\rho c/(\rho^2 - c^2), \qquad \cosh\alpha = (\rho^2 + c^2)/(\rho^2 - c^2)$$

thus in terms of ρ we have

$$V^2(\rho\,; L) = e^{2\psi(\rho)}\left(1 + \frac{L^2}{\rho^2}e^{2\psi(\rho)}\right) \geq 0 \tag{3.140}$$

which can be verified from the metric given by (3.5) (with $dz = 0$) also. We note, to compute V the metric function ψ is only required.

3.14.1 $n = 0$

Recall that the $n = 0$ (ring) solution

$$\psi_0 = -\sqrt{\cosh\alpha - \cos\beta}\, B\, P_{-1/2}(\cosh\alpha) \tag{3.141}$$

may be expanded in terms of spherical coordinates

$$\psi_0 = \sum_{l=0}^{\infty} \frac{a_l}{r^{l+1}} P_l(\cos\theta). \tag{3.142}$$

From section 3.6 the mass M_0 and quadrupole moment M_2 for the $n = 0$ solution are

$$M_0 = \sqrt{2}cB \tag{3.143}$$

$$M_2 = -\tfrac{\sqrt{2}}{6}c^3(3B + 4B^3). \tag{3.144}$$

From section 1.8.5 given M_0 and M_2 we have for the constants a_0 and a_2 in (3.142) (recall $a_1 = 0$ due to symmetry)

$$a_0 = -M_0 = -\sqrt{2}\, c\, B \tag{3.145}$$

$$a_2 = -\frac{1}{3}M_0^3 - M_2 = \frac{\sqrt{2}}{2}\, B\, c^3. \tag{3.146}$$

Let $B = 2^{-1/2}$ and relabel the coordinate scale factor: $c = m$. Thus the source has mass $M_0 = m$ and quadrupole moment $M_2 = -(5/6)m^3$. Given we are interested in motion confined to the $z = 0\,(\theta = \pi/2)$ plane then the expansion (3.142) begins with

$$\psi_0 = -\frac{m}{\rho} - \frac{m^3}{4\rho^3}. \tag{3.147}$$

We will use this result to calculate approximate solutions to the equation of motion (3.137). We note that this solution represents a field with classical quadrupole moment $-m^3/2$.

Similarly from (3.58) we have for the remaining metric function

$$\gamma_0 = -\frac{1}{2}\frac{m^2}{r^2}\sin^2\theta = -\frac{1}{2}\frac{m^2}{\rho^2}. \tag{3.148}$$

It is interesting to use (3.147) and compare the exact and approximate potential curves discussed in the previous section. This is illustrated in figure 3.20.

The agreement is excellent for large ρ. Close to the singular point $\rho = m = 1$ the two curves deviate. This could be improved upon by including more lower order terms in the expansion (3.147). Clearly for small ρ additional lower order terms will become important. For simplicity, and to facilitate the determination of an approximate solution for bounded geodesics we shall not include any more terms in the above approximation.

Let us examine the potential curves corresponding to this solution in more detail (we shall perform the analogous analysis of de Felice (1991) who studied the potential curves associated with the Curzon metric). Encouraged by the numerical evidence, let us simplify the analysis

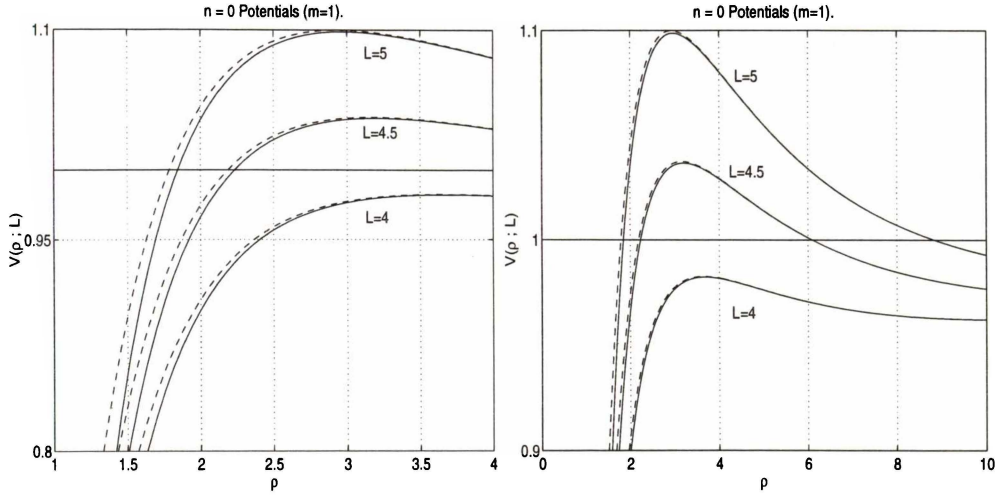

FIGURE 3.20: *Potential curves for the $n = 0$ solution in the $z = 0$ plane. The dashed line is the approximate potential determined by (3.140) and (3.147). The solid line is the potential determined by (3.139) and (3.141).*

by using the potential $V^2(\rho; L)$ and the approximate ψ solution given by (3.147). From Olver (1997) we have the asymptotic expansion

$$P_{-\frac{1}{2}}(\xi) \sim \frac{\sqrt{2}}{\pi} \frac{\ln \xi}{\xi^{1/2}} \qquad (\xi \to \infty) \tag{3.149}$$

thus the following limits hold ($\alpha \to \infty$ is equivalent to $\rho \to c$):

$$\lim_{\rho \to c=m} V^2(\rho; L) = 0 \qquad \text{and} \qquad \lim_{\rho \to \infty} V^2(\rho; L) = 1 \tag{3.150}$$

(the second results follows directly from the asymptotic flatness of ψ). The turning points of $V^2(\rho; L)$ are found as solutions of

$$4m\rho^4 + 3m^3\rho^2 + 2L^2 e^{2\psi} \left[3m^3 + 4m\rho^2 - 2\rho^3\right] = 0. \tag{3.151}$$

Or, by solving with respect to L^2 we have

$$L^2 = \frac{m\rho^2(4\rho^2 + 3m^2)}{2e^{2\psi}(2\rho^3 - 4m\rho^2 - 3m^3)} \equiv \delta. \tag{3.152}$$

As $\delta > 0$ then $\rho > 2.3\,m$ approximately. The minimum of δ occurs at $\rho \approx 5.7\,m$, corresponding to $L^2_{min} \approx 13m^2$. Thus $V^2(\rho; L)$ has turning points corresponding to real values of L only when $\rho > 2.3\,m$. We note that for the Curzon solution the corresponding turning points only occur for $\rho > 2m$ and the minimum of δ_c occurs at $\rho = (3 + \sqrt{5})m \approx 5.3m$ (de Felice, 1991).

Clearly for bounded motion the points corresponding to $V^2(\rho; L) = 1$ are important. This occurs at

$$L^2 = \rho^2 e^{-2\psi}(e^{-2\psi} - 1) \equiv \eta \tag{3.153}$$

which clearly becomes unbounded as $\rho \to c$ or ∞. The minimum value occurs when

$$e^{-2\psi} = \frac{4\rho^3 - 4m\rho^2 - 3m^3}{4\rho^3 - 8m\rho^2 - 6m^3}. \tag{3.154}$$

The minimum of η is also a point of the curve δ as can be verified by direct substitution.

Given an initial starting position $(\rho_0(\alpha_0), z = 0)$ and angular momentum L we use the potential curves to calculate the remaining constant E. Recall once E is fixed then the ranges of the coordinates α (or ρ) are fixed.

In particular, circular orbits occur only when $E^2 = \min(V^2(\rho; L)) < 1$. The radii of these of these orbits ρ_c, depend on L as can seen from (3.152). Additionally we have $5.7m \leq \rho_c < \infty$. The potential function for circular orbits is

$$\min(V^2(\rho; L)) = V^2(\rho; L^2 = \delta) = e^{2\psi}\left(\frac{4\rho^3 - 4m\rho^2 - 3m^3}{4\rho^3 - 8m\rho^2 - 6m^3}\right). \tag{3.155}$$

For $\rho_c = 5.7m = \rho^*$ the minimum energy for circular orbits E_{mc} is given by

$$E_{mc} = V(\rho^*; \delta) \approx 0.948. \tag{3.156}$$

As de Felice (1991) notes, it is interesting to compare this value* with the energy threshold for circular motion in the Schwarzschild space-time: $E_{mc}^{Sch} \approx 0.942$ which is slightly smaller of that for the ring solution (3.156). The corresponding threshold energy for the Curzon solution is $E_{mc}^{Cur} \approx 0.945$. Thus when considering circular orbits the $n = 0$ toroidal space-time produces (in the z plane) gravitational effects almost indistinguishable from that of the Schwarzschild or Curzon solutions.

Various energy values and radii of circular orbits, determined by (3.155) and (3.152) respectively, are shown in table 3.1. Recall these theoretical calculations are based on the expansion (3.147). We see that they compare favorably with the numerical results calculated from the exact potential equation (3.139) and (3.141).

	Numerical		Theoretical	
L	$\min(V^2)$	ρ_c	$\min(V^2)$	ρ_c
4.0	0.925256	10.6999	0.925258	10.7012
4.5	0.943924	15.4221	0.943921	15.4224
5.0	0.955931	20.4015	0.955930	20.4016
5.5	0.964298	25.7896	0.964298	25.7896
6.0	0.970420	31.6317	0.970419	31.6317
10.0	0.989789	95.8899	0.989791	95.8850

TABLE 3.1: *Numerical and theoretical comparisons of the location, ρ_c and energy, $E^2 = \min(V^2)$ values for circular orbits (in the $z = 0$ plane) for the ring ($n = 0$) toroidal solution.*

Let us assume, from the application of the potential curves described above, that E, L and the starting position of a test particle have been appropriately chosen so that the orbit will be bounded and the test particle oscillates between two extreme values.

*Of course this is calculated from the approximate solution (3.147), however as we have seen, as ρ^* is relatively large, this approximation should be accurate. Indeed this is evident in the results presented in table 3.1.

We will solve the geodesic equation (3.137) numerically, but will now present an approximate analytical solution to this problem. Further details of the following analysis can be found in section 2.5.6.

From the general Weyl metric we obtain the equation of motion

$$\left(\frac{d\rho}{ds}\right)^2 = e^{-2\gamma}\left[E^2 - \frac{L^2}{\rho^2}e^{4\psi} - e^{2\psi}\right] \tag{3.157}$$

here ψ and γ are functions of ρ and z. We are only concerned with motion in the $z = 0$ plane however. Furthermore, since we are interested in the shape of the orbit rather than its time evolution we introduce the dimensionless variables

$$u(\varphi) = \frac{m}{\rho}, \qquad \Lambda = \frac{m}{L} \tag{3.158}$$

from which we obtain

$$\left(\frac{du}{d\varphi}\right)^2 = (u')^2 = \Lambda^2 e^{-2\gamma-4\psi}\left[E^2 - \frac{u^2}{\Lambda^2}e^{4\psi} - e^{2\psi}\right] \tag{3.159}$$

we have from (3.147) and (3.148)

$$\psi(u) = -(u + \frac{1}{4}u^3) \qquad \text{and} \qquad \gamma(u) = -\frac{1}{2}u^2. \tag{3.160}$$

To proceed we simplify equation (3.159) by assuming that the test particle is moving at large distances from the gravitational source, thus expanding up to the order u^3 we obtain

$$(u')^2 = Au^3 + Bu^2 + Cu - D := F(u) \tag{3.161}$$

the coefficients are

$$A = \frac{1}{6}\Lambda^2(94E^2 - 23) \tag{3.162}$$

$$B = 3\Lambda^2(3E^2 - 1) - 1 \tag{3.163}$$

$$C = 2\Lambda^2(2E^2 - 1) \tag{3.164}$$

$$D = \Lambda^2(1 - E^2). \tag{3.165}$$

As discussed in section 2.5.6 it follows that motion is possible for $F(u) \geq 0$ as the geometry of the geodesics are determined by the roots, $0 < u_1 < u_2 < u_3$, of $F(u) = 0$. The roots are related by

$$u_1u_2 + u_2u_3 + u_3u_1 = \frac{12(2E^2 - 1)}{94E^2 - 23} \tag{3.166}$$

$$u_1u_2u_3 = \frac{6(1 - E^2)}{94E^2 - 23} \tag{3.167}$$

$$u_1 + u_2 + u_3 = \frac{6 - 18\Lambda^2(3E^2 - 1)}{\Lambda^2(94E^2 - 23)} \equiv \xi. \tag{3.168}$$

We shall consider the case when all roots are real and positive: it follows from (3.166) and (3.167) that this requires $\frac{1}{2} \leq E^2 \leq 1$ and $L^2 > 6m^2$ (in the extreme case $E = 1$). Let us write the three roots as

$$u_1 = \mu(1 - e), \qquad u_2 = \mu(1 + e), \qquad u_3 = \xi - 2\mu \tag{3.169}$$

here we have used (3.168) to determine u_3 and we have introduced $\mu = m/l$ and e where $l > 0$ is the latus rectum and e the eccentricity of the orbit. From (3.166) and (3.167) we have

$$2\mu\xi - \mu^2(3+e^2) = \frac{12(2E^2-1)}{94E^2-23} \tag{3.170}$$

$$\mu^2(1-e^2)(\xi-2\mu) = \frac{6(1-E^2)}{94E^2-23} \tag{3.171}$$

which relate explicitly the parameters μ and e, which describe the particles trajectory, with the parameters E, Λ and m which determine the particles energy, angular momentum and the mass of the source. From section 2.5.5, we can write the solution of (3.161) in terms of elliptic functions as

$$u = u_1 + (u_2 - u_1)\,\mathrm{sn}^2(\tfrac{1}{2}\sqrt{A(u_3-u_1)}\varphi, k) \tag{3.172}$$

where the elliptic modulus is given by

$$k^2 = \frac{2\mu e}{\xi - 3\mu + \mu e}. \tag{3.173}$$

In terms of ρ we have

$$\frac{l}{\rho} = 1 + e\,(\,2\,\mathrm{sn}^2(\tfrac{1}{2}\sqrt{A(u_3-u_1)}\varphi, k) - 1). \tag{3.174}$$

Trajectories derived by means of (3.174) are illustrated in figure 3.21. In each plot the approximate solution (3.174) and the numerical solution of (3.137) are shown. Each trajectory begins at $\rho = 70$ but have differing energy E and angular momentum values L.

As L is increased the perihelion (closest approach) radii increases, and in doing so the agreement between the true (numerical) and approximate solutions improves. This is anticipated as the approximate solution is based on the premise that the test particle move at large distances from the gravitational source. We note for all orbits the general features are maintained.

Clearly, as expected, the orbits are still periodic, but no longer of period 2π; rather it is of period $2\pi(1+\Delta\varphi)$. Table 3.2 summarizes the perihelion shifts, $\Delta\varphi$, of those orbits shown in figure 3.21. The numerical ($\Delta\varphi_N$) shifts* are compared to that predicted by the elliptic approximation given by (3.174). It is clear that this approximation becomes more accurate as the perihelion radii increases (effectively for orbits of higher L value).

We also compute the shift due to Fernández-Jambrina and Hoenselaers (2001) formulation based on the Geroch-Hansen multipoles† of the source ($\Delta\varphi_M$). This method is a post-Newtonian perturbative approximation (using the dimensionless parameter $\epsilon = m/L$ which typically should be a small parameter).

We use the complete approximation, up to order ϵ^{10}, which requires the first five Geroch-Hansen multipole moments, although the calculations are simplified as the metric is static and odd multipoles are null. It is therefore a little surprising that for orbits with smaller L values

*The average of several periods.

†In these calculations the multipole moment $M_4 = (947/840)m^5$ is required as shown in section 1.10.

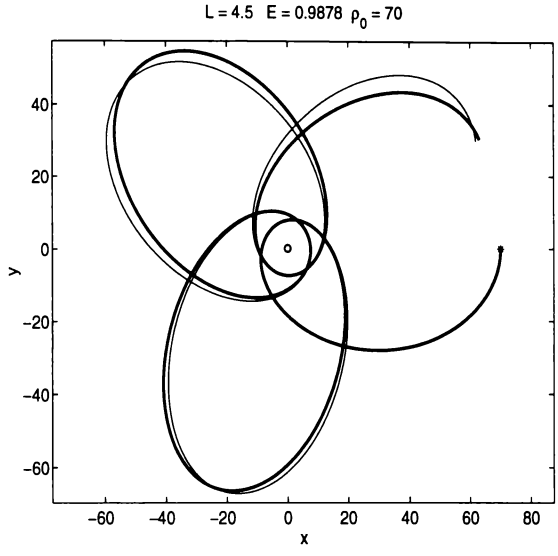

(a) $\xi = 1.2632$, $e = 0.8062$, $\mu = 0.07359$, $\rho_{min} = 7.5$

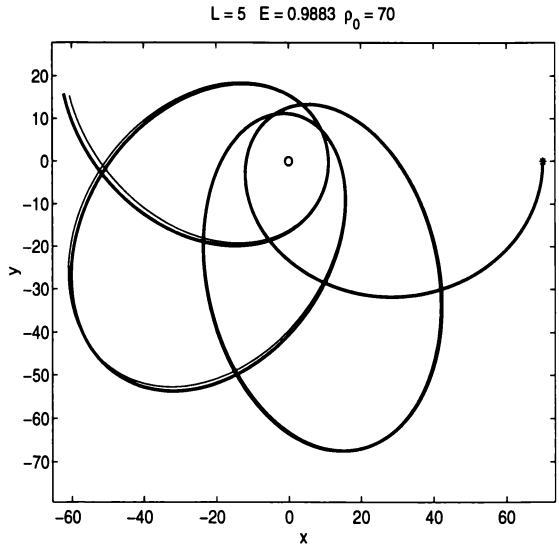

(b) $\xi = 1.6751$, $e = 0.7286$, $\mu = 0.052$, $\rho_{min} = 11.0$

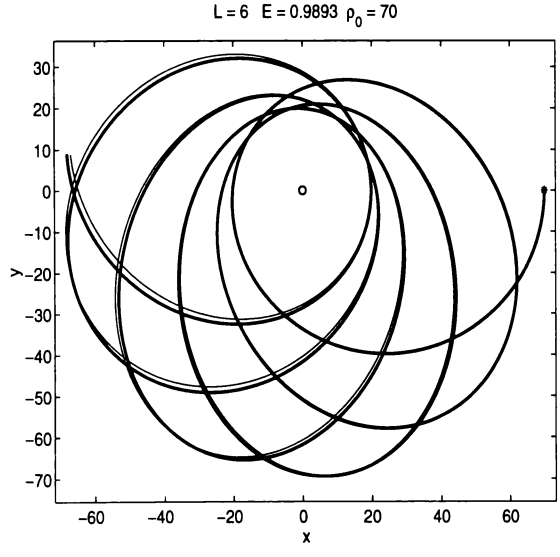

(c) $\xi = 2.6250$, $e = 0.5596$, $\mu = 0.03238$, $\rho_{min} = 19.8$

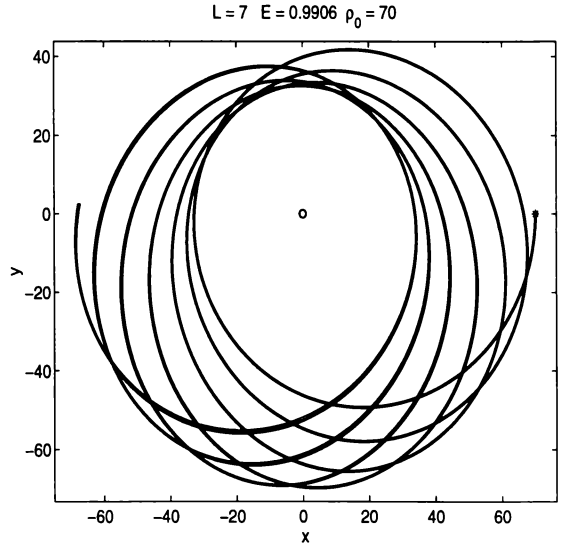

(d) $\xi = 3.7408$, $e = 0.3666$, $\mu = 0.0225$, $\rho_{min} = 32.6$

FIGURE 3.21: *Timelike geodesics in the equatorial plane of the $n = 0$ toroidal solution. The solid line is the numerical solution of equation (3.137) the thin line the analytic approximation given by (3.172). In each the mass of the source (the ring in the plots) and radius are both set to 1. The figure captions refer to the constants used in (3.172) and ρ_{min} refers to the perihelion value.*

($m = 1$ for all) this method does not agree well with the numerical perihelion shifts. Clearly higher order terms and thus the inclusion of higher order multipoles is required. Furthermore it is interesting to note that the elliptic approximation, although known to be inaccurate for these smaller L values, actually out-performs the the multipole method. For larger L values the multipole method is more accurate.

L	E	$\Delta\varphi_N$	$\Delta\varphi_M$	$\Delta\varphi_E$	$\lvert\Delta\varphi_N - \Delta\varphi_M\rvert$	$\lvert\Delta\varphi_N - \Delta\varphi_E\rvert$
4.5	0.9878	1.9471	1.805	1.9045	0.1421	0.0426
5.0	0.9883	1.2336	1.2110	1.2486	0.0226	0.0150
6.0	0.9897	0.6956	0.6941	0.7084	0.0015	0.0128
7.0	0.9906	0.4648	0.4647	0.4722	0.0001	0.0074

TABLE 3.2: *Numerical and theoretical precession rates for the ring solution (in the $z = 0$ plane). These results correspond to the geodesics of figure 3.21. $\Delta\varphi_N$ refers to the numerical perihelion shift (in radians). $\Delta\varphi_M$ is the predicted shift based on the relativistic multipole moments. $\Delta\varphi_E$ is the shift predicted by the elliptic solution (3.174). The final two columns illustrates the differences between the numerical and predicted shifts.*

We have concentrated on situations for which the motion of the test particle is bounded. This need not be the case, for completeness we conclude this section with two examples of the contrary. In figure 3.22 a test particle spirals into the ring (L is not sufficiently large enough) and the test particle has $E^2 > 1$ and the motion is unbounded and is scattered towards infinity.

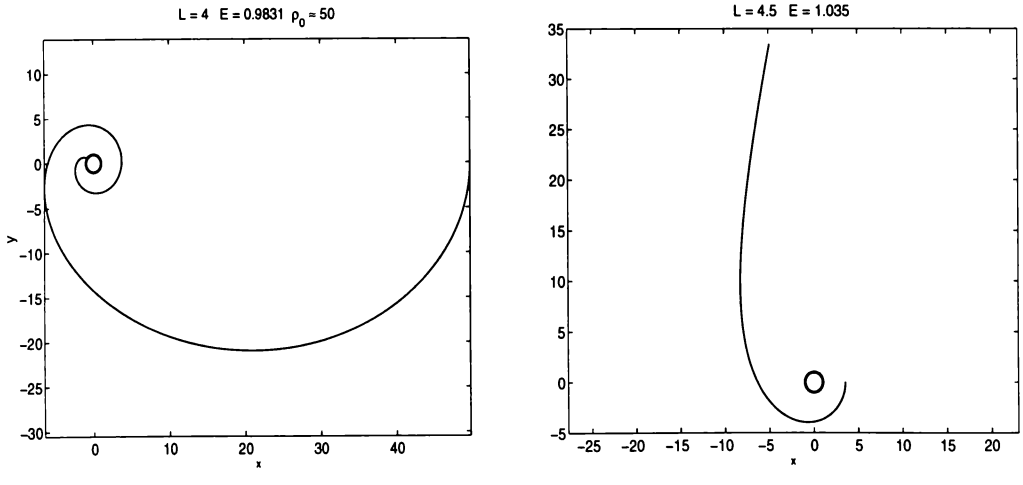

FIGURE 3.22: *Examples of unbounded orbits.*

3.14.2 $n = 0 + 1$

We shall now investigate the bounded geodesics of the $n = 0 + 1$ solution. We will restrict our study to motion within the $z = 0$ plane and consider the particular solutions for which this plane is a plane of symmetry.

We shall consider the trajectories of test particles outside the singular region (of unknown mass distribution) $\rho = c$, hence $\beta = 0$ and, without loss of generality, we shall set $c = 1$.

The relevant metric functions are (for brevity we omit the argument of the Legendre functions in (3.176))

$$\psi_{01} = -\sqrt{\cosh\alpha - 1}\left(B_0\, P_{-\frac{1}{2}}(\cosh\alpha) + B_1\, P_{\frac{1}{2}}(\cosh\alpha)\right) \tag{3.175}$$

$$\begin{aligned}\gamma_{01} = {} & \frac{1}{4}B_0^2\left[2\left(P_{-\frac{1}{2}}P_{\frac{1}{2}} - P^2_{-\frac{1}{2}}\cosh\alpha\right) + P^2_{-\frac{1}{2}} - P^2_{-\frac{1}{2}}\right] + \\ & B_0B_1\left[P^2_{\frac{1}{2}} + \tfrac{1}{2}\cosh\alpha\left(P^2_{-\frac{1}{2}} - P^2_{\frac{1}{2}} - 2P_{-\frac{1}{2}}P_{\frac{1}{2}}\right)\right] - \\ & \frac{1}{12}B_1^2\left[4\cosh^2\alpha\, P^2_{\frac{1}{2}} + \left(8P_{-\frac{1}{2}}P_{\frac{1}{2}} - 12P^2_{-\frac{1}{2}}\right)\cosh\alpha + \right. \\ & \left. 6\,P_{-\frac{1}{2}}P_{\frac{1}{2}} - P^2_{-\frac{1}{2}} - 3P^2_{\frac{1}{2}}\right].\end{aligned} \tag{3.176}$$

Given the mass m and quadrupole (relativistic) moment Q of the source, the constants* B_0 and B_1 are calculated from (see section 3.9).

$$B_0 = \tfrac{\sqrt{2}}{24}\left(15m + 2m^3 + 6Q\right), \qquad B_1 = -\tfrac{\sqrt{2}}{24}\left(3m + 2m^3 + 6Q\right). \tag{3.177}$$

Higher order multipole moments are fixed†, for example

$$M_4 = -(\tfrac{1}{5}m^5 + \tfrac{1}{2}m^3 + \tfrac{3}{8}m) - Q(\tfrac{8}{7}m^2 + \tfrac{3}{2}). \tag{3.178}$$

From these multipole values it follows from section 1.8.5 and equations (3.50) and (3.51) that in terms of spherical coordinates we have

$$\psi_{01} = -\frac{m}{r} - \frac{m^3 + 3Q}{3r^3}P_2(\cos\theta) - \frac{m^2}{35r^5}(7m^3 + 40Q)P_4(\cos\theta) + \cdots \tag{3.179}$$

$$\begin{aligned}\gamma_{01} = {} & \frac{m^2}{2r^2}(P_1^2 - P_0^2) + \frac{m}{2r^4}(m^3 + 3Q)(P_1P_3 - P_0P_2) \\ & + \frac{m^2}{6r^6}(m^3 + 3Q)^2(P_3^2 - P_2^2) + \cdots\end{aligned} \tag{3.180}$$

and in the $z = r\cos\theta = 0$ plane then

$$\psi_{01} \approx -\frac{m}{\rho} + \frac{m^3}{6\rho^3}q \tag{3.181}$$

$$\gamma_{01} \approx -\frac{m^2}{2\rho^2} + \frac{m^4}{4\rho^4}q. \tag{3.182}$$

Here q is a dimensionless parameter is given by

$$q = 1 + \frac{3Q}{m^3}. \tag{3.183}$$

As expected if we take $Q = -(\frac{1}{2}m + \frac{1}{3}m^3)$ which equals the value of the quadrupole moment (M_2) for the $n = 0$ solution (see (3.144) with $c = 1$) then the above solutions degenerate to those given by (3.147) and (3.148). This is consistent with substituting this value of Q into (3.177) from which $B_1 = 0$ and thus (3.175) is equal to the $n = 0$ solution (3.141).

*Recall that c has dimension of length. Thus from (3.76) and (3.77) m and Q have correct dimensionality.

†Although not considered, the interesting case when $m = 0$ with higher moments not vanishing is possible.

The exact potential curves determined by (3.175) and (3.139) and the approximate curves derived from (3.181) and (3.140) are illustrated in figure 3.25. The approximate ψ solution fails to replicate the exact solution for small ρ, nevertheless it does agree well with the exact solution for larger values of ρ. We will exploit this fact later to obtain an analytic solution describing bound geodesics. An indication of the domain of validity in using the approximate solution is illustrated in figure 3.23. For given L and Q values the ρ value is plotted for which the approximate and exact potentials (V^2) thereafter differ by no less than 10^{-4}.

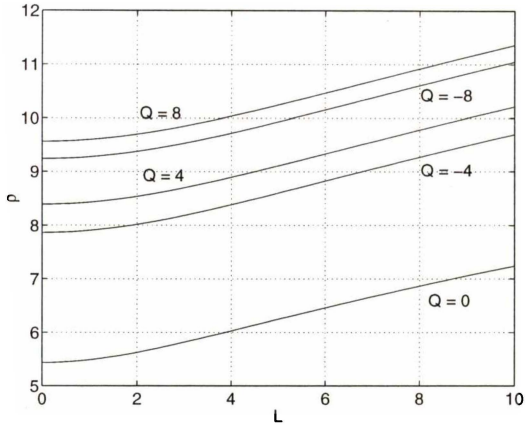

FIGURE 3.23: *The minimum ρ for which $|V^2_{exact} - V^2_{appx}| < 10^{-4}$ ($m = 1$).*

The turning points of the approximate potential $V^2(\rho; L)$ occur at

$$L^2 = \frac{\rho^2(2m\rho^2 - m^3 - 3Q)}{2e^{2\psi}(\rho^3 - 2m\rho^2 + m^3 + 3Q)}. \tag{3.184}$$

If $Q = 0$, the minimum of (3.184) occurs at $\rho \approx 4.9m$ and its value is $L^2_{min} \approx 11.986\, m^2$ (compare with the Schwarzschild values of $L^2_{min} = 12m^2$ at $\rho = 6m$). However, in light of the numerical evidence illustrated in figure 3.25 this is clearly incorrect as the potential has a minimum for all values of L.

Figure 3.24 illustrates how the radii of stable circular orbits, ρ_c, depend on L, Q and m. For fixed L, as Q increases so does ρ_c. The existence of ρ_c for $Q < 0$ depends upon m and L critically as the top two plots clearly demonstrate. The lower plot is of (3.184), the accuracy for ρ/m small is limited. We note for $L = 0$ the curves refer to radii for which the particle is stationary.

The first figure in 3.25 for which $L = 0$ indicates interesting features; the potential obtains a local minimum which indicates firstly that stationary motion and secondly that *oscillatory* motion along the ρ axis *is* possible.

For large $\xi\,(= \cosh\alpha)$, $P_{\frac{1}{2}}(\xi) \sim 2\sqrt{2}\pi^{-1}\xi^{1/2}$, (Olver, 1997) combining with (3.149) as $\rho \to c = 1$ ($\alpha \to \infty$) then the leading terms of (3.175) for large ξ are

$$\begin{aligned} \psi &\sim -(B_0 \ln\xi + 2B_1\xi) \sim -B_1\xi \\ &\sim (3m + 2m^3 + 6Q)\,\xi \end{aligned} \tag{3.185}$$

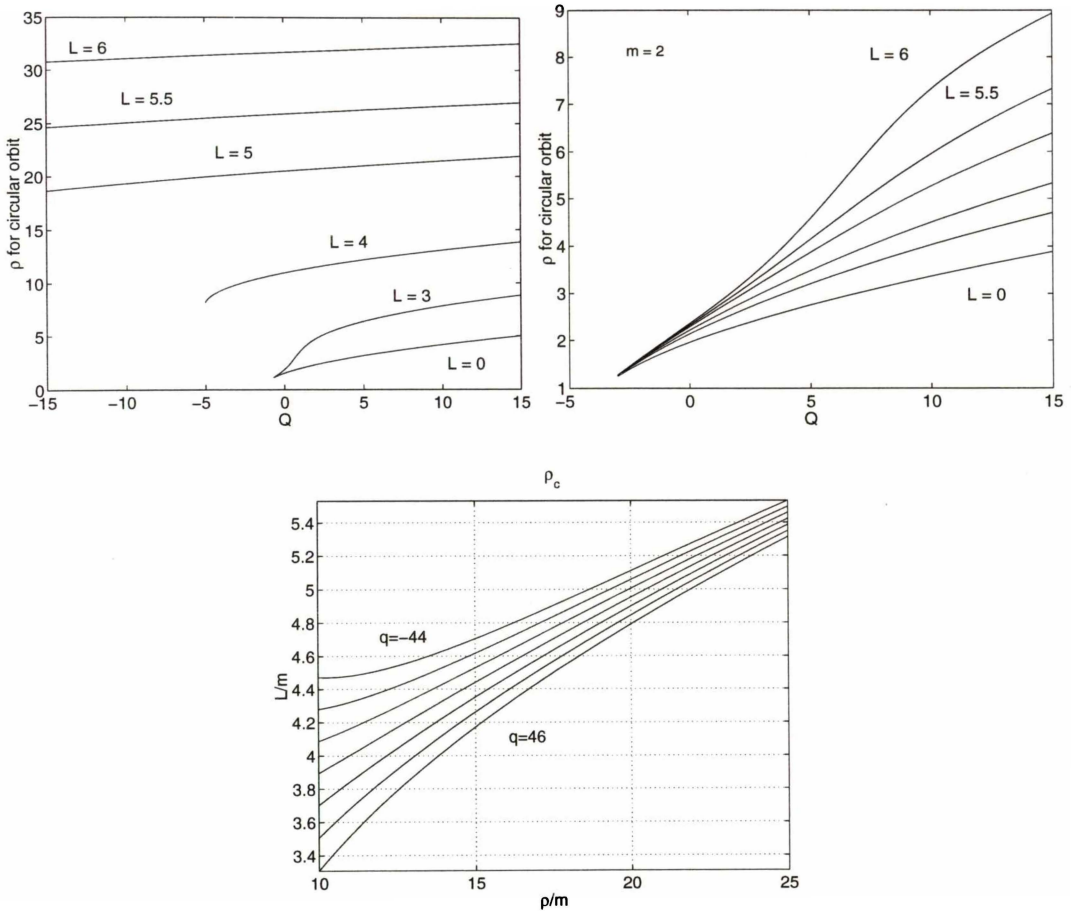

FIGURE 3.24: *The top plots* $(m = 1, 2)$ *plot the minimum locations of the potential* $V^2(\alpha; L)$ *representing the location stable circular orbits. The lower plot is computed from (3.184). Here* $q = -44, -29 \ldots 31, 46$. *For* $m = 1$ *these correspond to* $Q = -15, -10 \ldots 10, 15$ *and we can compare to the first figure.*

thus for fixed $m > 0$, if

$$Q > -\frac{m}{6}(3 + 2m^2) = \Omega \tag{3.186}$$

then the potential, which for large ξ looks like $V^2 \sim e^{4\psi}$, will become unbounded, thus no test particle can 'spiral' into the singular region. Similarly if $Q < \Omega$ then $V^2 \to 0$ as seen in the plots of figure 3.25 (in which $\Omega = -5/6$).

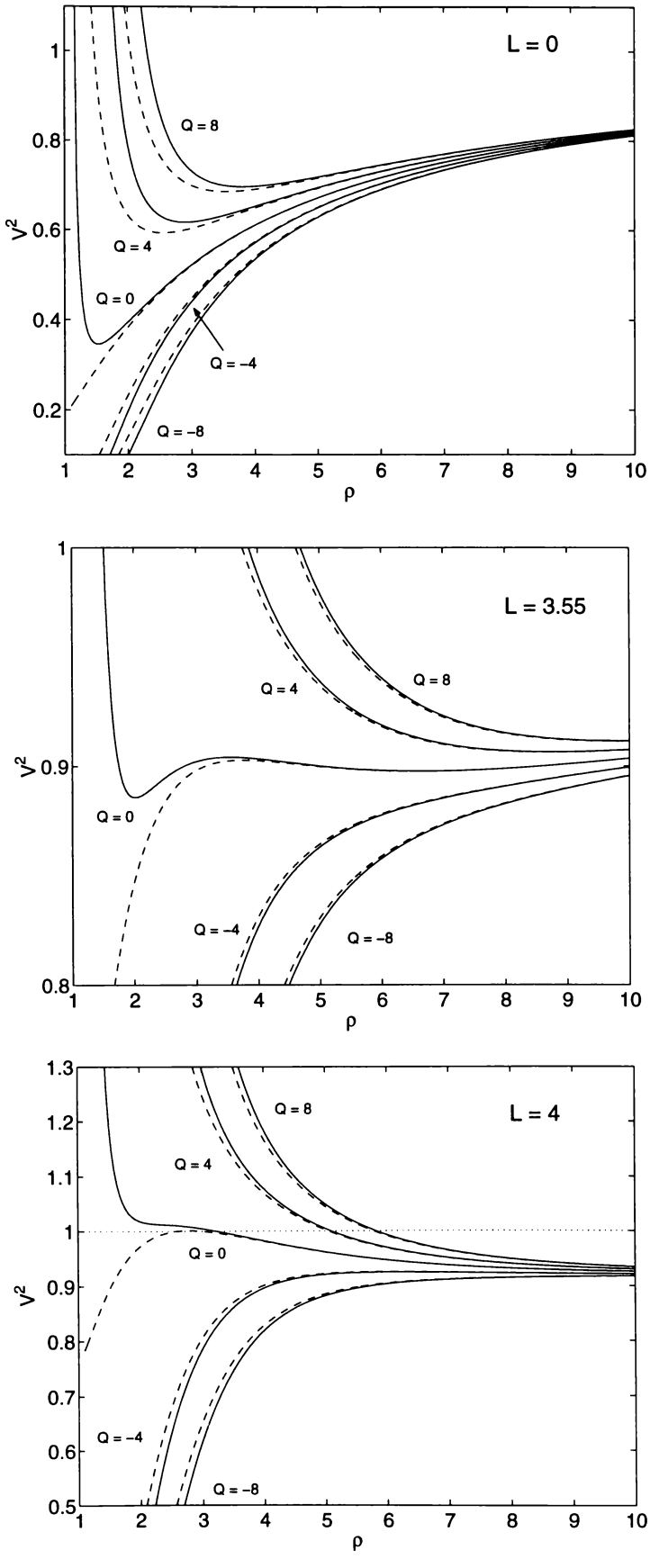

FIGURE 3.25: *Various potential curves and approximations (dashed curve) for fixed L and increasing quadrupole moment Q ($m = 1$). Note in the middle plot for $Q = 0$ there are two local minimum indicating two radii for which stable circular orbits are possible.*

Bound Geodesics

The potential curves illustrated above provide a means to determine the parameters, for example, L and E, for an orbit to be bounded. In particular we examine how the quadrupole moment Q alters the orbit. Such orbits are illustrated in figure 3.26*. It is evident that with increasing Q the perihelion shift decreases. This is also observed in the equatorial timelike geodesics of the Erez-Rosen spacetime (Quevedo, 1990). We also note the the perihelion advance is the same direction as the motion regardless of Q value.

We formulate an approximate solution as done for the $n = 0$ solution. This approximation assumes the motion of the test particle is far from the source. Details are given on page 98. From (3.181) and (3.182) the coefficient A in the cubic (3.161) becomes

$$A = \frac{1}{3}\Lambda^2\left[(1-2E^2)\,q + 44E^2 - 10\right] \tag{3.187}$$

the remaining coefficients are unchanged. Furthermore we have

$$\xi = \frac{3 - 9\Lambda^2(3E^2-1)}{\Lambda^2\left[(1-2E^2)\,q + 44E^2 - 10\right]} \tag{3.188}$$

$$2\mu\xi - \mu^2(3+e^2) = \frac{12(2E^2-1)}{94E^2-23} \tag{3.189}$$

$$\mu^2(1-e^2)(\xi - 2\mu) = \frac{6(1-E^2)}{94E^2-23} \tag{3.190}$$

which relate explicitly the parameters μ and e, which describe the particles trajectory, with the parameters E, Λ, m and q. The assumption of three positive roots of the cubic $F(u)$ has the further requirement dependent upon the quadrupole moment

$$q < (44E^2 - 10)(2E^2 - 1)^{-1}$$

and therefore as $E^2 \to 1$ then $Q < 11m^3$.

The numerical and approximate trajectories (of fixed mass and quadrupole moment) are given in figure 3.27, indicating as L is increased the accuracy of the approximate solution also improves. From the potential plots given earlier, we see as L increases (for fixed E) then in general, the perihelion radii increases and the assumption that the test particle is moving far from the source is more readily met and hence the observed improvement in accuracy of the approximate trajectory solution.

Comparisons of the shift in perihelion computed numerically, from the above elliptic approximation and those based on the relativistic multipole moments of the field due to Fernández-Jambrina and Hoenselaers (2001), are tabulated in figure 3.3 and plotted in figure 3.29. The multipole moment predictions agree well with the numerical shifts and converge quickly as indicated in figure 3.28 with increasing L for all values of Q. All, in particular as Q increases, approximate solutions fail to replicate the shifts (and hence orbits) well.

*These plots are generated by solving (numerically) the toroidal equation of motion (3.137) using (3.175).

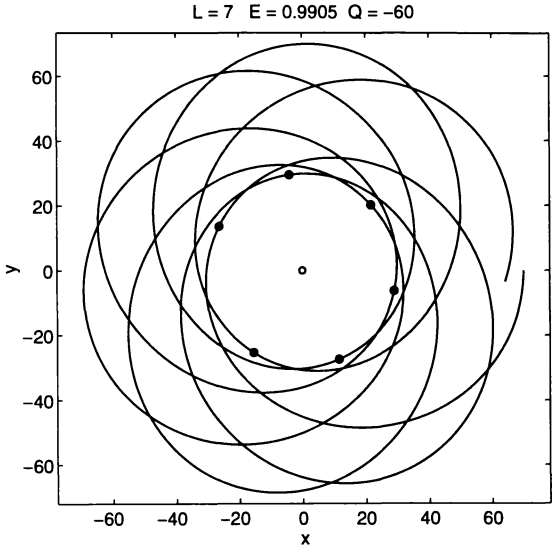

(a) $\Delta\varphi = 0.3301$

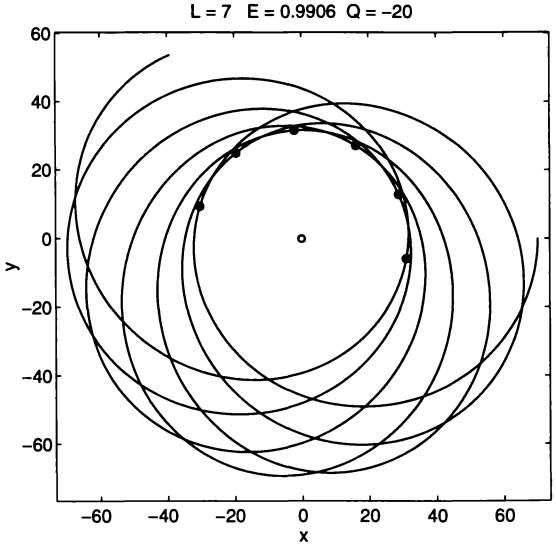

(b) $\Delta\varphi = 0.6042$

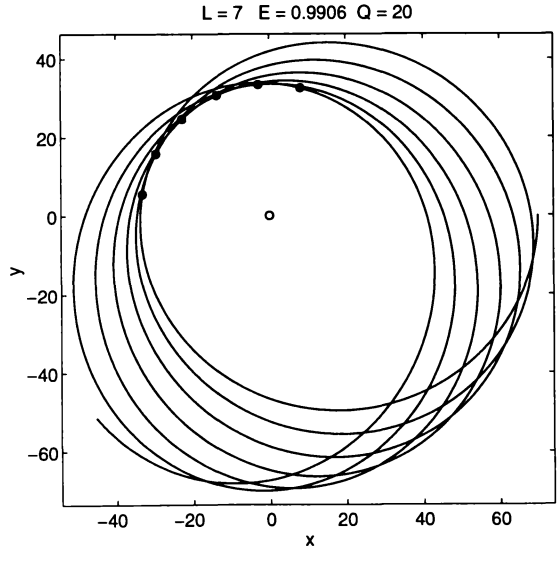

(c) $\Delta\varphi = 0.3301$

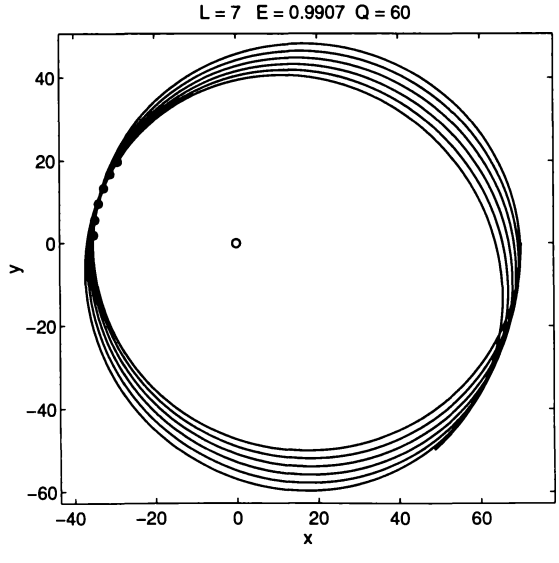

(d) $\Delta\varphi = 0.1083$

FIGURE 3.26: *Timelike geodesics in the equatorial plane of the $n = 0 + 1$ solution (numerical solution of (3.137)). The parameters of the orbit $L = 7$, $\rho_0 = 70$, $m = 1$ remain unchanged in all figures, whereas the quadrupole moment, Q, varies. One sees that the contribution of the quadrupole moment to the perihelion (marked on plots) shift is negative, i.e. with increasing Q the perihelion shift ($\Delta\varphi$) decreases.*

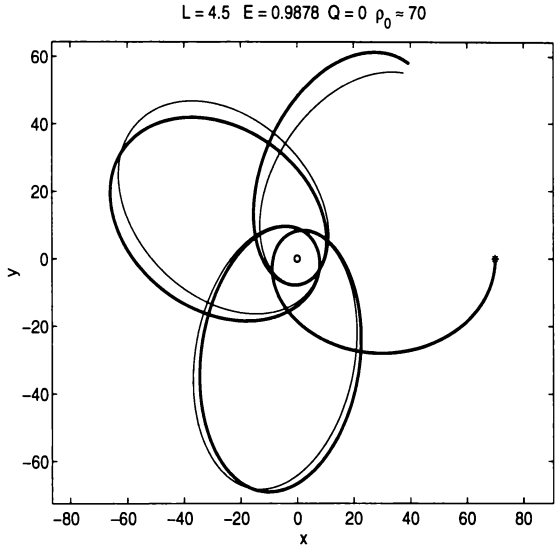

(a) $\xi = 1.3572$, $e = 0.804$, $\mu = 0.0729$, $\rho_{min} = 7.7$

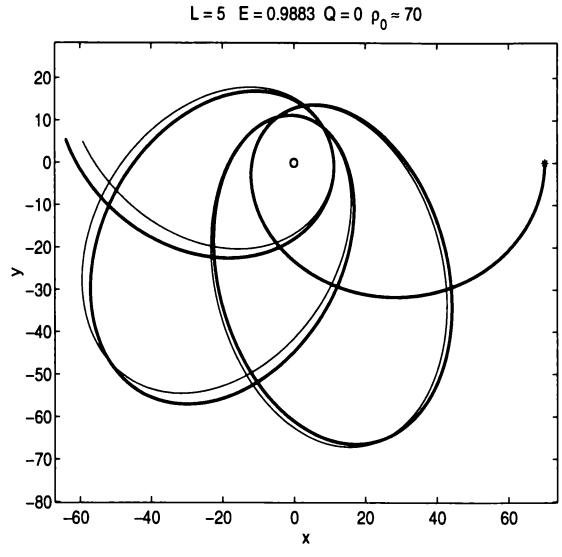

(b) $\xi = 1.7999$, $e = 0.7269$, $\mu = 0.0523$, $\rho_{min} = 11.1$

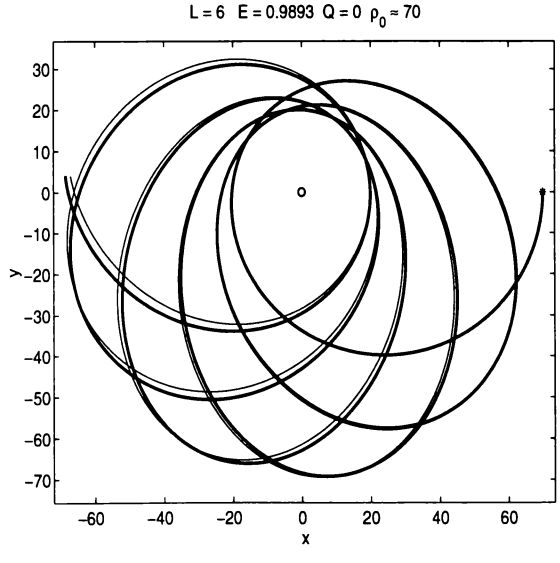

(c) $\xi = 2.8209$, $e = 0.5582$, $\mu = 0.0323$, $\rho_{min} = 19.9$

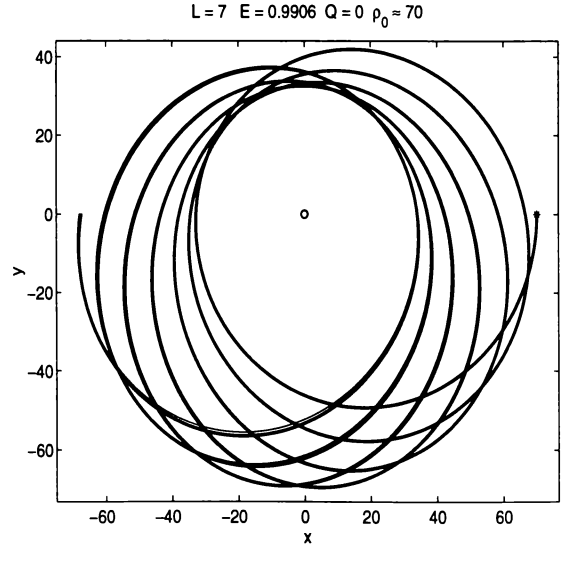

(d) $\xi = 4.0202$, $e = 0.3650$, $\mu = 0.0225$, $\rho_{min} = 32.6$

FIGURE 3.27: *Timelike geodesics in the equatorial plane of the $n = 0 + 1$ toroidal solution. The solid line is the numerical solution of equation (3.137) the thin line the analytic approximation given by (3.172). The quadrupole moment is zero, the mass of the source (the ring in the plots) and radius are both set to 1 in all plots. The figure captions refer to the constants used in (3.172) and ρ_{min} refers to the perihelion value. Compare with figure 3.21.*

	$L = 6$			$L = 7$			$L = 8$		
Q	$\Delta\varphi_E$	$\Delta\varphi_N$	$\Delta\varphi_M$	$\Delta\varphi_E$	$\Delta\varphi_N$	$\Delta\varphi_M$	$\Delta\varphi_E$	$\Delta\varphi_N$	$\Delta\varphi_M$
-5.0000	0.7570	0.7684	0.7622	0.4942	0.4936	0.4929	0.3539	0.3521	0.3520
-4.4737	0.7508	0.7590	0.7535	0.4914	0.4899	0.4893	0.3524	0.3504	0.3502
-3.9474	0.7446	0.7496	0.7447	0.4886	0.4863	0.4857	0.3509	0.3484	0.3484
-3.4211	0.7384	0.7403	0.7360	0.4858	0.4826	0.4821	0.3494	0.3466	0.3466
-2.8947	0.7323	0.7310	0.7274	0.4830	0.4790	0.4786	0.3479	0.3448	0.3448
-2.3684	0.7262	0.7218	0.7187	0.4803	0.4754	0.4750	0.3465	0.3430	0.3430
-1.8421	0.7201	0.7127	0.7101	0.4775	0.4717	0.4714	0.3450	0.3412	0.3412
-1.3158	0.7140	0.7037	0.7016	0.4747	0.4681	0.4679	0.3435	0.3394	0.3394
-0.7895	0.7080	0.6947	0.6931	0.4720	0.4646	0.4643	0.3420	0.3377	0.3376
-0.2632	0.7020	0.6858	0.6846	0.4692	0.4609	0.4608	0.3405	0.3358	0.3358
0.2632	0.6960	0.6770	0.6761	0.4665	0.4573	0.4572	0.3391	0.3341	0.3340
0.7895	0.6901	0.6683	0.6677	0.4638	0.4538	0.4537	0.3376	0.3323	0.3322
1.3158	0.6842	0.6596	0.6593	0.4610	0.4502	0.4502	0.3361	0.3305	0.3305
1.8421	0.6783	0.6510	0.6509	0.4583	0.4467	0.4467	0.3346	0.3286	0.328
2.3684	0.6724	0.6424	0.6426	0.4556	0.4432	0.4432	0.3332	0.3270	0.3269
2.8947	0.6666	0.6339	0.6343	0.4529	0.4396	0.4397	0.3317	0.3252	0.3251
3.4211	0.6608	0.6255	0.6261	0.4502	0.4361	0.4362	0.3302	0.3233	0.3233
3.9474	0.6550	0.6172	0.6178	0.4474	0.4326	0.4327	0.3288	0.3216	0.3213
4.4737	0.6492	0.6088	0.6097	0.4448	0.4291	0.4292	0.3273	0.3197	0.3198
5.0000	0.6435	0.6006	0.6015	0.4421	0.4256	0.4258	0.3258	0.3180	0.3180

TABLE 3.3: *Numerical and theoretical precession rates for the $n = 0 + 1$ solution of varying quadrupole moment Q (in the $z = 0$ plane,$m = 1$). $\Delta\varphi_N$ refers to the numerical perihelion shift (in radians). $\Delta\varphi_M$ is the predicted shift based on the relativistic multipole moments. $\Delta\varphi_E$ is the shift predicted by the elliptic solution (3.174). All trajectories begin at $\rho_0 = 70$ much like those presented in figure 3.26. This table is plotted in figure 3.29.*

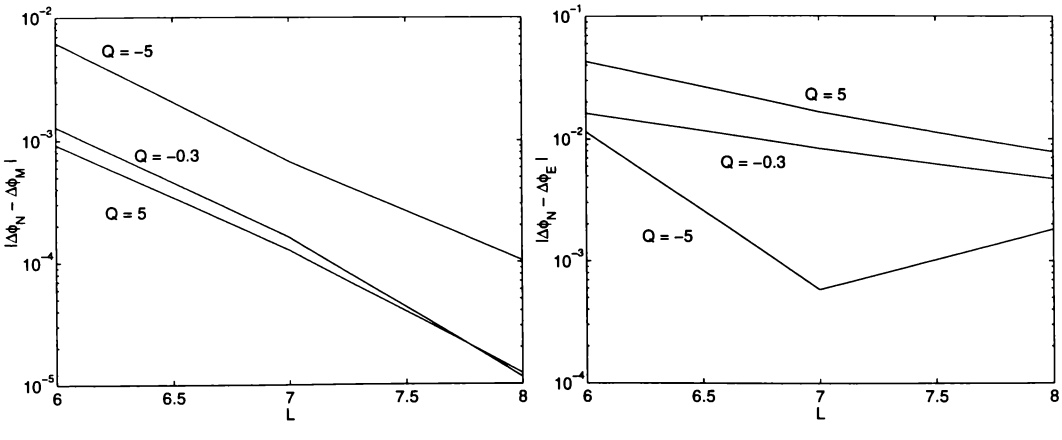

FIGURE 3.28: *The convergence of the predicted shifts $\Delta\varphi_E$ and $\Delta\varphi_E$ to the true precession shift $\Delta\varphi_N$, as L increases.*

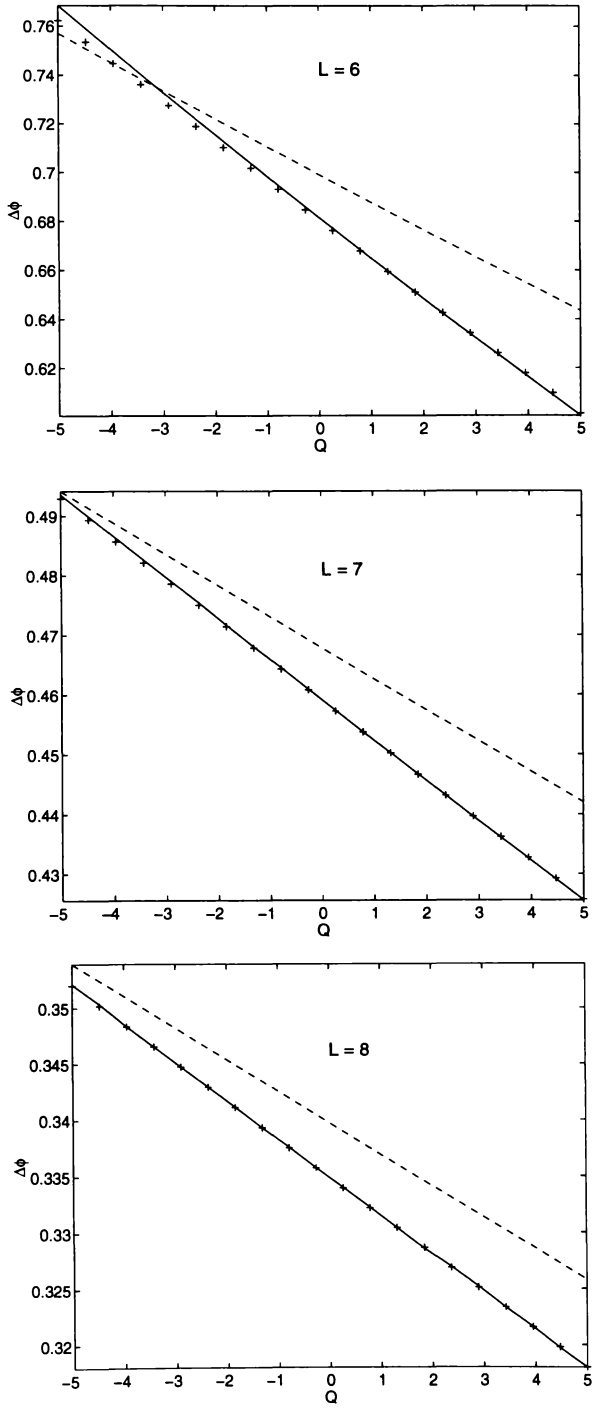

FIGURE 3.29: *Plot of the table 3.3. The dashed curve is $\Delta\varphi_E$ - the precession based on the elliptic approximation. The solid line is the numerical precession $\Delta\varphi_N$ and the markers + indicate the predicted precession based on the multipole moments $\Delta\varphi_M$.*

3.15 Summary

We have constructed various toroidal spacetimes and generated some timelike geodesics associated with them.

Given a toroidal harmonic function ψ, it is possible to determine the multipole structure of the spacetime and, as we have done here, select parameters to specify specific multipole moment characteristics. From the multipole structure it is then possible to expand the toroidal solutions in terms of spherical coordinates which are used in subsequent calculations to develop approximate potentials and equations describing the trajectories of test particles.

The greatest difficulty in constructing specific spacetimes was the formulation of the metric function γ. The calculation of γ lead to the integration of toroidal functions squared. We have shown a general method to evaluate such integrals, and in doing so were able to produce the $n = 1$, $n = 0 + 1$ and $n = 0 + 2$ γ functions. Numerical verification of the $n = 0 + 2$ solution was provided to give assurances of the methods used in the upcoming chapter.

The timelike geodesics of zero angular momentum resulted in many interesting results. For the $n = 0$ and $n = 1$ fields, observation of the test particle period of oscillation, along the z axis, increasing as the mass of the source increased, was perplexing. An explanation for this is still required, in particular for the more physically viable ring solution. The analysis of the Kretschmann scalar did indicate some insight but did not predict accurately the change from the counter-intuitive relativistic periods of motion to the Newtonian dependence upon the sources mass, i.e. decrease in period as the mass increases.

The elliptic approximations to the bounded timelike geodesics in general provide an adequate approximation to the orbit. In particular for the $n = 0 + 1$ solution where it was possible to alter the mass and quadrupole moments of the source, it was evident that not only for small angular momentum values (resulting in small perihelion radii) but additionally for increasing quadrupole moment this approximation become less reliable. This was evident in the comparison of perihelion shifts. As the angular momentum of the test particle is increased the numerical and predicted (via multipole moments) perihelion shift values agreed very well, where as those determined by the approximate solution, were less accurate.

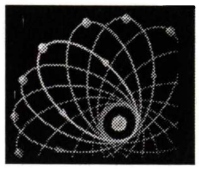

Chapter 4
Bicyclide Coordinates

4.1 Introduction

This chapter investigates the Weyl metric formulated in bicyclide* coordinates.

Contrary to earlier coordinate systems employed, this chapter is heavily reliant on numerical calculations not only to solve the orbit equations, but to generate the metric itself. This is primarily due to the inability to solve analytically the separated differential equations related to Laplace's equation, which is the cornerstone of any Weyl solution. Ultimately this separation, coupled with the necessary boundary conditions leads to the evaluation of *Lamé-Wangerin* functions. A major portion of this chapter is devoted to the calculation of such functions, their approximations and the subsequent numerical calculation of the metric function γ.

We begin by summarizing the work by Wangerin (Erdélyi *et al.* (1955a), Wangerin (1875)) who determined the most general systems of orthogonal curvilinear coordinates in which Laplace's equation is separable. By choosing an appropriate conformal transformation we obtain the two separable equations to be solved. One is solved analytically via a power series in elliptic functions, the remaining function is solved numerically.

We then proceed and calculate γ and show to satisfy the required boundary conditions a superposition of particular solutions is required.

Given this we calculate the multipole moments (relativistic and classical derivations) of certain two term solutions and then produce timelike geodesics pertaining to the space-time generated by these solutions.

*Also known as confocal bicircular quartics.

4.2 General Separation

In cylindrical coordinates (ρ, z, φ) Laplace's equation is

$$\frac{\partial^2\psi}{\partial\rho^2} + \frac{1}{\rho}\frac{\partial\psi}{\partial\rho} + \frac{\partial^2\psi^2}{\partial z^2} + \frac{1}{\rho^2}\frac{\partial^2\psi}{\partial\varphi^2} = 0. \tag{4.1}$$

Wangerin* determined, by letting $z = z(u, v)$ and $\rho = \rho(u, v)$, the most general systems of orthogonal curvilinear coordinates u, v for which (4.1) permits R-separable solutions of the form

$$\psi = R(u, v)U(u)V(v)\Phi(\varphi). \tag{4.2}$$

Here $R(u, v)$ is a fixed function and U, V and Φ are solutions of ordinary differential equations. Wangerin was to prove that solutions of this form require $R(u, v) = \rho^{-1/2}$ and the coordinates (u, v) may be taken so that the mapping of the (z, ρ) plane in the (u, v) plane is conformal. Thus there exists an analytic function f such that $z+i\rho = f(u+iv)$. Furthermore by assuming a solution of the form

$$\psi(u, v, \varphi) = \frac{1}{\sqrt{\rho}}\xi(u, v)e^{\pm im\varphi} \tag{4.3}$$

and inserting into (4.1) we obtain

$$\frac{\partial^2\xi}{\partial u^2} + \frac{\partial^2\xi}{\partial v^2} - (m^2 - \tfrac{1}{4})F(u, v)\,\xi = 0 \tag{4.4}$$

where

$$F(u, v) = \frac{|f'(u + iv)|^2}{[\mathbf{Im}f(u + iv)]^2} = \frac{|f'|^2}{\rho^2}. \tag{4.5}$$

Consequently to permit separable solutions $F(u, v)$ must be of the form

$$F(u, v) = F_1(u) + F_2(v) \tag{4.6}$$

and this occurs if and only if f is a solution of the ordinary differential equation

$$(f')^2 = a_0 + a_1 f + a_2 f^2 + a_3 f^3 + a_4 f^4 = P_4(f) \tag{4.7}$$

in which the a_i are real constants. We see that f is either an elementary or elliptic function. Assuming that P_4 has four distinct zeros, three cases arise for f, characterized by the type of zeros: four real, four complex, or two real and two complex. The standard forms of f for the three cases are the Jacobian elliptic functions,

1. $\mathrm{sn}(u + iv, k)$ corresponding to four real foci on the axis of rotation.
2. $i\,\mathrm{sn}(u + iv, k)$ no real foci on the axis.
3. $\mathrm{cn}(u + iv, k)$ two real foci on the axis.

This chapter concentrates on the *first case* for the form of f. In general if f satisfies (4.7), U and V satisfy the ordinary differential equations

$$\frac{d^2U}{du^2} + [\,h - (m^2 - \tfrac{1}{4})F_1(u)\,]U = 0 \tag{4.8}$$

$$\frac{d^2V}{dv^2} - [\,h - (m^2 - \tfrac{1}{4})F_2(v)\,]V = 0. \tag{4.9}$$

*Erdélyi *et al.* indicates, these results where repeated by Snow (1952) and Lagrange (1939), (1944).

4.3 Jacobi Elliptic Functions

It would be prudent at this point to present a summary of useful properties of the Jacobi elliptic functions. Further details are readily available from many sources, for example Abramowitz and Stegun (1965) and Erdélyi *et al.* (1955b).

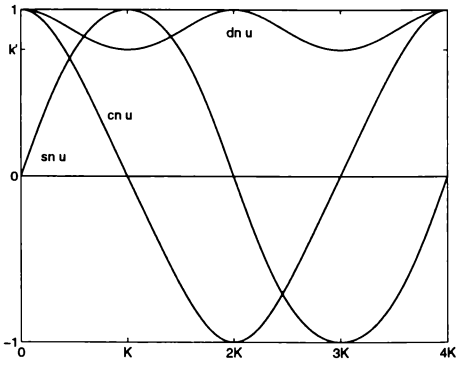

FIGURE 4.1: Jacobian elliptic functions.

Elliptic functions are inversions of elliptic integrals. The three basic functions are denoted $\mathrm{cn}(u,k)$, $\mathrm{sn}(u,k)$ and $\mathrm{dn}(u,k)$. k is known as the modulus, the complementary modulus, k', is related by $k^2+k'^2=1$. Often the k argument is suppressed for brevity, for example $\mathrm{sn}(u,k)$ can be written $\mathrm{sn}\,u$.

We have

$$\mathrm{sn}^2u+\mathrm{cn}^2u=1,\qquad k^2\,\mathrm{sn}^2u+\mathrm{dn}^2u=1,\qquad k^2\,\mathrm{cn}^2u+k'^2=\mathrm{dn}^2u \tag{4.10}$$

and in particular

$$\mathrm{sn}(u+i\mathbf{K}')=\frac{1}{k\,\mathrm{sn}u}\equiv\frac{1}{k}\,\mathrm{ns}\,u \tag{4.11}$$

where $\mathbf{K}(k)$, the quarter-period, is the complete elliptic integral of the first kind, $\mathbf{K}'(k)\equiv\mathbf{K}(k')$. The standard Jacobi elliptic functions all have singularities at the points

$$u=2m\mathbf{K}+i(2n+1)\mathbf{K}'\quad n,m\in\mathrm{I} \tag{4.12}$$

and as $u\to 0$ we have

$$\mathrm{sn}\,u = u-\tfrac{1}{3!}(1+k^2)u^3+O(u^5) \tag{4.13}$$

$$\mathrm{cn}\,u = 1-\tfrac{1}{2!}u^2+O(u^4) \tag{4.14}$$

$$\mathrm{dn}\,u = 1-\tfrac{1}{2!}k^2u^2+O(u^4). \tag{4.15}$$

Ratios of these functions are denoted by combining the first letter of the numerator function with the first of the denominator function, thus $\mathrm{sn}u/\mathrm{cn}u\equiv\mathrm{sc}u$, $\mathrm{cn}u/\mathrm{dn}u\equiv\mathrm{cd}u$ etc. The notation, for example $1/\mathrm{cn}u\equiv\mathrm{nc}u$ is also employed (also see (4.11)).

4.4 Bicyclide Coordinates

As mentioned in section 4.2 we will limit our analysis to the case when we introduce new coordinates (u,v) via the conformal transformation

$$z+i\rho=f(u+iv)=\mathrm{sn}(u+iv,k)\,. \tag{4.16}$$

This conformal mapping is analyzed in Erdélyi *et al.* (1955b) and Bowman (1953). The second case, when $f(u+iv)=i\,\mathrm{sn}(u+iv,k)$, which can be used to calculate the harmonics

of a flat ring has been discussed by Poole (1929, 1930). The three transformations presented above correspond, respectively to the three cyclide-coordinates presented in Moon and Spencer (1988).

From (4.16) Laplace's equation (4.1) becomes

$$\nabla^2\psi = \frac{\Upsilon^3}{\Omega^2\,\mathrm{cn}u\,\mathrm{dn}u\,\mathrm{sn}v\,\mathrm{cn}v}\left\{\mathrm{sn}v\,\mathrm{cn}v\,\frac{\partial}{\partial u}\left[\frac{\mathrm{cn}u\,\mathrm{dn}u}{\Upsilon}\frac{\partial\psi}{\partial u}\right]+\right.$$
$$\left.\mathrm{cn}u\,\mathrm{dn}u\,\frac{\partial}{\partial v}\left[\frac{\mathrm{sn}v\,\mathrm{cn}v}{\Upsilon}\frac{\partial\psi}{\partial v}\right]\right\}+\frac{\Upsilon^2}{\mathrm{cn}^2u\,\mathrm{dn}^2u\,\mathrm{sn}^2v\,\mathrm{cn}^2v}\frac{\partial^2\psi}{\partial\varphi^2}=0 \qquad (4.17)$$

where $\Upsilon = 1-\mathrm{dn}^2u\,\mathrm{sn}^2v$ and $\Omega^2 = (1-\mathrm{sn}^2u\,\mathrm{dn}^2v\,)(\mathrm{dn}^2v\,-k^2\mathrm{sn}^2u\,)$.

We are interested in solutions that are axially symmetric, thus ψ is independent of φ implying that in (4.3) we set $m=0$. Accordingly (4.17) reduces to

$$\mathrm{sn}v\,\mathrm{cn}v\,\frac{\partial}{\partial u}\left[\frac{\mathrm{cn}u\,\mathrm{dn}u}{\Upsilon}\frac{\partial\psi}{\partial u}\right]+\mathrm{cn}u\,\mathrm{dn}u\,\frac{\partial}{\partial v}\left[\frac{\mathrm{sn}v\,\mathrm{cn}v}{\Upsilon}\frac{\partial\psi}{\partial v}\right]=0 \qquad (4.18)$$

and from (4.5) and (4.16) we have

$$F_1(u)+F_2(v) = -\left\{(1-k)\,\mathrm{sn}\left[i(1+k)u,\frac{1-k}{1+k}\right]\right\}^2 \qquad (4.19)$$
$$+\left\{(1-k)\,\mathrm{sn}\left[(1+k)(v-i\mathbf{K}),\frac{1-k}{1+k}\right]\right\}^2 \qquad (4.20)$$

which leads to the separated ordinary differential equations corresponding to (4.18)

$$U'' - (1+k)^2\left[h+\tfrac{1}{4}\left\{\frac{1-k}{1+k}\,\mathrm{sn}\left(i(1+k)u,\frac{1-k}{1+k}\right)\right\}^2\right]U=0 \qquad (4.21)$$

$$V'' + (1+k)^2\left[h+\tfrac{1}{4}\left\{\frac{1-k}{1+k}\,\mathrm{sn}\left((1+k)(v-i\mathbf{K}),\frac{1-k}{1+k}\right)\right\}^2\right]V=0. \qquad (4.22)$$

It is advantageous (Erdélyi *et al.*, 1955a) to transform the equations for F_1 and F_2 containing the modulus

$$\frac{1-k}{1+k}=\dot{k} \qquad (4.23)$$

to that of the standard modulus k. This can be achieved by using the curvilinear coordinates u, v introduced by the conformal mapping*

$$z+i\rho = i\,a\frac{k'\mathrm{sn}(u+iv,k)}{\mathrm{cn}(u+iv,k)\,+\mathrm{dn}(u+iv,k)} = i\,a\frac{\mathrm{dn}(u+iv,k)\,-\mathrm{cn}(u+iv,k)}{k'\mathrm{sn}(u+iv,k)} \qquad (4.24)$$

where the foci of the confocal system

$$\rho=0,\quad z=\pm a\sqrt{\dot{k}},\ \pm a\sqrt{1/\dot{k}}$$

*This new transformation is more evident by comparison with *Landen's transformation*,

$$\mathrm{sn}(u,k) = -\frac{2i}{1+k}\frac{\mathrm{sn}(\dot{u},\dot{k})}{\mathrm{cn}(\dot{u},\dot{k})\,+\mathrm{dn}(\dot{u},\dot{k})},\qquad \dot{u}=i(1+k)u.$$

determine the constant $a > 0$ and the value of the modulus $0 < k < 1$. This transformation maps the rectangle with vertices (the four foci) $(0 \pm i\mathbf{K}', 2\mathbf{K} \pm i\mathbf{K}')$ in the (u, v) plane on the half-plane $\rho > 0$.

Figure 4.2 illustrates some important features of the transformation (4.24). Corresponding points are denoted by the same letter.

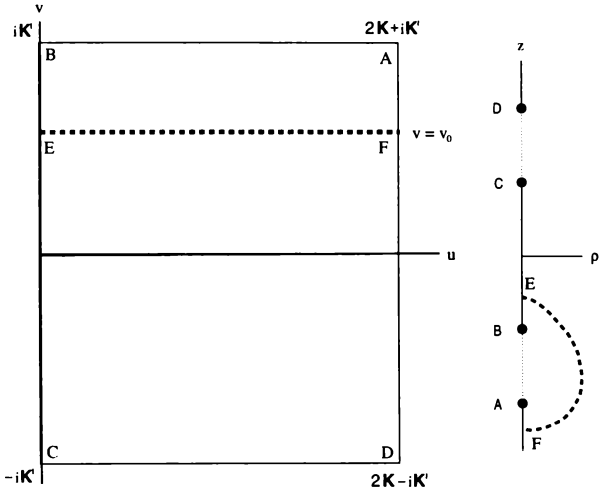

FIGURE 4.2: *The mapping (4.24). Adapted from Erdélyi et al. (1955a).*

The real form of the transformation (4.24) is

$$\rho = \frac{ak' \operatorname{sn}(u,k) \operatorname{cn}(v,k')}{\operatorname{cn}(u,k) \operatorname{dn}(v,k') + \operatorname{dn}(u,k)} \tag{4.25}$$

$$z = \frac{-ak' \operatorname{sn}(v,k')}{\operatorname{cn}(u,k) \operatorname{dn}(v,k') + \operatorname{dn}(u,k)} \tag{4.26}$$

where

$$u \in [0, 2\mathbf{K}] \quad \text{and} \quad v \in [-\mathbf{K}', \mathbf{K}']. \tag{4.27}$$

The z-axis divides into five regions, summarized in the table below. The origin corresponds to $u = v = 0$ and $r = \sqrt{\rho^2 + z^2} \to \infty$ as $u \to 2\mathbf{K}$ and $v \to 0$. The ρ plane is specified by setting $v = 0$, and $\rho \to \infty$ as $u \to 2\mathbf{K}$.

Region	u	v
$-\infty < z < A$	$2\mathbf{K}$	$(0, \mathbf{K}')$
$A < z < B$	$(0, 2\mathbf{K})$	$\mathbf{K}'$
$B < z < C$	0	$(-\mathbf{K}', \mathbf{K}')$
$C < z < D$	$(0, 2\mathbf{K})$	$-\mathbf{K}'$
$D < z < \infty$	$2\mathbf{K}$	$(-\mathbf{K}', 0)$

TABLE 4.1: *The five regions on the z axis. Refer to figure 4.2 for labels.*

4.5 Metric

From (4.25) and (4.26) the Weyl metric becomes

$$ds^2 = e^{2\psi}dt^2 - \frac{a^2k'^2\,e^{-2\psi}}{(\mathrm{cn}u\,\mathrm{dn}v\,+\mathrm{dn}u)^2}\left[e^{2\gamma}(1-\mathrm{dn}^2u\,\mathrm{sn}^2v\,)(du^2+dv^2)+\mathrm{sn}^2u\,\mathrm{cn}^2v\,d\varphi^2\right]. \quad (4.28)$$

The domains of u and v are given by (4.27). To complete the determination of the metric the functions $\psi(u,v)$ and $\gamma(u,v)$ are required.

4.6 Calculating ψ

The metric term ψ is a harmonic function of the form

$$\psi = \rho^{-1/2}U(u)V(v) = \left(\frac{\mathrm{cn}u\,\mathrm{dn}v\,+\mathrm{dn}u}{\mathrm{sn}u\,\mathrm{cn}v}\right)^{\frac{1}{2}}U(u)\,V(v). \quad (4.29)$$

From equations (4.25) and (4.26), we calculate

$$\begin{aligned} F(u,v) &= \frac{|f'|^2}{\rho^2} = \frac{1}{\mathrm{sn}^2(u,k)} - k^2\mathrm{sn}^2(iv,k) \\ &= [\,k\,\mathrm{sn}(u+i\mathbf{K}',k)\,]^2 - [\,k\,\mathrm{sn}(iv,k)\,]^2 \end{aligned} \quad (4.30)$$

from which the ordinary differential equations (4.8) and (4.9) for U and V become

$$U'' + \left[h + \tfrac{1}{4}k^2\,\mathrm{sn}^2(u+i\mathbf{K}',k)\right]U = 0 \quad (4.31)$$

$$V'' - \left[h + \tfrac{1}{4}k^2\,\mathrm{sn}^2(iv,k)\right]V = 0. \quad (4.32)$$

In general we will seek solutions that are finite for constant u or v. This requires both (4.31) and (4.32) to be finite at their respective endpoints. Additionally ψ must be asymptotically flat as $r \to \infty$, or equivalently as $u \to 2\mathbf{K}$, $v \to \pm 0$.

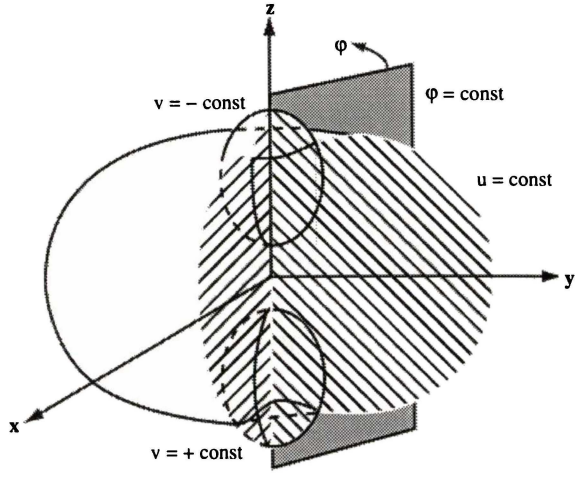

FIGURE 4.3: *Coordinates surfaces generated by (4.16). They are similar to bispherical coordinates, but with 4th degree surfaces instead of 2nd degree.*

4.6.1 Lamé-Equation

Clearly we require solutions to equations (4.31) and (4.32), both are of the form

$$\frac{d^2\Lambda}{d\zeta^2} + \left\{h - n(n+1)\left[k\,\mathrm{sn}(\zeta,k)\right]^2\right\}\Lambda = 0 \tag{4.33}$$

which is called the *Jacobian form of Lamé's equation* or simply *Lamé's equation.* Here ζ is in general a complex variable, h a parameter, characteristic values of which are determined either by a periodicity requirement or by a finiteness condition. The variables n and k, are both typically real (one exception is generated by the conformal transformation, case 3, from section 4.2, which results in the modulus k in (4.33) being complex).

Lamé's equation has been investigated since the nineteenth century and the results of these investigation are scattered in many distant branches of mathematical physics. Both Erdélyi *et al.* (1955a) and Arscott (1964) however provide comprehensive works that consolidate the major results regarding these equations.

For example, when $n = \frac{1}{2}$ and $h = \frac{1}{4}(1 + k^2)$, Lamé's equation has solutions

$$\Lambda(\zeta) = (\mathrm{dn}\,\zeta \pm \mathrm{cn}\,\zeta)^{1/2}.$$

For integral n and all h, Lamé's equation has either one solution whose square is a polynomial of degree n in $\mathrm{sn}^2\zeta$, or two solutions whose product is such a polynomial (Whittaker and Watson, 1940). Contemporary solutions can be found, for example, in Khare and Sukhatme (1999) and Ritter (1998), both of which present new solutions for n integral and positive half-integral values.

However, suffice to say, for our problem for which (refer to (4.31))

$$n = -\frac{1}{2} \tag{4.34}$$

forms an auspicious void in the knowledge regarding Lamé functions - comparatively little is known about the solutions for this value of n. This chapter thus goes some way in filling this void.

4.6.2 Boundary Conditions

Given that $u \in [0, 2\mathbf{K}]$ and $v \in [-\mathbf{K}', \mathbf{K}']$ and from (4.12) we see that (4.30)

$$F(u,v) = \left[k\,\mathrm{sn}(u + i\mathbf{K}', k)\right]^2 - \left[k\,\mathrm{sn}(iv, k)\right]^2$$

becomes infinite for $u = 0, 2\mathbf{K}$ or for $v = \pm\mathbf{K}'$. Thus the end-points of the intervals of u and v correspond to singular points of the ordinary differential equations for U and V, given by (4.31) and (4.32). Therefore in general we require harmonic functions that are finite at two singularities of Lamé's equation. Erdélyi *et al.* (1955a) refers to such solutions as *Lamé-Wangerin* functions. Importantly, solutions exist for only certain characteristic values of h.

Let $F_n^r(\zeta, k^2)$ denote a Lamé-Wangerin function (Erdélyi *et al.*) for which $\sqrt{\mathrm{sn}\,\zeta}\, F_n^r(\zeta, k^2)$ is bounded, and has r zeros in the open interval $(i\mathbf{K}', 2\mathbf{K} + i\mathbf{K}')$. Furthermore, if $F(\zeta)$ is a Lamé-Wangerin function, so are the functions

$$F(2\mathbf{K} + 2i\mathbf{K}' - \zeta) \quad \text{and} \quad F(\zeta) \pm F(2\mathbf{K} + 2i\mathbf{K}' - \zeta)$$

and the analysis may be restricted to the investigation of Lamé-Wangerin functions which are even or odd functions of $\zeta - \mathbf{K} - i\mathbf{K}'$. Accordingly if $F_n^r(\zeta, k^2)$ is such a function it will be an even or odd function of $\zeta - \mathbf{K} - i\mathbf{K}'$ if r is even or odd. Therefore solutions of (4.33), for which

$$(\mathrm{sn}\,\zeta)^{1/2}\Lambda(\zeta) \quad \text{are bounded at} \quad \zeta = i\mathbf{K}' \tag{4.35}$$

also satisfy one of the following boundary conditions

$$\Lambda'(\mathbf{K} + i\mathbf{K}') = 0 \qquad r \text{ even} \tag{4.36}$$

$$\Lambda(\mathbf{K} + i\mathbf{K}') = 0 \qquad r \text{ odd.} \tag{4.37}$$

McCrea and Newing (1933) showed, using singular Sturm-Liouville theory, that for each $r = 0, 1, \ldots$ there is *one* Lamé-Wangerin function, and the eigenvalue, h, belonging to these functions form an increasing unbounded sequence. Furthermore if $0 < k < 1$ and $n \geq -1/2$ in (4.33) then h is also real.

4.6.3 U Solutions

We now endeavor to solve the first Lamé equation

$$U'' + \left[h + \tfrac{1}{4}k^2\,\mathrm{sn}^2(u + i\mathbf{K}', k)\right] U = 0, \qquad 0 \leq u \leq 2\mathbf{K} \tag{4.38}$$

or equivalently from (4.30) or (4.11)

$$U'' + \left[h + \frac{1}{4\,\mathrm{sn}^2(u, k)}\right] U = 0. \tag{4.39}$$

The boundary condition (4.35) is now restated as

$$(\mathrm{sn}\,u)^{-1/2}\,U(u) \quad \text{is bounded at} \quad u = 0. \tag{4.40}$$

Paramount in the determination of these solutions is the accurate evaluation of the eigenvalue h. This is accomplished by various means. We will begin our discussion on evaluating U by providing an approximate solution.

4.6.4 Bessel Approximations

Let us begin by constructing a solution for which the first boundary condition (4.40) is met. For small u and from (4.13) we can approximate (4.39) by

$$U'' + \left(h + \tfrac{1}{12}(1 + k^2) + \tfrac{1}{4}\,u^{-2}\right) U = 0 \tag{4.41}$$

which permits the general solution

$$U(u) = c_1 \sqrt{u}\, J_0(Hu) + c_2 \sqrt{u}\, Y_0(Hu) \tag{4.42}$$

here c_1 and c_2 are constants, J_0 and Y_0 are the Bessel and Neumann functions of order zero respectively and

$$H = \sqrt{h + \tfrac{1}{12}(1 + k^2)}. \tag{4.43}$$

For simplicity let us discard the Y_0 solution and normalize the remaining term by choosing c_1 so that the absolute global maximum is unity. Thus our inner solution (in reference to the expansion near the origin) satisfying the boundary condition (4.35) is

$$U_i = c_1 \sqrt{u}\, J_0(Hu). \tag{4.44}$$

Now let us in turn, consider the remaining boundary conditions (4.36) and (4.37).

Let $x = u - \mathbf{K}$. Given $\mathrm{sn}(x + \mathbf{K}) = \mathrm{cd}(x)$, we have from (4.14, 4.15) for $x \approx 0$

$$\mathrm{sn}(x + \mathbf{K}) \approx 1 + \tfrac{1}{2}(k^2 - 1)x^2 + \cdots$$

and near $x = 0$ (4.39) becomes

$$U''(x) + \left(h + \tfrac{1}{4}(1 + (1 - k^2)x^2 \right)) U(x) = 0. \tag{4.45}$$

The outer solution has the general form

$$U_o(u) = c_3 \cos(A(u - \mathbf{K}) + \beta_1) \tag{4.46}$$

here c_3, β_1 and $A = \sqrt{h + \frac{1}{4}}$ are constants. For even (+) solutions we require $U_o'(\mathbf{K}) = 0$, and for odd (-) solutions $U_o(\mathbf{K}) = 0$ thus from (4.46) we obtain (we set $c_3 = 1$)

$$U_o^+(u) = \cos(A(u - \mathbf{K}) + n\pi) \tag{4.47}$$

$$U_o^-(u) = \cos(A(u - \mathbf{K}) + n\pi + \tfrac{\pi}{2}). \tag{4.48}$$

Let us assume that h is large. Clearly $H \sim A \sim \sqrt{h}$, and from the asymptotic behaviour of J_0 (Abramowitz and Stegun, 1965) we see that (4.44) behaves like

$$U_i \sim \cos(\sqrt{h}\, u - \tfrac{1}{4}\pi). \tag{4.49}$$

Thus in some region of overlap we have $U_i \sim U_o^{\pm}$ hence

$$\cos(\sqrt{h}\, u - \tfrac{1}{4}\pi) \sim \begin{cases} \cos(\sqrt{h}(u - \mathbf{K}) + n\pi) & \text{(Even)} \\ \cos(\sqrt{h}(u - \mathbf{K}) + n\pi + \frac{\pi}{2}) & \text{(Odd).} \end{cases} \tag{4.50}$$

Matching these arguments we obtain the quantization conditions for h,

$$\mathbf{K}(k)\sqrt{h} = (n + \tfrac{1}{4})\pi \qquad \text{(Even)} \tag{4.51}$$

$$\mathbf{K}(k)\sqrt{h} = (n + \tfrac{3}{4})\pi \qquad \text{(Odd).} \tag{4.52}$$

Solutions with h values generated for the even $n = 1$ quantization (4.51) are illustrated in figures 4.4(a) and 4.4(b). Here we plot the inner Bessel solution (4.44) and the outer cosine solution (4.47). It is observed as $k \to 1\,(\mathbf{K} \to \infty)$, h decreases and the region of overlap of these solutions (in particular about $\mathbf{K}$) reduces. This is anticipated as the analysis assumes that h is large*. Figures 4.4(c) and 4.4(d) represent solutions with perturbed h values. Both plots demonstrate the importance of using relations (4.51) and (4.52) to determine h. Similar results hold for odd solutions.

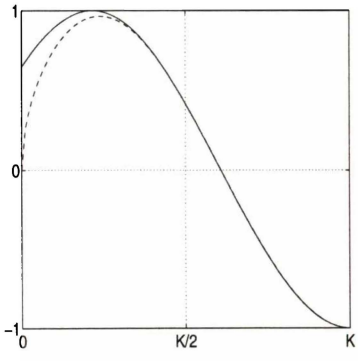

(a) $k = 0.1$, $h = 6.22$, $\mathbf{K} = 1.57$

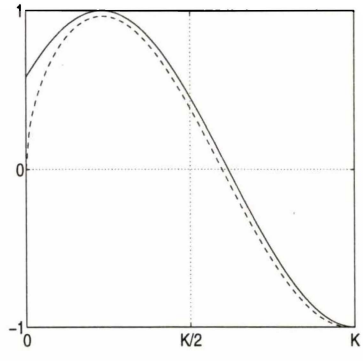

(b) $k = 0.9$, $h = 2.97$, $\mathbf{K} = 2.28$

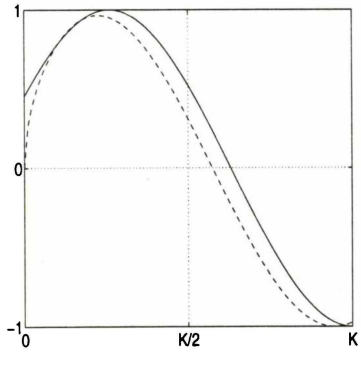

(c) $k = 0.1$, $h = 7.0$

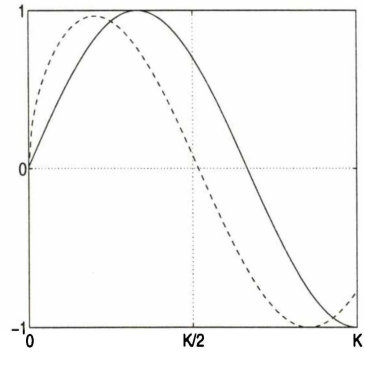

(d) $k = 0.9$, $h = 4.0$

FIGURE 4.4: *Regions of overlap. Dashed line (- -) represent the (normalized) inner Bessel solution (4.44). Solid line is the outer solution (4.47).*

The solution (4.44), sufficiently normalized (c_1) and the parameter H calculated appropriately (h large), will satisfy the prescribed boundary conditions and represent an approximate solution of (4.39) applicable throughout the complete interval $0 \leq u \leq 2\mathbf{K}$.

Values of $h = h(k)$ calculated by equations (4.51) and (4.52) are shown in table 4.2.

We will introduce the following notation that will be applied throughout the remainder of this chapter. The eigenvalues h_m will refer to the number of zeros, m, the corresponding eigenfunction has in the interval $u \in [0, 2\mathbf{K}]$. This parallels the classifications of general Lamé-Wangerin functions outlined in section 4.6.2 earlier.

*This requirement can be obtained in two ways: choosing k small or n large.

k	h_0	h_1	h_2	h_3	h_4	h_5
0.1	0.248748	2.238729	6.218691	12.188635	20.148559	30.098465
0.2	0.244962	2.204656	6.124043	12.003125	19.841900	29.640369
0.3	0.238551	2.146960	5.963777	11.689004	19.322639	28.864682
0.4	0.229347	2.064119	5.733663	11.237979	18.577067	27.750928
0.5	0.217067	1.953600	5.426668	10.636269	17.582404	26.265073
0.6	0.201247	1.811224	5.031177	9.861107	16.301014	24.350898
0.7	0.181076	1.629682	4.526894	8.872713	14.667138	21.910169
0.8	0.154939	1.394455	3.873487	7.592035	12.550099	18.747679
0.9	0.118604	1.067440	2.965111	5.811617	9.606958	14.351135

TABLE 4.2: *Approximate eigenvalues.*

4.6.5 Series I

Ince (1940) investigated various series solutions of the (typical) form $U = \sum A_{2m}\,\mathrm{sn}^{2m}\,\zeta$ to the general Lamé equation (4.33). Here he assumed that $0 < k < 1$, n is real and $\geq -1/2$ but not necessarily an integer and $0 \leq \zeta \leq 2\mathbf{K}$ or $0 \leq \zeta \leq 4\mathbf{K}$. He also discusses how the associated recurrence relations can be used to evaluate h.

For the series solution of the form ($a_0 \neq 0$)

$$U(u) = \sum_{n=0}^{\infty} a_n\,\mathrm{sn}^{2n+\alpha}(u,k) \tag{4.53}$$

to be a formal solution of (4.39) we require $\alpha = \frac{1}{2}$ and the coefficients to satisfy the recurrence relations

$$4a_1 + \left[h - \tfrac{1}{4}(1+k^2)\right] a_0 = 0 \tag{4.54}$$

$$\begin{aligned} 4(n+1)^2\,a_{n+1} + \left[h - \tfrac{1}{4}(1+k^2)(4n+1)^2\right] a_n + \\ \tfrac{1}{4}k^2(4n-1)(4n-3)\,a_{n-1} \;=\; 0 \quad (n \geq 1). \end{aligned} \tag{4.55}$$

This series satisfies boundary conditions (4.40) and (4.36) and therefore represents an even solution to (4.39). In general we write (4.54)

$$\gamma_1\,a_1 + \beta_0\,a_0 = 0 \tag{4.56}$$

and (4.55) as

$$\gamma_n\,a_{n+1} + \beta_n(h)\,a_n + \alpha_n\,a_{n-1} = 0 \tag{4.57}$$

with obvious definitions for the new terms. Furthermore define $\alpha_n \to \alpha$, $\beta_n \to \beta$ and $\gamma_n \to \gamma$ as $n \to \infty$. If t_1 and t_2 are the roots of the quadratic equation

$$\alpha + \beta t + \gamma t^2 = 0 \tag{4.58}$$

and $|t_1| < |t_2|$ then in general (Perron (1929), Flammer (1957))

$$\lim_{n\to\infty}\left(\frac{a_n}{a_{n-1}}\right) = t_2. \tag{4.59}$$

If h has one of its sequence of characteristic values (eigenvalue) then the limit in (4.59) tends to the smaller t_1 value. This is vital when considering the convergence of (4.53), it will now converge in a more extensive region which includes at least two singularities.

In particular from (4.55) we calculate that $\alpha = 4k^2n^2$, $\beta = -4(1+k^2)n^2$ and $\gamma = 4n^2$ and so solutions to (4.58) are then $t_1 = k^2$ or $t_2 = 1$. The series (4.53) converges when

$$\lim_{n\to\infty} \left| \frac{a_n}{a_{n-1}} \right| |\operatorname{sn} u|^2 < 1 \tag{4.60}$$

and if h has a characteristic value, the series is therefore absolutely and uniformly convergent through any region in which $|k \operatorname{sn} u| < 1$. Clearly our specific problem for which $0 < k < 1$ and $0 \leq u \leq 2\mathbf{K}$ satisfies this condition.

Pivotal in these results is the accurate calculation of h. From (4.57) write

$$\frac{a_n}{a_{n-1}} = -\frac{\alpha_n}{\beta_n(h) + \gamma_n a_{n+1}/a_n} \tag{4.61}$$

from which by repeated application leads to the infinite continued fraction

$$C_n = -\cfrac{\alpha_n}{\beta_n(h) - \cfrac{\alpha_{n+1}\gamma_n}{\beta_{n+1}(h) - \gamma_{n+1}\, a_{n+2}/a_{n+1}} \cdots} \tag{4.62}$$

which converges as $|t_1| < |t_2|$ (Erdélyi *et al.*, 1955a). h is determined by solving the transcendental equation

$$\beta_0 = C_1\gamma_1. \tag{4.63}$$

Computationally we proceed as follows. Assume for $n = N$ that $a_N = 0$. Calculate the *finite* continued fraction C_1 given by (4.62) and solve (4.63). Repeat this process with a neighboring value of N until the values of h are unaffected by larger values of N. For example, let $k = 0.1$ and $N = 2$ and accordingly set $a_2 = 0$. From (4.63) we obtain

$$\left(h - \tfrac{101}{400}\right)\left(h - \tfrac{101}{16}\right) + \tfrac{3}{400} = 0$$

giving the first estimates of h to be approximately 0.254 and 6.311. By choosing $N = 2$ equation (4.63) is a quadratic equation. For larger values of N numerical methods must be employed, to solve higher order equations. This was achieved by using `Maple`.

A summary of the first three even eigenvalues are shown in table 4.3. The second entry per eigenvalue (e.g. 4 for the $h_0(0.1)$ value) represent the number of terms, N required so that the difference between successive calculations was no more than 1×10^{-7}.

For $k > 0.7$ (with the exception of $h_0(0.7)$) this procedure failed to calculate convergent eigenvalues. Similar shortcomings are also noted in Ince (1940).

Comparing these results with those in table 4.2 we see the values given there approximate the *true* h_0 values poorly and the h_2 and h_4 eigenvalues reasonably well, the discrepancy between the two methods becomes less pronounced as the value of the eigenvalue increases. This result is to be expected as the approximation used to calculate the earlier values assumed that h was large.

k	h_0		h_2		h_4	
0.1	0.247496	4	6.217440	6	20.147308	7
0.2	0.239932	5	6.119018	8	19.836875	9
0.3	0.227146	7	5.952398	10	19.311257	12
0.4	0.208838	9	5.713238	12	18.556635	15
0.5	0.184507	11	5.394322	15	17.550039	18
0.6	0.153326	15	4.983734	20	16.253527	24
0.7	0.113847	21	-	-	-	-

TABLE 4.3: *First three even eigenvalues determined by (4.63) and (4.55).*

An odd solution satisfying boundary conditions (4.40) and (4.37) is given by

$$U(u) = \mathrm{cn}(u,k) \sum_{n=0}^{\infty} b_n \, \mathrm{sn}^{2n+1/2}(u,k) \tag{4.64}$$

where the coefficients satisfy the recurrence relations

$$16b_1 - \left[9 + k^2 - 4h\right] b_0 = 0 \tag{4.65}$$

$$16(n+1)^2 \, b_{n+1} + \left[4h + k^2(4n+2)^2 - (4n+3)^2\right] b_n + k^2(4n+1)(4n-1)\, b_{n-1} = 0 \quad (n \geq 1). \tag{4.66}$$

This series has identical $t_{1,2}$ values as the even solution (4.53), and if h is chosen appropriately the same region of convergence: $|k\mathrm{sn}u| < 1$. Table 4.4 lists the first three odd eigenvalues calculated by the method described earlier (with the same convergence criteria). Again, when comparing with the earlier approximate values for these eigenvalues, we see the difference diminishes as h increases. Furthermore we notice, as in the even scenario, this method fails to converge for values of $k > 0.7$.

k	h_1		h_3		h_5	
0.1	2.237477	4	12.187383	6	30.097213	7
0.2	2.199633	5	11.998100	8	29.635344	9
0.3	2.135591	7	11.677623	9	28.853300	12
0.4	2.043726	9	11.217548	12	27.730494	15
0.5	1.921340	11	10.603909	15	26.232705	18
0.6	1.763969	15	9.813632	19	24.303405	23
0.7	1.563815	20	-	-	-	-

TABLE 4.4: *First three odd eigenvalues determined by (4.63) and (4.64).*

4.6.6 Series II

Ideally we would like series solutions that emit convergent h values for any k value. The following series provides a solution to this problem, and in particular enables the computation of h associated with higher k values absent in tables 4.3 and 4.4.

An even solution is given by the series (Erdélyi *et al.*, 1955a)

$$U(u) = \sum_{n=0}^{\infty} f_n = \sum_{n=0}^{\infty} a_n \left(\frac{k \,\mathrm{sn}u}{1 + \mathrm{dn}\, u} \right)^{2n+1/2} \tag{4.67}$$

and the recurrence relations

$$2k^2 a_1 + \left[2h + \tfrac{1}{4}(2 - k^2) \right] a_0 = 0 \tag{4.68}$$

$$\begin{aligned} 4(n+1)^2 k^2 \, a_{n+1} + \tfrac{1}{2} \left[8h + k^2 - (4n+1)^2 (2 - k^2) \right] a_n + \\ k^2 (2n-1)^2 \, a_{n-1} \quad = \quad 0 \quad (n \geq 1). \end{aligned} \tag{4.69}$$

While an odd solution can be generated from

$$U(u) = \mathrm{cs}\, u \sum_{n=0}^{\infty} b_n \left(\frac{k \,\mathrm{sn}u}{1 + \mathrm{dn}\, u} \right)^{2n+3/2} \tag{4.70}$$

and the recurrence relations

$$4k^2 b_1 + \left[4h + 5k^2 - 9 \right] b_0 = 0 \tag{4.71}$$

$$\begin{aligned} 4(n+1)^2 k^2 \, b_{n+1} + \tfrac{1}{2} \left[8h + k^2 - (4n+3)^2 (2 - k^2) \right] b_n + \\ k^2 (2n+1)^2 \, b_{n-1} \quad = \quad 0 \quad (n \geq 1). \end{aligned} \tag{4.72}$$

For both solutions, the roots of the quadratic equation (4.58) are ($k^2 + k'^2 = 1$)

$$t_1 = \frac{1 - k'}{1 + k'}, \quad t_2 = \frac{1 + k'}{1 - k'}. \tag{4.73}$$

Now $|\mathrm{sn}u/(1 + \mathrm{dn}u)|^2 \leq 1/(1 + k')^2$, thus if h has one of its eigenvalues then the ratio of two successive terms of (4.69) or (4.72) tends to t_1 and we have

$$\left| \frac{f_{n+1}}{f_n} \right| \leq \frac{k^2}{(1 + k')^2} = \left[\frac{1 - k'}{1 + k'} \right]^2 \tag{4.74}$$

so the convergence is at least as good of a geometric series with ratio (4.74) (Erdélyi *et al.* (1955a), Arscott (1964)).

Tables 4.5 and 4.6 illustrate the effectiveness of these new series. To emphasize the improved convergence, the second entry per eigenvalue represent the number of terms, N required in (4.63) so that the difference between successive calculations was no more than 1×10^{-10} rather than the previous criteria of 1×10^{-7}.

k	h_0		h_2		h_4	
0.1	0.2474958124	2	6.2174395784	4	20.1473076408	5
0.2	0.2399319651	3	6.1190183558	4	19.8368748197	6
0.3	0.2271463830	4	5.9523978834	5	19.3112568140	6
0.4	0.2088381836	4	5.7132374511	6	18.5566345105	7
0.5	0.1845070937	5	5.3943222624	6	17.5500390453	8
0.6	0.1533259726	6	4.9837334400	7	16.2535266060	9
0.7	0.1138468121	7	4.4606436406	9	14.6007965335	11
0.8	0.0631804409	9	3.7836569995	11	12.4600855493	13
0.9	-0.0063256442	12	2.8440902810	15	9.4855418446	18

TABLE 4.5: *First three even eigenvalues determined by (4.63) and (4.67).*

k	h_1		h_3		h_5	
0.1	2.2374773868	3	12.1873830255	4	30.0972134156	5
0.2	2.1996326122	3	11.9980995629	4	29.6353439815	6
0.3	2.1355904898	4	11.6776224391	5	28.8533002539	6
0.4	2.0437264333	4	11.2175481723	6	27.7304939824	7
0.5	1.9213400019	5	10.6039092111	7	26.2327053357	8
0.6	1.7639693334	6	9.8136314006	8	24.3034045624	9
0.7	1.5638148779	7	8.8063955652	9	21.8438162100	11
0.8	1.3053626804	9	7.5020694870	11	18.6576426356	13
0.9	0.9478098467	13	5.6903014607	16	14.2296710664	19

TABLE 4.6: *First odd even eigenvalues determined by (4.63) and (4.70).*

4.6.7 Eigenfunctions

We now present graphically the solutions to (4.39) developed in the preceding sections. In addition to these analytic results we provide numerical solutions generated by the `Fortran-NAG` routine `D02KEF`*.

This routine calculates a specified eigenvalue and its associated eigenfunction of a regular singular second-order Sturm-Liouville system by combining a Pruefer transformation and shooting method techniques†. To implement this method a ratio of an approximate solution and its derivative near the singular points $u = 0, 2\mathbf{K}$ is required. By symmetry we use (4.44) for the approximation. It was encouraging to find that at worst, the numerical eigenvalues computed agreed only to the sixth decimal figure shown in tables 4.5 and 4.6. The $h_0(k)$ values agreed up to the tenth decimal.

Figure 4.5 illustrates the computation of the $h_0(0.9)$ and $h_1(0.9)$ solutions. All eigenfunctions displayed below have been normalized so $\max|U| = 1$. In the Bessel approximation

*D02KEY- Nag Fortran Library Routine Mark 18.

†Details of this algorithm can be found in Birkhoff and Rota (1962).

(4.44), the respective h values from tables 4.5 or 4.6 are used. We have chosen these values deliberately as they are respectively the lowest eigenvalues for the first even or odd solution. It is clear from even these two plots, representing the worst case scenario (small h), that as h increases the approximate solution agrees remarkably well with the numerical and series solutions (§4.6.6), which are indistinguishable at this scale. In figure 4.6 the first three eigenfunctions (series generated) are shown for $k = 0.1$.

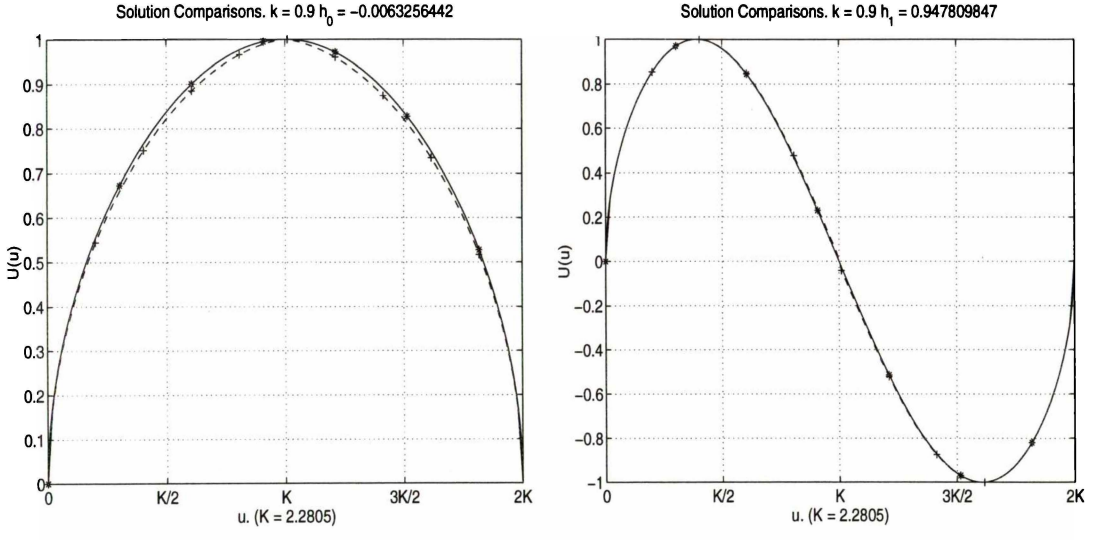

(a) $h_0(0.9)$ even eigenfunction.

(b) $h_1(0.9)$ odd eigenfunction.

FIGURE 4.5: *Comparison of computed eigensolutions. The +dash line is the Bessel approximation. The* indistinguishable *⋆lines are the numerical and series (§4.6.6) solutions.*

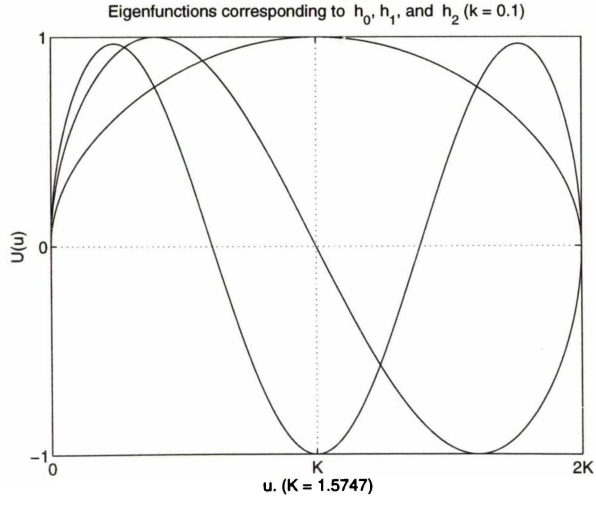

FIGURE 4.6: *First three U eigenfunctions.*

4.6.8 V Solutions

To complete the determination of ψ, we now turn our attention to the solutions of

$$V'' - \left[h + \tfrac{1}{4}k^2 \operatorname{sn}^2(iv, k) \right] V = 0, \qquad -\mathbf{K}' \leq v \leq \mathbf{K}' \tag{4.75}$$

or equivalently, as $\operatorname{sn}(iv, k) = i\operatorname{sc}(v, k')$,

$$V'' - \left[h - \tfrac{1}{4}k^2 \operatorname{sc}^2(v, k') \right] V = 0. \tag{4.76}$$

In these equations the parameter $h = h(k)$ is now fixed, and has been evaluated as described in the previous sections. In general we seek solutions that are bounded at the singular points $v = \pm\mathbf{K}'$. This condition corresponds, for fixed u, that the potential $\psi = \rho^{-1/2}V(v)U(u)$ is finite on the z axis, or the analogous condition*

$$\left[\operatorname{sc}(v, k') \right]^{-1/2} V(v) \quad \text{is bounded at} \quad v = \mathbf{K}'. \tag{4.77}$$

For a prescribed h, two solutions are possible: an even solution for which $V'(0) = 1$ and an odd $V(0) = 0$. Attempts to obtain solutions to (4.76) paralleled that of section 4.6.3. Initially, various series solutions where constructed, but ultimately all of these solutions failed to produce convergent results. Thus we where restricted to solve (4.76) numerically.

4.6.9 Numerical Solutions

Numerical solutions to the boundary value problem (4.76) where generated by the `Matlab v6` code `bvp4c`†. To implement this code an approximate solution near the singular endpoints $v = \pm\mathbf{K}'$ is provided and numerically matched in the interior region. Furthermore this code returns the first derivative of this solution, which is paramount in the determination of the metric function γ (section 4.7).

Calculation of the approximate solutions near the endpoints $v = \pm\mathbf{K}'$ satisfying (4.77) is obtained in an analogous manner as described in section 4.6.4.

Let $v = w \pm \mathbf{K}'$, and given, $k^2 \operatorname{sc}^2(w \pm \mathbf{K}', k') = \operatorname{cs}^2(w, k') \approx w^{-2} - \frac{1}{3}(1 + k^2) + \cdots$ as $w \to 0$, equation (4.76) becomes

$$V'' - \left[h + \tfrac{1}{12}(1 + k^2) - \tfrac{1}{4}w^{-2} \right] V = 0. \tag{4.78}$$

The solutions of (4.78) near the left or right endpoints are

$$V_{l,r} = \sqrt{v \pm \mathbf{K}'}\, I_0(H(v \pm \mathbf{K}')) + \sqrt{v \pm \mathbf{K}'}\, K_0(H(v \pm \mathbf{K}')) \tag{4.79}$$

where I_0 and K_0 are the modified Bessel functions of the first and second kind (of zeroth order) respectively, the constant H is given by (4.43). In practice (in reference to the numerical scheme) we need only provide the lowest order terms of the series expansion of these solutions

*By symmetry this entails that the solution is also finite at the remaining endpoint $v = -\mathbf{K}'$.

†Note this algorithm does not combine the *shooting* technique, `bvp4c` implements a collocation method.

near the endpoints*. Thus we supply to the code the approximations $V_l \approx \sqrt{v + \mathbf{K}'}$ and $V_r \approx c\sqrt{v - \mathbf{K}'}$ for the left and right solutions, furthermore in the right hand approximation we set $c = 1$ to generate even solutions (about $v = 0$) and for odd $c = -1$.

Various even and odd solutions with $h(k) = h_0, h_1, h_2$ are shown in figure 4.7. Here all solutions are normalized so that the maximum value of any eigenfunction is one.

We recall that the labeling on the eigenvalue h, for example h_1, refers to the number of zeros the corresponding U solution has, but serves no method of characterizing the particular V solutions generated by this value of h.

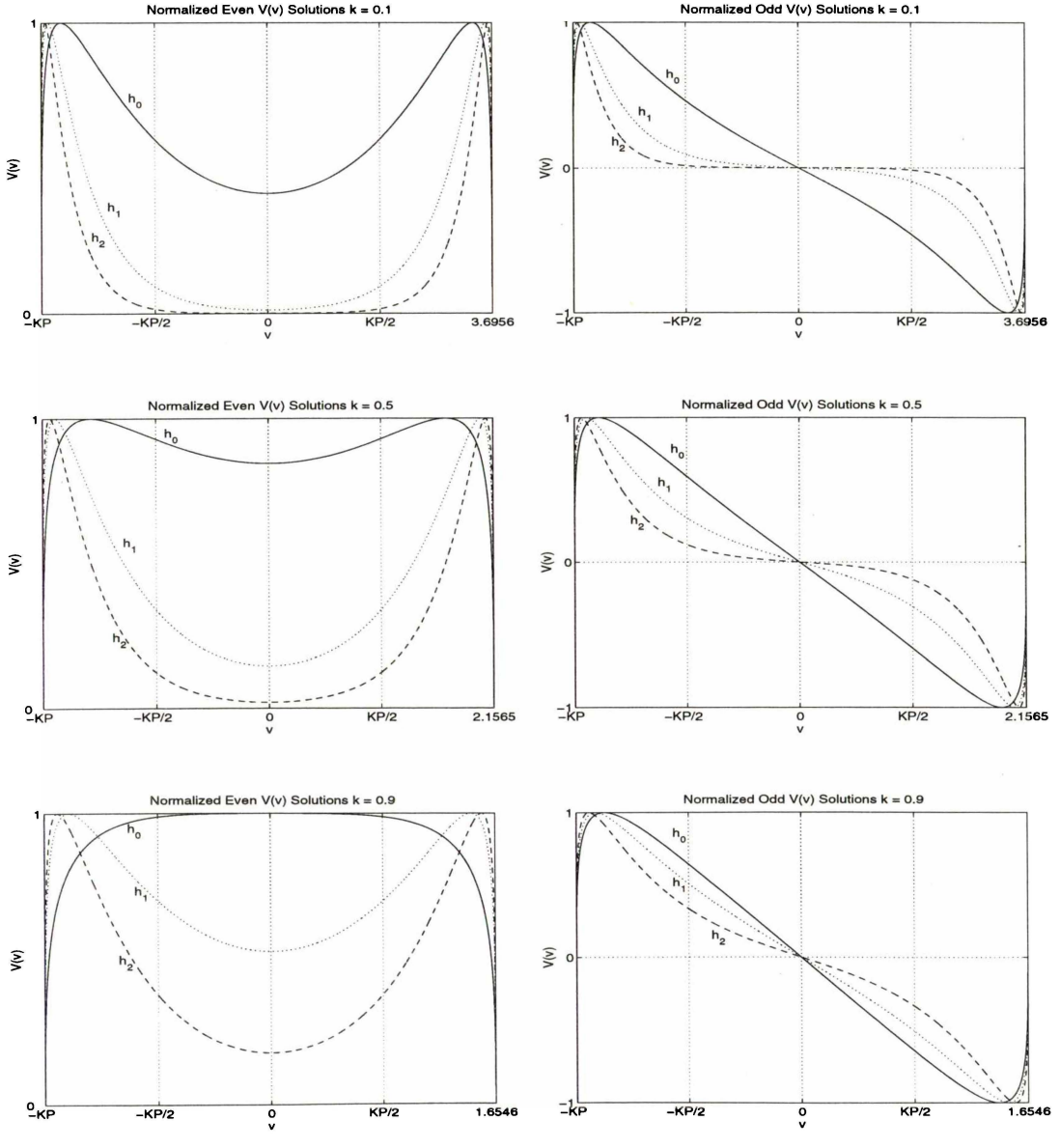

FIGURE 4.7: *Various even and odd solutions for* $k = 0.1, 0.5, 0.9$. h_0 *etc. refers to the value of* h *used. Note* $KP \equiv \mathbf{K}'$.

*Trials with the retention of higher order terms had no significant effects on the computed solutions.

4.6.10 Approximations

As in section 4.6.4, the K_0 solution presented in (4.79)

$$V_{l,r}(v) = \sqrt{v \pm \mathbf{K}'}\, K_0(H(v \pm \mathbf{K}')) \tag{4.80}$$

valid near the endpoints, in fact turns out for large h to be in excellent agreement with the actual (numerical) solution*. Figure 4.8 displays the comparison of even solutions for the two values $k = 0.1$ and $k = 0.5$ (due to symmetry we use the half interval $-\mathbf{K}' \leq v \leq 0$ and use the V_l solution). We see for the smallest eigenvalue h_0 the difference is large, but for higher h values agreement is good. Additionally the inner boundary condition at $v = 0$, requiring the derivative of the function here to be zero, improves as h increases. This is to be expected as

$$V_l \approx e^{-\sqrt{h}(v+\mathbf{K}')} \quad \text{as} \quad h \uparrow \quad \text{and} \quad v \to 0. \tag{4.81}$$

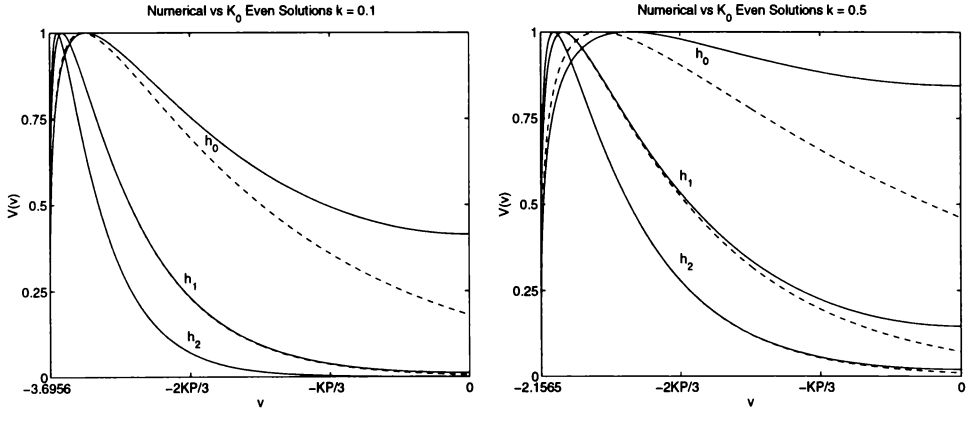

(a) $h_0 = 0.247 \quad h_1 = 2.237 \quad h_2 = 6.217$ (b) $h_0 = 0.185 \quad h_1 = 1.921 \quad h_2 = 5.394$

FIGURE 4.8: *Numerical solution versus the K_0 approximation (dashed line).*

For small v equation (4.76) to lowest order becomes $V'' - hV = 0$, with general solution $V = A\sinh(\sqrt{h}\,v) + B\cosh(\sqrt{h}\,v)$. Here A and B are constants, clearly for odd solutions we take solutions of the form

$$V = A\sinh(\sqrt{h}\,v) \tag{4.82}$$

and for even solutions

$$V = B\cosh(\sqrt{h}\,v). \tag{4.83}$$

Examples of these inner approximations are shown in figure 4.9. Both approximations, regardless of k or h values, match the numerical solution well even for this exaggerated domain (recall these are solutions for $v \approx 0$). The constant B is determined so that the numerical and approximate solutions agree at $v = 0$, whereas A is determined by matching the derivatives of the approximation and numerical solutions at the origin.

*The I_0 solution can be eliminated from this possibility on its asymptotic behaviour.

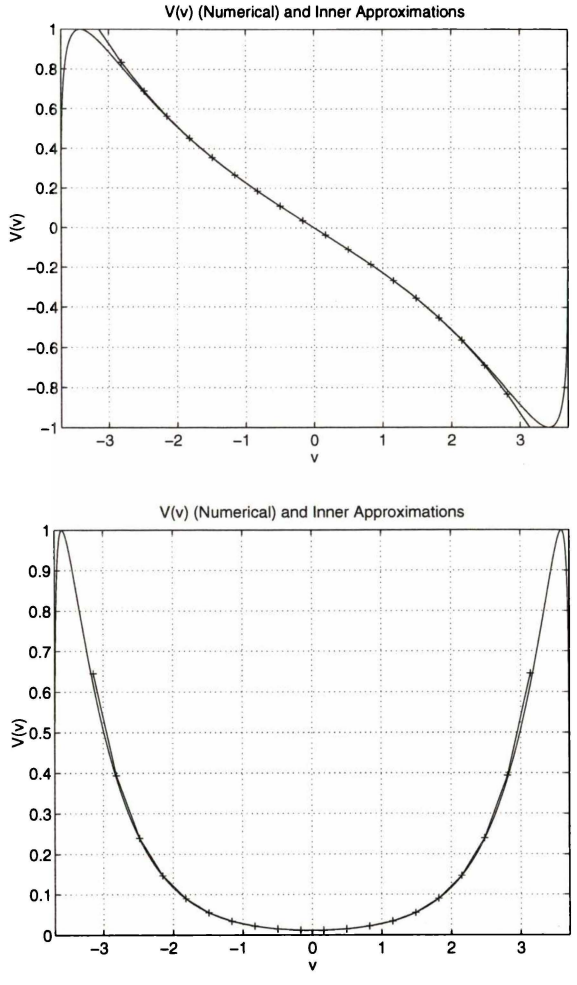

FIGURE 4.9: *Hyperbolic inner approximations (+). The eigenfunctions are those belonging to the parameters* $k = 0.1$ $h = 0.2475$.

4.6.11 Summary

Let us summarise the previous sections which discussed the formulation of

$$\psi = \sqrt{R(u,v)}\, U(u)V(v) = \left(\frac{\mathrm{cn}u\,\mathrm{dn}v + \mathrm{dn}u}{\mathrm{sn}u\,\mathrm{cn}v}\right)^{\frac{1}{2}} U(u)\,V(v). \tag{4.84}$$

By meeting the imposed finiteness conditions (4.40) and (4.77) for U and V respectively, ψ is then bounded on the z-axis. Furthermore as $w = u - 2\mathbf{K} \to 0$ and $v \to 0$, $r \to \infty$ and

$$\psi \sim \sqrt{w^2 + v^2}\, w^{-1/2}\, U(w)\, V(v) \to 0 \tag{4.85}$$

as the term $w^{-1/2}\, U$ is the finite condition (4.40), and so ψ is asymptotically flat.

In all subsequent work requiring the computation of ψ, the factor $U(u)$ will be generated by the series solutions presented in section 4.6.6.

4.7 Determining γ

To complete the determination of the metric (4.28) the function $\gamma(u,v)$ must be calculated. In terms of Weyl's original cylindrical coordinates γ satisfies $\gamma_\rho = \rho\,(\psi_\rho^2 - \psi_z^2)$ and $\gamma_z = 2\,\rho\,\psi_\rho\,\psi_z$. With $\psi(u,v)$ given by (4.84), and introducing the notation

$$s_1 = \mathrm{sn}(u,k), \quad s_2 = \mathrm{sn}(v,k') \quad \text{etc}$$

we write our new coordinates (section 4.4) as

$$\rho = s_1 c_2 \Lambda^{-1} \quad z = -s_2 \Lambda^{-1} \qquad \Lambda = c_1 d_2 + d_1. \tag{4.86}$$

The equations for γ become

$$\frac{\partial\gamma}{\partial\zeta} = \frac{s_1}{D}\left[A\left(\frac{\partial\psi}{\partial u}\right)^2 + B\,\frac{\partial\psi}{\partial u}\frac{\partial\psi}{\partial v} + C\left(\frac{\partial\psi}{\partial v}\right)^2\right] \qquad \zeta = u, v \tag{4.87}$$

where ($\Lambda_1 = d\Lambda/du$ etc)

$$D = \left(c_1 d_1 s_2{}^2 d_2\Lambda + c_1 d_1 c_2 s_2 \Lambda_2 - c_1 d_1 d_2 \Lambda + s_1 d_2 \Lambda_1\right)^2 \Lambda \tag{4.88}$$

and the functions A, B and C when $\zeta = u$ are

$$\begin{aligned}
A = {} & -c_1{}^3 d_1 s_2{}^4 d_2{}^2 \Lambda^3 - 2\,c_1{}^3 d_1 c_2 s_2{}^3 d_2 \Lambda^2 \Lambda_2 + c_1{}^2 s_1 s_2{}^4 d_2{}^2 \Lambda^2 \Lambda_1 + \\
& c_1{}^3 d_1 s_2{}^4 \Lambda\,\Lambda_2{}^2 + c_1{}^3 d_1 s_2{}^2 d_2{}^2 \Lambda^3 + 2\,c_1{}^2 s_1 c_2 s_2{}^3 d_2 \Lambda\,\Lambda_1 \Lambda_2 + \\
& 2\,c_1 d_1 s_2{}^4 d_2{}^2 \Lambda^3 + 2\,c_1{}^3 d_1 c_2 s_2 d_2 \Lambda^2 \Lambda_2 - c_1{}^2 s_1 s_2{}^4 \Lambda_1 \Lambda_2{}^2 - \\
& c_1{}^2 s_1 s_2{}^2 d_2{}^2 \Lambda^2 \Lambda_1 + 4\,c_1 d_1 c_2 s_2{}^3 d_2 \Lambda^2 \Lambda_2 - 2\,c_1{}^3 d_1 s_2{}^2 \Lambda\,\Lambda_2{}^2 - \\
& 2\,c_1{}^2 s_1 c_2 s_2 d_2 \Lambda\,\Lambda_1 \Lambda_2 - 2\,c_1 d_1 s_2{}^4 \Lambda\,\Lambda_2{}^2 - 3\,c_1 d_1 s_2{}^2 d_2{}^2 \Lambda^3 + \\
& +2\,c_1{}^2 s_1 s_2{}^2 \Lambda_1 \Lambda_2{}^2 - 4\,c_1 d_1 c_2 s_2 d_2 \Lambda^2 \Lambda_2 + s_1 s_2{}^2 d_2{}^2 \Lambda^2 \Lambda_1 \\
& c_1{}^3 d_1 \Lambda\,\Lambda_2{}^2 + 3\,c_1 d_1 s_2{}^2 \Lambda\,\Lambda_2{}^2 + c_1 d_1 d_2{}^2 \Lambda^3 + 2\,s_1 c_2 s_2 d_2 \Lambda\,\Lambda_1 \Lambda_2 - \\
& c_1{}^2 s_1 \Lambda_1 \Lambda_2{}^2 - s_1 s_2{}^2 \Lambda_1 \Lambda_2{}^2 - s_1 d_2{}^2 \Lambda^2 \Lambda_1 - c_1 d_1 \Lambda\,\Lambda_2{}^2 + s_1 \Lambda_1 \Lambda_2{}^2
\end{aligned} \tag{4.89}$$

$$\begin{aligned}
B = {} & 2\,c_1{}^4 s_1 c_2 s_2{}^3 d_2 \Lambda^3 + 2\,c_1{}^4 s_1 c_2 s_2 d_2{}^3 \Lambda^3 - 2\,c_1{}^4 s_1 s_2{}^4 \Lambda^2 \Lambda_2 - \\
& 2\,c_1{}^4 s_1 s_2{}^2 d_2{}^2 \Lambda^2 \Lambda_2 + 4\,c_1{}^3 d_1 c_2 s_2{}^3 d_2 \Lambda^2 \Lambda_1 - 2\,c_1{}^4 s_1 c_2 s_2 d_2 \Lambda^3 - \\
& 4\,c_1{}^3 d_1 s_2{}^4 \Lambda\,\Lambda_1 \Lambda_2 - 2\,c_1{}^2 s_1 d_1{}^2 c_2 s_2 d_2 \Lambda^3 - 2\,c_1{}^2 s_1 c_2 s_2{}^3 d_2 \Lambda\,\Lambda_1{}^2 - \\
& 2\,c_1{}^2 s_1 c_2 s_2 d_2{}^3 \Lambda^3 + 6\,c_1{}^4 s_1 s_2{}^2 \Lambda^2 \Lambda_2 + 4\,c_1{}^4 s_1 d_2{}^2 \Lambda^2 \Lambda_2 - \\
& 4\,c_1{}^3 d_1 c_2 s_2 d_2 \Lambda^2 \Lambda_1 + 2\,c_1{}^2 s_1 s_2{}^4 \Lambda_1{}^2 \Lambda_2 + 2\,c_1{}^2 s_1 s_2{}^2 d_2{}^2 \Lambda^2 \Lambda_2 - \\
& 4\,c_1 d_1 c_2 s_2{}^3 d_2 \Lambda^2 \Lambda_1 + 8\,c_1{}^3 d_1 s_2{}^2 \Lambda\,\Lambda_1 \Lambda_2 + 2\,c_1{}^2 s_1 c_2 s_2 d_2 \Lambda^3 + \\
& 2\,c_1{}^2 s_1 c_2 s_2 d_2 \Lambda\,\Lambda_1{}^2 + 4\,c_1 d_1 s_2{}^4 \Lambda\,\Lambda_1 \Lambda_2 - \\
& 4\,c_1{}^4 s_1 \Lambda^2 \Lambda_2 - 2\,c_1{}^2 s_1 d_1{}^2 \Lambda^2 \Lambda_2 - 2\,c_1{}^2 s_1 s_2{}^2 \Lambda^2 \Lambda_2 - \\
& 4\,c_1{}^2 s_1 s_2{}^2 \Lambda_1{}^2 \Lambda_2 - 4\,c_1{}^2 s_1 d_2{}^2 \Lambda^2 \Lambda_2 + 4\,c_1 d_1 c_2 s_2 d_2 \Lambda^2 \Lambda_1 - \\
& 4\,c_1{}^3 d_1 \Lambda\,\Lambda_1 \Lambda_2 - 8\,c_1 d_1 s_2{}^2 \Lambda\,\Lambda_1 \Lambda_2 - \\
& 2\,s_1 c_2 s_2 d_2 \Lambda\,\Lambda_1{}^2 + 4\,c_1{}^2 s_1 \Lambda^2 \Lambda_2 + 2\,c_1{}^2 s_1 \Lambda_1{}^2 \Lambda_2 + \\
& 2\,s_1 s_2{}^2 \Lambda_1{}^2 \Lambda_2 + 4\,c_1 d_1 \Lambda\,\Lambda_1 \Lambda_2 - 2\,s_1 \Lambda_1{}^2 \Lambda_2
\end{aligned} \tag{4.90}$$

$$
\begin{aligned}
C &= -{c_1}^5 d_1 {s_2}^4 \Lambda^3 - {c_1}^5 d_1 {s_2}^2 {d_2}^2 \Lambda^3 + 3\,{c_1}^4 s_1 {s_2}^4 \Lambda^2 \Lambda_1 + \\
&\quad 3\,{c_1}^4 s_1 {s_2}^2 {d_2}^2 \Lambda^2 \Lambda_1 + 3\,{c_1}^5 d_1 {s_2}^2 \Lambda^3 + 2\,{c_1}^5 d_1 {d_2}^2 \Lambda^3 + \\
&\quad 3\,{c_1}^3 d_1 {s_2}^4 \Lambda\, {\Lambda_1}^2 + {c_1}^3 d_1 {s_2}^2 {d_2}^2 \Lambda^3 - 9\,{c_1}^4 s_1 {s_2}^2 \Lambda^2 \Lambda_1 - \\
&\quad 6\,{c_1}^4 s_1 {d_2}^2 \Lambda^2 \Lambda_1 - {c_1}^2 s_1 {s_2}^4 {\Lambda_1}^3 - 3\,{c_1}^2 s_1 {s_2}^2 {d_2}^2 \Lambda^2 \Lambda_1 - \\
&\quad 2\,{c_1}^5 d_1 \Lambda^3 - {c_1}^3 {d_1}^3 \Lambda^3 - {c_1}^3 d_1 {s_2}^2 \Lambda^3 - 6\,{c_1}^3 d_1 {s_2}^2 \Lambda\, {\Lambda_1}^2 - \\
&\quad 2\,{c_1}^3 d_1 {d_2}^2 \Lambda^3 - 2\,c_1 d_1 {s_2}^4 \Lambda\, {\Lambda_1}^2 + 6\,{c_1}^4 s_1 \Lambda^2 \Lambda_1 + \\
&\quad 3\,{c_1}^2 s_1 {d_1}^2 \Lambda^2 \Lambda_1 + 3\,{c_1}^2 s_1 {s_2}^2 \Lambda^2 \Lambda_1 + 2\,{c_1}^2 s_1 {s_2}^2 {\Lambda_1}^3 + \\
&\quad 6\,{c_1}^2 s_1 {d_2}^2 \Lambda^2 \Lambda_1 + 2\,{c_1}^3 d_1 \Lambda^3 + 3\,{c_1}^3 d_1 \Lambda\, {\Lambda_1}^2 + 5\,c_1 d_1 {s_2}^2 \Lambda\, {\Lambda_1}^2 - \\
&\quad 6\,{c_1}^2 s_1 \Lambda^2 \Lambda_1 - {c_1}^2 s_1 {\Lambda_1}^3 - s_1 {s_2}^2 {\Lambda_1}^3 - 3\,c_1 d_1 \Lambda\, {\Lambda_1}^2 + s_1 {\Lambda_1}^3 \qquad (4.91)
\end{aligned}
$$

and for $\zeta = v$ we have

$$
\begin{aligned}
A &= ({c_1}^2 {c_2}^2 s_2 {d_2}^3 \Lambda^3 + 3\,{c_1}^2 {c_2}^3 {d_2}^2 \Lambda^2 \Lambda_2 - 3\,{c_1}^2 {c_2}^2 s_2 d_2 \Lambda\, {\Lambda_2}^2 - \\
&\quad {c_1}^2 s_2 {d_2}^3 \Lambda^3 - {c_1}^2 {c_2}^3 {\Lambda_2}^3 - 3\,{c_1}^2 c_2 {d_2}^2 \Lambda^2 \Lambda_2 + s_2 {d_2}^3 \Lambda^3 + \\
&\quad c_2 {d_2}^2 \Lambda^2 \Lambda_2 + s_2 d_2 \Lambda\, {\Lambda_2}^2 + c_2 {\Lambda_2}^3) s_1 c_2 \qquad (4.92) \\
B &= 2\,(-c_1 d_1 \Lambda + s_1 \Lambda_1)(-{c_1}^2 {c_2}^2 {d_2}^2 \Lambda^2 + \\
&\quad 2\,{c_1}^2 c_2 s_2 d_2 \Lambda\, \Lambda_2 + {c_1}^2 {c_2}^2 {\Lambda_2}^2 + {c_1}^2 {d_2}^2 \Lambda^2 - {d_2}^2 \Lambda^2 - {\Lambda_2}^2) {c_2}^2 \qquad (4.93) \\
C &= ({c_1}^2 s_1 {d_1}^2 {c_2}^2 s_2 d_2 \Lambda^3 + 2\,{c_1}^3 d_1 {c_2}^2 s_2 d_2 \Lambda^2 \Lambda_1 + \\
&\quad {c_1}^2 s_1 {d_1}^2 {c_2}^3 \Lambda^2 \Lambda_2 + 2\,{c_1}^3 d_1 {c_2}^3 \Lambda\, \Lambda_1 \Lambda_2 - {c_1}^2 s_1 {c_2}^2 s_2 d_2 \Lambda\, {\Lambda_1}^2 - \\
&\quad {c_1}^2 s_1 {c_2}^3 {\Lambda_1}^2 \Lambda_2 - 2\,c_1 d_1 c_2 \Lambda\, \Lambda_1 \Lambda_2 - s_1 s_2 d_2 \Lambda\, {\Lambda_1}^2 + s_1 c_2 {\Lambda_1}^2 \Lambda_2) c_2. \qquad (4.94)
\end{aligned}
$$

4.7.1 Numerical Method

It is obvious that we will have to resort to numerical methods in the evaluation of γ.

Elementary flatness requires that $\gamma = 0$ at the vacuum parts of the axis (Synge, 1960; Bonnor, 1992). We integrate from $u = v = 0$ ($z = \rho = 0$) to a given point $(\tilde{u}, \tilde{v})$, through a region devoid of matter. Initially for diagnostic purposes we will compute γ using the two paths, *ABC* and *ADC*, illustrated in figure 4.10. This method has been discussed in section 3.11 of the toroidal chapter.

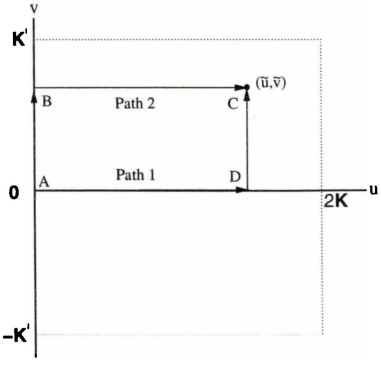

FIGURE 4.10: *Integration paths.*

From (4.87) we have for path one

$$
\gamma_{p1} = \gamma(\tilde{u}, \tilde{v}) = \int_0^{\tilde{u}} \left.\frac{\partial \gamma}{\partial u}\right|_{v=0} du + \int_0^{\tilde{v}} \left.\frac{\partial \gamma}{\partial v}\right|_{u=\tilde{u}} dv \qquad (4.95)
$$

with $v = 0$ considerable simplification can be obtained and we can write

$$
\gamma_{p1} = \int_0^{\tilde{u}} s_1 (\psi_u^2 - \psi_v^2)\Big|_{v=0} du + \int_0^{\tilde{v}} \gamma_v \Big|_{u=\tilde{u}} dv. \qquad (4.96)
$$

We note however, the first integrand of equation (4.96) evaluated at the lower limit becomes singular. Consider the generalized solution

$$\psi(u,v) = \left(\frac{c_1 d_2 + d_1}{s_1 c_2}\right)^{1/2} \left[\alpha_1 U_1 V_1 + \alpha_2 U_2 V_2 + \cdots\right] \tag{4.97}$$

here α_i are constants and the $U_i V_i$ terms are distinct eigensolutions. Recall (see §4.6.4) as $u \approx 0$ then $U_i \approx \sqrt{u} J_0(H_i u)$ and as $u, v \to 0$ we have

$$\begin{aligned} \psi(u,v) &\approx A_1(\alpha_1 V_1(0) + \cdots) + A_2(\alpha_1 V_1'(0) + \cdots)\, v + A_3(\alpha_1 V_1(0) + \cdots)\, u^2 + \cdots \\ &= \bar{A}_1 + \bar{A}_2\, v + \bar{A}_3 u^2 + \cdots \end{aligned} \tag{4.98}$$

where $\bar{A}_i$ are finite constants. Thus $s_1(\psi_u^2 - \psi_v^2) \approx u$ as $u \to 0, v = 0$. We can therefore avoid this singular point by beginning the integration slightly from the origin and noting that this will have negligible effect on the computed value of the integral.

Evaluating γ via path two reduces to

$$\gamma_{p2} = \int_0^{\tilde{u}} \left.\frac{\partial \gamma}{\partial u}\right|_{v=\tilde{v}} du. \tag{4.99}$$

as there is no contribution along AB due to the s_1 factor in γ_v.

Unlike earlier chapters ψ is not known analytically*. As the evaluation of γ in theory is path independent the comparison of values obtained via path one and two will serve as a means to check the validity of our solutions. The numerical quadrature was facilitated by the `Matlab` routine `quadl` which approximates the integral of a function using recursive adaptive Lobatto quadrature.

4.7.2 Examples

Figures 4.12, 4.13 and 4.14 illustrate the typical absolute differences found between the evaluation of γ via the two paths described above for various single term ψ solutions.

Due to the large gradients in the V near the endpoints ($v \to \pm\mathbf{K}'$, $V'(v) \to (v \mp \mathbf{K}')^{-1/2}$) we have avoided the regions close to $v = \pm\mathbf{K}', 0 \le u \le 2\mathbf{K}$.

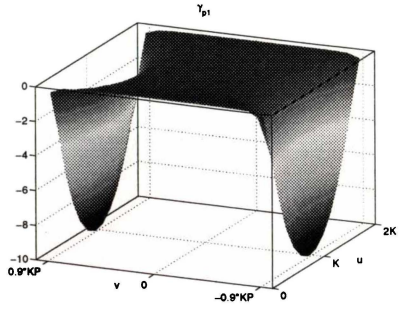

FIGURE 4.11: γ_{p1} *of figure 4.12*

Recall from table 4.1 (p.118) that these regions correspond to two finite bars along the z-axis. Given that the metric function γ is not zero at these regions (figure 4.11) would suggest that the ψ potentials generating γ are those of two finite bars along the z-axis.

The following plots show that the differences between the paths are reasonable. We would expect some discrepancy due to the errors generated in the numerical integration coupled with

*Recall we know V and V' numerically.

the additional errors introduced by the function V and its derivative which are only known numerically.

By altering the integration tolerance values, it was found that the minimum, maximum difference achievable was approximately 5×10^{-7}, corresponding to an integration tolerance of 1×10^{-7}. The plots shown are those computed at this value.

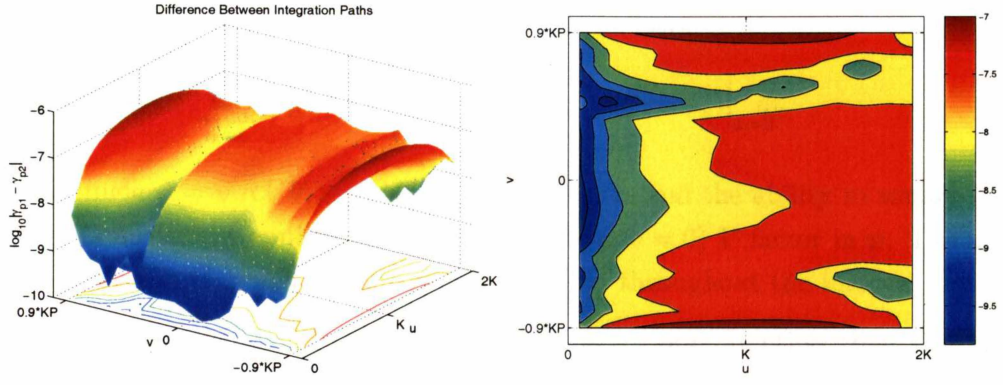

FIGURE 4.12: $k = 0.1, h = h_0$, V *is odd.*

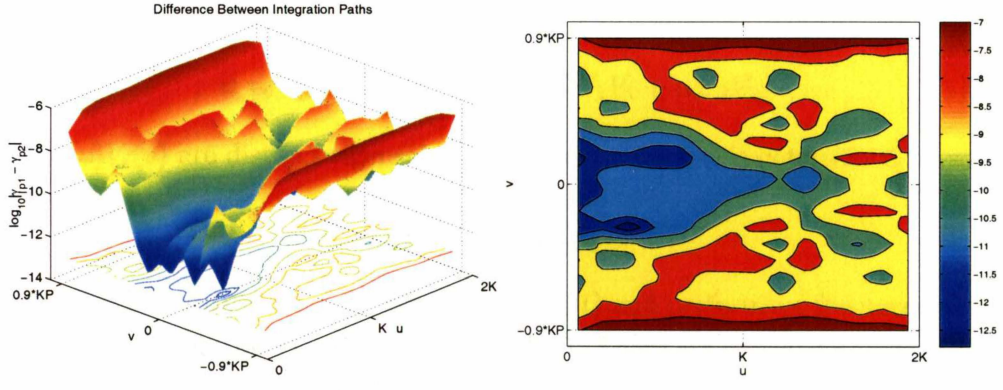

FIGURE 4.13: $k = 0.1, h = h_2$, V *is odd.*

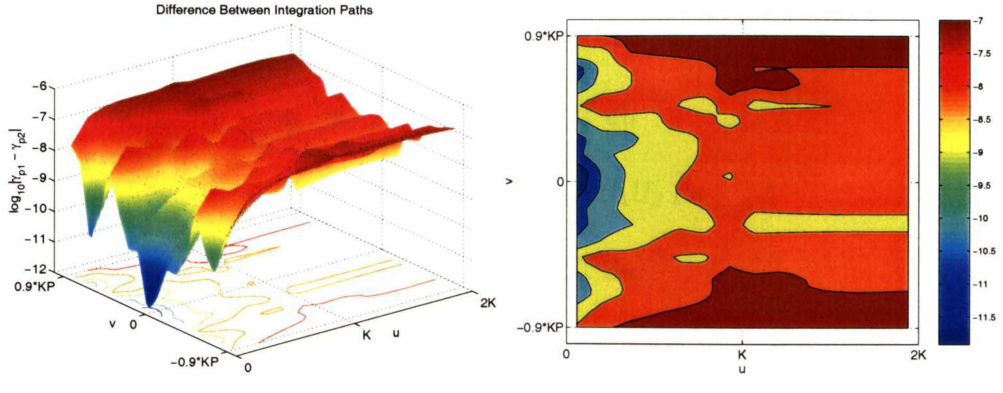

FIGURE 4.14: $k = 0.5, h = h_1$, V *is even.*

4.7.3 γ Boundary Conditions

To complete the determination of γ we must have that this function satisfies the requirements of elementary flatness. We will now address this boundary condition:

$$\lim_{r\to\infty} \gamma(u,v) = 0 \equiv \lim_{\substack{u\to 2\mathbf{K} \\ v\to 0}} \gamma(u,v) = 0 \tag{4.100}$$

or, from the previous section, by employing path one we have

$$\lim_{\substack{u\to 2\mathbf{K} \\ v\to 0}} \gamma(u,v) = 0 = \lim_{\tilde{u}\to 2\mathbf{K}} \int_0^{\tilde{u}} s_1(\psi_u^2 - \psi_v^2)\Big|_{v=0} du. \tag{4.101}$$

The use of a single $\psi = \sqrt{R}UV$ solution is too restrictive and the ability to satisfy (4.101) is not possible. Consider the application of an even (about $v = 0$) V factor in ψ. The integrand in (4.101) becomes $s_1\psi_u^2$ which is positive (fig. 4.15(b)) throughout the interval $0 \le u \le 2\mathbf{K}$.

Similarly for the remaining possibility that V is an odd function then the integrand degenerates to a function that is negative throughout the range of integration (fig. 4.15(a)). Thus for either possibility γ is not asymptotically flat.

Clearly one term solutions will not suffice. To continue this study we will now generate metrics based on the *two* term solution

$$\psi = \psi_1 + \alpha\,\psi_2 = \sqrt{R(u,v)}\,[U_1V_1 + \alpha\,U_2V_2\,] \tag{4.102}$$

where the $U_i(u)V_i(v)$ are distinct eigensolutions. The constant α is determined by solving the quadratic equation

$$a\alpha^2 + b\alpha + c = 0 \tag{4.103}$$

where the coefficients are obtained by expanding (4.101) and performing the necessary quadrature. Clearly for real solutions we require $b^2 - 4ac > 0$. There are four distinct cases dependent upon the parity of V_1 and V_2. We shall now consider these differing scenarios (throughout these calculations $v = 0$, thus $R \equiv R(u,0)$ and $R_v(u,0) = 0$ and so forth).

Case I: V_1 and V_2 odd

If V_1 and V_2 are both odd then $V_1(0) = V_2(0) = 0$ and the coefficients of (4.103) are

$$a = -V_2'^2 \int_0^{2\mathbf{K}} s_1 R U_2^2\, du \tag{4.104}$$

$$b = -2V_1'V_2' \int_0^{2\mathbf{K}} s_1 R U_1 U_2\, du \tag{4.105}$$

$$c = -V_1'^2 \int_0^{2\mathbf{K}} s_1 R U_1^2\, du. \tag{4.106}$$

For $0 \le u \le 2\mathbf{K}$

$$s_1 R = c_1 + d_1 \ge 0 \tag{4.107}$$

thus for real solutions we need

$$\left[\int_0^{2\mathbf{K}} s_1 R U_1 U_2\, du\right]^2 > \int_0^{2\mathbf{K}} s_1 R U_1^2\, du \int_0^{2\mathbf{K}} s_1 R U_2^2\, du. \tag{4.108}$$

From Schwarz's Inequality (SI) (Abramowitz and Stegun, 1965, equ. 3.2.11) the left hand side of (4.108) satisfies

$$\left[\int_0^{2\mathbf{K}} (s_1 R)^{1/2} U_1 \, (s_1 R)^{1/2} U_2 \, du\right]^2 \leq \int_0^{2\mathbf{K}} s_1 R U_1^2 \, du \int_0^{2\mathbf{K}} s_1 R U_2^2 \, du \tag{4.109}$$

from which we conclude that (4.108) is not possible, and so the linear superposition of two odd V solutions will not permit an asymptotically flat γ solution.

Case II: V_1 and V_2 even

Given these assumptions it follows that $V_1'(0) = V_2'(0) = 0$ and

$$a = V_2^2 \int_0^{2\mathbf{K}} \frac{s_1}{4R}(2RU_2' + R_u U_2)^2 \, du \tag{4.110}$$

$$b = \frac{1}{2} V_1 V_2 \int_0^{2\mathbf{K}} \left(\frac{s_1}{R}\right)^{\frac{1}{2}} (2RU_2' + R_u U_2) \left(\frac{s_1}{R}\right)^{\frac{1}{2}} (2U_1' R + R_u U_1) \, du \tag{4.111}$$

$$c = V_1^2 \int_0^{2\mathbf{K}} \frac{s_1}{4R}(2RU_1' + R_u U_1)^2 \, du. \tag{4.112}$$

Again from SI we have

$$b^2 \leq \frac{1}{4} V_1^2 V_2^2 \int_0^{2\mathbf{K}} \frac{s_1}{R}(2RU_1' + R_u U_1)^2 \, du \int_0^{2\mathbf{K}} \frac{s_1}{R}(2RU_2' + R_u U_2)^2 \, du \tag{4.113}$$

therefore, $b^2 - 4ac \not> 0$ and so solutions containing two even V solutions will not suffice.

Case III: V_1 even V_2 odd

We now have $V_1'(0) = 0$ and $V_2(0) = 0$ from which we have

$$a = -V_2'^2 \int_0^{2\mathbf{K}} s_1 R U_2^2 \, du \tag{4.114}$$

$$b = 0 \tag{4.115}$$

$$c = V_1^2 \int_0^{2\mathbf{K}} \frac{s_1}{4R}(2RU_1' + R_u U_1)^2 \, du. \tag{4.116}$$

Given that $a < 0$ and $c > 0$ then $4ac < 0$ and thus real solutions are permissible.

Case IV: V_1 odd V_2 even

This situation is similar that of the previous case. a and c are interchanged and subscripts $1 \rightarrow 2$ (not s_1). It follows then the this combination also permits real solutions to (4.103).

Thus we have shown that a superposition containing V solutions of differing parity enables (4.103) to have two real solutions. Furthermore as $b = 0$ under these assumptions we have solutions of the form $\pm\alpha$. By choosing either α value, γ will then exhibit the desirable asymptotic behavior, condition (4.100), however one must be careful in the selection of which root to use. Further clarification of this point is discussed in the following section.

4.8 Multipole Moments

We now turn our attention to the calculation of the relativistic multipole moments of the metric generated by ψ solutions of the form $\psi = \sqrt{R}[U_1V_1 + \alpha U_2V_2]$. Recall* that the moments are determined by the values of the derivative of ψ (on the z-axis) with respect to $\bar{z} = 1/z$ at the point $\bar{z} = 0$ which corresponds to $u = 2\mathbf{K}$, $v \to 0^-$ in bicyclide coordinates.

We have (note the introduction of the constant μ)

$$\begin{aligned}\psi &= \mu\sqrt{\frac{c_1d_2 + d_1}{s_1c_1}}\left[U_1\,V_1 + \alpha\,U_2V_2\right] \\ &= \mu\sqrt{\frac{c_1d_2 + d_1}{c_2}}\left[\frac{U_1}{\sqrt{s_1}}V_1 + \alpha\frac{U_2}{\sqrt{s_1}}V_2\right]\end{aligned} \tag{4.117}$$

and as $u \to 2\mathbf{K}$ we have from the series representations, equations (4.67) and (4.70), and by symmetry that†

$$\lim_{u\to 2\mathbf{K}^-}\frac{U(u)}{\sqrt{\mathrm{sn}u}} \to \begin{cases} +a_0\left(\frac{k}{2}\right)^{1/2} & \text{(Even)} \\ -b_0\left(\frac{k}{2}\right)^{3/2} & \text{(Odd)}\end{cases} \tag{4.118}$$

and by appropriate selection of a_0 and b_0 we can normalize the U solutions so that

$$\lim_{u\to 2\mathbf{K}^-}\frac{U(u)}{\sqrt{\mathrm{sn}u}} \to 1.$$

This is the normalization that will be used for all subsequent calculations.

We shall now assume that V_1 represents an odd solution and V_2 an even solution. This ordering will be used throughout the remainder of this chapter.

To avoid ambiguity between labeling of the eigenvalues associated with each U_iV_i pair, h_{I} will refer to the eigenvalue associated with the first U_1V_1 solution and h_{II} with the second (refer to the eigenvalue labeling on pg. 131).

As $v \to 0$ we can use the approximations presented in section 4.6.10

$$V_1 \approx A\sinh\left(\sqrt{h_{\mathrm{I}}}\,v\right) \qquad \text{and} \qquad V_2 \approx B\cosh\left(\sqrt{h_{\mathrm{II}}}\,v\right). \tag{4.119}$$

We shall renormalize the V solutions so

$$A = B = 1. \tag{4.120}$$

Hence, for $u = 2\mathbf{K}$ and $v \to 0$ we obtain

$$\begin{aligned}\psi(v) \approx \frac{\mu k'}{\sqrt{2}}\Big[&\alpha\,v + \sqrt{h_{\mathrm{I}}}\,v^2 + \frac{1}{24}\alpha(12\,h_{\mathrm{II}} + 2 - k'^2)\,v^3 \\ &+ \frac{1}{24}A\sqrt{h_{\mathrm{I}}}\,(4h_{\mathrm{I}} + 2 - k'^2)\,v^4 + \cdots\Big].\end{aligned} \tag{4.121}$$

*See section 1.8.4.

†The following result is a manifestation of the Lame-Wangerin boundary conditions discussed in section 4.6.2, which require ψ to be bounded on the z axis.

To enable to nullify a possible dipole moment let $z \to z + \epsilon$ where ϵ is a constant and from (4.26) we define

$$\bar{z}(v) = -\frac{1}{z+\epsilon} = \frac{1-d_2}{ak's_2 - \epsilon + \epsilon d_2} \tag{4.122}$$

thus as $v \to 0$, $z \to \infty$ and $\bar{z} \to 0$. From (4.121) and (4.122) we calculate (see §1.8.4) the $(M_0 = M)$ mass moment as

$$M = -\lim_{v\to 0}\left(\frac{d\psi}{dv}\frac{dv}{d\bar{z}}\right) = -\mu\sqrt{2}\,a\,\alpha \tag{4.123}$$

and by introducing the constant m via

$$\mu = -\frac{m}{\sqrt{2}\,a\,\alpha} \tag{4.124}$$

then

$$M = m \tag{4.125}$$

so that the constant $m > 0$ now determines the mass of the gravitational source. Similarly we calculate the dipole moment as*

$$D = \frac{m(k'\epsilon\alpha + 2a\sqrt{h_{\rm I}})}{k'\alpha} \tag{4.126}$$

which is eliminated by setting

$$\epsilon = -\frac{2a\sqrt{h_{\rm I}}}{\alpha k'} = -a\,\delta. \tag{4.127}$$

In doing so the quadrupole moments becomes

$$\begin{aligned} Q &= -\frac{1}{3}m^3 - \frac{m\,a^2}{2\,k'^2}\left[k'^2 - 2 - 4h_{\rm II} + \frac{8h_{\rm I}}{\alpha^2}\right] \\ &= -\frac{1}{3}m^3 - ma^2\zeta \end{aligned} \tag{4.128}$$

which may also be nullified by setting the positive coordinate scale factor

$$a = \frac{|2\alpha k' m|}{\sqrt{6\alpha^2(4h_{\rm II} + 2 - k'^2) - 48h_{\rm I}}} \equiv a_* \tag{4.129}$$

In general

$$\begin{aligned} M_3 &= ma^3\frac{4\sqrt{h_{\rm I}}}{3\alpha k'^3}\left[h_{\rm I} - 2 + k'^2 - 9h_{\rm II} + \frac{12h_{\rm I}}{\alpha^2}\right] \\ &= ma^3\eta \end{aligned} \tag{4.130}$$

which is not possible to transform away, thus the source cannot posses equatorial symmetry.

In the previous section it was mentioned that the selection of the constant α needed some further consideration. Recall that this constant (a root of a quadratic equation) was determined so the the metric function γ was asymptotically flat. Furthermore, it must be chosen so that ψ (now containing the constant μ) behaves asymptotically in a manner that is

*When negative eigenvalues are used for $h_{\rm I}$ or $h_{\rm II}$ then the approximations for V given by (4.119) naturally transform into their trigonometric counterparts. The multipole formulae are unaltered except $h_{\rm I,II} \to |h_{\rm I,II}|$.

physical, that is, for example, in the $z = 0\,(v = 0)$ plane as $\rho \to \infty$, $\psi \propto -\rho^{-1}$. Henceforth we will determine (4.124) by using the negative root $-\alpha$ so

$$\mu = \frac{m}{\sqrt{2}\,a\,|\alpha|} > 0 \tag{4.131}$$

and choose the remaining value for α (the superposition constant) so that the correct asymptotic behaviour is evident. An example of this is given in figure 4.15(c).

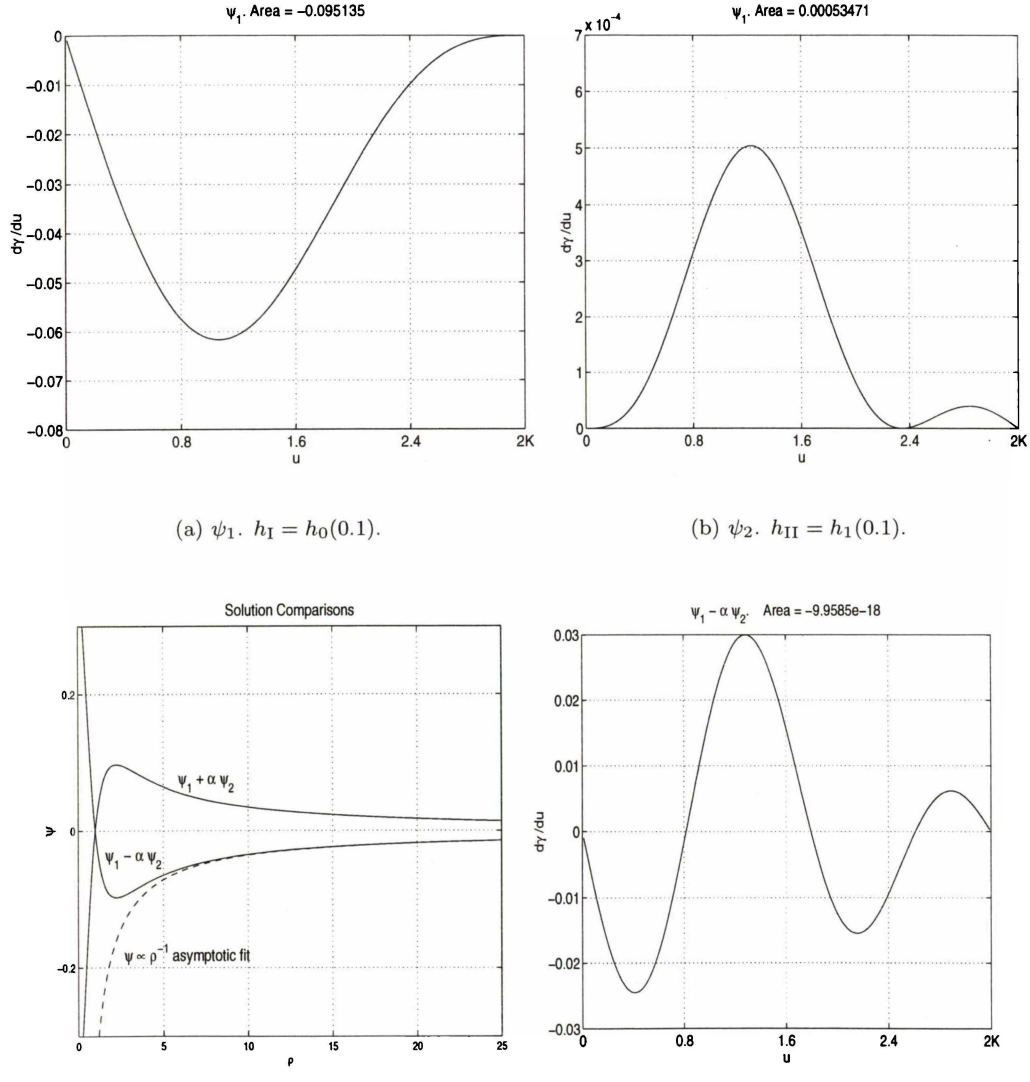

(a) ψ_1. $h_{\mathrm{I}} = h_0(0.1)$.

(b) ψ_2. $h_{\mathrm{II}} = h_1(0.1)$.

(c) $\psi_1 \pm \alpha\psi_2$

(d) $\psi_1 - 0.575798\,\psi_2$.

FIGURE 4.15: *An example of determining the sign of α. Figures (a) and (b) show $d\gamma/du$ given the individual solutions ψ_1 (with odd V_1 factor) and ψ_2 (even V_2). From (c) we see that the negative α value is needed for a physical solution. (d) shows that this linear combination of the solutions makes the area zero.*

In table 4.7, various values for the superposition constant α and the constants δ, ζ and η associated with the multipole moments are shown. The notation ψ_{101} represents the solution generated with $k = 0.1$, $h_{\mathrm{I}} = h_0$ and $h_{\mathrm{II}} = h_1$. Similarly ψ_{502} is the solution generated with $k = 0.5$, $h_{\mathrm{I}} = h_0$ and $h_{\mathrm{II}} = h_2$.

From table 4.7 we observe, that solutions that are formed with $h_{\rm I} = h_0$ and $h_{\rm II} = h_2$, i.e. both U solutions are even eigenfunctions, require a positive α value to generate solutions with the required physical behaviour. Excluding these solutions, we note as k increases, for fixed eigenvalues (eg. $\psi_{101}, \psi_{501}, \psi_{901}$), the value of the multipole moments decrease monotonically. We also note the (relativity) large moment values for the ψ_{i02} solutions.

It was possible to set a given by (4.129) so that $Q = 0$. This was only possible for U with differing parity. Results are shown in table 4.8.

	α	$-\delta$ (ϵ)	ζ (Q)	η (M_3)
ψ_{101}	-0.575798	1.736705	-2.014114	13.965977
ψ_{501}	-0.529595	1.873110	-2.448367	17.421315
ψ_{901}	-0.128476	2.840418	-6.67219	57.159351
ψ_{102}	0.022296	44.85	1998	178721
ψ_{502}	0.102035	9.72	79	1409
ψ_{902}	0.043943	8.31	34	347
ψ_{103}	-0.376864	2.653453	-18.090265	159.989336
ψ_{503}	-0.344591	2.878746	-20.823744	199.220809
ψ_{903}	-0.081900	4.455750	-44.807357	651.943

TABLE 4.7: *Constants associated with various solutions. The notation* ψ_{101} *represents the solution generated with* $k = 0.1$, $h_{\rm I} = h_0$ *and* $h_{\rm II} = h_1$.

	a_*	ϵ	$a_*^3\eta$
ψ_{101}	0.406815	0.706518	0.940293
ψ_{501}	0.368979	0.691137	0.875153
ψ_{901}	0.223515	0.634877	0.638276
ψ_{103}	0.135743	0.360187	0.400167
ψ_{503}	0.126522	0.364224	0.403488
ψ_{903}	0.086251	0.384313	0.418315

TABLE 4.8: *When* $a = a_*$ *then the quadrupole moment vanishes. The resulting* ϵ *and* M_3/m *multipole moments, given* a_*, *are listed.*

4.8.1 Classical Mass and Dipole Moments

Geroch (1970b) has shown the mass and dipole moments of any asymptotically flat Weyl solution are the same as those of the potential ψ, in flat space, generating the Weyl metric.

By introducing the new coordinate $w = u - 2\mathbf{K}$, from equations (4.25) and (4.26) we have

$$r^2 = \rho^2 + z^2 = \frac{a^2 k'^2 (\mathrm{sn}^2 w\, \mathrm{cn}^2 v + \mathrm{sn}^2 v)}{(\mathrm{cn} w\, \mathrm{dn} v - \mathrm{dn} w)^2}. \tag{4.132}$$

From the expansions (4.13)-(4.14) as $w, v \to 0$ then

$$r \sim \frac{2a}{k'} \frac{1}{\sqrt{w^2+v^2}} \equiv \frac{\sigma}{\sqrt{w^2+v^2}} \to \infty. \tag{4.133}$$

Similarly, given $z = r\cos\theta$ and $\rho = r\sin\theta$ as $w, v \to 0$ we have the asymptotic relations

$$v \sim \frac{\sigma\cos\theta}{r} \tag{4.134}$$

$$w \sim \frac{\sigma\sin\theta}{r}. \tag{4.135}$$

We have ($s_1 = \mathrm{sn}w$ etc)

$$\psi = \mu\sqrt{\frac{c_1 d_2 + d_1}{s_1 c_1}}\left[U_1 V_1 + \alpha U_2 V_2\right] = \mu\sqrt{ak'}\sqrt{\frac{s_1}{\rho}}\left[\frac{U_1}{\sqrt{s_1}}V_1 + \alpha\frac{U_2}{\sqrt{s_1}}V_2\right]. \tag{4.136}$$

From our normalization we have that $U_i/\sqrt{s_1} \to 1$ and $\sqrt{s_1} \sim \sqrt{w}$ as $w \to 0$ and $V_1 \sim \sqrt{h_\mathrm{I}}\, v$ and $V_2 \sim 1 + \frac{1}{2}h_{\mathrm{II}}v^2$ as $v \to 0$. Thus as $r \to \infty$ we have from (4.134) and (4.135)

$$\psi \approx -\mu\sqrt{ak'\sigma}\left[-\frac{\alpha}{r} - \sqrt{h_\mathrm{I}}\frac{\sigma\cos\theta}{r^2} - \frac{h_{\mathrm{II}}}{2}\alpha\frac{\sigma^2\cos^2\theta}{r^3} + \cdots\right] \qquad (r \to \infty) \tag{4.137}$$

thus the mass moment is

$$M = -\mu\sqrt{2}\alpha a \tag{4.138}$$

which agrees with the relativistic value given by (4.123) and the dipole moment

$$D = -\frac{1}{k'}\mu 2\sqrt{2}a^2\sqrt{h_\mathrm{I}} \tag{4.139}$$

also agrees with the unshifted ($\epsilon = 0$) relativistic moment given by (4.126).

4.8.2 Interpretation

The physical interpretation of the metric generated by these solutions is obscure. By considering the singular regions of ψ and γ (as commonly done eg. see Bonnor (1992) although applications to these coordinates is not discussed there) the metric could be that of two finite line masses located between the four foci* on the z axis (figure 4.2, pg. 118).

At best this is only a tentative interpretation, the exact details are somewhat hidden behind numerical results, the intractability of the coordinates and to some degree the inability to compute the Kretschmann scalar. Given that the metric does not posses equatorial symmetry (the existence of odd multipole moments) this suggests the mass per unit length in each 'bar', if believed to be a true interpretation, is not constant. Clearly further work in pin pointing the true physical nature of these metrics is needed.

In figure 4.16, the singular behaviour near the boundaries of the functions $\psi_{101}(u,v)$ and $\gamma(u,v)$ is clearly seen. The singular behaviour near the four foci on the axis is further illustrated in figure 4.17 where the functions $\psi_{101}(\rho,z)$ and $\gamma_{101}(\rho,z)$ near the z axis are shown. Figure 4.18 shows the typical behaviour of a ψ_{i02} solution. We observe when comparing with the earlier figure the singular type behaviour of the γ function is more evident near the foci on the axis. This may be related to the high multipole moments corresponding to these particular solutions.

*For the subsequent plots the foci location are given by equation (4.149) in the following section.

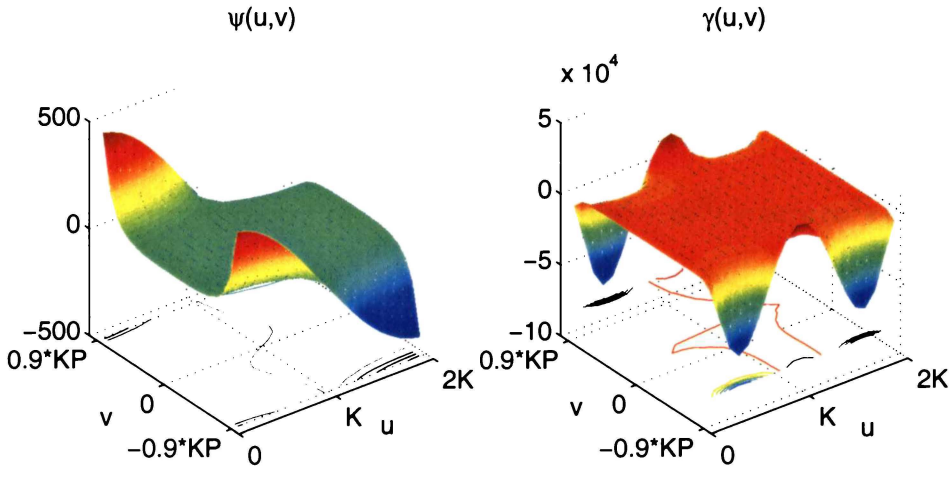

FIGURE 4.16: $\psi_{101}(u,v)$ *and corresponding* $\gamma(u,v)$ *function* $(m=1)$.

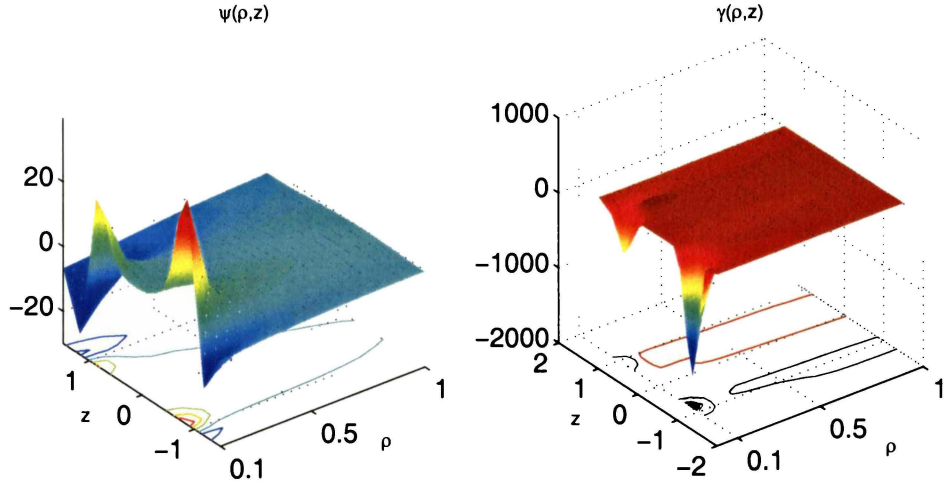

FIGURE 4.17: $\psi_{101}(\rho,z)$ *and corresponding* $\gamma(\rho,z)$ *function close to the* z *axis* $(m=1)$.

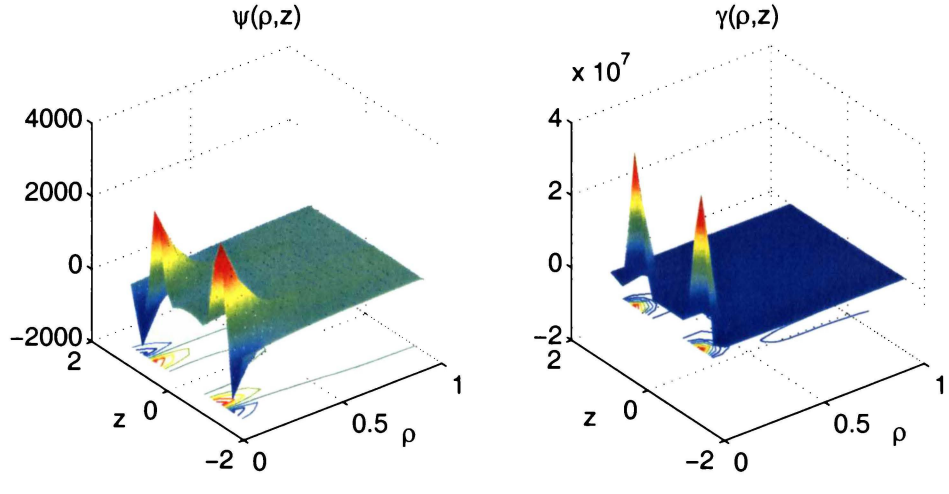

FIGURE 4.18: $\psi_{102}(\rho,z)$ *and corresponding* $\gamma(\rho,z)$ *function close to the* z *axis* $(m=1)$.

4.9 Geodesics

The previous sections have discussed the formulation of the functions ψ and γ needed to determine the metric

$$ds^2 = e^{2\psi}dt^2 - \frac{a^2k'^2\,e^{-2\psi}}{(\mathrm{cn}u\,\mathrm{dn}v + \mathrm{dn}u)^2}\left[e^{2\gamma}(1-\mathrm{dn}^2u\,\mathrm{sn}^2v)(du^2+dv^2) + \mathrm{sn}^2u\,\mathrm{cn}^2v\,d\varphi^2\right]. \quad (4.140)$$

The remainder of this chapter will concentrate on the time-like geodesics of this bicyclide space-time. To formulate the equations of motion, let

$$X(u,v) = \frac{a^2k'^2e^{-2\psi}}{(c_1d_2+d_1)^2} \qquad Y(u,v) = e^{2\gamma}(1-d_1^2s_2^2) \qquad Z(u,v) = (s_1c_2)^2 \quad (4.141)$$

from which the Lagrangian associated with (4.140) is

$$2\mathcal{L} = e^{2\psi}\dot{t}^2 - XY(\dot{u}^2+\dot{v}^2) - XZ\dot{\varphi}^2. \quad (4.142)$$

From the Euler-Lagrange equations, the cyclic coordinates t and φ enable the familiar constants E and L to be introduced by

$$\dot{t} = Ee^{-2\psi} \qquad \dot{\varphi} = -L(XZ)^{-1}. \quad (4.143)$$

The remaining geodesic equations are then

$$\ddot{u} = -\frac{1}{XY}\left[E^2\psi_u\,e^{-2\psi} + \tfrac{1}{2}(XY)_u(\dot{u}^2-\dot{v}^2) + (XY)_v\dot{u}\,\dot{v} - \frac{L^2}{2X^2Z^2}(XZ)_u\right] \quad (4.144)$$

$$\ddot{v} = -\frac{1}{XY}\left[E^2\psi_v\,e^{-2\psi} - \tfrac{1}{2}(XY)_v(\dot{u}^2-\dot{v}^2) + (XY)_u\dot{u}\,\dot{v} - \frac{L^2}{2X^2Z^2}(XZ)_v\right] \quad (4.145)$$

here subscripts refer to partial differentiation. Equations (4.143), (4.144) and (4.145) form the system of differential equations which are solved (numerically) to obtain the geodesic plots*. In determining the metric function γ we use integration path one, discussed in section 4.7.1, whilest the derivatives are computed directly from (4.87).

4.9.1 $L = 0$ Geodesics

We begin looking at the *simpler* timelike geodesics of zero angular momentum ($L = 0$). We shall consider the trajectories of test particles which start from rest ($\dot{u} = \dot{v} = 0$) at some finite distance and fall towards the source(s) located on the z axis.

Given an initial location (ρ_i, z_i) we numerically invert

$$\rho_i = \frac{ak'\,s_1(u_i)\,c_2(v_i)}{c_1(u_i)\,d_2(v_i)+d_1(u_i)} \qquad z_i = \frac{-ak'\,s_2(v_i)}{c_1(u_i)\,d_2(v_i)+d_1(u_i)} \quad (4.146)$$

to obtain the corresponding initial (u_i, v_i) values. For time-like geodesics it is possible to set $2\mathcal{L} = 1$ in (4.142). The starting location is related to the constant E by

$$\ln E = \psi(u_i, v_i). \quad (4.147)$$

*As in previous work the numerical method employed is a Runge-Kutta 4/5th order adaptive integrator.

We set in this section

$$a = \left(\frac{1-k}{1+k}\right)^{1/2} \tag{4.148}$$

so the four foci on the axis are now located at (refer to §4.4, pg 116.)

$$z = \pm 1 \ (= \pm f_1), \quad z = \pm\frac{1-k}{1+k} \ (= \pm f_2) \qquad (\rho = 0). \tag{4.149}$$

Given the multipole moments for various superpositions of ψ solutions (see table 4.7) we shall concentrate on the geodesics generated by the ψ_{101} solution, whose moments are the smaller of the various solutions.

Figure 4.19 illustrates typical $L = 0$ geodesics calculated for the ψ_{101} solution ($m = 1$). Here we have plotted $z(s)$ versus $\rho(s)$.

Plots (a)–(d) show the trajectories beginning at increasing ρ_0 positions, released from the seven z_0 values: $z_0 = \pm\epsilon$, ± 1, $\pm f_2$, 0. ϵ, given by (4.127), is the center-of-mass plane (dipole moment is null), $\pm 1, \pm f_2$ are the four foci positions given by (4.149).

It is clear that the majority of the trajectories are converging towards upper foci on the z axis. Although this does not occur for certain test particles released close to the z axis. There is no evidence of any plane for which the paths are symmetric. This is anticipated as we have shown that the odd-multipole moments are non vanishing*. In subsequent plots there does seem some symmetry in the trajectories of test particles in the field generated by the solutions ψ_{102} and ψ_{502}.

Plots (a) and (b) best illustrate some peculiar properties of test trajectories that are released from *close* vicinity of the z axis. It is useful to recall Hoenselaers (1992) comments against taking Weyl coordinates too seriously close to singularities of the potential - the observed repulsion is mostly likely to be caused by the lack of validity of the coordinates employed in regions of high curvature. This is somewhat similar to the *observed* repulsion in geodesic studies of Weyl rings (Semerák *et al.*, 1999a). It would be instead desirable to use something having more geometrical meaning so that the motion, in particular near the axis, is better portrayed.

This anti-intuitive behaviour does in any case serve to illustrate that the singularity (representing the source of the gravitational field) has a non-trivial structure - the typical directional dependence that is common for all Weyl fields (Scott, 1988). The horizon, which for Weyl fields may appear only as part of the symmetry axis (Semerák *et al.*, 1999a), is apparent when we plot coordinate time t against proper time s, for example see figure 4.21.

To provide a means of confirmation of the accuracy of the numerical integration, the system of differential equations derived from the equations of motions given in §4.9 where augmented with the additional equation

$$\ddot{t} = -2\dot{t}\,[\psi_u \dot{u} + \psi_v \dot{v}] \qquad (\dot{t} = Ee^{-2\psi}). \tag{4.150}$$

*Although these are calculated at *infinity*, the existence of non vanishing odd moments indicates non symmetry even in the vicinity of the source.

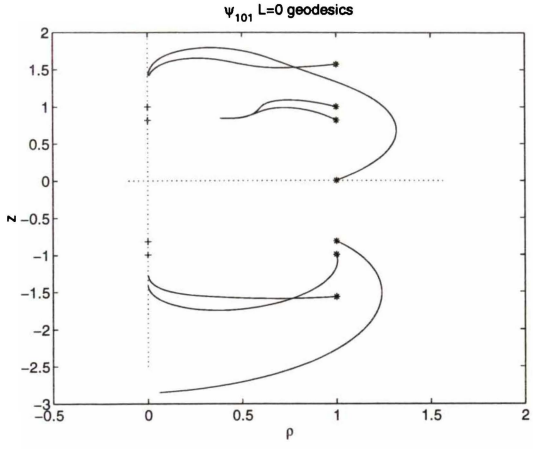

(a) $\rho_0 = 1$. Note the repulsive behaviour.

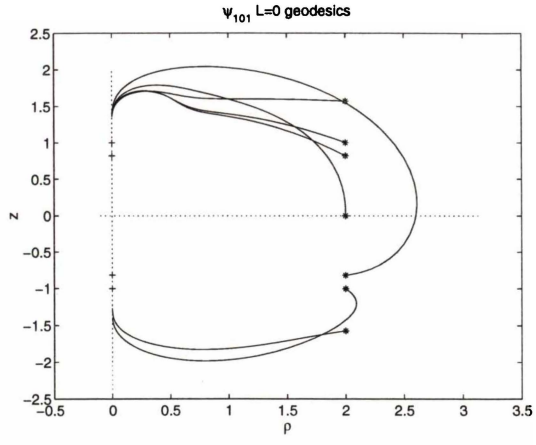

(b) $\rho_0 = 2$. Again repulsive motion is evident.

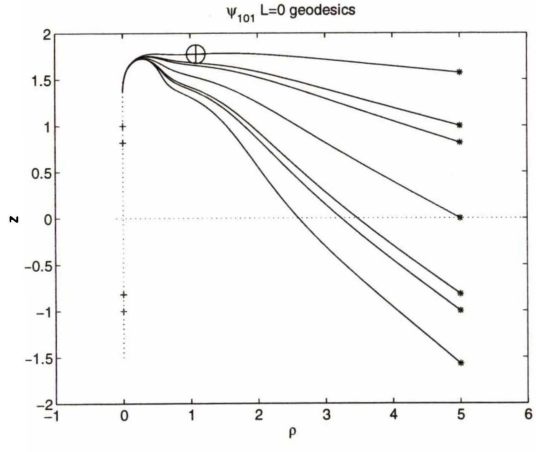

(c) $\rho_0 = 5$. The marker on the top plot refers to the same marked position on figure 4.21

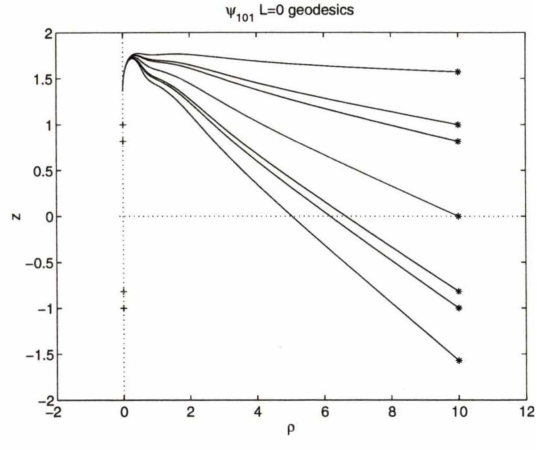

(d) $\rho_0 = 10$

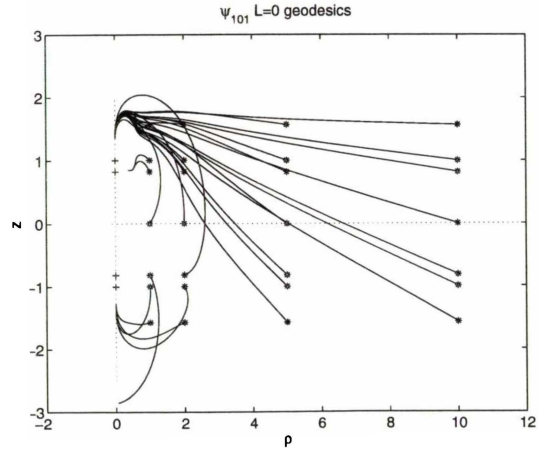

(e) Overlay of previous plots.

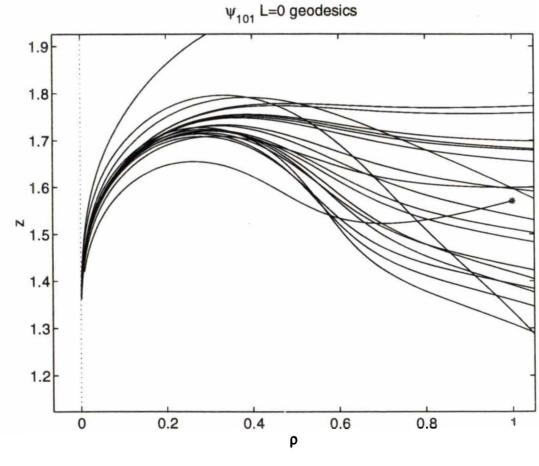

(f) Near the positive z axis.

FIGURE 4.19: *Various $L = 0$ geodesics generated with the ψ_{101} solution. Integration is terminated when $t > 1 \times 10^7$. The star indicates the initial position.*

This was done to improve the accuracy of $\dot{t}$, necessary to compute the constant E at a given s. By integrating (4.150) we compute $\dot{t}$ to $O(h^4)$, where h is the step size used by the Runge-Kutta integrator.

Typical results are shown in figure 4.20, in which the absolute difference between the initial E value and $E_{num} \equiv E(s) = \dot{t}e^{2\psi}$ is plotted, ΔE. Both plots demonstrate that the ability to conserve E diminishes as the test particle approaches the axis. In the far-field region, where the motion of the test particle is approximately linear the conservation of E is pleasing. The accuracy diminishes as the test particle approaches the axis, as indicated in figure 4.21, due to the large dt/ds values in this region.

It was also observed that ΔE decreases as the integration tolerances became smaller. A limiting value, based on the convergence of ΔE of approximately 10^{-7} was possible for the integration tolerance – this was a reflection upon the maximum accuracy possible for the numerical evaluation of $V(v)$ and $\gamma(u, v)$ functions.

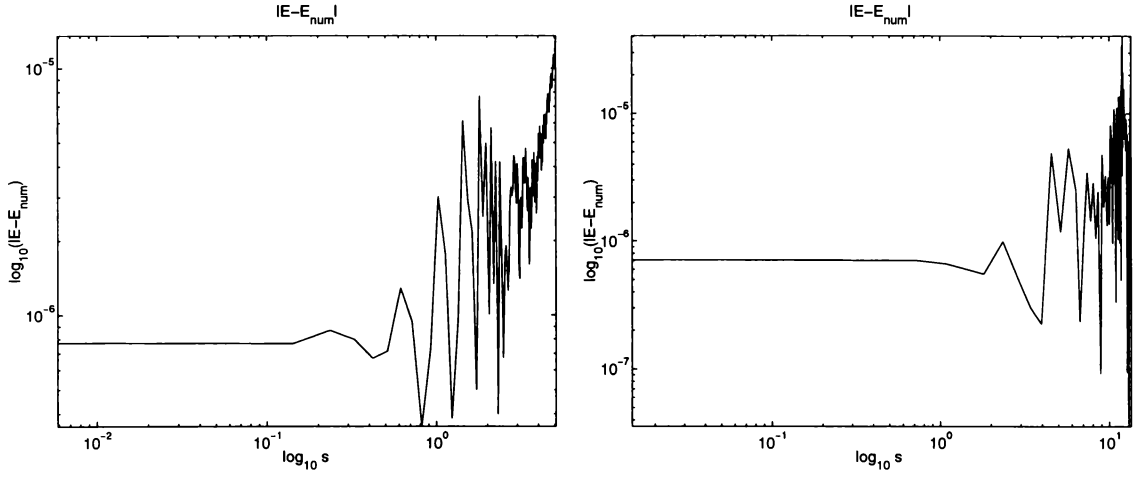

FIGURE 4.20: *Conservation of E. Here the absolute difference between E and* $E(s) = \dot{t}e^{2\psi}$ *is plotted. On the left the trajectory beginning at* $\rho_0 = 1$, $z = -\epsilon$ *is shown, while on the right, that beginning at* $\rho_0 = 5$, $z = -\epsilon$. *Both correspond to the respective* ψ_{101} *orbits shown in the previous figures 4.19(a) and 4.19(c).*

Figure 4.22 shows how the trajectories alter when the mass of the source, determined by (4.124), for the ψ_{101} solution is increased. As expected the departure from the initial linear motion becomes more rapid as m increases, a consequence of the increasing curvature. We note in the $m = 6$ plot the upper trajectory now terminates at a new position.

We conclude this section with figures 4.23, 4.24 and 4.25 which illustrate some trajectories (all released from $\rho_0 = 5$) generated with various ψ solutions other than the ψ_{101} solution. Again there are regions of repulsion close to the axis. All show the typical initial linear motion then the abrupt deflection near the axis (the bulge), this occurring at greater *distances* from the axis, as the eigenvalue is increased (eg. compare ψ_{902} vs ψ_{903} plots).

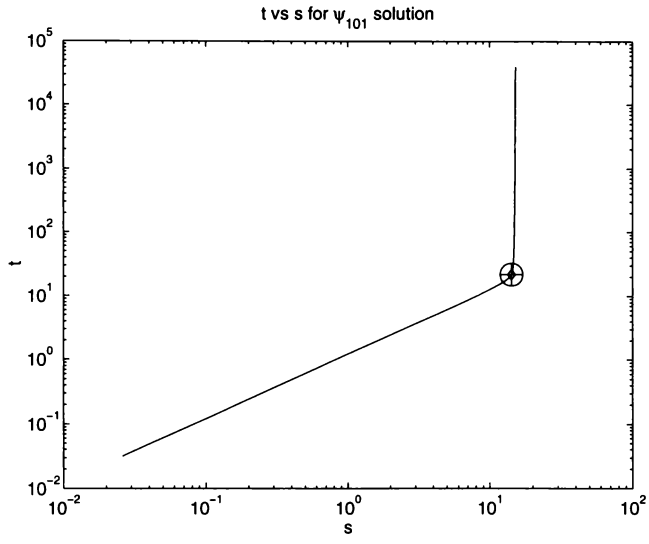

FIGURE 4.21: $\log t$ *vs* $\log s$ *for the top trajectory in figure 4.19(c). As the test particle approaches the axis the coordinate time* t *rapidly increases, indicative behaviour of a horizon.*

4.9.2 Bound Orbits

This section will concentrate on the geodesics of bounded timelike orbits generated by the two solutions formed from the ψ_{101} and ψ_{103} solutions. In section 4.8 it was shown that the coordinate scale factor a could be adjusted so that the quadrupole moment vanished. In this section we will set $a = a_*$ so that $Q = 0$. Furthermore we recall from table 4.8 that in doing so the two solutions ψ_{101} and ψ_{103} generate, respectively, fields of the maximum and minimum M_3 moments. Unless stated otherwise in all proceeding calculations $m = 1$.

For bounded orbits we have from equations (4.142) and (4.143)

$$\dot{u}^2 + \dot{v}^2 = \frac{1}{XY}\left[E^2 e^{-2\psi} - 1 - \frac{L^2}{XZ}\right] \equiv F(u, v; E; L). \tag{4.151}$$

Since the equations of motion are not separable in u and v we can only solve for the zeros of F at these points we have $\dot{u} = 0$ and $\dot{v} = 0$ simultaneously. The permitted ranges of the u and v coordinates are then fixed by the inequality $F \geq 0$. Solving F with respect to E we get

$$E^2 \geq e^{2\psi}\left(1 + \frac{L^2}{XZ}\right) \equiv V^2(u, v; L). \tag{4.152}$$

Here $V^2(u, v; L)$ is the potential function for the timelike geodesics and its graph describes a family of surfaces parameterized by L.

Figures 4.26(a) and 4.26(b) illustrate the potential *curves*, $V(\rho, z)$, for various L values for the two ψ solutions. They are drawn in the center of mass plane, that is $z = \epsilon$, so that the dipole moment is transformed away, and as already mentioned, a is also chosen so the Q moment is zero. On these potential curves the minimum points have been drawn. In figure 4.26(b) careful observation indicates further inner minimum points – we have neglected the study of trajectories beginning at these locations, as we have seen in the previous section that

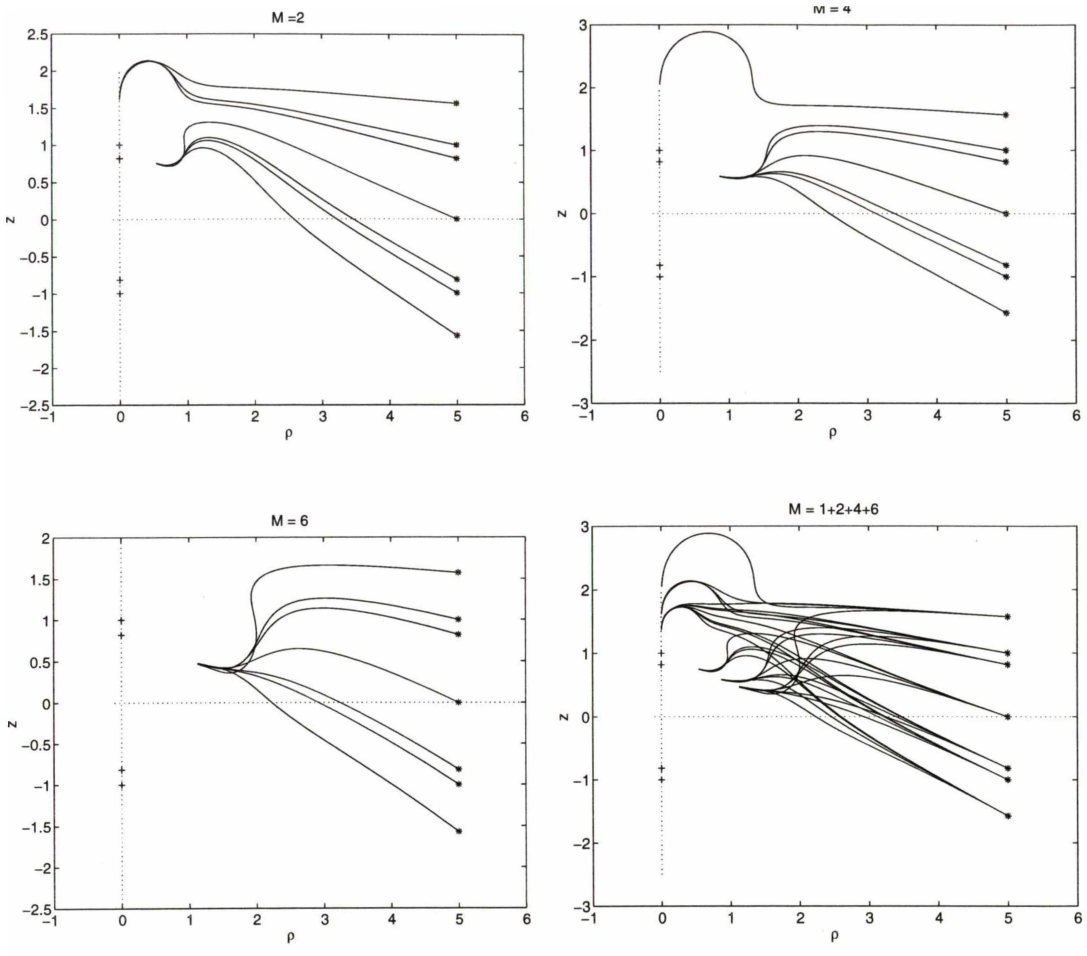

FIGURE 4.22: $L = 0$, $\rho_0 = 5$ *geodesics for the* ψ_{101}, *solution with increasing mass moment. The fourth plot includes the* $m = 1$ *plot shown in figure 4.19(c).*

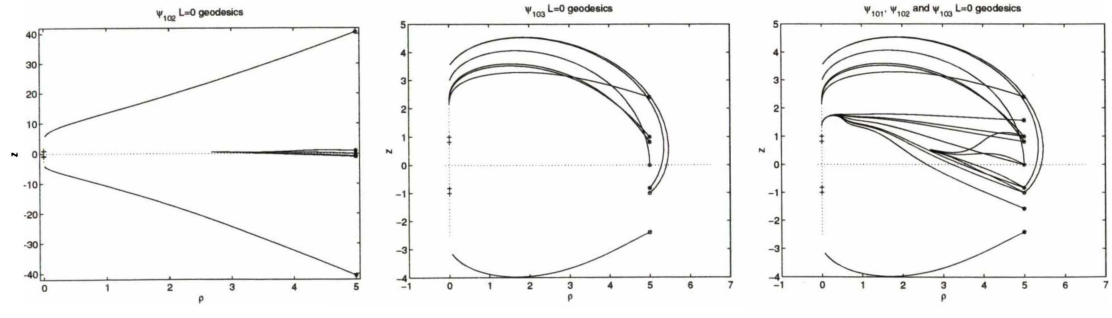

FIGURE 4.23: $L = 0$ *geodesics generated with various* $k = 0.1$ *eigenfunctions. The first plot shows the orbits for the* ψ_{102} *solution (note the apparent symmetry in the upper and lower-most trajectories). The second, those formed by the* ψ_{103} *solution. The final plot overlays the previous two plots and that of the* ψ_{101} *plot in figure 4.19(c).*

the validity of the coordinates close to the z axis is poor. We concentrate on the *outer* turning points only. We note that as $\rho \to \infty$ the locations of the minimum for the two ψ solutions coalesce.

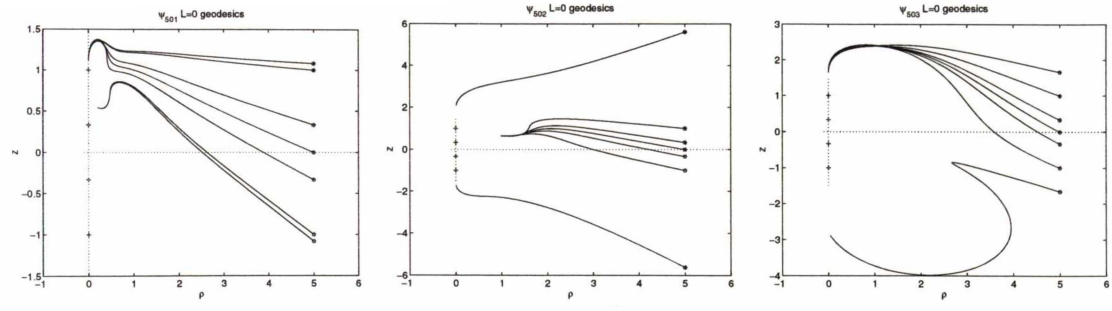

FIGURE 4.24: $L = 0$, $\rho_0 = 5$ *geodesics for the* ψ_{501}, ψ_{502} *and* ψ_{503} *solutions. Note the apparent symmetry in the two extreme geodesics of the second plot.*

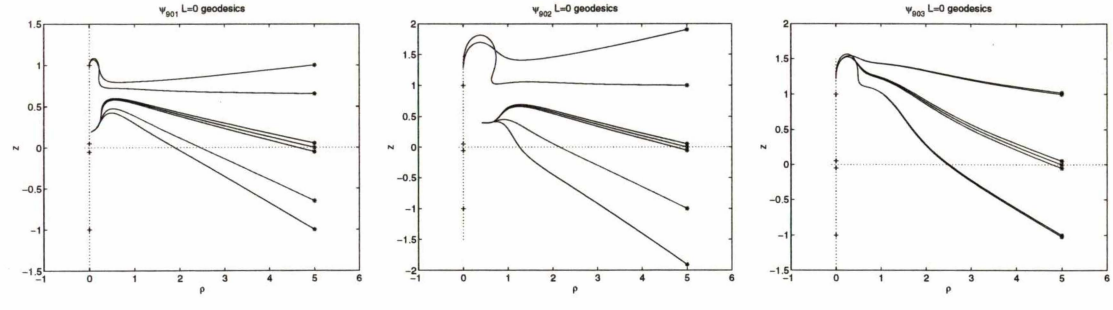

FIGURE 4.25: $L = 0$, $\rho_0 = 5$ *geodesics for the* ψ_{901}, ψ_{902} *and* ψ_{903} *solutions.*

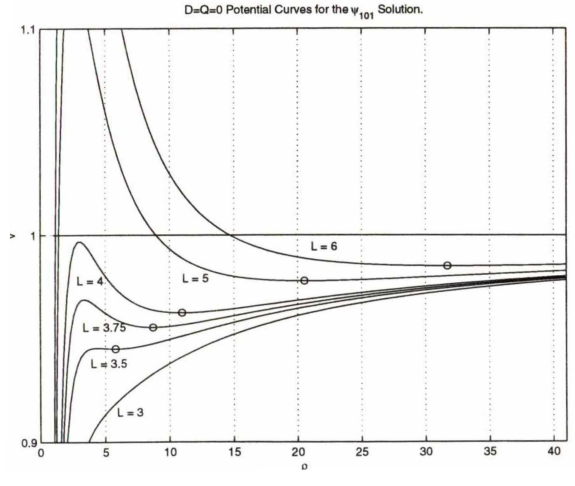

(a) ψ_{101} potential curves. The turning points, indicated by circles they occur at: ρ_{min} = 5.7976, 8.6562, 10.9551, 20.4903, 31.6847.

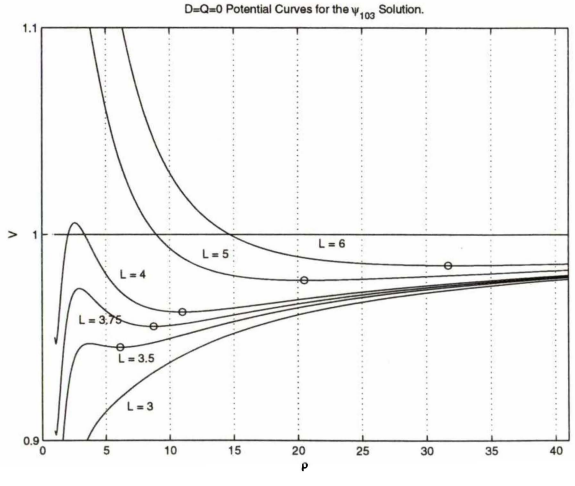

(b) ψ_{103} potential curves. Turning points occur at ρ_{min} = 6.1149, 8.7522, 10.9900, 20.5005, 31.6893

FIGURE 4.26: *Various potential curves* ($D = Q = 0$ *plane*) *for the* ψ_{101} *and* ψ_{103} *solutions.*

Furthermore it is interesting to note that broadly speaking, both potential curves resemble the potential curves of the Schwarzschild metric (Misner *et al.*, 1973; Chandrasekhar, 1983) of same parameter values (m, L).

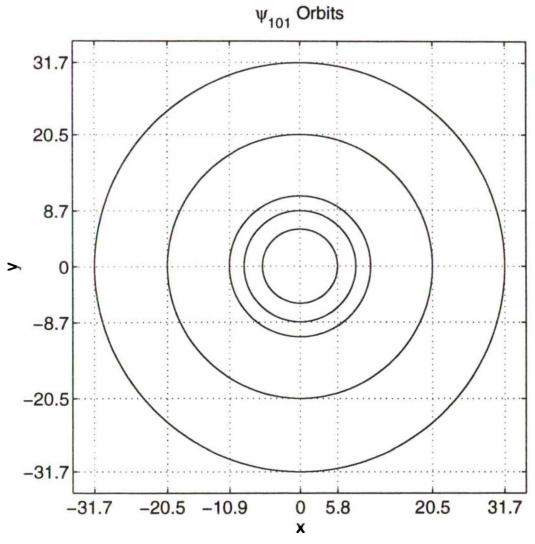

(a) The orbits, corresponding to the turning points indicted in figure 4.26(a), projected in the xy plane.

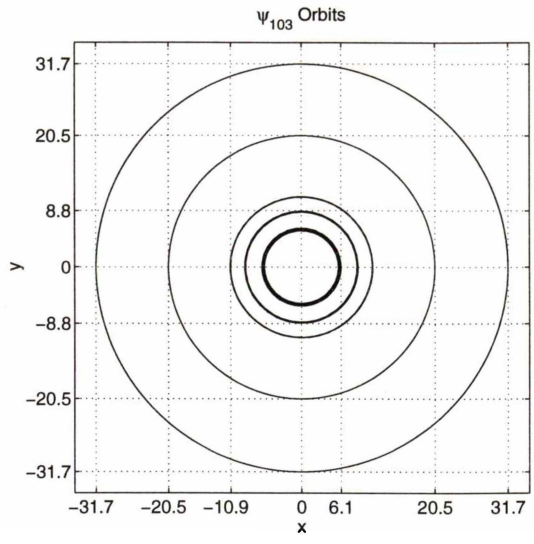

(b) The orbits, corresponding to the turning points indicted in figure 4.26(b), projected in the xy plane.

FIGURE 4.27: *Circular orbits of the ψ_{101} and ψ_{103} solutions.*

Figures 4.27 and 4.28 illustrate the orbits of test particles that are released from the minimum points indicated on the potential curves. As the higher order moments do not vanish this plane is not an invariant plane and the motion will not be confined to it – although the deviation from the initial plane for all orbits is small and the orbits are nearly circular.

As $\rho_0 \to \infty$ we would anticipate that any motion out of this plane would become less pronounced as the curvature diminishes. This is indeed observed, in particular for those orbits starting close to axis (figures 4.28(a) and 4.28(c)) the deviation is greater than those starting further out, where the gravitational field is weaker (figures 4.28(b) and 4.28(d)). This small deviation is further illustrated in figures 4.27 in which the orbits (in the xy plane) are *circular*. Some indication of this deviation is seen in the inner orbits of 4.27(b), where the trajectories become thicker.

It is also observed that the ψ_{103} orbits have less deviation from the initial plane than the ψ_{101} orbits - this is a reflection of the strength of the higher non-vanishing multipole moments. In particular the M_3 moment is smaller for the ψ_{103} solution, although the inner (figure 4.28(c)) z oscillations have a less periodic structure (c.f. figures 4.28(a)(c)(d)).

Figure 4.30 displays an orbit released from $z_0 = -\epsilon$, i.e. not in the plane that the dipole moment is null. The initial conditions are chosen so that the test particle is released from the minimum of the corresponding potential curve through this plane. It is readily observed that there is greater deviation in the z direction when compared to the earlier plots. The orbit is nearly circular however.

The final figure 4.31 shows a typical trajectory when the initial release point does not correspond to a minimum point of the potential curve. This plots complements figure 4.26(a)

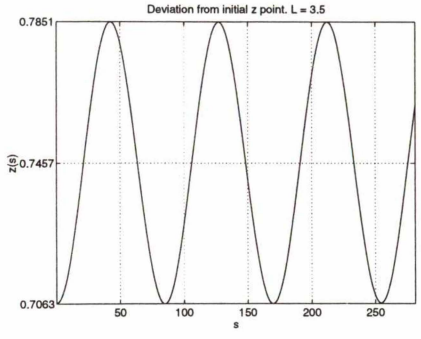

(a) $z(s)$ for the ψ_{101} solution. $\rho_0 = \rho_{min}$ $(L = 3.5)$.

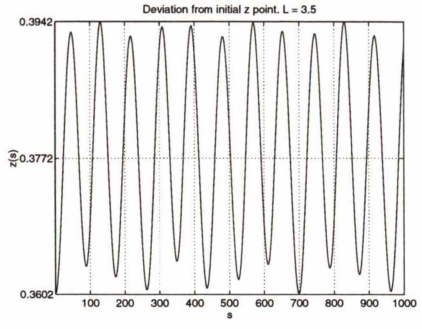

(b) $z(s)$ for the ψ_{103} solution. $\rho_0 = \rho_{min}$ $(L = 3.5)$.

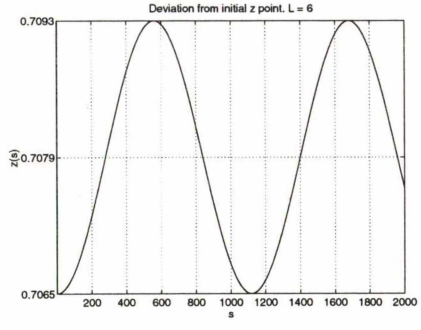

(c) $z(s)$ for the ψ_{101} solution. $\rho_0 = \rho_{min}$ $(L = 6)$.

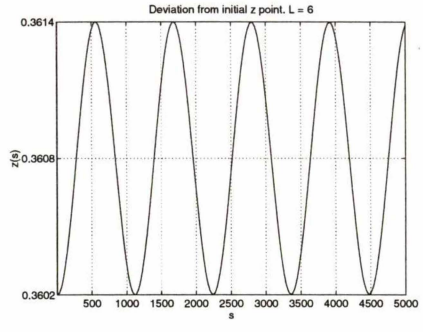

(d) $z(s)$ for the ψ_{103} solution. $\rho_0 = \rho_{min}$ $(L = 6)$.

FIGURE 4.28: *Deviations from the initial plane.*

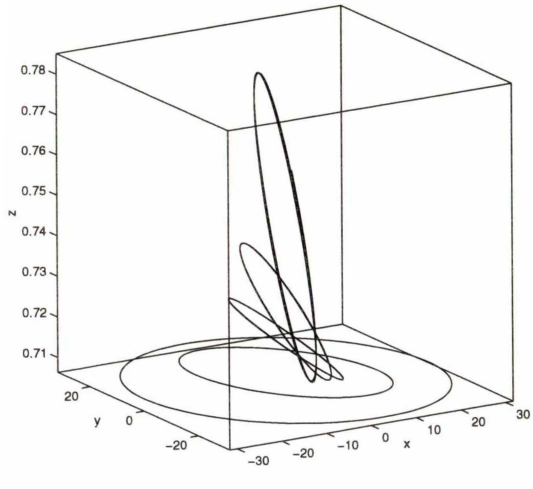

(a) ψ_{101}

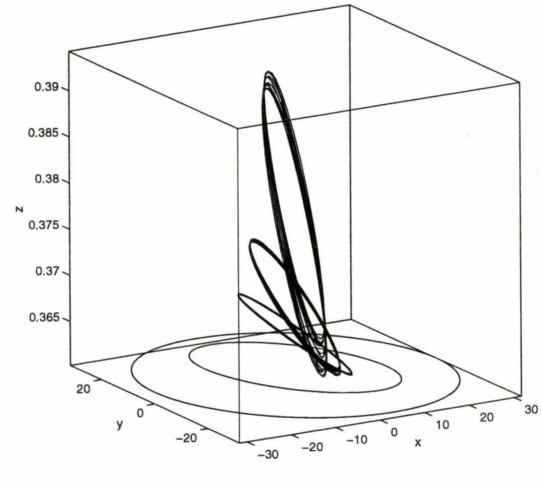

(b) ψ_{103}

FIGURE 4.29: *The respective orbits of the two differing solutions, with initial positions indicated by the turning points in the potential curves of figure 4.26. Note the vertical (z) axis is not to scale, but illustrates the relative deviations of particular orbits.*

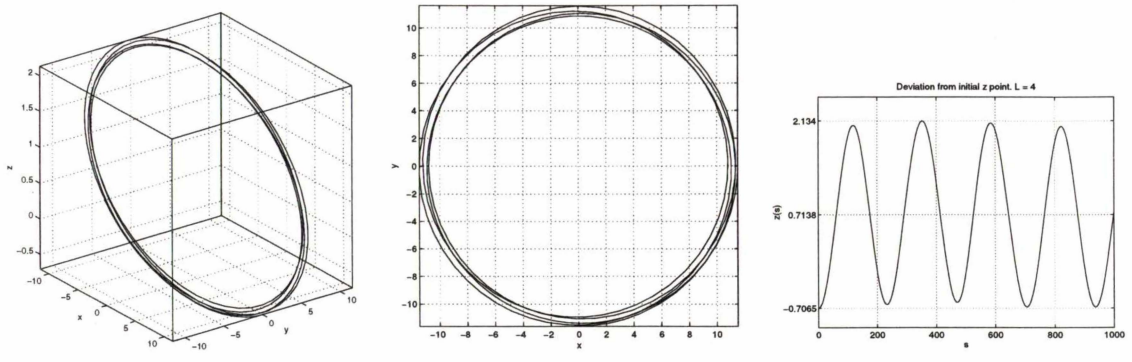

(a) Orbit (b) Projection in to the xy plane. (c) Deviation from initial plane.

FIGURE 4.30: ψ_{101} *orbit of a test particle released from* $z = -\epsilon$, $\rho_0 = \rho_{min}$, $L = 4$.

$L = 5$ plot. Here the test particle is released with perihelion value $\rho_o \approx 15$. From the potential curve we anticipate an aphelion value ≈ 30 if, as we know is incorrect, the motion is confined to the plane.

Nevertheless as the motion out of this plane (figure 4.31(c)) is relatively minimal, to a good level of approximation the orbit does obtain these aphelion and perihelion values, as shown in figure 4.31(b).

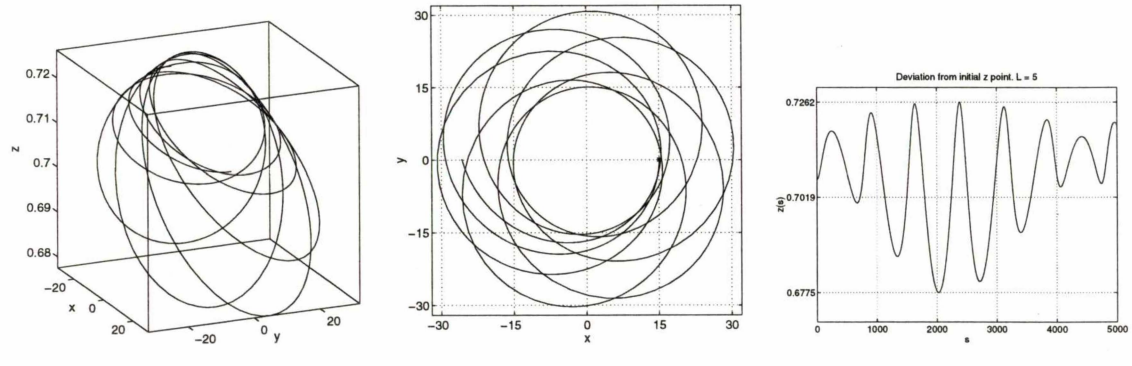

(a) Orbit (b) Projection in to the xy plane. (c) Deviation from initial plane.

FIGURE 4.31: ψ_{101} *orbit of a test particle released from* $z = \epsilon$, $\rho_0 \approx 15$, $L = 5$.

4.10 Summary

This chapter has developed the essential features required to study the Weyl space time in terms of bicyclide coordinates.

Calculating the harmonic function ψ required the construction of Lamẽ-Wangerin eigenfunctions, which were dependent upon the accurate determination of eigenvalues.

The eigenvalues where calculated using a truncated *infinite* continued fraction and verified using numerical methods. An approximation to the U solutions in terms of Bessel functions was given and shown for all but the (numerical) lowest eigenfunctions, to agree well with the true solution. Similar methods to solve the second separable equation for V proved to be unsuccessful and the numerical determination of these functions was required. Approximations near $v = 0$ were possible which proved paramount in subsequent calculations regarding the multipole structure of the generated field.

Calculating the remaining metric function γ was determined via numerical quadrature. Evidence was given to support the requirement that the line integral was path independent, or at least to approximately, the same level of accuracy of the numerical solution V for which the integrals contained. It was further shown that to satisfy the condition of elementary flatness the superposition of at least two particular ψ solutions was necessary. Analysis showed that only solutions with specific parity could enable the boundary conditions to be met.

Using appropriate approximations for the eigensolutions on the z axis, the multipole moments where obtained, and it was evident by the non vanishing of the higher odd multipole moments that the fields generated by various superpositions of eigensolutions did not have an invariant plane for which geodesics motion would be confined. This is subsequently shown in the numerical solution of the time like geodesic trajectories, although the deviation out of certain planes, namely those for which the dipole and quadrupole moments vanished, was relatively small. This deviation was enhanced when the motion was started from planes for the dipole and quadrupole moment were not nullified. The use of potential curves served under certain criteria to give good approximations of aphelion and perihelion values of elliptic orbits.

Timelike geodesics of zero angular momentum where also presented. Generally, the initial motion was of a radial type, although all experienced some deviation and repulsion before terminating close to the horizon on the z axis. The interpretation of this repulsion region is still unclear but as often experienced in geodesic studies of Weyl fields, it is not wise to attach physical meaning on the coordinates near regions of high curvature.

The physical interpretation of the sources generating these fields is still obscure. The singular regions of ψ would indicate that the field is that of two finite line masses located between the two pairs of foci. This is a tentative prediction as, for example, no attempt to compute the Kretschmann scalar, which is often employed to probe the locations of the sources (and directional behaviour), was not made. This is an obvious extension to this chapter.

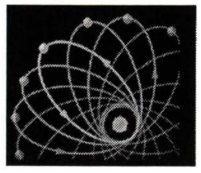

Chapter 5
Review and Future Work

In this thesis we have presented new axially symmetric static spacetimes and examined certain timelike geodesics within these solutions.

Our studies have generally concentrated on trajectories of test particles that are confined to equatorial planes. The predictions based on the relativistic multipole moments agreed well with the numerical values of the precession rates of the perihelion.

Small deviations from circular orbits were discussed in the bispherical chapter and the corresponding precession of the nodes was calculated, again numerical and theoretical results were consistent. Similar calculations could be carried out for the ring like solutions developed in the toroidal chapter. Of course for both coordinate systems we could further generalize by relaxing the assumption that the out-of-the plane geodesics slightly deviates from the reference circular orbit.

One common thread for all coordinate systems considered here was the repulsive like behaviour observed for geodesics of zero angular momentum. Attempts in the bispherical chapter to introduce a more physical radial coordinate in which to plot the trajectories failed to solve this enigma. Further study is needed here to understand this phenomena.

The toroidal solutions warrant a special mention. Contrary to Newtonian mechanics it was observed if the mass of the source was greater than a certain value the period of the oscillation for a test particle along the z axis increased as the mass of the source increased. The ergodic nature of certain orbits is also surprising. There is also the interesting case of oscillating trajectories along the ρ axis ($L = 0$) in the $n = 0 + 1$ solution.

The beauty of the bispherical and toroidal solutions presented here is that they are exact. This was clearly not possible in the bicyclide chapter. The physical nature of the sources for the solutions developed here are uncertain. Although geodesics were produced no attempts to calculate precession rates of perihelion and nodes was done. Incidentally, this could be used to verify the multipole moments calculated based on the approximate solutions to the metric functions.

Finally, throughout we have concentrated on timelike geodesics. Clearly an examination of the null geodesics in these spacetimes remains.

Bibliography

Abramowitz, M. and Stegun, I., editors, Handbook of Mathematical Functions. Dover (1965).

Armenti, Jr., A., "A classification of particle motions in the equatorial plane of a gravitational monopole-quadrupole field in Newtonian mechanics and general relativity." *Celestial Mech.* **6**, 383 (1972).

Arscott, F. M., Periodic Differential Equations. An Introduction to Mathieu, Lamé, and Allied Functions. Pergamon Press (1964).

Bach, R. and Weyl, H., "Neue Lösungen der Einsteinschen Gravitationsgleichungen. B. Explizite Aufstellung statischer axialsymmetrischer Felder. Mit einem Zusatz über das statische Zweikörperproblem von H. Weyl." *Mathematische Zeitschrift* **13**(134) (1922).

Beig, R., "The multipole expansion in general relativity." *Acta Phys. Austriaca* **53**(4), 249 (1981).

Beig, R. and Simon, W., "On the multipole expansion for stationary space-times." *Proc. Roy. Soc. Lond. Ser. A.* **376**(1765), 333 (1981a).

Beig, R. and Simon, W., "Proof of a multipole conjecture due to Geroch." *Comm. Math. Phys.* **78**(1), 75 (1981b).

Bergmann, P. G., Introduction to the Theory of Relativity. Prentice-Hall (1942).

Birkhoff, G. and Rota, G. C., Ordinary Differential Equations. Ginn & Co. (1962).

Bičák, J., Lynden-Bell, D. and Katz, J., "Relativistic disks as sources of static vacuum space-times." *Phys. Rev. D.* **47**(4334) (1993).

Bondi, H. and Rindler, W., "The multipole expansion far from an isolated source." *Gen. Relativity Gravitation* **23**(4), 487 (1991).

Bonnor, W. B., "Physical interpretation of vacuum solutions of Einstein's equations. Part I. Time-independent solutions." *Gen. Relativity Gravitation* **24**(5), 551 (1992).

Bowman, F., Introduction to Elliptic Functions. English Universities Press (1953).

Carminati, J. and Sarracino, R. S., "R-separable solutions of Einstein's field equations." *J.Phys. A: Math. Gen.* **15**, 2401 (1981).

Chandrasekhar, S., The Mathematical Theory of Black Holes. The International Series of Monographs on Physics, Clarendon Press (1983).

Clarke, C. J. S. and Sciama, D. W., "Static gravitational multipoles—the connection between field and source in general relativity." *Gen. Relativity Gravitation* **2**, 331 (1971).

Cooperstock, F.I. and Junevicus, G.J., "Singularities in Weyl gravitational fields." *Int. J. Theo. Physics.* **9**(59) (1974).

Curzon, H. E. J., "Bipolar solutions of Einstein's gravitation equations." In "Proceedings of the London Mathematical Society," volume 23, page 447 (1924).

de Felice, F., "Potential surfaces for time-like geodesics in the Curzon metric." *Gen. Relativity Gravitation* **23**(2), 135 (1991).

de Felice, F. and Clarke, J. S., Relativity on Curved Manifolds. Cambridge Monographs on Mathematical Physics, Cambridge University Press (1990).

Dietz, W. and Hoenselaers, C., "Stationary system of two masses kept apart by their gravitational spin-spin interaction." *Phys. Rev. Lett.* **48**(12), 778 (1982).

Doroshkevich, A. G., Zel'dovich, Ya. B. and Novikov, I. D., "Gravitational collapse of non-symmetric and rotating masses." *Soviet Physics JETP* **22**(122) (1966).

Einstein, A. and Rosen, N., "Two-body problem in general relativity." *Phys. Rev.* **49**(404) (1936).

Erdélyi, A., Magnus, W., Oberhettinger, F. and Tricomi, F. G., editors, Higher Transcendental Functions, volume III. McGraw-Hill (1955a).

Erdélyi, A., Magnus, W., Oberhettinger, F. and Tricomi, F. G., editors, Higher Transcendental Functions, volume II. McGraw-Hill (1955b).

Erez, G. and Rosen, N., "The gravitational field of a particle possessing a multipole moment." *Bull. Res. Council Israel Sect. F* **8F**, 47 (1959).

Fernández-Jambrina, L. and Hoenselaers, C., "High order relativistic corrections to Keplerian motion." *J. Math. Phys.* **42**(2), 839 (2001).

Flammer, C., Spheroidal Wave functions. Stanford University Press (1957).

Fodor, G., Hoenselaers, C. and Perjés, Z., "Multipole moments of axisymmetric systems in relativity." *J. Math. Phys.* **30**(10), 2252 (1989).

Gautreau, R., "On equipotential areas and directional singularities." *Phys. Lett.* **28A**, 606 (1969).

Gautreau, R. and Anderson, J. L., "Directional singularities in Weyl gravitational fields." *Phys. Lett.* **25A**, 291 (1967).

Geroch, R., "Multipole moments. I. Flat Space." *J. Math. Phys.* **11**(6), 1955 (1970a).

Geroch, R., "Multipole moments. II. Curved Space." *J. Math. Phys.* **11**(8), 2580 (1970b).

Gleiser, Reinaldo J. and Pullin, Jorge A., "Appell rings in general relativity." *Classical Quantum Gravity* **6**(7), 977 (1989).

Goldstein, H., Classical Mechanics. Addison-Wesley Publishing Co., Reading, Mass., second edition (1980).

Gradshteyn, I. S. and Ryzhik, I. M., Table of Integrals, Series, and Products. Academic Press (1980).

Hansen, R. O., "Multipole moments of stationary space-times." *J. Math. Phys.* **15**, 46 (1974).

Hawking, S. W. and Ellis, G. F. R., The large scale structure of space-time. Cambridge University Press (1973), Cambridge Monographs on Mathematical Physics, No. 1.

Henry, R. C., "Kretschmann scalar for a Kerr-Newman black hole." *Astrophys. J.* **535**, 350 (2000).

Hernandez, W. C. *Phys. Rev.* **153**, 1359 (1967).

Hernãndez-Pastora, J. L. and Martin, J., "Monopole-quadrupole static axisymmetric solutions of Einstein's equations." *Gen. Relativity Gravitation* **26**(9), 877 (1994).

Herrera, L. and Hernández-Pastora, J. L., "Measuring multipole moments of Weyl metrics by means of gyroscopes." *J. Math. Phys.* **41**(11), 7544 (2000).

Herrera, L., Paiva, F. M. and Santos, N. O., "Geodesics in the γ spacetime." *Internat. J. Modern Phys. D* **9**(6), 649 (2000).

Hoenselaers, C., "On multipole moments in general relativity." In "Proceedings of the 14th Yamada Conference on Gravitational Collapse and Relativity," pages 176–185, Singapore: World Scientific (1986).

Hoenselaers, C., "Axisymmetric stationary solutions of Einstein's equations." In "Rotating Objects and Relativistic Physics," pages 29–53, Springer-Verlag (1992).

Hoenselaers, C., "The Weyl solution for a ring in a homogeneous field." *Class. Quantum Grav.* **12**, 141 (1995).

Hoenselaers, C. and Ernst, F. J., "Remarks on the Tomimatsu-Sato metrics." *J. Math. Phys.* **24**(7), 1817 (1983).

Ince, E. L., "The periodic Lamé functions." *Proc. Roy. Soc. Edin.* **60**, 47 (1940).

Islam, J. N., Rotating fields in General Relativity. Cambridge University Press (1985).

Israel, W., "Line sources in general relativity." *Phys.Rev D.* **15**, 935 (1977).

Khare, A. and Sukhatme, U., "New solvable and quasiexactly solvable periodic potentials." *J. Math. Phys.* **40**(11), 5473 (1999).

Kramer, D., Stephani, K., Herlt, K. E. and MacCallum, M., Exact Solutions of Einstein's Field Equations. Cambridge University Press (1980).

Krori, K. D. and Sarmah, J. C., "A geodesic study of the Erez-Rosen space-time." *Gen. Relativity Gravitation* **23**(7), 801 (1991).

Kundu, P., "Multipole expansion of stationary asymptotically flat vacuum metrics in general relativity." *J. Math. Phys.* **22**(6), 1236 (1981a).

Kundu, P., "On the analyticity of stationary gravitational fields at spatial infinity." *J. Math. Phys.* **22**(9), 2006 (1981b).

Lagrange, R., "Les familles de surfaces de révolution qui possèdent des harmoniques." *Acta. Math.* **71**, 283 (1939).

Lagrange, R., "Sur une classe d'harmoniques associés aux cyclides de révolution." *Bull. Soc. Math. France* **72**, 169 (1944).

Landau, L. D. and Lifshitz, E. M., Classical Theory of Fields. Pergamon Press (1971).

Lebedev, N. N., Special Functions and their Applications. Dover (1972).

Levi-Civita, T. *Atti della Accad. dei Lincei Rendiconti* **27**(2) (1918).

Magnus, W., Oberhettinger, F. and Soni, R. P., Formulas and Theorems for the Special Functions of Mathematical Physics. Springer-Verlag, third edition (1966).

Marek, J. J. J. *Phys. Rev.* **163**, 1373 (1967).

Martin, J., Ruiz, E. and Senosiain, M. J., Multipole particles in general relativity: The Weyl and Kerr Metrics. Number 212 in Lecture Notes in Physics, Springer-Verlag (1984), p. 29–39.

McCrea, W. H. and Newing, R. A. *Proc. Lond. Math. Soc.* **2**(37), 520 (1933).

Mikkola, S., Palmer, P. and Hashida, Y., "An implementation of the logarithmic Hamiltonian method for artificial satellite orbit determination." *Celestial Mech. Dynam. Astronom.* **82**(4), 391 (2002).

Miller, W. Jnr., Symmetry and Separation of Variables, volume 4 of *Encyclopedia of Mathematics and its Applications*. Addison-Wesley Publishing Company (1977).

Misner, C. W., Thorne, K. S. and Wheeler, J. A., Gravitation. Freeman (1973).

Misra, M., "Some axially symmetric empty gravitational fields." *Proc. Natl. Inst. Sci. India* **A26**(673) (1960).

Misra, M., "The external gravitational fields due to toroidal and lens-shaped distributions." *Proc. Natl. Inst. Sci. India* **A27**(373) (1961).

Moon, P. and Spencer, D. E., Field Theory Handbook. Including coordinate systems, differential equations and their solutions. Springer-Verlag, second edition (1988).

Morgan, L. and Morgan, T., "Gravitational field of shells and disks in general relativity." *Phys. Rev. D (3)* **2** (1970).

Olver, F. W. J., Asymptotics and Special Functions. AKP Classics, A K Peters. (1997), reprint of the 1974 original [Academic Press].

Perlick, V., "Bertrand spacetimes." *Class. Quantum Grav.* **9**(4), 1009 (1992).

Perron, O., Die Lehre von den Kettenbrüchen. Leipzig: B.G. Teubner (1929).

Piquette, J. C. and Van Buren, A. L., "Technique for evaluating indefinite integrals involving products of certain special functions." *Siam J.Math Anal.* **15**(4), 845 (1984).

Poole, E. G. C., "Dirichlet's principle for a flat ring." *Proc. Lond. Math. Soc.* **2**(29), 342 (1929).

Poole, E. G. C., "Dirichlet's principle for a flat ring." *Proc. Lond. Math. Soc.* **2**(30), 174 (1930).

Press, W. H., Flannery, B. P., Teukolsky, S. A. and Vetterling, W. T., Numerical recipes. Cambridge: Cambridge University Press (1986), the art of scientific computing.

Quevedo, H., "Class of stationary axisymmetric solutions of Einstein's equations in empty space." *Phys. Rev. D (3).* **33**(2), 324 (1986).

Quevedo, H., "Multipole moments in general relativity – static and stationary vacuum solutions." *Fortschritte Der Physik* **38**(10), 733 (1990).

Quevedo, H. and Parkes, L., "Geodesics in the Erez-Rosen spacetime." *Gen. Relativity Gravitation* **23**(4), 495 (1991).

Regan, H. M., "Von Neumann stability analysis of symplectic integrators applied to Hamiltonian PDEs." *J. Comput. Math.* **20**(6), 611 (2002).

Ritter, S., "On the computation of Lamé functions, of eigenvalues and eigenfunctions of some potential operators." *Z. Angew. Math. Mech.* **1**(78), 66 (1998).

Scott, S. M., "A survey of the Weyl metrics." In R. Bartnik, editor, "Conference on Mathematical Relativity,," pages 175–195, Centre for Mathematical Analysis, Australian National University (1988).

Scott, S. M. and Szekeres, P., "The Curzon singularity. I: Spatial Sections." *Gen. Relativity Gravitation* **18**(6), 557 (1986a).

Scott, S. M. and Szekeres, P., "The Curzon singularity. II: Global Picture." *Gen. Relativity Gravitation* **18**(6), 571 (1986b).

Semerák, O., "Circular orbits in stationary axisymmetric spacetimes." *Gen. Relativity Gravitation* **30**(8), 1203 (1998).

Semerák, O., Žáček, M. and Zellerin, T., "Test-particle motion in superposed Weyl fields." *Mon. Not. R. Astron. Soc.* **308**, 705 (1999a).

Semerák, O., Zellerin, T. and Žáček, M., "The structure of superposed Weyl fields." *Mon. Not. R. Astron. Soc.* **308**, 691 (1999b).

Sengupta, S., "Charged particle trajectories in a toroidal magnetic and rotation-induced electric field around a black hole." *Internat. J. Modern Phys. D.* **6**(5), 591 (1997).

Silberstein, L., "Two-centers solution of the gravitational field equations, and the need for a reformed theory of matter." *Phys. Rev.* **49**, 268 (1936).

Snow, C., "Hypergeometric and Legendre functions with applications to integral equations of potential theory." National Bureau of Standards (1952), Applied Mathematics Series 19.

Spiegel, M. R., Schaum's Outlines: Mathematical Handbook. McGraw-Hill (1997).

Stewart, B. W., Papadopoulos, D., Witten, L., Berezdivin, R. and Herrera, L., "An interior solution for the gamma metric." *Gen. Relativity Gravitation* **14**(1), 97 (1982).

Synge, J. L., Relativity: The General Theory. North-Holland (1960).

Szego, G., Orthogonal Polynomials, volume XXIII of *Colloquium Publications*. American Mathematical Society (1939).

Szekeres, P., "Multipole particles in equilibrium in general relativity." *Physical Review* **176**(5), 1446 (1968).

Tang, Yi-Fa, Xiao, Ai-Guo and Chen, Jing-Bo, "Is the formal energy of the mid-point rule convergent?" *Comput. Math. Appl.* **43**(8-9), 1171 (2002).

Thorne, K. S., "Multipole expansions of gravitational radiation." *Reviews of Modern Physics* **52**(2), 299 (1980).

Voorhees, B. H., "Static axially symmetric gravitational fields." *Phys. Rev. D.* **2**, 2119 (1970).

Wangerin, A., Reduction der Potentialgleichung fur gewisse Rotationskorper auf eine gewohnliche Differentialgleichung. Leipzig: S.Hirzel (1875).

Weyl, H., "Zur Gravitationstheorie." *Ann.Phys.* **54**(117) (1917).

Weyl, H., "Bemerkung über die axialsymmetrischen Lösungen der Einsteinschen Gravitationsgleichungen." *Ann.Phys.* **59**(185) (1919).

Whittaker, E. T. and Watson, G. N., Modern Analysis. Cambridge University Press (1940).

Zel'dovich, Ya. B. and Novikov, I. D., "Relativistic astrophysics. I." *Soviet Physics Uspekhi* (1965).

Zel'dovich, Ya. B. and Novikov, I. D. *Relyativistskaya Astrofizika* **106** (1967).

Zipoy, D. M., "Topology of some spheroidal metrics." *J. Math. Phys.* **7**(6), 1137 (1966).

We live in a Newtonian world of Einsteinian physics ruled by Frankenstein logic.

— David Russell —

There was a blithe certainty that came from first comprehending the full Einstein field equations, arabesques of Greek letters clinging tenuously to the page, a gossamer web.
They seemed insubstantial when you first saw them, a string of squiggles.
Yet to follow the delicate tensors as they contracted, as the superscripts paired with subscripts, collapsing mathematically into concrete classical entities
– potential; mass; forces vectoring in a curved geometry –
that was a sublime experience.
The iron fist of the real, inside the velvet glove of airy mathematics.

— Gregory Benford - Timescape —